Coupled-channel dynamics in hadronic systems

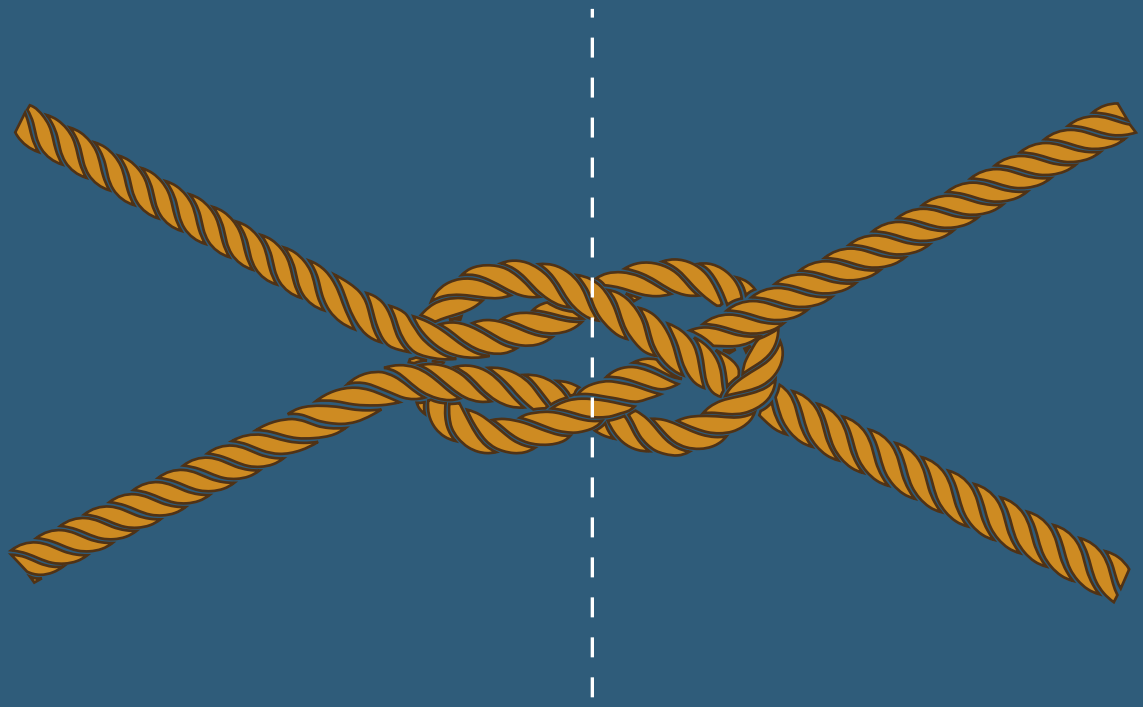

Oleksandra Deineka

Coupled-channel dynamics in hadronic systems

Dissertation
zur Erlangung des Grades
„ Doktor der Naturwissenschaften “

am Fachbereich Physik, Mathematik und Informatik
der Johannes Gutenberg-Universität Mainz

vorgelegt von
Oleksandra Deineka
geboren in Kyiv (Ukraine)

Mainz, 2022

Abstract

The description of the hadron dynamics still challenges modern theoretical physics. The current approaches are striving to meet the demands of increasing experimental precision. They either incorporate the massive amounts of data in various channels or rely on the theoretical assumptions, which are valid only in a limited number of cases. In this context, it is crucial to develop techniques which allow the accurate description of the existing data and simultaneously have a predictive power achieved through their model-independent nature. This thesis is dedicated to the partial-wave dispersion relation approach, which is built upon the fundamental properties of the scattering matrix, such as unitarity and analyticity.

We first apply this approach to study the S-wave $\pi\pi \to \pi\pi$ and $\pi K \to \pi K$ reactions, in which the lightest scalar resonances $\sigma/f_0(500)$, $f_0(980)$ and $\kappa/K^*(700)$ show up. The contributions from the left-hand cuts are accounted for using the power expansion in a suitably constructed conformal variable. The expansion coefficients are determined in a data-driven manner by fitting the phase shifts to experimental and lattice data as well as Roy analyses. For the $\pi\pi$ scattering, we present both a single- and coupled-channel analysis by additionally including the $K\bar{K}$ channel. For the latter, the central result is the Omnès matrix, which is consistent with the most recent dispersive results on $\pi\pi \to \pi\pi$ and $\pi\pi \to K\bar{K}$, respectively. By performing an analytic continuation to the complex plane, we found poles associated with the resonances $\sigma/f_0(500)$, $f_0(980)$ and $\kappa/K^*(700)$ for the physical pion mass value and in the case of $\sigma/f_0(500)$, $\kappa/K_0^*(700)$ also for unphysical pion mass values.

The knowledge of the $\pi\pi \to \pi\pi$ amplitude allows us to perform a dispersive analysis of the double-virtual photon-photon scattering to two pions which is very sensitive to hadronic final state interaction through unitarity. This process is particularly important since it contributes to the hadronic light-by-light scattering part of the anomalous magnetic moment of the muon. For the S-wave, we use the obtained coupled-channel $\pi\pi$, $K\bar{K}$ Omnès matrix to account for the $\sigma/f_0(500)$ and $f_0(980)$ resonances simultaneously. For higher energies, the $f_2(1270)$ resonance shows up as a dominant structure which we approximate by a single channel $\pi\pi$ rescattering in the D-wave. In the dispersive approach, the latter requires taking into account t- and u-channel vector-meson exchange left-hand cuts, which exhibit an anomalous-like behaviour for large space-like virtualities. We show how to incorporate such behaviour using an appropriate contour deformation. We also focus on the kinematic constraints of helicity amplitudes and explicitly show their correlations.

We furthermore extend the dispersive approach to the $\gamma\gamma \to D^+D^-$ and $\gamma\gamma \to D^0\bar{D}^0$ processes, which are expected to contain the two charmonium resonances: $\chi_{c0}(2P)$ and $\chi_{c2}(2P)$. While the latter is relatively well established from both experimental and theoretical sides, the identification of the former remains dubious. For the S-wave contribution, we again adopt a partial-wave dispersive representation and the D-wave $\chi_{c2}(3930)$ state is described as a Breit-Wigner resonance. The resulting fits are consistent with the data on the invariant mass distribution of the $e^+e^- \to J/\psi D\bar{D}$ process. Performing an analytic continuation to the complex s-plane, we find no evidence of a pole corresponding to the $\chi_{c0}(2P)$ candidate $X(3860)$ reported by the Belle Collaboration. Instead, we find a clear bound state below the $D\bar{D}$ threshold at $\sqrt{s_B} = 3695(4)$ MeV, confirming the previous phenomenological and lattice predictions.

Zusammenfassung

Die Beschreibung der Hadronendynamik ist nach wie vor eine Herausforderung für die moderne theoretische Physik. Mit verschiedenen Ansätzen versucht man derzeit, den Anforderungen der zunehmenden experimentellen Präzision gerecht zu werden. Sie beziehen entweder die riesigen Datenmengen mit verschiedenen Kanälen ein oder stützen sich auf theoretische Annahmen, die nur in einer begrenzten Anzahl von Fällen gültig sind. In diesem Zusammenhang ist es von entscheidender Bedeutung, Techniken zu entwickeln, die eine genaue Beschreibung der vorhandenen Daten ermöglichen und gleichzeitig eine Vorhersagekraft besitzen, die durch ihre Modellunabhängigkeit erreicht wird. Diese Arbeit widmet sich dem Ansatz der Partialwellen Dispersionsrelation, der auf den grundlegenden Eigenschaften der Streumatrix, wie Unitarität und Analytizität, aufbaut.

Wir wenden diesen Ansatz zunächst an, um die S-Wellenreaktionen $\pi\pi \to \pi\pi$ und $\pi K \to \pi K$ zu untersuchen, bei denen die leichtesten skalaren Resonanzen $\sigma/f_0(500)$, $f_0(980)$ und $\kappa/K^*(700)$ auftreten. Die Beiträge aus den linken Schnitten werden mit Hilfe der Potenzentwicklung in einer geeignet konstruierten konformen Variablen berücksichtigt. Die Expansionskoeffizienten werden datengesteuert durch Anpassung der Phasenverschiebungen an experimentelle Daten und Gitterdaten sowie Roy-Analysen bestimmt. Für die $\pi\pi$-Streuung präsentieren wir sowohl eine Einzel- als auch eine gekoppelte Kanalanalyse, indem wir zusätzlich den $K\bar{K}$-Kanal einbeziehen. Für letzteren ist das zentrale Ergebnis die Omnès-Matrix, die mit den neuesten dispersiven Ergebnissen für $\pi\pi \to \pi\pi$ bzw. $\pi\pi \to K\bar{K}$ übereinstimmt. Durch eine analytische Fortsetzung in die komplexe Ebene fanden wir Pole, die mit den Resonanzen $\sigma/f_0(500)$, $f_0(980)$ und $\kappa/K^*(700)$ für den physikalischen Pionenmassenwert und im Fall von $\sigma/f_0(500)$ und $\kappa/K_0^*(700)$ auch für unphysikalische Pionenmassenwerte zusammenhängen.

Die Kenntnis der $\pi\pi \to \pi\pi$-Amplitude erlaubt es uns, eine dispersive Analyse der doppeltvirtuellen Photon-Photon-Streuung an zwei Pionen durchzuführen, die durch Unitarität sehr empfindlich auf die hadronische Endzustandswechselwirkung ist. Dieser Prozess ist besonders wichtig, da er zum hadronischen Halpern-Streuungsanteil des anomalen magnetischen Moments des Myons beiträgt. Für die S-Welle verwenden wir die ermittle gekoppelte Kanal $\pi\pi$, $K\bar{K}$ Omnès Matrix, um die $\sigma/f_0(500)$- und $f_0(980)$-Resonanzen gleichzeitig zu berücksichtigen. Für höhere Energien zeigt sich die $f_2(1270)$-Resonanz als eine dominante Struktur, die wir durch eine einkanalige $\pi\pi$-Rückstreuung in der D-Welle approximieren. Im dispersiven Ansatz erfordert letzteres die Berücksichtigung von t- und u-Kanal-Vektor-Meson-Austausch-Linksschnitten, die ein anomales Verhalten für große raumartige Virtualitäten zeigen. Wir zeigen, wie man ein solches Verhalten mit Hilfe einer geeigneten Konturdeformation einbeziehen kann. Wir konzentrieren uns auch auf die kinematischen Beschränkungen der Helizitätsamplituden und zeigen explizit deren Korrelationen.

Darüber hinaus erweitern wir den dispersiven Ansatz auf die Prozesse $\gamma\gamma \to D^+D^-$ und $\gamma\gamma \to D^0\bar{D}^0$, von denen erwartet wird, dass sie die beiden Charmoniumresonanzen enthalten: $\chi_{c0}(2P)$ und $\chi_{c2}(2P)$. Während letztere sowohl experimentell als auch theoretisch relativ gut etabliert ist, bleibt die Identifizierung der ersteren zweifelhaft. Für den S-Wellen-Beitrag verwenden wir erneut eine dispersive Partialwellendarstellung, und der D-Wellenzustand $\chi_{c2}(3930)$ wird als Breit-Wigner-Resonanz beschrieben. Die sich daraus ergebenden Anpassungen sind konsistent mit den Daten über die invariante Massenverteilung des $e^+e^- \to J/\psi D\bar{D}$-Prozesses. Bei der analytischen Fortsetzung in die komplexe s-Ebene finden wir keinen Hinweis auf

einen Pol, der dem von der Belle-Kollaboration berichteten $\chi_{c0}(2P)$-Kandidaten $X(3860)$ entspricht. Stattdessen finden wir einen klaren gebundenen Zustand unterhalb der $D\bar{D}$-Schwelle bei $\sqrt{s_B} = 3695(4)$ MeV, was die früheren phänomenologischen und Gittervorhersagen bestätigt.

List of publications

[1] Igor Danilkin, Oleksandra Deineka, and Marc Vanderhaeghen, "Dispersive analysis of the $\gamma^*\gamma^* \to \pi\pi$ process",
Phys. Rev. D **101** (2020) no.5, 054008, arXiv:1909.04158 [hep-ph].

[2] Igor Danilkin, Oleksandra Deineka, and Marc Vanderhaeghen, "Data-driven dispersive analysis of the $\pi\pi$ and πK scattering",
Phys. Rev. D **103** (2021) no.11, 114023, arXiv:2012.11636 [hep-ph].

[3] Oleksandra Deineka, Igor Danilkin, and Marc Vanderhaeghen, "Dispersive analysis of the $\gamma\gamma \to D\bar{D}$ data and the confirmation of the $D\bar{D}$ bound state",
Phys. Lett. B **827** (2022), 136982, arXiv:2111.15033 [hep-ph].

Conference proceedings

[4] Oleksandra Deineka, Igor Danilkin, and Marc Vanderhaeghen,
"On the Importance of Left-hand Cuts in the $\gamma\gamma^* \to \pi\pi$ Process",
Acta Phys. Polon. B **50** (2019), 1901-1910.

[5] Oleksandra Deineka, Igor Danilkin, and Marc Vanderhaeghen,
"Dispersive analysis of the $\pi\pi$ and πK scattering data",
arXiv:2203.02215 [hep-ph].

[6] G. Colangelo, M. Davier, A.X. El-Khadra, M. Hoferichter, C. Lehner, ..., O. Deineka,
"Prospects for precise predictions of a_μ in the Standard Model",
arXiv:2203.15810 [hep-ph].

White paper

[7] T. Aoyama, N. Asmussen, M. Benayoun, J. Bijnens, T. Blum, ..., O. Deineka,
"The anomalous magnetic moment of the muon in the Standard Model",
Phys. Rept. **887** (2020), 1-166, arXiv:2006.04822 [hep-ph].

Contents

Chapter 1

Introduction

"Man, he took his time in the sun
Had a dream to understand
A single grain of sand"
"The Greatest Show on Earth",
Nightwish

From a physicist's point of view, the highest form of appreciation for a theory is to subject it to the immense number of tests designed to disprove it. It is this attitude that has allowed many mathematically beautiful theories to be discarded as irrelevant to the observable world. In this light, a theory that has withstood all theoretical and experimental scrutiny and predicted phenomena that became observable decades after its formulation is so exceptional. A prime example of such a theory is the *Standard Model* (SM) of particle physics. Established throughout the late 1960s and early 1970s [8–11] it is now a commonly accepted theory of the elementary particle physics, hence the name.

Three out of four fundamental forces of nature: electromagnetic, weak and strong interactions between elementary particles, are described within the Standard Model in the form of gauge theories[1]. In 1979 Glashow, Salam, and Weinberg received the Nobel prize for the unification of the electromagnetic and the weak interaction to the electroweak force [8–10]. Another Nobel Prize to Higgs and Englert was awarded much later, in 2013, after the discovery of the Higgs boson at the Large Hadron Collider (LHC) at CERN [14, 15]. The existence of such a boson was predicted nearly 60 years ago by Higgs [16], Brout and Englert [17], and Guralnik, Hagen and Kibble [18], yet only with its experimental discovery the SM became fully confirmed. The discovery of the Higgs boson was considered a significant success for the SM since it resolved the long-standing question of the mass generation of fundamental particles. The latter can be classified into fermions and bosons. The matter content of the SM includes three generations of spin-1/2 quarks and leptons, the fundamental interactions are mediated by spin-1 gauge boson fields, and the spin-0 Higgs boson is responsible for the Yukawa-type interaction. Schematically, the family of the SM particles is depicted in Fig. 1.1.

Well before the discovery of the Higgs boson, it was known that SM could not provide a comprehensive description of nature. It fails to incorporate the fourth known fundamental force - gravity, encoded into Einstein's theory of general relativity. Another evidence of SM incompleteness comes from the rotational curves of galaxies, which suggest the existence of an entirely new type of matter - dark matter. On top of that, the cosmological observations of the curvature of the universe add dark energy to the discussion. Furthermore, the neutrino oscillations are only possible if the neutrinos have finite masses, contradictory to the SM formulation. Recently, the precise value of the mass of the W-boson, first observed in 1983 [19] seems to be at variance with SM predictions [20]. These and numerous other limitations have opened the discussion of the possible physics scenarios *beyond the Standard Model* (BSM). For the BSM searches, there are two possible pathways - either a direct search for new particles,

[1]For the pedagogical overview, we refer the interested reader to [12, 13]

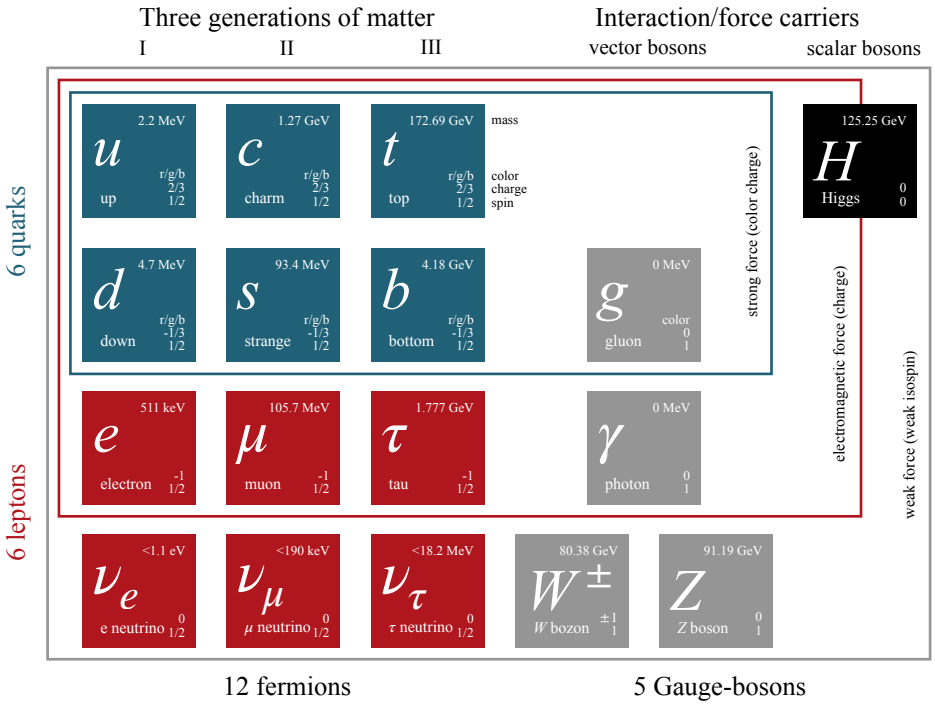

Figure 1.1: A schematic overview of the fundamental constituents of the Standard Model.

e.g. the supersymmetric partners of the SM particles at high energies, or the search for the BSM signatures at low-energy and high-precision frontiers.

The prime example of the latter approach is the *anomalous magnetic moment of muon* $(g-2)_\mu$ problem, which shows a 4.2σ deviation between the current ultra-precise measurements and the SM calculations, those indicating the possible BSM contributions. The theoretical evaluation of this quantity, however, carries significant uncertainty. This uncertainty mainly arises from the contributions of hadrons - composite objects made of quarks bound together by the strong force. Hadrons are further divided into mesons made of an equal number of quarks and antiquarks and baryons containing the odd number of valence quarks. Unfortunately, the SM sector responsible for the strong interaction - the *Quantum Chromodynamics* (QCD) - cannot describe the hadron dynamics employing standard perturbative techniques. This problem originates in the behaviour of the strong coupling constant, discovered by Gross, Wilczek [21] and Politzer [22] in 1973. Therefore, while accounting for the underlying QCD properties, it is essential to develop theoretical frameworks capable of describing the hadron behaviour.

In fact, the first hadrons were proposed and observed long before the formulation of QCD. The first meson - pion (π) - was proposed as the nuclear force carrier by Yukawa in 1935 [23] and discovered in cosmic rays in 1947 [24]. In the same year, a second meson - kaon (K) - was discovered [25]. The rapid advances of the experimental setups created a cornucopia of the newly observed hadrons, which until the formulation of QCD, were considered as elementary particles. Fortunately, the knowledge of QCD supplemented by the techniques targeted to describe the hadron interactions allows questioning their internal structure. In the original formulation of QCD, only the most economical content was considered, namely quark and antiquark pair for mesons and three quarks for baryons. The existence of more complicated combinations, like four-quark meson, was not excluded; however, at that time, there were no experimentally observed candidates for such configurations. Since then, a significant effort

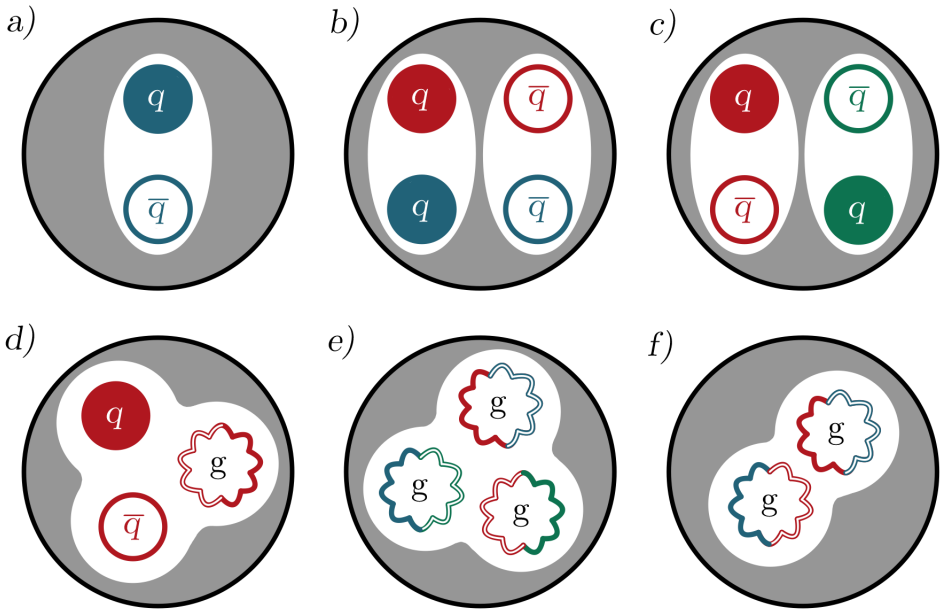

Figure 1.2: Schematic representation of the conventional (a) and different non-conventional mesons: tetraquark (b), molecule (c), hybrid (d) and glueballs (e, f). Here q and $\bar{q}$ denotes the quark and antiquark, respectively, and g stands for gluon.

has been put into searching for the so-called non-conventional hadrons, for instance, a pentaquark discovery at LHCb [26]. Regarding the mesons, the possible non-standard mesonic configurations are shown in Fig. 1.2. Usually, the searches for the non-conventional candidates are mainly concentrated on looking for meson resonances with exotic quantum numbers that cannot be formed from a fermion-antifermion pair. However, the already observed scalar mesons with masses below 1 GeV, $\sigma/f_0(500)$, $\kappa/K^*(700)$, $a_0(980)$, and $f_0(980)$ are frequently considered as candidates for multiquark states - either tetraquarks or hadronic molecules.

In the grand scheme of things, the work outlined in this thesis aims to improve our current understanding of the dynamics of different mesonic resonances, which are crucial in providing the data-driven assessment of the theoretical hadronic error of the anomalous magnetic moment of the muon. The relevant theoretical concepts are outlined in Chapter 2. First, we give an overview of the physics of strongly interacting particles within the Standard Model framework. We also denote the tools developed to deal with the Quantum Chromodynamics in non-perturbative regime: lattice QCD and effective field theories, particularly the Chiral Perturbation Theory. The S-matrix theory, which gives rise to the dispersion relation approach widely used in this thesis, is also discussed in the first Chapter. This Chapter concludes with the anomalous magnetic moment of the muon problem, which motivates our study of two-photon fusion reactions with a light meson final states. Chapter 3 is dedicated to the meson-meson scattering in the N/D framework and the study of the lightest scalar resonances appearing therein. We apply the data-driven dispersive approach to the $\pi\pi \to \pi\pi$ and $\pi K \to \pi K$ systems. For the $\pi\pi$ system, we also take into account the coupled-channel effects from intermediate $K\bar{K}$ states. We extend the single-channel approach from the experimental data to the lattice data, accounting for the dependence on the pion mass. All in all, this allows us to recover the amplitude of meson-meson scattering needed to describe the final state interaction in the $\gamma\gamma \to \pi\pi$ process, which is discussed in Chapter 4. There, we start

from the kinematics of the process, which involves space-like photons and the construction of the basis of partial wave amplitudes free of kinematic singularities. Dispersive treatment of this process encounters an anomalous threshold problem appearing at certain values of photon virtualities, which we address in an elegant and compact manner. The application of this approach leads to the prediction for the cross section of the $\gamma^*\gamma^* \to \pi\pi$ process for low photon virtualities relevant for the anomalous magnetic moment of the muon problem. In Chapter 5 we apply the partial wave dispersive approach to study the states involving heavier particles: $\gamma\gamma \to D\bar{D}$. This process may contain the long-searched $\chi_{c0}(2P)$ state, and we discuss what is indeed hidden near the $D\bar{D}$ threshold. Finally, in Chapter 6 we give a summary and outlook. The technical details and derivations are collected in the Appendices.

Chapter 2

Theoretical background

The primary goal of this chapter is to introduce the essential concepts and the foundations of modern hadron physics. Naturally, an attempt to give a comprehensive overview of this broad topic, including everything from the simplistic phenomenological models to the cutting edge numerical simulations, let alone the rapid evolution of the experimental precision, would be somewhat naïve and impractical. Therefore, while still striving to preserve the generality, we will concentrate mainly on the theoretical aspects required throughout this thesis.

In Sec. 2.1, we start with the Standart Model sector, which is responsible for the strong interactions - Quantum Chromodynamics. While embodying the theoretical elegance, due to its non-Abelian nature and the limitations of the perturbative techniques, this theory does not allow direct analytical predictions in terms of quark and gluon degrees of freedom in the low-energy region, where the observable particles - hadrons - reside. We then discuss several strategies developed to circumvent the limitations of genuine QCD. First, we briefly touch on the effective field theories concept that amalgamates the ideas of old pion theories with the internal symmetries of the QCD Lagrangian through the Weinberg conjecture. Second, we consider lattice QCD, providing direct numerical calculations in the non-perturbative region, which is thriving now in the era of steadily improving numerical techniques and growing computational power. Then, aiming to construct the primary tool used throughout this thesis - the dispersive formalism we dedicate a separate section to the scattering theory. In particular, in Sec. 2.2 we pay additional attention to the discussion of the fundamental properties of the S-matrix, such as unitarity, analyticity and crossing symmetry. These properties eventually allow the construction of the non-perturbative approach, based on the partial-wave dispersion relations commonly used to describe the hadron physics phenomena. Altogether, the material given in this chapter culminates in Sec. 2.3 with the description of the anomalous magnetic moment of the muon problem, rooted either in the imperfections of the Standard Model itself or our current understanding of it - a question which partially requires the model-independent dispersive treatment of the hadronic contributions to be evaluated.

2.1 QCD at low energies

In this thesis, we are interested in the reactions involving *hadrons* - the composite subatomic particles made of quarks confined together by the strong interaction. Hadrons fall into two families: *baryons* containing the odd number of quarks and, hence, fermions and *mesons* - bosons made of an even number of quarks.

In the naïve quark model, mesons are described as a bound state of quark-antiquark pair. They are classified by their quantum numbers J^{PC} with parity $P = (-1)^{L+1}$, charge conjugation $C = (-1)^{L+S}$ and the total angular momentum $|L - S| \leq J \leq |L + S|$, where L is the orbital momentum of the quark-antiquark system and $S = 0, 1$ is the total spin. It is sometimes also convenient to use the non-relativistic *spectroscopic notation* $n^{2S+1}L_J$, where n denotes the number of radial excitation. The states with $L = 0$ are called pseudoscalar $J^{PC} = 0^{-+}$ and vector $J^{PC} = 1^{--}$ mesons and their radial excitations with $L = 1$ are called

scalar $J^{PC} = 0^{++}$, axial-vector $J^{PC} = 1^{++}, 1^{+-}$ and tensor $J^{PC} = 2^{++}$ mesons. In principle, the above definition of meson allows for states with broader quark and gluon content: *tetraquarks, hybrids, glueballs*, which are usually referred as *exotic* mesons and can produce the quantum numbers, not allowed otherwise, e.g. $J^{PC} = 1^{-+}$.

Unfortunately, Quantum Chromodynamics, which describes the interaction of quarks and gluons, is not applicable through the standard perturbative approach in the low-energy region, which is relevant to understand processes involving light hadrons. At the scale of interest, the light pseudoscalar mesons themselves may serve as effective degrees of freedom. However, it is still crucial to understand the underlying quark interaction and the internal QCD symmetries upon which some methods more suitable for the description of the hadron dynamics are built.

This section is organized as follows. We start with the Lagrangian of Quantum Chromodynamics and discuss its symmetries and other properties, including the running coupling constant and the properties related to it. In Sec. 2.1.2, we briefly touch on the concept of the effective field theories and a prominent example is the Chiral Perturbation Theory. The section concludes with a very brief survey of lattice QCD in Sec. 2.1.3, which allows for many ab initio numerical results in the non-perturbative regime, yet requires a lot of the computational power.

2.1.1 QCD as a field theory

Quantum Chromodynamics (QCD) is the non-Abelian Yang-Mills theory that describes strong interaction within the Standard Model. It is based on the $SU(3)_c$ symmetry group, where index c stands for colour. The fundamental degrees of freedom are spin-1/2 fermions, called *quarks* and vector gauge bosons - *gluons*, which mediate the strong interaction. The quarks are characterized by mass, electrical charge and the colour charge, a quantum number inherent to the QCD; gluons also carry the color charge. The quarks come in six different flavours: $f = \{u, d, s, c, b, t\}$ in addition to their three possible colours: red, green and blue. The Lagrangian of QCD is given by:

$$\mathcal{L}_{\text{QCD}} = \sum_f \bar{q}_f \left(i\gamma^\mu D_\mu - m_f\right) q_f - \frac{1}{4} G^{(a)}_{\mu\nu} G^{(a)\mu\nu} \,, \tag{2.1}$$

where γ^μ are the Dirac γ-matrices, q_f represent the quark bispinor field, and D_μ is the covariant derivative

$$D_\mu = \partial_\mu - i g_s t^a A^a_\mu \,. \tag{2.2}$$

Here g_s denotes the strong coupling constant, $t^a = \lambda^a/2$ are the fundamental representation group generators and A^a_μ are the $N_c^2 - 1 = 8$ Yang-Mills gluon fields, i.e. there are eight kinds of gluons. The $G^{(a)}_{\mu\nu}$ term stands for the field strength tensor

$$G^{(a)}_{\mu\nu} = \partial_\mu A^{(a)}_\nu - \partial_\nu A^{(a)}_\mu + g_s f^{abc} A^{(b)}_\mu A^{(c)}_\nu \,, \tag{2.3}$$

where f_{abc} are the structure constants of $SU(3)$ Lie algebra, defined as

$$f_{abc} = \frac{1}{4i} \text{Tr}([\lambda_a, \lambda_b]\lambda_c) \,. \tag{2.4}$$

The Gell-Mann matrices λ_a form the basis of all complex, traceless, Hermitian 3×3 matrices, which represent the fact, that the interaction between gluon and quark rotates the quark colour.

The non-Abelian nature of QCD manifests itself in the term of the field strength tensor (2.3), which is quadratic in the gluon field $A^{(a)}_\mu$ and gives rise to three-gluon interaction terms

(proportional to g_s) and four-gluon interaction terms (proportional to g_s^2). Eventually, it leads to the *asymptotic freedom* property, which we will discuss later. The phenomenon of gluon self-interaction in QCD is unique: in abelian theory like *Quantum Electrodynamics* (QED) there is no corresponding self-interaction between photons at tree level. Any interaction between two photons arises from quantum loop effects.

The gauge principle imposes the local $SU(3)$ transformation

$$q_f \to q'_f = \exp\left(-i\sum_{a=1}^{8}\Theta_a(x)\frac{\lambda^{(a)}}{2}\right)q_f = Uq_f\,, \tag{2.5}$$

where $U \in SU(3)$ and $\Theta_a(x) = [\Theta_1(x), \ldots, \Theta_8(x)]$ is a set of independent real parameters. The quark fields transform according to the fundamental representation of the $SU(3)$ gauge group, forming a colour triplet for each flavour f, while the gluon belongs to the adjoint representation, forming a colour octet.

From the gauge-invariance, the QCD Lagrangian could also include the so-called σ-term of a type

$$\mathcal{L}_\theta = \frac{g_s^2\bar{\theta}}{64\pi^2}\epsilon^{\mu\nu\rho\sigma}\sum_{a=1}^{8}G^{(a)}_{\mu\nu}\tilde{G}^{(a)\rho\sigma}\,, \tag{2.6}$$

where $\tilde{G}^{(a)\rho\sigma}$ is the dual of the gluon field tensor. This implies an explicit P and CP violation, but is considered to be extremely small: the current limits from neutron electric dipole moment best measured limits yield $\bar{\theta} \lesssim 10^{-10}$.

In fact, the QCD coupling constant $\alpha_s = g_s^2/4\pi$ is not constant at all. In QCD, the energy dependence strongly affects the whole nature of the theory. This dependence is shown in Fig. 2.1 and it is a defining feature of QCD, encoded in $\beta_s(Q)$ function of the *renormalization group equation*:

$$\mu^2\frac{d\alpha_s}{d\mu^2} = \beta(a_s) = -\alpha_s\left(\beta_0\frac{\alpha_s}{4\pi} + \beta_1\left(\frac{\alpha_s}{4\pi}\right)^2 + \beta_2\left(\frac{\alpha_s}{4\pi}\right)^3 + \ldots\right)\,. \tag{2.7}$$

Hence the effective QCD coupling is defined as

$$\alpha_s(\mu^2) = \frac{4\pi}{\beta_0\ln(\mu^2/\Lambda^2)}\left[1 - \frac{2\beta_1}{\beta_0^2}\frac{\ln[\ln(\mu^2/\Lambda^2)]}{\ln(\mu^2/\Lambda^2)} + \ldots\right]\,, \tag{2.8}$$

where $\beta_0 = 11 - 2/3n_f$, $\beta_1 = 51 - 19/3n_f$ and n_f is the number of flavours of quarks with mass less than the characteristic scale Λ.

In the equation (2.7) for $\beta_0 > 0$, there is an overall negative sign, which implies that the coupling constant decreases at high energy. This property is known as the asymptotic freedom, which allows for a standard perturbative expansion in terms of quarks and gluons degrees of freedom. In contrast, for low energies, α_s increases, resulting in the strong-coupling regime. The scale Λ in equation (2.8) is the QCD parameter that defines the scale where the theory becomes strongly coupled. The large value of α_s at low energies is thought to be responsible for *confinement* - the fact that the quarks and gluons are not observed as free particles but are bound together to form the colour-singlet states - hadrons. The confinement poses a severe challenge to our understanding of strong interaction. While QCD in principle encodes as information regarding the strong interaction at all scales, the inability to use standard perturbative techniques in the low energy regime and the fact that the underlying degrees of freedom of QCD, quarks and gluons, are confined within hadrons hinders the connection to the observable hadronic phenomena. Therefore, describing the strong interaction at low-energies is a formidable task, which has lead to the development of several approaches operating on QCD as a fundamental underlying theory. One of them is the *effective field theory* approach,

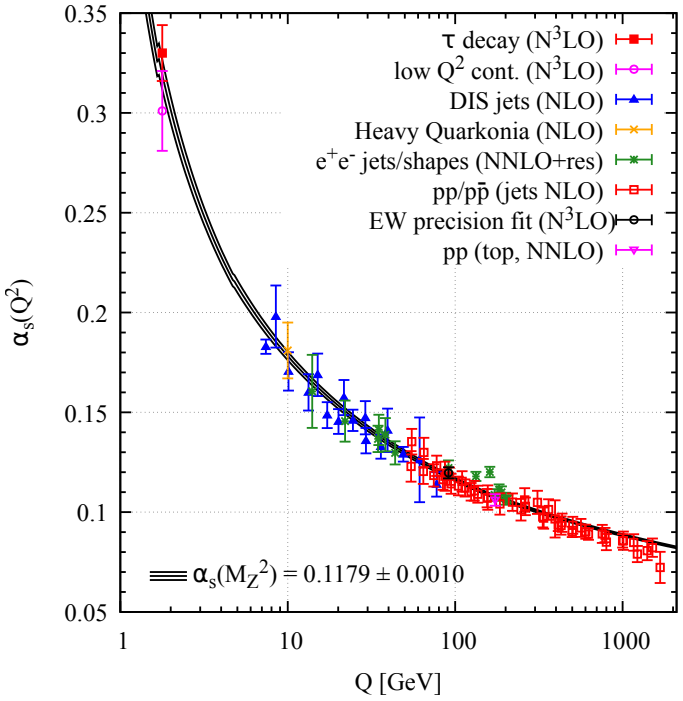

Figure 2.1: The QCD coupling constant a_s as the function of the respective energy scale Q. The figure is taken from [27] and the detailed explanation of each measurement can be found therein.

which we will briefly describe in Sec. 2.1.2. It requires knowledge of QCD symmetries, where in particular we will focus on the *chiral symmetry*.

In QCD, there is a large gap between the quark masses, three of them are much lighter than the typical hadronic scale 1 GeV, and three are heavier. In the so-called chiral limit one can put $m_u, m_d, m_s \to 0$[1]. The scale of 1 GeV is associated with the masses of ρ-meson, $m_\rho = 770$ MeV or with the scale of the chiral symmetry breaking[2]. In the *chiral limit*, the QCD Lagrangian containing only u, d, and s quarks can be rewritten as:

$$\mathcal{L}^0_{\mathrm{QCD}} = \sum_{f=u,d,s} (\bar{q}_{f,R} i\gamma^\mu D_\mu q_{f,R} + \bar{q}_{f,L} i\gamma^\mu D_\mu q_{f,L}) - \frac{1}{4} G^a_{\mu\nu} G^{a\mu\nu}\,, \tag{2.9}$$

where the left (L) and the right (R) chiral components do not interact with each other

$$q_R = \frac{1}{2}(1+\gamma_5)q\,, \quad q_L = \frac{1}{2}(1-\gamma_5)q\,. \tag{2.10}$$

In the massless limit, the *chirality* eigenstates (means being left or right) coincide with the helicity eigenstates. The Lagrangian $\mathcal{L}^0_{\mathrm{QCD}}$ has the global symmetry

$$\underbrace{SU(3)_L \times SU(3)_R}_{\text{chiral group}} \times U(1)_V \times U(1)_A\,,$$

[1] There is some freedom to choose the set of the lightest quarks, the s quark sometimes is not included, because it has the mass $m_s = 95$ MeV, while $m_u = 2.3$ MeV, $m_d = 4.8$ MeV [27], therefore $SU(3)$ symmetry is less precise than $SU(2)$.

[2] The scale of chiral symmetry breaking is usually defined based on the dimensional analysis of NLO terms compared to LO terms as $4\pi f_\pi \approx 1170$ MeV, where f_π is the pion decay constant

where $V = L + R$ (vector) and $A = L - R$ (axial). The Noether theorem implies the existence of conserved currents associated with each symmetry of the Lagrangian. For our future investigation, we drop the question of the quark number symmetry $U(1)_V$ saying that it is realized as a baryon number on the hadronic level and concentrate on the axial group $U(1)_A$ and the chiral group. The eight currents L and R transform under the $SU(3)_L \times SU(3)_R$ as an octet and a singlet. Instead of using the chiral currents, one often uses the vector and axial linear combinations

$$\begin{aligned} V^{a\mu} &= R^{a\mu} + L^{a\mu} = \bar{q}\gamma^\mu \frac{\lambda^a}{2} q\,, \\ A^{a\mu} &= R^{a\mu} - L^{a\mu} = \bar{q}\gamma^\mu\gamma_5 \frac{\lambda^a}{2} q\,. \end{aligned} \tag{2.11}$$

The axial symmetry group $U(1)_A$ gives the current, which is conserved on the classical level. However, this symmetry is broken on the quantum level giving rise to the so-called axial anomaly. For the singlet axial current, it holds

$$A^\mu = \bar{q}\gamma^\mu\gamma_5 q \Rightarrow \partial_\mu A^\mu = \frac{3g_s^2}{32\pi^2}\epsilon_{\mu\nu\rho\sigma}G^{a\mu\nu}G^{a\rho\sigma}\,. \tag{2.12}$$

We expect to see that the chiral symmetry is preserved in the hadron spectrum. However, it turns out that the chiral symmetry is spontaneously broken down to the vector subgroup $SU(3)_V$. The *Goldstone theorem* states that if there is a spontaneously broken symmetry, i.e. the ground state is not invariant under the chiral rotations, new massless bosons, so-called *Goldstone bosons*, appear. The number of the Goldstone bosons is then equal to the number of the broken axial generators of the $SU(3)_A$. From the analysis of the hadron spectrum, one can identify the eight light pseudoscalar mesons with appropriate quantum numbers: $\pi^+, \pi^-, K^+, K^-, K^0, \bar{K}^0$ and η with $J^P = 0^-$. Their masses are relatively small compared to the typical hadronic scale, though they are non-zero, so they appear as the *pseudo-Goldstone* bosons.

Due to the small but non-zero quark masses of quarks, the mixing between the left- and the right-hand quark fields appear, and therefore there is an additional explicit symmetry breaking. The mass term $M = \mathrm{diag}\{m_u, m_d, m_s\}$ then appear as

$$\mathcal{L}_M = -\left(\bar{q}_R M q_L + \bar{q}_L M q_R\right)\,. \tag{2.13}$$

The presence of the mass term modifies the divergence of currents, so together with the symmetry breaking of the axial group and the vector group symmetry conservation, we obtain

$$\begin{aligned} \partial_\mu V^{a\mu} &= i\bar{q}\left[M, \frac{\lambda^a}{2}\right]_- q\,, \\ \partial_\mu A^{a\mu} &= i\bar{q}\left[M, \frac{\lambda^a}{2}\right]_+ \gamma_5 q\,, \\ \partial_\mu V^\mu &= 0\,, \\ \partial_\mu A^\mu &= 2i\bar{q}M\gamma_5 q + \frac{3g_s^2}{32\pi^2}\epsilon_{\mu\nu\rho\sigma}G^{a\mu\nu}G^{a\rho\sigma}\,. \end{aligned} \tag{2.14}$$

Now we can summarize all the symmetries of the strong interaction in terms of different current properties. In the chiral limit, all of the currents are conserved, except the singlet axial current A^μ, which has the anomaly. Due to the non-zero quark masses, all of the currents obtain additional divergences, though the singlet vector current V^μ being the sum of three flavour currents, is always conserved. The eight vector currents $V^{(a)\mu}$ are conserved in the case of equal quark masses $m_u = m_d = m_s$, because $[\lambda^a, 1]_- = 0$.

In addition to the chiral symmetry, the QCD Lagrangian has another global symmetry. In the limit $m_u = m_d \neq m_s$, $\mathcal{L}_{\text{QCD}}$ is invariant under the global $SU(2)$ transformation. The mass difference $m_u - m_d$ is very small compared to Λ_{QCD}, so this approximate symmetry is rather accurately realized. Similarly to spin, which is also a $SU(2)$ symmetry, it is called *isospin*. Electromagnetic interactions, however, violate isospin symmetry since u- and d- quarks have different electrical charges. If the electromagnetic interactions are turned off, the SM as a whole becomes symmetric under isospin transformation if $m_u = m_d$. In this *isospin limit* the proton and neutron have equal masses.

2.1.2 Effective field theories

The main idea of effective field theories (EFT) is relatively intuitive. It states that as long as we restrict ourselves to a specific energy domain, the physics at scales much bigger than the chosen one should not influence the description of the system strongly and can be absorbed into a set of low energy constants [28]. Therefore, the relevant degrees of freedom may be different from the ones of the underlying theory. Regarding the strong interaction theory, this comes naturally if one looks at the mass separation between the quarks and the observable hadrons mentioned in the previous section. Moreover, the hadronic states are assumed to be appropriate degrees of freedom due to the confinement. The application of the EFT relies on the prominent statement by Weinberg [29][3]. It states that

> *Quantum field theory itself has no content beyond analyticity, unitarity, cluster decomposition and symmetry,*

and therefore provides a link between the underlying theory and the effective one, which allows ensuring that the obtained EFT is not just another phenomenology [32]. To imply this theorem into the perturbation theory, one should write the most general Lagrangian consistent with all symmetry principles of the underlying theory and use it to calculate the S-matrix for any theory below a certain scale. Further, we will ascertain that the EFT approach can significantly simplify the calculation. Moreover, for Quantum Chromodynamics in the non-perturbative region, it gives a possibility to obtain the physical values in terms of observable degrees of freedom.

It is crucial to define the scale separation for the construction of the EFT since the expansion is considered to be in terms of the soft scale over the hard scale. Within the relevant example of *Chiral Perturbation Theory* (χPT), the identification of both scales is discussed further on.

The Chiral Perturbation Theory is the theory describing the dynamics of the Goldstone bosons. It combines the concept of the EFT together with the chiral symmetry properties of QCD. Since we have already investigated the symmetry properties, we now need to identify the scale separation to construct the proper effective theory. The hard scale comes naturally as the mass m_ρ, while the soft scales are the Goldstone boson masses and the typical momentum p of the process.

To construct the corresponding expansion, we need to choose the parametrization of the Goldstone boson octet[4]

$$U = \exp\left(\frac{i\phi}{f_0}\right), \qquad \phi = \sum_{a=1}^{8} \lambda^a \phi^a \equiv \begin{pmatrix} \pi^0 + \frac{1}{\sqrt{3}}\eta & \sqrt{2}\pi^+ & \sqrt{2}K^+ \\ \sqrt{2}\pi^- & -\pi^0 + \frac{1}{\sqrt{3}}\eta & \sqrt{2}K^0 \\ \sqrt{2}K^- & \sqrt{2}\bar{K}^0 & -\frac{2}{\sqrt{3}}\eta \end{pmatrix}, \tag{2.15}$$

[3] In the referred work, it was mentioned as the known theorem, which was proven in [30, 31]

[4] Analogously, it can be done for the SU(2) theory. In this case, the matrix ϕ would consist only of pions.

where f_0 is the pion decay constant in the chiral limit coming from the matrix element of $\pi^+ \to \mu^+\nu_\mu$ decay.

The effective Lagrangian should be invariant under the $SU(3)_L \times SU(3)_R \times U(1)_V$, moreover, due to the spontaneous symmetry breaking, its ground state should be invariant under the subgroup $SU(3)_V \times U(1)_V$. The global $U(1)_V$ symmetry is satisfied trivially because the pseudoscalar mesons have zero baryon number. The ground state of the system is $\phi = 0$ and therefore $U(\phi = 0) = 1$ is invariant under the $SU(3)_V$. The matrix U is unitary and transforming as

$$U \to U' = RUL^\dagger\,, \quad R \in SU(3)_R\,, \quad L \in SU(3)_L\,. \tag{2.16}$$

For now, we have all constituents to construct the effective Lagrangian of χPT. It is organized as a series of terms with an increasing number of derivatives

$$\mathcal{L}_{\text{eff}} = \mathcal{L}_2 + \mathcal{L}_4 + \mathcal{L}_6 + \dots\,, \tag{2.17}$$

where only terms with even numbers of the derivatives are present due to the Lorentz invariance. The total number of terms is infinite, hence the number of generated Feynman diagrams. However, this is no longer a problem involving the Weinberg power counting scheme, which allows comparing the importance from the different diagrams by ordering them according to the scaling p/Λ.

The leading order (LO) term of the effective Lagrangian containing the minimal number of derivatives together with the contribution from the broken symmetry in the absence of the external fields has the following form

$$\mathcal{L}_2 = \frac{f_0^2}{4}\mathrm{Tr}(\partial_\mu U \partial^\mu U^\dagger) + \frac{f_0^2 B_0}{2}\mathrm{Tr}(MU^\dagger + UM^\dagger)\,, \tag{2.18}$$

where the constant B_0 is connected to the chiral quark condensate so that

$$B_0 = -\frac{\langle \bar{q}q \rangle}{3f_0^2}\,. \tag{2.19}$$

The constants f_0 and B_0 are the part of so-called *low-energy constants* (LEC's). With the increasing number of terms in the Lagrangian, new LEC's come into play. They can be determined from the experiment or the underlying theory, making the construction of the next-to-leading terms even more difficult. For instance, $\mathcal{L}_4$ contains 12 LEC's and $\mathcal{L}_6$ is more than 100.

Together with the complications of calculating the higher orders of the χPT Lagrangian, the theory itself has the limitation provided by the definition of the high-energy scale. A considerable amount of the hadronic interaction lies above the energy of 770 MeV, so different methods are needed at higher energies (see Sec. 2.2). Still, the χPT is a powerful tool that can impose essential constraints in the low energy region.

2.1.3 Lattice QCD

Aside from the effective field theories, there is another powerful approach aimed to tackle the strong interaction in a non-perturbative manner - the *lattice QCD*. The main objective of this technique is the QCD path integral, which is impossible to solve analytically, and the numerical methods have to be implemented. The conceptual breakthrough occurred in 1974 when Wilson proposed to formulate the long-distance QCD on a Euclidean space-time lattice [33], hence the name. This discretization implies that the quarks sit on the lattice sites and interact through interconnected gluon links. Lattice QCD allows for a numerical solution

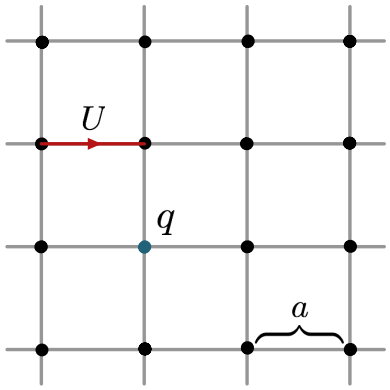

Figure 2.2: The schematic representation of the discretized Euclidean space-time. Here q denotes the quark fields, U is the link variable connected to the gluon field and a is the lattice spacing.

involving the Monte-Carlo generation of random samples of the possible lattice configurations, weighted with a probability given by the QCD action.

In the path integral formalism [34], various observable parameters, for instance, the hadron masses, can be studied in terms of the expectation values of the corresponding gauge-invariant operators or *correlation functions*. For operator $\mathcal{O}$ this quantity is given by

$$\langle \mathcal{O} \rangle = \frac{1}{\mathcal{Z}} \int \mathcal{D}A \prod_f \mathcal{D}q_f \mathcal{D}\bar{q}_f \mathcal{O}(q_f, \bar{q}_f, A) e^{iS_{\mathrm{QCD}}(q_f, \bar{q}_f, A)} , \tag{2.20}$$

where the partition function $\mathcal{Z}$ reads as

$$\mathcal{Z} = \int \mathcal{D}A \prod_f \mathcal{D}q_f \mathcal{D}\bar{q}_f e^{iS_{\mathrm{QCD}}(q_f, \bar{q}_f, A)} . \tag{2.21}$$

From Eq. (2.1) follows, that the QCD action $S_{\mathrm{QCD}}(q_f, \bar{q}_f, A) = \int d^4x \mathcal{L}_{\mathrm{QCD}}$ can be further separated into a sum of gluonic $S_G(A)$ and fermionic $S_F(q_f, \bar{q}_f, A)$ parts:

$$S_{\mathrm{QCD}}(q_f, \bar{q}_f, A) = S_G(A) + S_F(q_f, \bar{q}_f, A) = S_G(A) + \int d^4x \sum_f \bar{q}_f (i\gamma^\mu D_\mu - m) q_f . \tag{2.22}$$

The imaginary exponent in the integrand of Eq. (2.20) poses a problem for the numerical integration since it oscillates strongly. It can be circumvented using the Wick rotation [35], which implies the transition from the real time t to imaginary $\tau = ix^0$ and thus from Minkowski to Euclidean space-time. The expectation value in Eq. (2.20) is then

$$\langle \mathcal{O} \rangle = \frac{1}{\mathcal{Z}} \int \mathcal{D}A \prod_f \mathcal{D}q_f \mathcal{D}\bar{q}_f \mathcal{O}(q_f, \bar{q}_f, A) e^{-S^E_{\mathrm{QCD}}(q_f, \bar{q}_f, A)} , \tag{2.23}$$

where $S^E_{\mathrm{QCD}}(q_f, \bar{q}_f, A)$ is the Euclidean action given by

$$S^E_{\mathrm{QCD}}(q_f, \bar{q}_f, A) = \int d^4x \mathcal{L}^E_{\mathrm{QCD}} = S_G(A) + \int d^4x \sum_f \bar{q}_f (\gamma^\mu D_\mu + m_f) q_f , \tag{2.24}$$

and the partition function $\mathcal{Z}$ modifies accordingly

$$\mathcal{Z} = \int \mathcal{D}A \prod_f \mathcal{D}q_f \mathcal{D}\bar{q}_f e^{-S^E_{\mathrm{QCD}}(q_f, \bar{q}_f, A)} . \tag{2.25}$$

Here the integral runs over all possible quark q_f, anti-quark $\bar{q}_f$ and gluon A fields configurations. In order to numerically evaluate the obtained integrals, the Euclidean space-time is then discretized to a hypercubic lattice Λ:

$$\Lambda = \{x_\mu \in \mathbb{R}^4 | x_\mu = a n_\mu; n_0 = 0, 1, \ldots, N_t - 1; n_1, n_2, n_3 = 0, 1, \ldots, N_s - 1\}\,, \tag{2.26}$$

with N_s lattice points in the spatial and N_t lattice points in the time direction, which are separared by the lattice spacing a (see Fig. 2.2)[5]. Therefore, it has a size of $N_t \cdot a$ in time and $N_s \cdot a$ in spatial direction, which is equivalent to the spatial volume $V_3 = (N_s a)^3$. The lattice spacing acts like an ultraviolet regulator, thus making the theory finite. Naturally, the continuous theory is recovered by taking the limit of vanishing lattice spacing $a \to 0$ and the infinite volume $V_3 \to \infty$.

The quark fields are defined on the lattice sites, i.e. $q(x), \bar{q}(x) \to q(n), \bar{q}(n)$ with $n \equiv n_\mu \in \Lambda$. To preserve the QCD gauge symmetry, the discretized gluon field has to be encoded in the form of link variables, which connect the neighboring lattice sites:

$$U_\mu(n) = e^{iaA_\mu(n)}\,, \tag{2.27}$$

so that it acts like a gauge transporter. The details on how the operators can be transcribed to the discretized space-time can be found elsewhere [36, 37].

Considering the path integral from Eq. (2.25), one can notice that the Grassman-valued quark fields can be integrated out, thus leading to

$$\mathcal{Z} = \int \mathcal{D}U e^{-S_G(U)} \prod_f \det(D(U) + m_f)\,, \tag{2.28}$$

where $D(U)$ is a lattice Dirac operator. If the operator $\mathcal{O}$ depends on the quark and antiquark fields q_f and $\bar{q}_f$, integrating these fields out leads not only to the fermion determinant in the denominator of Eq. (2.23) but also to a series of quark propagators $(D(U) + m_f)^{-1}$. The evaluation of the fermion determinant is exceptionally challenging since it requires $\mathcal{O}((N_s^3 \times N_t)^3)$ computations. Early lattice simulations were limited to the *quenched approximation*, where this determinant was put to 1. Physically, this approximation neglects the effect of the vacuum quark loops. Instead, the determinant can be rewritten in terms of an integral over so-called *pseudofermion fields*, which in turn introduces the different effective action depending on the inverse Dirac operator $(D(U)+m_f)^{-1}$. From the computational perspective, it implies inverting the large sparse matrix in order to evaluate the pseudofermionic action. For $(D(U)+m_f)$, the smallest eigenvalue is proportional to m_f; hence the computational cost is inversely proportional to the quark mass. For this reason, the current lattice simulations operate with higher quark and consecutively, pion masses (see Sec. 3.3.2 and 3.4.2).

In addition, there are several core issues arising from the lattice discretization. First, in practical calculations, the lattice spacing a is non-zero, leading to the discretisation errors, which can be controlled by carrying out the calculations at decreasing value of a and extrapolating the results. Second, the lattice discretisation breaks the rotational invariance, i.e. the spatial rotational symmetry is reduced to the cubic symmetry group. Finally, the finite lattice volume also introduces additional systematic errors.

However, despite the listed limitations, lattice QCD has shown tremendous progress in recent years due to the rapid development of high-performance computing systems. For instance, it was able to estimate the mesonic excitation spectrum shown in Fig. 2.3 by studying the correlation functions of a type

$$C_{ij}(t) = \langle 0 | \mathcal{O}_i(t) \mathcal{O}_j(t) | 0 \rangle\,, \tag{2.29}$$

[5] The typical present day lattices are asymmetric and have sizes of $N_s^3 \times N_t \sim 64^3 \times 128$ with the lattice spacing of $a \approx 0.05 - 0.1$ fm.

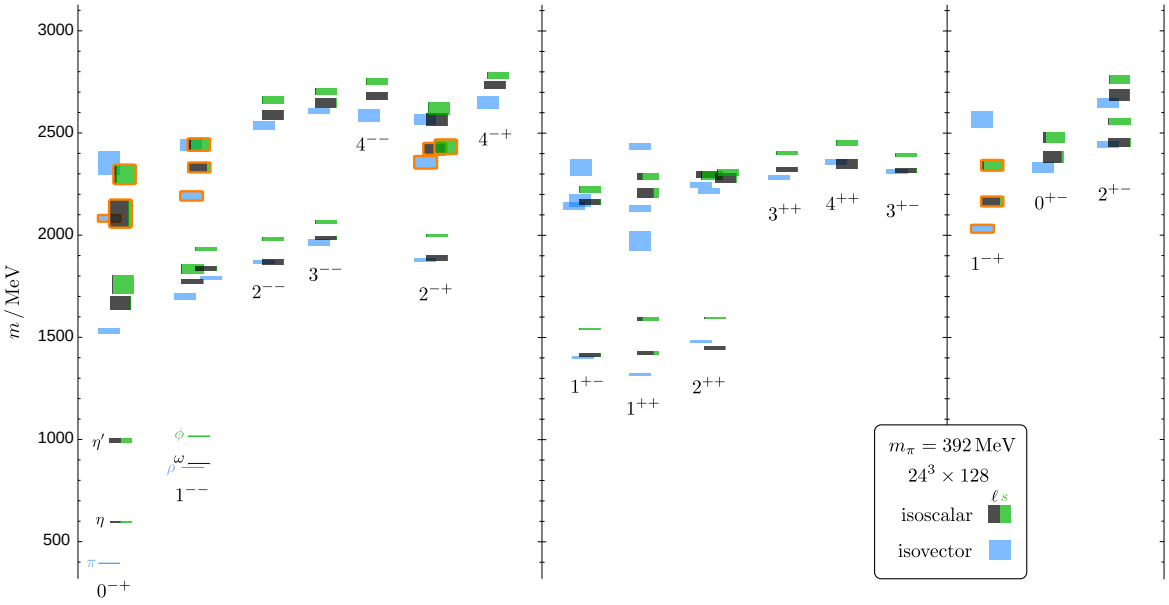

Figure 2.3: Lattice QCD results for the light-quark isoscalar (green/black) and isovector (blue) meson spectrum. Each column corresponds to a given J^{PC}. The calculations are performed with m_π= 391 MeV on $24^3 \times 128$ lattice. The figure is taken from [38].

where $\mathcal{O}$ is a hadron creation operator constructed from quark and gluon fields, which, when acting on the QCD vacuum $|0\rangle$ creates a so-called *trial state* with the quantum numbers J, P, C of some hadron. In general, this trial state is not a hadron of interest but a linear superposition of all states with these quantum numbers. More details on the structure and action of these operators can be found, for instance, in [36, 38].

In this thesis, we are mainly interested in studying not the stable particles but resonances (see Sec. 2.2.6) for which many fruitful results have become available in recent years. While lattice QCD simulations cannot directly provide the resonance properties, methods have been developed to circumvent this problem. In particular, the *Lüsher formalism* [39] relates infinite-volume hadron scattering amplitude to the discrete spectrum of hadron states in a finite volume and thus allows to extract the scattering amplitudes as the functions of energy. The analytical parametrisation of the obtained scattering amplitudes can then be examined for their resonance content. For instance, the $\sigma/f_0(500)$ resonance was studied in this manner in both single and coupled channel $\pi\pi$ scattering on lattice [40, 41]. The single-channel result will be discussed in more detail in Sec. 3.3.2.

Finally, the lattice QCD contribution in the study of the anomalous magnetic moment of muon problem can hardly be overestimated, especially regarding the hadronic vacuum polarisation part (see Sec. 2.3).

2.2 S-matrix formalism

The effective field theories, including χPT, while leading to many accurate results in the hadronic reactions below the characteristic scale, break down in an attempt to describe the processes in the resonance region. This limitation can hardly be underestimated in light of the recent experimental discoveries, enriching the spectrum of the observable particles with the plethora of heavier states. In particular, the various resonance phenomena trial the boundaries of the effective field theories' applicability. For instance, already the processes involving the first resonances of the $\pi\pi$ scattering: $\sigma/f_0(500)$ and $\rho(770)$ put limits on the standard χPT

scheme. On the other hand, lattice QCD, capable of producing numerous results from the first principles, still struggles with the computational constraints to perform calculations for the light quark mass values.

In fact, the hadronic sector has not yet been described flawlessly within one concept. The S-matrix theory we will briefly cover in this section neither provides an ultimate solution nor is novel, dating back to the proposal by Heisenberg in 1943 [42]. It is well suited to the description of the hadronic processes due to the short range of the strong interactions; still, it is not universal. This theory operates on the notion of the asymptotic states, meaning that a long time before the interaction, the participating particles are effectively free with well-defined quantum numbers, and the interaction itself happens in a finite time interval.

Despite the cautionary remarks mentioned above, the S-matrix theory is still one of the most potent tools in hadronic physics. It abandons the question of the nature of underlying fields and thus avoids the problems related to perturbative expansion in coupling constant. Instead, the main focus of the S-matrix theory is the transition amplitude of the physical process. Starting from the fundamental principles of the unitarity and maximal analyticity, it allows to recover the full amplitude from the discontinuity across the branch cuts by employing the dispersion relations. The resulting formalism yields model-independent results, which can then be tested with experiment.

This section is dedicated to the main principles of the S-matrix theory, which result in the dispersion relation approach extensively used throughout this work. We start with the main objectives of the scattering theory, the kinematics, and the fundamental principles of unitarity and the analyticity for the scattering amplitude. Then we will proceed with the dispersion relations and discuss their most general form. We will also touch on the topic of resonances which within the given framework arise naturally as the poles of the scattering amplitude on the unphysical Riemann sheets. A more detailed yet pedagogical overview of the considered topics can be found in [43–45].

2.2.1 The scattering process

Virtually all pieces of evidence regarding the behavior of subatomic particles that we possess today come from *scattering experiments*. In such experiments, the particles collide and interact, and the emerging particles are detected. There are two types of scattering events: elastic and inelastic. In an *elastic* scattering event, the final state consists of the same particles as the initial state. If the final state contains different particles, then the scattering event is said to be *inelastic*. Following this definition, the *decay process* is always inelastic since it has one particle in the initial state and multiple decays products in the final.

The particles entering the scattering experiment are considered to be effectively free, meaning that a long time before scattering takes place, they are well-separated and do not interact with each other. The same applies to the particles after the scattering. The states which consist of such particles are called *asymptotic states*. We denote the initial state as $|i\rangle$ and the final state as $|f\rangle$. The transition between the initial and final states can then be written as

$$S_{fi} = \langle f | \, S \, | i \rangle \ , \tag{2.30}$$

where S is called the *scattering operator*, which contains all the information regarding the time-evolution from one asymptotic state to another. It is defined by the matrix elements between all possible initial and final states. Altogether, these matrix elements form a scattering matrix, or the *S-matrix*. It is Lorentz invariant, meaning that each matrix element is a scalar under Lorentz transformations.

There are two ways how the final state $|f\rangle$ can emerge from the initial state $|i\rangle$. First, the particles could not interact at all, so that the amplitude of this transition is given as $\langle f|i\rangle$.

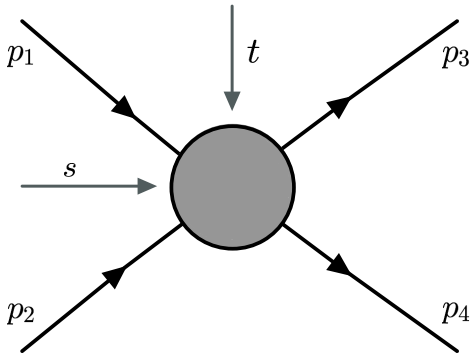

Figure 2.4: Schematic representation of the elastic $2 \to 2$ scattering of the identical spinless particles and the definition of the s and t-channel processes

Therefore, the S-matrix can be decomposed into the trivial part and the part describing an actual interaction, called the interaction or $\mathcal{T}$-*matrix*:

$$S = \mathbb{1} + i\mathcal{T}\,, \tag{2.31}$$

and the total matrix element will be a sum $\langle f|\, S\, |i\rangle = \langle f|i\rangle + i\,\langle f|\, \mathcal{T}\, |i\rangle$.

The initial and final state can consist of the arbitrary number of particles. The general scattering process involving N particles with momenta p_i, $i = 1 \dots N$ can be conveniently described using a set of Lorenz-invariant variables, the number of which can be counted as follows. There is a set of N four-momenta giving $4 \times N$ variables and N on-shell condition $p_i^2 = 0$. Another four constraints come from the total momentum conservation $\sum_i k_i^\mu = 0$, $\mu = 0 \dots 3$. In addition, there are three rotations and three Lorentz boosts, which characterize the reference frame and do not affect the invariant amplitude. Hence, the total number of the invariants needed to describe the N-point amplitude is

$$4(N-1) - N - 3 - 3 = 3N - 10\,. \tag{2.32}$$

The initial states of actual experiments consist of only two particles, and the number of particles in the final state is limited by the total energy and quantum numbers of initial and final states. Moreover, the multiparticle final state implies the complicated analytical structure of the scattering amplitude and, hence, lies beyond the pedagogical introduction to the scattering theory. Therefore, in this section we consider only $2 \to 2$ scattering where all particles are on the mass-shell. For simplicity, we also narrow down to the elastic scattering of the identical particles with masses $m_i = m$ and momenta p_i, where $i = \{1, 2, 3, 4\}$. This process is schematically shown in Fig. 2.4.

In principle, aside from mass and momentum, each particle entering the scattering process is characterized by certain discrete quantum numbers like spin and isospin. However, to cover the main properties of the S-matrix theory, it is sufficient to consider the scattering of the scalar particles. Such $2 \to 2$ process can be described with the following invariants, called *Mandelstam variables* [46]:

$$\begin{aligned} s &= (p_1 + p_2)^2 = (p_3 + p_4)^2\,, \\ t &= (p_1 - p_3)^2 = (p_2 - p_4)^2\,, \\ u &= (p_1 - p_4)^2 = (p_2 - p_3)^2\,. \end{aligned} \tag{2.33}$$

These variables are connected through the kinematic relation of the following form

$$s + t + u = \sum_i m_i^2 = 4m^2\,. \tag{2.34}$$

hence only two of them are independent in accordance with the relation (2.32).

For the process shown on Fig. 2.4 the initial and final states are defined as $|i\rangle = |p_1, p_2\rangle$, $|f\rangle = |p_3, p_4\rangle$ and the transition matrix element, which determines the relevant part of the scattering amplitude is given by

$$\mathcal{T}_{fi} \equiv \langle f| \mathcal{T} |i\rangle = \langle p_3, p_4| \mathcal{T} |p_1, p_2\rangle \ . \tag{2.35}$$

The Lorentz invariant *transition amplitude* T is then related to the elements from the $\mathcal{T}$-matrix by a momentum conserving δ-function

$$\mathcal{T}_{fi} = (2\pi)^4 \delta(p_1 + p_2 - p_3 - p_4) T(s,t,u) \, . \tag{2.36}$$

From the relation (2.34) follows that the amplitude $T(s,t,u)$ depends only on two Mandelstam invariants, the choice of which is specific to a particular process. Hereafter, we choose to use $T(s,t)$, or, recalling the kinematic relations for the Mandelstam variables (see App. 3.A), $T(s, \cos\theta)$, where θ is the scattering angle in the center-of-mass system. The amplitude $T(s, \cos\theta)$ can be decomposed into the infinite series of partial waves. For the spinless particles the s-channel *partial wave expansion* can be performed using the *Legendre polynomials*

$$T(s, \cos\theta) = \mathcal{N} \sum_{J=0}^{\infty} (2J+1) P_J(\cos\theta) t_J(s) \, , \tag{2.37}$$

where we introduced factor $\mathcal{N} = 2$ for identical particles in initial and final states and $\mathcal{N} = 1$ for non-identical. We introduced this factor to have the same unitarity relation for identical and non-identical particles (see below). For the $\pi\pi \to K\bar{K}$ system, considered in Chapter 3, $\mathcal{N} = 1/\sqrt{2}$.

The partial wave decomposition allows to transfer the angular dependence to the functions with well-defined properties and to study the resonances and other features since they occur in the channels with definite spin. Further, throughout this thesis, the partial wave amplitude $t_J(s)$, will be the main object of our study. In the experiment, however, neither the partial wave nor the total amplitude is observed. The principal experimentally observable quantity, the cross section $\sigma(s)$, is proportional to the squared modulus of amplitude. We will come back to this definition in the relevant sections.

2.2.2 Analyticity, unitarity, and crossing symmetry

To describe various hadronic phenomena, the dispersion relations we will be using are built upon the fundamental principles, such as unitarity, analyticity and other invariance properties of the S-matrix.

Regardless of interaction type, the total probability of the system starting from an initial state $|i\rangle$ to end up in some state $|f\rangle$ must be conserved, i.e. $\sum_f P_{i\to f} = 1$. This transition probability can be defined simply as the squared matrix element

$$1 = \sum_f P_{i\to f} = \sum_f |\langle f| S |i\rangle|^2 = \langle i| S^\dagger S |i\rangle \ , \tag{2.38}$$

Therefore, the conservation of probability requires that the S-matrix is unitary

$$S^\dagger S = S S^\dagger = \mathbb{1} \, . \tag{2.39}$$

By inserting Eq. (2.31) into Eq. (2.39), in terms of the interaction matrix $\mathcal{T}$, the above unitarity relation translates into

$$\mathcal{T} - \mathcal{T}^\dagger = i \mathcal{T} \mathcal{T}^\dagger \, . \tag{2.40}$$

If the intermediate states $|n\rangle$ are physically allowed, we can insert a complete set of them to obtain

$$\langle f|\,\mathcal{T}\,|i\rangle - \langle f|\,\mathcal{T}^\dagger\,|i\rangle = i(2\pi)^4 \sum_n \delta^4(p_n - p_i)\,\langle f|\,\mathcal{T}^\dagger\,|n\rangle\,\langle n|\,\mathcal{T}\,|i\rangle\ . \tag{2.41}$$

Equivalently, it can be written recalling the notation (2.35):

$$\mathcal{T}_{fi} - \mathcal{T}^*_{if} = i(2\pi)^4 \sum_n \delta^4(p_n - p_i)\mathcal{T}_{fn}\mathcal{T}^*_{in}\,. \tag{2.42}$$

As the consequence of time reversal invariance, which holds for the strong interaction of hadrons, there is a symmetry of the matrix elements, i.e. $\langle f|\,S\,|i\rangle = \langle i|\,S\,|f\rangle$. In the trivial case of no interaction, the symmetry condition is automatically fulfilled $\langle f|i\rangle = \langle i|f\rangle$, hence the $\mathcal{T}$ matrix elements are symmetric $\mathcal{T}_{fi} = \mathcal{T}_{if}$ and the unitarity condition (2.42) can be simplified as

$$2\mathrm{Im}\mathcal{T}_{fi} = (2\pi)^4 \sum_n \delta^4(p_n - p_i)\mathcal{T}_{fn}\mathcal{T}^*_{in}\,. \tag{2.43}$$

For the scattering amplitude T defined as in Eq. (2.36), below the inelastic threshold the unitarity relation (2.43) implies:

$$2\mathrm{Im}T_{fi} = \sum_n \int d\Phi_n T_{fn}T^*_{in}\,, \tag{2.44}$$

where $d\Phi_n$ is a phase space of the intermediate multi-particle state n. In case of the elastic, i.e. $|i\rangle = |f\rangle$, $2 \to 2$ scattering the phase space factor is defined as

$$d\Phi_2 = \frac{\beta(s)}{32\pi^2} d\Omega\,, \tag{2.45}$$

where $\beta(s) = 2p_{\mathrm{cm}}/\sqrt{s} = \sqrt{1 - 4m^2/s}$. To avoid the angular integration over $d\Omega$, it is useful to obtain the unitarity relation for the partial wave amplitudes (2.37)

$$\mathrm{Im}\ t(s) = \frac{\beta(s)}{16\pi}|t(s)|^2\theta(s - 4m^2)\,, \tag{2.46}$$

where we omitted the index J. The Heaviside-θ function is now included to emphasize that the unitarity relation is valid above the two-particle threshold. The relation above refers to the elastic unitarity or the *single-channel* process and works in the energy regime below any inelastic threshold. It can be generalized for the case of two- and more *coupled-channels* unitarity by replacing the single amplitude and the corresponding phase space factor with matrices, introducing the matrix index ab, so that

$$\mathrm{Im}\ t_{ab}(s) = \sum_c t_{ac}(s)\rho_c(s)t^*_{cb}(s)\,, \tag{2.47}$$

where the sum goes over all intermediate states

$$\rho_c = \frac{1}{16\pi}\beta_c(s)\theta(s - s_{c,\mathrm{thr}})\,, \tag{2.48}$$

where $s_{c,\mathrm{thr}}$ is the threshold of the corresponding two particle system.

The unitarity relation constraints the real and imaginary parts of the amplitude. In single channel, from the Eq. (2.46) follows that

$$|t(s)| \leq \frac{1}{\rho(s)}\,. \tag{2.49}$$

In addition, the amplitude $t(s)$ can be parametrized as

$$t(s) = \frac{e^{2i\delta(s)} - 1}{2i\rho(s)}\,, \quad \text{Re}\; t(s) = \frac{\sin 2\delta(s)}{2\rho(s)}\,, \quad \text{Im}\; t(s) = \frac{1 - \cos 2\delta(s)}{2\rho(s)}\,. \tag{2.50}$$

By taking into account the limits of sin and cos functions, the resulting *unitarity bound* reads as following

$$-\frac{1}{2\rho(s)} \leq \text{Re}\; t(s) \leq \frac{1}{2\rho(s)}\,, \quad 0 \leq \text{Im}\; t(s) \leq \frac{1}{\rho(s)}\,. \tag{2.51}$$

Analogously, we can derive similar constraints for the coupled-channel case, however, we postpone it until Chapter 3.

Eq. (2.44) and subsequent ones imply that the unitarity property of the S-matrix has a consequence on the analytical structure of the scattering amplitude. The first threshold generates a branch cut of the amplitude in the complex s-plane starting at $s = 4m^2$ and spanning to infinity. With growing energies, each new intermediate state produces an additional term in the unitarity relation giving rise to further branch points at the inelastic thresholds. In principle, only the positions of these branch points are fixed by unitarity relation and the choice for the cuts to run along the positive real axis is a matter of commonly accepted convention, hence the name *right-hand cuts*.

The purpose of the branch cuts is to unambiguously define the amplitude by selecting a single sheet of the Riemann surface to arrive to the single-valued function. As long as we do not cross any of the cuts, there is only one Riemann sheet, called the *physical sheet* on which the physical value of the amplitude resides. Other Riemann sheets, called *unphysical*, can be reached by burrowing through one or more branch cuts. Each sheet is specified by the branch cut, that must be crossed to reach the physical sheet. Further we will see that establishing connection between the amplitude behaviour on different Riemann sheets is essential for understanding the properties of physical resonances.

The second attribute of the S-matrix, which causes the non-analytic structures of the scattering amplitude is called *crossing symmetry*. It states, that the different kinematical regions can be related to each other by means of the analytical continuation. Consider again the process depicted on Fig. 2.4, described by the set of Mandelstam variables (2.33) for which s represents the energy in the center-of-mass system

$$1(p_1)2(p_2) \to 3(p_3)4(p_4)\,. \tag{2.52}$$

There are the following crossed processes

$$\begin{aligned} 1(p_1)\bar{3}(-p_3) &\to \bar{2}(-p_2)4(p_4)\,, \\ 1(p_1)\bar{4}(-p_4) &\to \bar{2}(-p_2)3(p_3)\,, \\ 1(p_1) &\to \bar{2}(-p_2)3(p_3)4(p_4)\,, \end{aligned} \tag{2.53}$$

where bars denote the antiparticles. The first two processes are called t-channel, u-channel respectively, depending on which variable is chosen as the center-of-mass energy. The third line in (2.53) represents the decay process, which requires the particle $1(p_1)$ to be unstable and is written for the completeness only, as for the particles with equal masses this process is impossible. Note also, that this simple relations hold only for the full amplitude $T(s,t,u)$, while the partial-wave amplitudes are fixed in the certain channel. The physically allowed regions for each channel are shown in Fig. 2.5.

In principle, the unitarity relation of the form (2.44) exists in each channel since there is no prefered Mandelstam invariant. Therefore, each channel exhibits a branch cut starting from

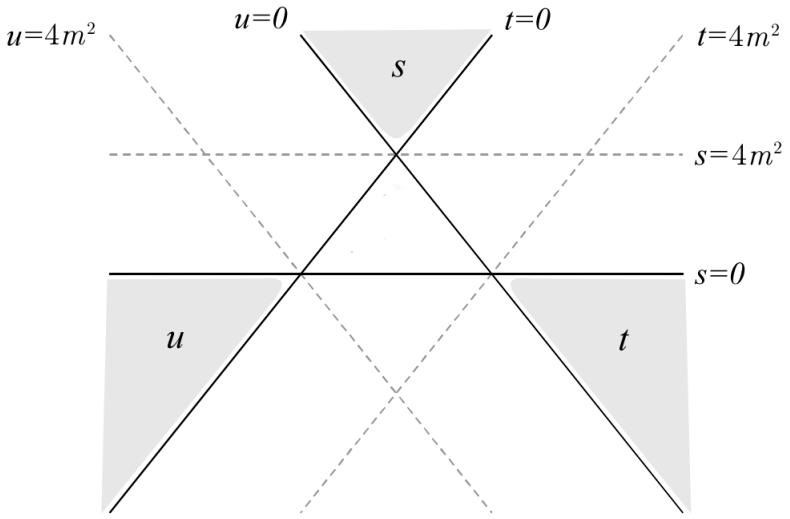

Figure 2.5: The Mandelstam plane for the elastic scattering of two particles in symmetrical representation. The physical regions for each channel are depicted in light gray. Note that in case of the unequal masses of interacting particles, there is also a decay region according to Eq. 2.53 and the plane structure is more complicated.

$4m^2$. The cuts in t- and u-channels are connected to the s-channel by means of the relation (2.34). If we fix a certain value $t = t_0$, the first u-channel branch cut $u \geq 4m^2$ begins at

$$s = -t_0 - u_{\text{thr}} + 4m^2 = -t_0 \,, \tag{2.54}$$

and goes to the minus infinity $s \to -\infty$. Analogously if we fix $u = u_0$, the first t-channel branch cut is given as $s = (-\infty, -u_0]$. These branch cuts in the complex s-plane are called the *left-hand cuts*.

Summarizing, together with the right-hand cuts running from $4m^2$ to infinity inherited directly from the unitarity, the amplitude in general also has the left-hand cuts from the crossed channels. This knowledge of the cut structure allows to consider the general analytic properties of the amplitude[6]. The principle of the maximal analiticity [46, 47] states that the amplitude has no other singularities that thus demanded by unitarity and crossing symmetry. We note first, that the amplitude acquires an imaginary part due to the right and left-hand cuts. In addition, for s below the lowest threshold the amplitude is typically real. According to the Schwarz reflection principle, which states that for some analytic function, real on a segment of the real axis, the following relation holds

$$T(s^*, t, u(s^*)) = T^*(s, t, u(s)) \,. \tag{2.55}$$

If for some real values of s the amplitude acquires an imaginary part, i.e. Im $T \neq 0$, the Schwarz reflection principle implies the appearance of the cut

$$T(s - i\epsilon, t, u) = T^*(s + i\epsilon, t, u) \neq T(s + i\epsilon, t, u) \,. \tag{2.56}$$

Therefore, in principle two limits of the amplitude on the first Riemann sheet exist due the presence of the branch cut - one above it and one below and it is essential to distinguish, which

[6] In fact, the demand of the amplitude $T(s, t, u)$ to be an analytical function stems from the causality requirement [44].

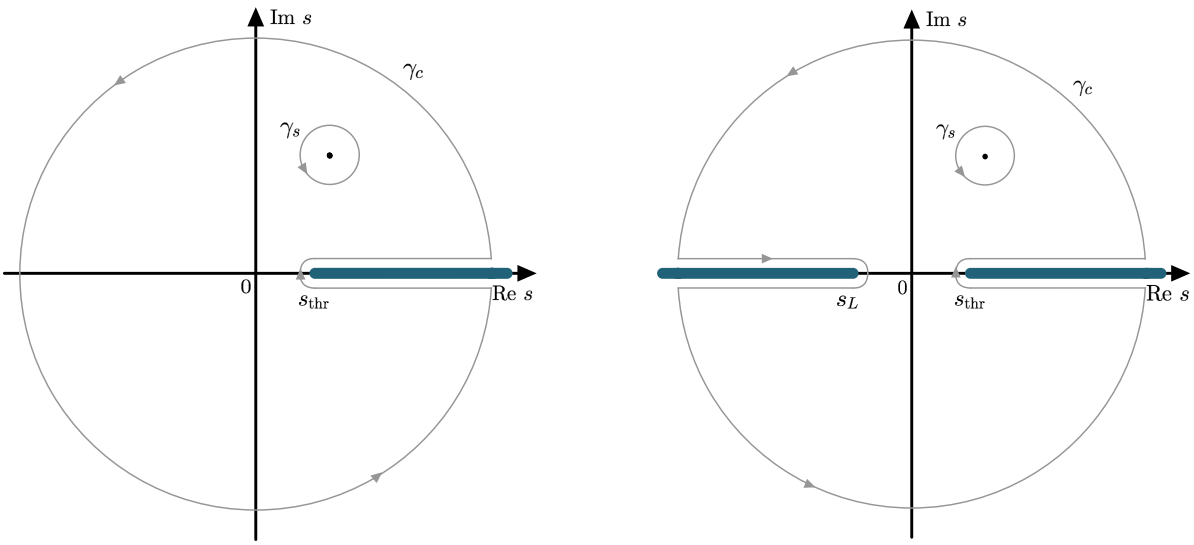

Figure 2.6: The he integration contour for the Cauchy theorem; left panel: the case with right-hand cut only, e.g. pion vector form factor, right panel: the analytic structure of the scattering amplitude with both left- and right-hand cuts.

one givess the correct physical result. From the perturbation theory follows that the physical amplitude is given by approaching the right-hand cut from the upper-half of the s-plane

$$T_{\text{physical}} = \lim_{\epsilon \to 0+} T(s + i\epsilon)\,, \tag{2.57}$$

which is obtained from the $i\epsilon$ prescription of Feynman propagators (see [43] for the details).

Note, that Schwarz' reflection principle requirements are not always satisfied. For instance, the physical systems exist for which the left and right hand cuts overlap and therefore, there is no region where $T(s,t,u)$ is real[7]. In this case, the imaginary part in the left hand side of the Eq. (2.43) should be replaced by the discontinuity across the branch cut

$$\text{Disc}\; T(s) = \frac{T(s+i\epsilon) - T(s-i\epsilon)}{2i}\,. \tag{2.58}$$

However, such systems are beyond the scope of this thesis and further we will concentrate on cases, where the left and right hand cuts are well-separated.

2.2.3 Dispersion relations

The above discussion of the general properties of the S-matrix aside from its pedagogical value, has served the purpose to build foundation for the dispersion relations. Arguments concerning the origin of analyticity from the causality requirement can be made in various branches of classical physics, particularly in the theory of dispersion in optics, hence the name.

To construct the dispersion relation we invoke the *Cauchy's integral formula*. For the complex valued funtion $t(s)$, which has only the right-hand cut, the following integral representation holds:

$$t(s) = \frac{1}{2\pi i} \oint\limits_{\gamma_s} \frac{t(s')}{s' - s} ds'\,, \tag{2.59}$$

[7] In addition, for the general process, there is no symmetry of the matrix element, i.e. $\langle f|\, S\,|i\rangle \neq \langle i|\, S\,|f\rangle$ so that the amplitude, which gives $\mathcal{T}^*_{if}$ is related to $\mathcal{T}_{fi}$ only by analytic continuation [48].

where the integration contour γ_s encircles the point on the s-plane as it shown in Fig. 2.6 (left panel). If the function is analytic everywhere, except for the branch cuts , then the contour can be deformed in a way, that it evades the cut and goes along the big circle γ_c. Let us assume, that $t(s) \to 0$ as $|s| \to \infty$. Then the contribution of the integral from the curved part of the contour γ_c vanishes and only the integral over the branch cut remains:

$$t(s) = \frac{1}{2\pi i} \int\limits_{s_{\rm thr}}^{\infty} \frac{t(s'+i\epsilon) - t(s'-i\epsilon)}{s'-s} ds' = \frac{1}{\pi} \int\limits_{s_{\rm thr}}^{\infty} \frac{\text{Disc } t(s')}{s'-s} ds' \,. \tag{2.60}$$

The *dispersion relation* (2.60) allows to reconstuct the function $t(s)$ in the whole complex plane, provided the discontinuity along the right-hand cut. In case of the amplitude, this discontinuity is fixed by the unitarity relation.

If the integral over the large circle does not vanish sufficiently fast, it is essential to introduce *subtractions*, meaning that the additional power of s has to be included in the denominator of the integral. One subtraction in Eq. (2.59) leads to

$$t(s) = \frac{1}{\pi} \int\limits_{s_{\rm thr}}^{\infty} \frac{\text{Disc } t(s)}{s'-s} ds' = t(s_M) + \frac{s-s_M}{\pi} \int\limits_{s_{\rm thr}}^{\infty} \frac{\text{Disc } t(s')}{(s'-s_M)(s'-s)} ds' \,, \tag{2.61}$$

where s_M is a so-called subtraction point and $t(s_M)$ is a subtraction constant formally given by

$$t(s_M) = \frac{1}{\pi} \int\limits_{s_{\rm thr}}^{\infty} \frac{t(s')}{s'-s_M} \,. \tag{2.62}$$

Note, that this integral is only convergent if $t(s)$ drops with some positive power for $s \to \infty$. The additional power of s in Eq. (2.61) results in an improved convergence at $|s| \to \infty$. This procedure can be performed as many times as required. If the amplitude behaves as the polynomial of power $n-1$, the formula (2.61) can be generalized

$$t(s) = \sum_{i=0}^{n-1} \frac{1}{i!} t^{(i)}(s_M)(s-s_M)^i + \frac{(s-s_M)^n}{\pi} \int\limits_{s_{\rm thr}}^{\infty} \frac{\text{Disc } t(s')}{(s'-s)(s'-s_M)^n} ds' \,. \tag{2.63}$$

The disadvantage of this method is that the $(n-1)$ additional parameters appear, that should be determined independently. Note also that sometimes the dispersion relation is oversubtracted in order to reduce the dependence on the unknown high energy region. The subtraction constants $t(s_0)$, can be fixed from χPT or experiment and then serve as a check of how much the sum rule is saturated.

Some physical quantities hold the same analytical properties as the function $t(s)$ considered above, for instance, the pion vector form factor which will be discussed in more details in Section 2.2.5. The total and partial wave scattering amplitudes have also the left-hand cuts so the relation (2.60) has to be modified following the same arguments

$$t(s) = \frac{1}{\pi} \int\limits_{-\infty}^{s_L} \frac{\text{Disc } t(s')}{s'-s} ds' + \frac{1}{\pi} \int\limits_{s_{\rm thr}}^{\infty} \frac{\text{Disc } t(s')}{s'-s} ds' \,, \tag{2.64}$$

where s_L denotes the starting poing of the left-hand cut. In addition, some amplitudes may have a singularity on the real axis corresponding to the bound state, which will be discussed in the next sections. However, the power of the approach is already obvious - it allows to reconstruct the amplitude on the whole s-plane having only the knowledge of its analytical structure.

2.2.4 N/D approach

Aiming to solve the Eq. (2.64), we first note that the unitatiry condition guarantees that the partial-wave amplitudes at infinity approach at most constants. In accordance with that, we can make one subtraction to suppress the high energy contribution under the dispersive integral. Thus we rewrite the dispersion relation (2.64) as

$$t(s) = t(s_M) + \frac{s - s_M}{\pi} \int\limits_{-\infty}^{s_L} \frac{ds'}{s' - s_M} \frac{\text{Disc } t(s')}{s' - s} + \frac{s - s_M}{\pi} \int\limits_{s_{\text{thr}}}^{\infty} \frac{ds'}{s' - s_M} \frac{\text{Disc } t(s')}{s' - s}\,, \tag{2.65}$$

the subtraction constant together with the left-hand cuts contributions can be combined into the function $U(s)$, so that

$$t(s) = U(s) + \frac{s - s_M}{\pi} \int\limits_{s_{\text{thr}}}^{\infty} \frac{ds'}{s' - s_M} \frac{\text{Disc } t(s')}{s' - s}\,. \tag{2.66}$$

The choice of the subtraction point s_M will be discussed latter. We note, that at the subtraction point the function $U(s)$ is equal to the scattering amplitude

$$t(s_M) = U(s_M)\,. \tag{2.67}$$

The equation (2.66) can then be solved by means of the N/D ansatz [49]:

$$t(s) = \frac{N(s)}{D(s)}\,, \tag{2.68}$$

where the contributions of the left- and right-hand cuts are separated into $N(s)$ and $D(s)$ functions, respectively. The unitarity relation for the amplitude $t(s)$ along the right-hand cut then implies

$$\begin{aligned} &\text{Disc}_{\text{r.h.c}} t(s) = \rho(s)|t(s)|^2 = \rho(s)\frac{|N(s)|^2}{|D(s)|^2}\,, \\ &\text{Disc}_{\text{r.h.c}} t(s) = N(s)^* \text{Disc}_{\text{r.h.c}} \left(\frac{1}{D(s)}\right) + \frac{1}{D(s)} \text{Disc}_{\text{r.h.c}} N(s) = -N^*(s) \frac{\text{Disc}_{\text{r.h.c}} D(s)}{|D(s)|^2}\,, \end{aligned} \tag{2.69}$$

from which follows the unitarity relations for the D-function

$$\text{Disc}_{\text{r.h.c}} D(s) = -\rho(s) N(s)\,. \tag{2.70}$$

Up to *Castillejo-Dalitz-Dyson ambiguity* (CDD) [50], which arises from the fact that the unitarity relation Eq. (2.47) does not uniquely determine $D(s)$ if $t(s)$ vanishes at some value of s_{CDD}[8], the once-subtracted dispersive representation for the D-function is given by

$$D(s) = 1 - \frac{s - s_M}{\pi} \int\limits_{s_{\text{thr}}}^{\infty} \frac{ds'}{s' - s_M} \frac{N(s')\rho(s')}{s' - s}\,, \tag{2.71}$$

where due to the non-uniqueness of the N/D ansatz, we have normalized the $D(s)$ function in a way that $D(s_M) = 1$ and $s_M < s_{\text{thr}}$. To arrive at an integral equation for the $N(s)$ function,

[8] For detailed discussion of the CDD ambiguity in the N/D context we refer the reader to [51–57].

we can write a once subtracted dispersion relation for the function $(t(s) - U(s))D(s)$, taking into account that

$$\begin{aligned} \mathrm{Disc}_{\mathrm{r.h.c}}((t(s) - U(s))D(s)) &= U(s)\rho(s)N(s)\,, \\ \mathrm{Disc}_{\mathrm{l.h.c}}((t(s) - U(s))D(s)) &= 0\,. \end{aligned} \tag{2.72}$$

Therefore, the dispersion relation for this function has the following form:

$$(t(s) - U(s))D(s) = a + \frac{s - s_M}{\pi} \int\limits_R \frac{ds'}{s' - s_M} \frac{U(s')\rho(s')N(s')}{s' - s}\,. \tag{2.73}$$

Recalling the relation (2.67) we can fix the subtraction constant a, so that

$$\begin{aligned} \frac{N(s)}{D(s)} - U(s) &= \frac{1}{D(s)} \frac{s - s_M}{\pi} \int\limits_{s_{\mathrm{thr}}}^{\infty} \frac{ds'}{s' - s_M} \frac{U(s')\rho(s')N(s')}{s' - s}\,, \\ N(s) &= U(s)D(s) + \frac{s - s_M}{\pi} \int\limits_{s_{\mathrm{thr}}}^{\infty} \frac{ds'}{s' - s_M} \frac{U(s')\rho(s')N(s')}{s' - s}\,. \end{aligned} \tag{2.74}$$

By inserting the dispersive representation for the D-function (2.71) we finally obtain the integral equation for the N-function

$$N(s) = U(s) + \frac{s - s_M}{\pi} \int\limits_{s_{\mathrm{thr}}}^{\infty} \frac{ds'}{s' - s_M} \frac{\rho(s')N(s')(U(s') - U(s))}{s' - s}\,. \tag{2.75}$$

This integral equation can be solved numerically provided the input of $U(s)$. Knowing the $N(s)$ function on the right-hand cut, the $D(s)$ function is calculated from the dispersion relation 2.71 and the partial wave amplitude is reconstructed as $N(s)/D(s)$. In other words, if the discontinuities across all the left-hand cuts were known, the exact solution can be obtained by N/D method. An important property of the equation (2.75) is that the input of $U(s)$ is only needed above the threshold, i.e. on the right-hand cut.

We mentioned before, that apart from the left- and right-hand cuts, the amplitude may have poles on the real axis. This poles correspond to the bound states, with the binding energy s_B that can be found by searching for the zero of the D function below threshold:

$$D(s_B) = 0\,, \quad s_B < s_{\mathrm{thr}}\,. \tag{2.76}$$

From this condition follows that

$$1 - \frac{s_B - s_M}{\pi} \int_R \frac{ds'}{s' - s_M} \frac{N(s')\rho(s')}{s' - s_B} = 0\,. \tag{2.77}$$

Hence around the bound state it holds

$$t(s) \simeq \frac{N(s_B)}{D'(s_B)(s - s_B)}\,, \quad g_B^2 = -\frac{N(s_B)}{D'(s_B)}\,, \tag{2.78}$$

where g_B denotes the bound state coupling constant.

In this case the solution obtained using the set of N/D equations with input from $U(s)$ satisfies the dispersive representation (2.66) combined with the pole term

$$t(s) = U(s) + \frac{s - s_M}{s_B - s_M} \frac{g_B^2}{s_B - s} + \frac{s - s_M}{\pi} \int\limits_{s_{\mathrm{thr}}}^{\infty} \frac{ds'}{s' - s_M} \frac{\mathrm{Disc}\ t(s')}{s' - s}\,, \tag{2.79}$$

Including such a pole term into the definition of $U(s)$ does not change the solution of N/D equations or the integral equation for the $N(s)$ function. We can show it explicitly by introducing the function $\tilde{U}(s)$ in a way that

$$\tilde{U}(s) = U(s) + \frac{s - s_M}{s_B - s_M} \frac{g_B^2}{s_B - s} \,. \tag{2.80}$$

We start with the function $\tilde{N}(s)$ given by (2.75) where we replaced $U(s)$ with $\tilde{U}(s)$:

$$\begin{aligned}
\tilde{N}(s) &= \tilde{U}(s) + \frac{s - s_M}{\pi} \int\limits_{s_{\text{thr}}}^{\infty} \frac{ds'}{s' - s_M} \frac{\rho(s')\tilde{N}(s')(\tilde{U}(s') - \tilde{U}(s))}{s' - s} \,, \\
&= U(s) + \frac{s - s_M}{s_B - s_M} \frac{g_B^2}{s_B - s} + \frac{s - s_M}{\pi} \int\limits_{s_{\text{thr}}}^{\infty} \frac{ds'}{s' - s_M} \frac{\rho(s')N(s')(U(s') - U(s))}{s' - s} \\
&\quad + \frac{s - s_M}{\pi} \int\limits_{s_{\text{thr}}}^{\infty} \frac{ds'}{s' - s_M} \rho(s')N(s') \frac{\frac{s'-s_M}{s_B-s_M}\frac{g_B^2}{s_B-s'} - \frac{s-s_M}{s_B-s_M}\frac{g_B^2}{s_B-s}}{s' - s} \,, \\
&= N(s) + \frac{s - s_M}{s_B - s_M} \frac{g_B^2}{s_B - s} D(s_B) \equiv N(s) \,.
\end{aligned} \tag{2.81}$$

The last term in the above equation is eliminated by using the bound state condition (2.76).

The unitarity relation (2.70) implies, that for the inverse of D-function the following holds

$$\text{Disc}\left(\frac{1}{D(s)}\right) = -\frac{\text{Disc}D(s)}{|D(s)|^2} = \rho(s)t(s)\left(\frac{1}{D(s)}\right)^* \,. \tag{2.82}$$

The function, that satisfies the above unitarity relations is called *Omnés function*: $\Omega(s)$ [58]

$$\text{Disc}\ \Omega(s) = t(s)\rho(s)\Omega^*(s) \,. \tag{2.83}$$

It is analytic everywhere and contains the information regarding the right hand cuts. Therefore, it satisfies the dispersion relation of the form:

$$\Omega(s) = 1 + \frac{s - s_M}{\pi} \int\limits_{s_{\text{thr}}}^{\infty} \frac{ds'}{s' - s_M} \frac{\text{Disc}\ \Omega(s)}{s' - s} \,. \tag{2.84}$$

The simple relation (2.83) between the Omnés and D-functions holds only in the abscence of bound state due to the condition (2.76). If there is a bound state in the system, this relation changes:

$$\Omega(s) = \frac{s - s_B}{s_M - s_B} \frac{1}{D(s)} \,. \tag{2.85}$$

The advantage of the Omnés approach, is that for the single-channel case, the Omnés function can be obtained in the analytic form. We first parametrize it in terms of the phase shift $\delta(s)$:

$$\Omega(s \pm i\epsilon) = |\Omega(s)|e^{\pm i\delta(s)} \,, \tag{2.86}$$

with the convention $\delta(s_{\text{thr}}) = 0$. It is then frequently computed directly from the existing parametrizations of the phase shift data and various assumptions about its asymptotic behaviour at infinity.

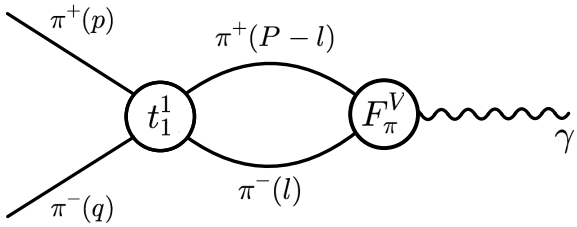

Figure 2.7: The schematic representation of the pion vector form factor F_π^V

The discontinuity of the Omnés function in the form (2.86) can be found as

$$\frac{1}{2i}(\Omega(s+i\epsilon)-\Omega(s-i\epsilon)) = \Omega(s+i\epsilon)\sin\delta(s)e^{-i\delta(s)}\,,$$
$$\text{Disc}\,(\ln\Omega(s)) = \delta(s)\,. \tag{2.87}$$

Invoking the once subtracted dispersion relation for the logarithm

$$\ln\Omega(s) = \frac{1}{\pi}\int\limits_{s_{\text{thr}}}\frac{\text{Disc}(\ln\Omega(s'))}{s'-s}ds' = \frac{1}{\pi}\int\limits_{s_{\text{thr}}}\frac{\delta(s')}{s'-s}ds'\,, \tag{2.88}$$

we obtain the dispersive representation for the Omnés function

$$\Omega(s) = \exp\left(a+\frac{s-s_M}{\pi}\int\limits_{s_{\text{thr}}}^{\infty}\frac{\delta(s')}{s'-s}ds'\right) = \exp\left(\frac{s-s_M}{\pi}\int\limits_{s_{\text{thr}}}^{\infty}\frac{\delta(s')}{s'-s}ds'\right)\,, \tag{2.89}$$

with the subtraction constant a defined by the normalisation condition $\Omega(s_M)=1$. Such simple analytic form of the Omnés function can be obtained only in the single-channel case. In the coupled-channel case it is essential to solve the full system of the N/D equations.

2.2.5 Pion vector form factor

The Omnés function has numerous applications in the scattering theory. In order to illustrate how this method works in practice, we consider a classical problem showing the usefulness of the dispersion relation approach: the pion vector form factor $F_\pi^V(s)$, which has only the right hand cuts.

On one hand, at low energy it can be calculated from NLO χPT as [59]:

$$F_\pi^V(s) = 1+\frac{1}{6}\frac{1}{(4\pi f_\pi)^2}(L_6-1)s+\frac{1}{6f_\pi^2}(s-4m_\pi^2)\bar{J}(s)+\mathcal{O}(s^2)\,,$$
$$\bar{J}(s) = \frac{1}{16\pi^2}\left(2+\beta_\pi(s)\ln\frac{\beta_\pi(s)-1}{\beta_\pi(s)+1}\right)\,, \tag{2.90}$$

where L_6 is the NLO low-energy constant, $\beta_\pi(s)=\sqrt{1-4m_\pi^2/s}$ and m_π is a pion mass. However, this description breaks down very fast as the energy increases.

Aiming to implement the dispersive approach, we first note that the matrix element corresponding to the transition of a photon to a pair of pions (see Fig. 2.7) is defined as

$$\langle\pi^+(p)\pi^-(q)|\,J_\mu(0)\,|0\rangle = (p-q)_\mu F_\pi^V(s)\,, \tag{2.91}$$

where J_μ is the electromagnetic current. The pion vector form factor is normalized as $F_\pi^V(0)=1$ to the value of the pion electric charge. The factor $(p-q)_\mu$ imposes the gauge invariance

when both pions are on-shell. The analytic structure of this amplitude is simple, as there are no crossed channel exchanges and hence, only the right-hand cuts are present (see Fig. 2.6). The discontinuity of this process can be calculated employing the standard Cutkosky rules [60]

$$(p-q)_\mu \text{Disc } F_\pi^V(s) = \frac{i}{2}\int \frac{d^4l}{(2\pi)^4}(2\pi)\delta(l^2-m_\pi^2)\delta((P-l)^2-m_\pi^2)T^I(s,z)(P-2l)_\mu F_\pi^V(s)\,, \quad (2.92)$$

where $T^I(s,z)$ denotes the $\pi\pi$ amplitude of isospin I and $P=p+q$, $P^2=s$. Performing the momentum integration, we obtain

$$(p-q)_\mu \text{Disc } F_\pi^V(s) = \frac{i}{64\pi}\beta_\pi(s)F_\pi^V(s)\int d\Omega_l T_I^*(s,z)(P-2l)_\mu\,, \quad (2.93)$$

Invoking the partial wave decomposition (2.37) and the orthogonality condition for the Legendre polynomials

$$(2J+1)\int_{-1}^{1} dz P_J(z)P_{J'}(z) = 2\delta_{JJ'}\,, \quad (2.94)$$

it can be shown that only the $J=1$ partial-wave amplitude remains. Hence, up to inelastic corrections we have

$$\text{Disc } F_\pi^V(s) = \rho(s)F_\pi^V(s)t_1^{1*}(s)\theta(s-4m_\pi^2)\,, \quad (2.95)$$

where appart from the spin $J=1$, we also restored the isospin $I=1$ index of the $\pi\pi$ amplitude $t_1^{1*}(s)$. In this case the Watson final state interaction theorem, that states that the phase of the form factor below inelastic thresholds is given by the two-particle scattering phase shift, reads as

$$\delta_{F_\pi^V} = \delta_1^1(s)\,. \quad (2.96)$$

The form factor can then be represented using a simple polynomial function $P(s)$ and Omnés function $\Omega_1^1(s)$

$$F_\pi^V(s) = P(s)\Omega_1^1(s)\,. \quad (2.97)$$

Perturbative QCD suggests that up to logarithmic corrections $F(\infty)\to 1/s$ and assuming $\delta_1^1(s\to\infty)=\pi$, the polynomial function simplifies to $P(s)=1$. Therefore, for the pion vector form factor we have a simple expression:

$$F_\pi^V(s) = \exp\left(\frac{s}{\pi}\int_{4m_\pi^2}^{\infty}\frac{\delta_1^1(s)}{s'(s-s')}\right)\,, \quad (2.98)$$

which requires the input for the phase shift $\delta_1^1(s)$ above threshold. Fortunately, for the p-wave $\pi\pi$ scattering, the phase shift has been measured experimentally [61] and therefore the form factor can be reconstructed in a data-driven manner.

The comparison between the NLO χPT (2.90) and dispersive (2.98) results is shown in Fig. 2.8. It is clear, that further away from the threshold region the NLO χPT becomes inadequate, while the dispersive result is far more accurate. Naturally, the above model does not account for the full complexity of the pion vector form factor. Apart from the leading two-pion intermediate contribution, there are additional isospin breaking effects resulting in the narrow structures at ω and ϕ masses (see, for instance, [63] and references therein), however, this lies far beyond the pedagogical example of Omnés function application.

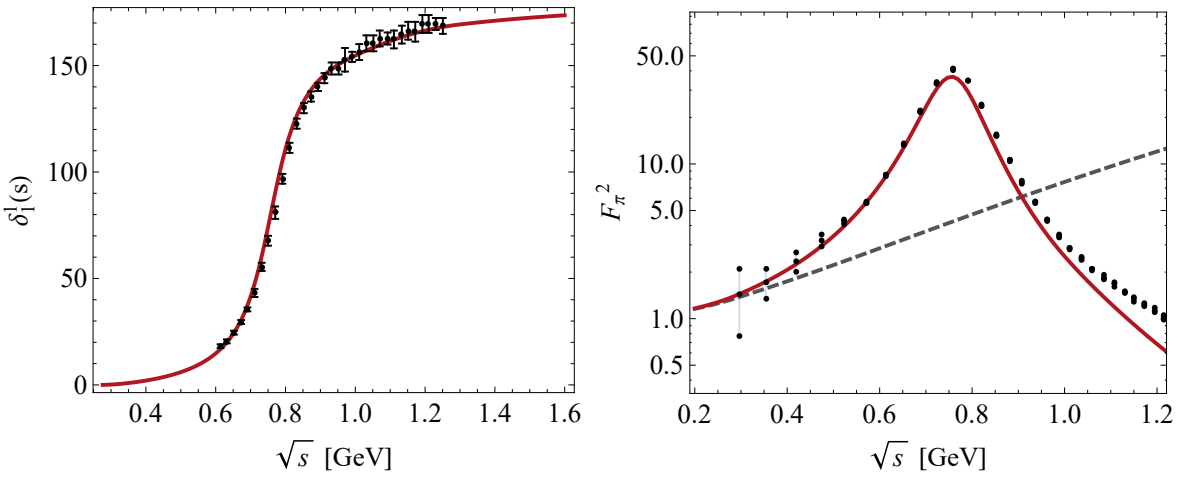

Figure 2.8: Energy dependence on the p-wave $\pi\pi$ phase shift (left) compared to the data from [61] and pion vector form factor (right) against the data [62]. The dashed line denotes the NLO χPT result and the solid line the dispersive result.

2.2.6 Resonances

Aside from the construction of the dispersion relations, knowledge of the analytical structure of the scattering amplitude is vital for studying the resonance phenomena. The resonance is an unstable and short-living state, which cannot be directly measured by experiment and has to be analyzed from its more long-lived decay products. For the isolated resonance the mass distribution is usually approximated by the non-relativistic Breit-Wigner formula (see App. 5.A). While from the data perspective, the resonance appears as, for instance, some peak in the total cross section, most of the time [64] there is a direct correspondence between this enhancement and an underlying feature of the scattering amplitude - either a pole or zero. The position of the corresponding feature distinguishes the nature of states. The pole which lies on the physical *Riemann sheet* corresponds to a *bound states*, while a *resonance* pole is located in the complex plane on the unphysical Riemann sheets.

The study of the resonances is often impossible without analytical continuation of the scattering amplitude to the complex s-plane. Some symmetric resonances can be approximated with simple models, while for others, it may lead to wrong conclusions (see Chapter 5). In addition, the broad resonances like $\sigma/f_0(500)$ cannot be in principle described by the simple parametrization. Moreover, the situation becomes even more complicated when there are overlapping resonances with the same quantum numbers. Therefore, we have to rely on the general analytical properties of the amplitudes.

For the partial wave amplitude t_J^I on the first Riemann sheet (I), the unitarity relation implies

$$
\begin{aligned}
&t_J^I(s+i\epsilon) - t_J^I(s-i\epsilon) = 2i\rho(s) t_J^I(s+i\epsilon) t_J^I(s-i\epsilon)\,, \\
&t_J^I(s+i\epsilon) = \frac{t_J^I(s-i\epsilon)}{1-2i\rho(s) t_J^I(s-i\epsilon)}\,, \\
&t_J^I(s+i\epsilon) \overset{\epsilon\to 0}{=} t_J^{II}(s-i\epsilon)\,,
\end{aligned}
$$

where t_J^{II} is the amplitude on the second Riemann sheet. We obtain that the value of the amplitude at a given point on the unphysical sheet is now functionally determined by the value

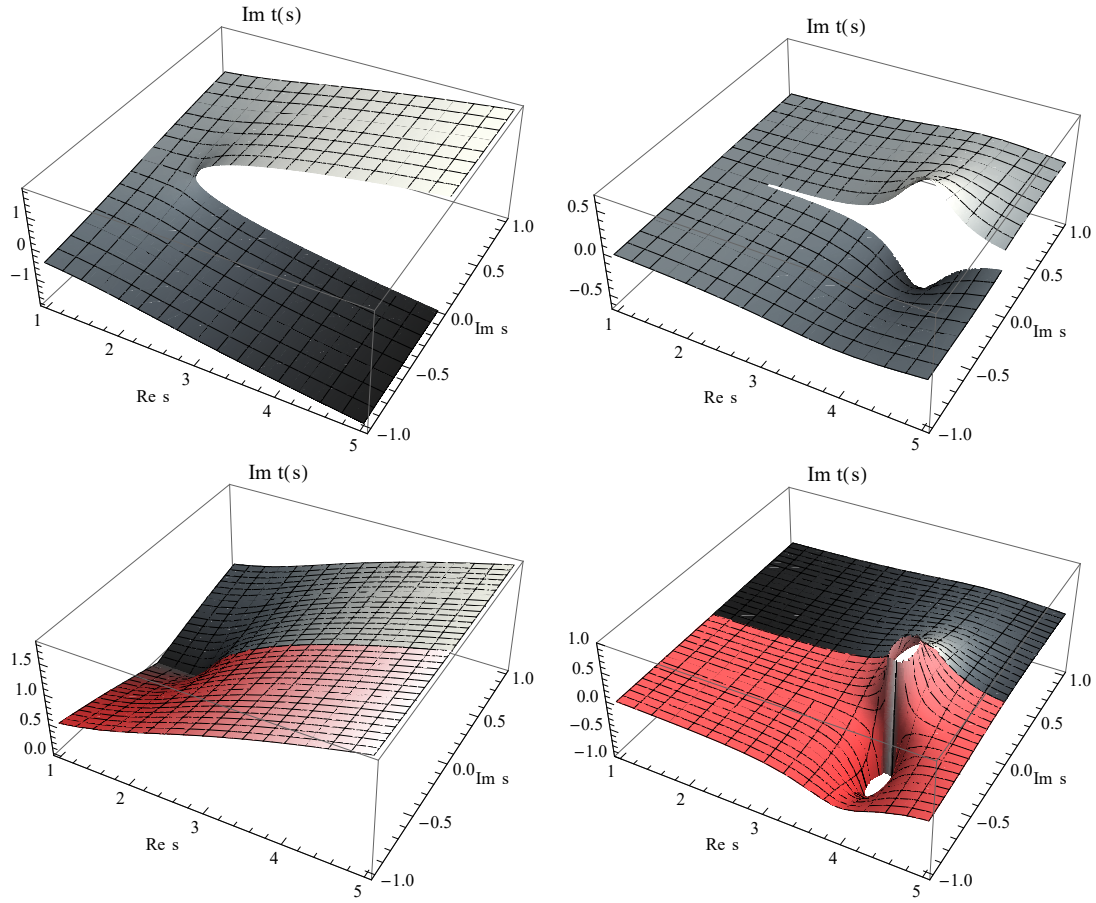

Figure 2.9: Imaginary part of a typical single–channel scattering amplitude without (left) and with isolated resonance (right). The first Riemann sheet is shown in black and the analytical continuation to the second Riemann sheet is shown in red.

of the physical amplitude. From the above relations follows the condition of the resonance:

$$t_J^{II}(s) = \frac{t_J^I(s)}{1 - 2i\rho(s)t_J^I(s)}\,, \quad \text{resonance: } 1 - 2i\rho(s)t_J^I(s) = 0\,. \tag{2.99}$$

While all resonances considered in this work are located on the second Riemann sheet, it is instructive to mention more complicated cases with multiple relevant thresholds and hence, unphysical Riemann sheets. Since each opening channel starts a branch cut, it is clear than in coupled-channel system the search for the resonances must not be limited only to the sheet closest to the physical one. In principle, the amplitude can be analytically continuated to any number of sheets and only the sign of the imaginary part will change with each crossing. As an example, consider the system with two relevant thesholds. It is the case for the $\gamma\gamma \to \pi\pi$ scattering, where first threshold is $\pi\pi$ and the second one is $K\bar{K}$. The first resonance of interest, $\sigma/f_0(500)$ is located far from the KK threshold, yet it experience some effects from it (see Chapter 3). The $f_0(980)$ resonance is located in the vicinity of the $K\bar{K}$ theshold, but also on the second Riemann sheet. A more interesting case of the $\gamma\gamma \to \pi\eta$ scattering. There, the $a_0(980)$ resonance is located on the fourth Riemann sheet [65], which results in its cusp-like appearance on the total cross section [66].

2.3 Anomalous magnetic moment of muon

The significant part of this thesis is dedicated to the dispersive analysis of the two-photon fusion reactions to a pair of pseudoscalar mesons (see Chapter 4). While the two-photon processes are a very powerful probe to reveal the composition of the hadronic resonances [67], their significance also cannot be underestimated in the light of another enigma of particle physics - *the anomalous magnetic moment of muon*. Being one of the pinnacles of modern precision experiments, this number challenges the Standard Model itself due to the discrepancy of around 4 standard deviations between the experimental value and the theoretical prediction. The second-largest contribution to the theoretical uncertainty arises from the hadronic light-by-light scattering, to which the $\gamma^*\gamma^* \to \pi\pi, \pi\eta, K\bar{K}\ldots$ reactions involving the space-like photons, serve as an essential building block. Therefore, in this section, we aim to give a brief overview of the anomalous magnetic moment of muon problem, concentrating on the contributions relevant to this thesis. This section is based mostly on [68–71] and further details can be found therein.

First, we briefly remind the general notion of the magnetic moment. For the elementary particle of mass m with intrinsic angular momentum, or, spin $\vec{S}$ and charge q, the magnetic moment is given as

$$\vec{\mu} = g\frac{q}{2m}\vec{S}\,, \tag{2.100}$$

where g is the gyromagnetic ratio. For electron, the relativistic quantum mechanics predicts $g = 2$ [72]; however, this quantity acquires additional contributions from the radiative corrections in relativistic quantum field theory. The first order QED correction was calculated by Schwinger in 1948 and increased the value of g by α/π [73], where α is the fine structure constant. Since then, significant progress has been made not only for the electron but for other charged leptons as well, as they all naturally exhibit the *magnetic anomaly* a_l, defined as the deviation from the Dirac theory prediction of $g_l = 2$:

$$a_l = \frac{g_l - 2}{2}\,, \tag{2.101}$$

where l stands for electron (e), muon (μ) or τ-lepton. This quantity can be very precisely studied by experiment from the analysis of lepton's motion in an external magnetic field [70] and predicted theoretically, both with extremely high precision and, therefore, serve as a test of the Standard Model. Any discrepancy between theoretical and experimental values has been investigated thoroughly over the last decades due to the potential indication of the so-called *new physics*, or *physics beyond the Standard Model*, contributions.

For the anomalous magnetic moment of electron, the most recent experimental measurement achieved a precision of 0.24 parts-per-billion (ppb) [74]. On the other hand, while being equivalently precise, the theoretical prediction is sensitive to the experimentally measured fine structure constant. Depending on the value of α used as an input, the current tension between the experimental and theoretical a_e reaches $-2.5, -1.7$ or $+1.6\sigma$ [68]. Even though measurements on the electron are the most precise among all other leptons, its anomalous magnetic moment is rather insensitive to strong and weak interactions. The study of heavier leptons allows testing all sectors of the Standard Model, as they contribute significantly. Moreover, aiming to unveil the possible effects of new physics, which contribution to a_l is expected to be proportional to

$$a_l^{\mathrm{NP}} \sim \frac{m_l^2}{\Lambda^2}\,, \tag{2.102}$$

where m_l is a lepton mass and Λ is a scale of new physics, the anomalous magnetic moment of τ-lepton would be an ideal candidate. However, the τ-lepton has a relatively short lifetime, thus resulting in the poor accuracy of experiment [75].

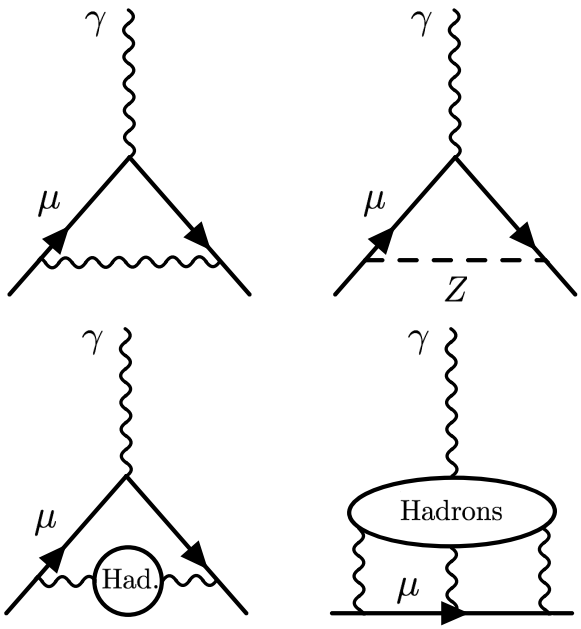

Figure 2.10: Schematic representation of the Standard Model contributions to the anomalous magnetic moment of muon. Left to right: one-loop QED, one-loop EW with Z-boson exchange, leading order HVP and HLbL contributions.

Therefore, it is not surprising that the anomalous magnetic moment of the remaining lepton - muon has generated significant interest from both experimental and theoretical sides. Compared to the electron, the larger mass of muon increases the sensitivity to the possible new physics effects and enhances the hadronic sector contribution, which we will discuss later. At the same time, experiments involving muon currently reach the unprecedented precision of 0.46 parts-per-million (ppm), resulting in a total number [76, 77]:

$$a_\mu^{\text{exp}} = 116\,592\,061(41) \times 10^{-11}\,. \tag{2.103}$$

Moreover, having more considerable uncertainty compared to the electron, the anomalous magnetic moment of muon is also less sensitive to the experimental input of the fine structure constant.

The most up-to-date Standard Model prediction gives out the following value of a_μ [7]:

$$a_\mu^{\text{SM}} = 116\,591\,810(43) \times 10^{-11}\,. \tag{2.104}$$

The resulting difference between the experimental and theoretical values $a_\mu^{\text{exp}} - a_\mu^{\text{SM}} = (251 \pm 59) \times 10^{11}$ has a significance of 4.2σ, which further motivates both the searches for the physics beyond the Standard Model and better understanding of already included contributions.

The Standard Model prediction of the anomalous magnetic moment of muon consists of the sum of the following contributions:

$$a_\mu^{\text{SM}} = a_\mu^{\text{QED}} + a_\mu^{\text{EW}} + a_\mu^{\text{HVP}} + a_\mu^{\text{HLbL}}\,, \tag{2.105}$$

which are schematically shown in Fig. 2.10.

The QED contribution a_μ^{QED}, which includes all photonic and leptonic loops starting from the Schwinger result of $\alpha/2\pi$ has already been calculated up to the five-loop order resulting in $a_\mu^{\text{QED}} = 116\,584\,718.931(104) \times 10^{-11}$. The electroweak contribution a_μ^{EW} consist of all

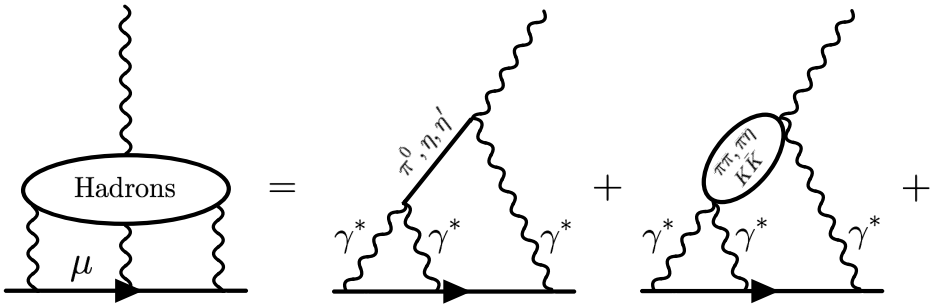

Figure 2.11: Schematic representation of the hadronic light-by-light contributions to the anomalous magnetic moment of muon.

interactions including at least one of W, Z or Higgs bosons and due to their masses is highly suppressed: $a_\mu^{\mathrm{EW}} = 153.6(1.0) \times 10^{-11}$. The theoretical uncertainties of a_μ mainly originate from the hadronic contributions, which can be divided into two constituents: *hadronic vacuum polarization* (HVP) and *hadronic light-by-light* (HLbL) processes.

At present, the HVP contribution dominates the overall theoretical uncertainty with the value $a_\mu^{\mathrm{HVP}} = 6845(40) \times 10^{-11}$, which includes the results of the data-driven approaches based on the $e^+e^- \to$ hadrons cross section data. This data serves as an input into the dispersion relation. In addition, lattice QCD has made significant progress towards the estimation of the HVP contribution, however, until recently the uncertainties of most analyses were still comparatively large [7]. In 2021, a first lattice result by BMW collaboration [78] with a sub-percent uncertainty appeared, providing estimation for the leading order HVP contribution, which favours the experimentally measured value of a_μ over the results based on the dispersive predictions.

Unlike the HVP contribution, for quite some time, the existing calculations of the HLbL part were based on the hadronic models rather than being determined from data [71]. Since HLbL gives the second largest contribution to overall theoretical uncertainty, it was crucial to construct a data-driven model-independent approach to reduce it. The current phenomenological approach to HLbL scattering is mainly based on the dispersion relations and results in the following contribution [7]:

$$a_\mu^{\mathrm{HLbL}} = 92(19) \times 10^{-11}\,. \tag{2.106}$$

The HLbL scattering is schematically shown in Fig. 2.11. It describes the process in which an external photon interacts with three virtual photons via hadronic intermediate states. These off-shell photons are then coupled to the muon. There is a clear hierarchy among the different intermediate state contributions based on their mass. At low energies, there is an exchange of light pseudoscalar mesons π^0, η, η'. Then there is a contribution from heavier scalar resonances like $f_0(980), a_0(980)$, axial-vector mesons $a_1(1260), f_1(1285)$ and tensor $f_2(1270), a_2(1320)$ above 1 GeV. In addition, there are loops with charged pions and kaons, three pion and other multi-hadron intermediate states. Furthermore, the question of the HLbL behavior at the asymptotically large values of momenta, or *short-distance constraints* (SDCs), should be adressed as well. The contributions of the various intermediate states that have been estimated and put together here do not satisfy the SDCs, which is still a subject for a future work [6, 7].

In a similar manner, it is possible to include further intermediate states like $\pi\eta$ and $K\bar{K}$ up to $a_0(980)$ region, which requires proper dispersive treatment of $\pi\eta, K\bar{K}$ coupled-channel system.

The light pseudoscalar mesons π^0, η, η' contributions have been evaluated within the dispersive approach with uncertainty originating from the input of the transition form factors (see for

instance [79]). The two-pion intermediate state in the $f_0(500)$ region was also accounted for in the model-independent way [80]. This analysis was recently extended to the coupled-channel $\pi\pi, K\bar{K}$ scenario [81] using the input from [2] described in Chapter 3 and compared to the narrow width approximation used before for the $f_0(980)$.

Finally, it is important to list a few possible new physics explanations of the current discrepancy between experimental and theoretical values of a_μ. First, one of the natural explanations involves the supersymmetric particle loops. However, there is yet no direct evidence in support of the supersymmetry interpretation. Another scenario, currently disfavored, involves a dark photon, a hypothetical vector boson from the dark matter sector. For the comprehensive overview of the beyond the Standard Model contributions to muon's anomalous magnetic moment, we refer to [82].

Chapter 3

Data-driven dispersive analysis of the $\pi\pi$ and πK scattering

The ideas and methods described in the previous chapter have found numerous applications in different strongly-interacting physics processes. The hadron-hadron interaction is a prime example of such reactions. This Chapter will concentrate on describing the interaction of light pseudoscalar mesons - the pion and the kaon, namely $\pi\pi \to \pi\pi$ and $\pi K \to \pi K$ scattering. The importance of these processes can hardly be overestimated since they, in many instances, appear as a part of the final state interaction of many reactions. Until recently, $\sigma/f_0(500)$, $f_0(980)$, and $\kappa/K^*(700)$ resonances appearing in the spectrum of these reactions were seen as enigmatic due to their properties dissimilar to the expectations for the standard $q\bar{q}$ states. Thus they are serving as the candidates for the lightest exotic hadrons. Following an extensive theoretical effort over the last decades, the various dispersive analyses have established the pole positions corresponding to these resonances and described the $\pi\pi$ and πK amplitudes with utmost precision.

However, the power of these analyses partially results from the inclusion of all possible data input. Thus being meticulous in the description of the $\pi\pi \to \pi\pi$ and $\pi K \to \pi K$ scattering for which the data is comparatively abundant, these analyses can not be straightforwardly extended to the description of processes that are not so well understood from an experimental point of view. In addition, with the increasing computational power, lattice QCD has become a source of an entirely new type of data, requiring to extend the scope to values of the pion mass larger than its value in nature. This valuable input is, however, still analysed within the K-matrix approach, which, while being easy to implement, in many ways, is far from ideal and sometimes even problematic. Thus, both the importance of $\pi\pi \to \pi\pi$ and $\pi K \to \pi K$ scattering per se and the need to extend the existing theoretical developments to the new types of data and less well-studied processes calls for a data-driven approach, which fully accounts for the unitarity and analyticity requirements. This partial-wave dispersive approach and its successful application to the $\sigma/f_0(500)$, $f_0(980)$ and $\kappa/K^*(700)$ resonances will be the main focus of this Chapter.

The Chapter is based on [2, 5] and it is organised as follows. In the next section, we will briefly outline the importance of studying the $\pi\pi \to \pi\pi$ and $\pi K \to \pi K$ processes and related resonances. In Sec. 3.2, we will focus on the formalism that we adopt. We will deepen the ideas of the N/D method, particularly for the coupled-channel system and the left-hand cut input required to solve the dispersion relation. Also, we will briefly comment on the input from Chiral Perturbation Theory, which, although unable to describe the considered processes in the resonance region, still provides important low-energy constraints that should be taken into account. In Secs. 3.3 and 3.4, we will then present the numerical results. We will start with $I = 0$, $\pi\pi$ single-channel analysis of both experimental and lattice data, which is followed by the coupled-channel $\{\pi\pi, K\bar{K}\}$ analysis of the experimental data. Finally, in Sec. 3.4, we will focus on the πK, $I = 1/2$ scattering where $\kappa/K^*(700)$resonance reside. The analysis will be performed for both experimental and lattice data. At the end of Secs. 3.3 and 3.4 we will also show the results for the non-resonant channels. The Chapter ends with a summary of our main results and a discussion of their importance for the following chapters and future applications.

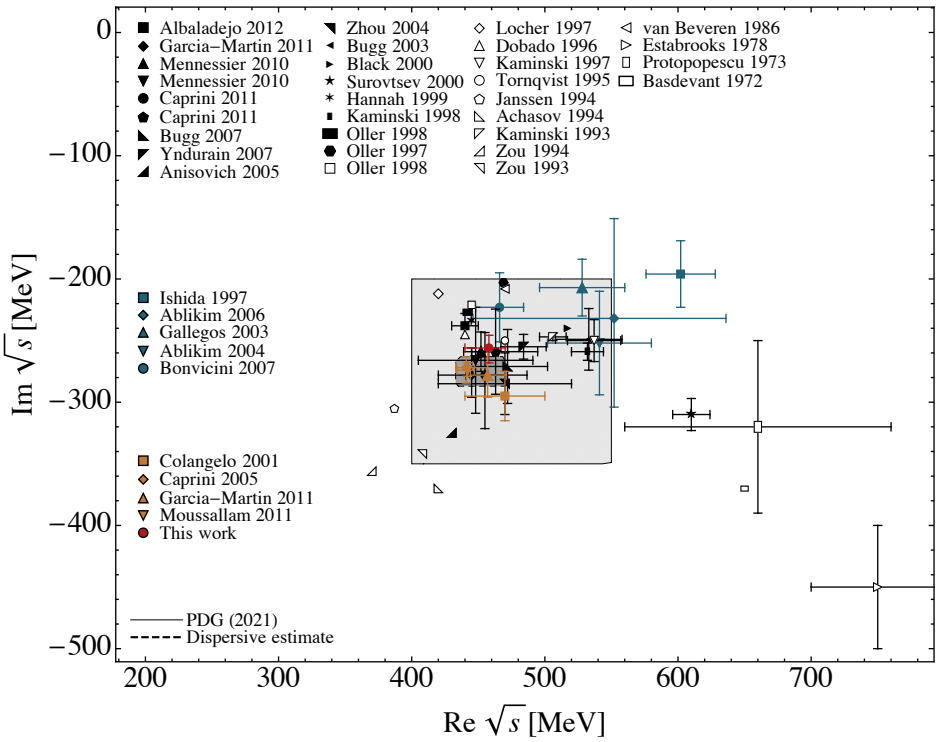

Figure 3.1: $\sigma/f_0(500)$ pole positions from various analyses included in PDG (2021) [83] listings. Blue points denote the results of the Breit-Wigner analyses, orange points - the most accurate dispersive predictions from [84–87]. The gray shaded area covers the PDG estimate, while the darker area shows the conservative dispersive estimate. Finally, the red point shows the result of the coupled-channel analysis of the $\{\pi\pi, K\bar{K}\}$ system presented in the present Chapter.

In App. 3.A we will provide the kinematical conventions for the $2 \to 2$ process and in App. 3.B we introduce the bootstrap method, extensively used for uncertainty calculation in the present and the following chapters.

3.1 Introduction

Understanding the strong interactions in the low-energy regime was always strongly connected to investigating the hadron-hadron reactions. In particular, the meson-meson scattering has long served as a tool to test both the low-energy and precision frontier of strong physics. In addition, there is a renewed interest in the hadron spectroscopy, motivated by recent discoveries of unexpected exotic hadron resonances [26, 92–94]. Currently, LHCb, BESIII, and COMPASS collected data with unprecedented statistics, Belle-II and GlueX started to operate, and more facilities are planned in the near future, such as PANDA and EIC. Besides, lattice QCD has been applied to a broad range of hadron processes and recently was able to calculate the lowest excitation spectrum with the masses of the light quarks near their physical values [95, 96].

Among others, the scalar mesons, especially the ones below 1 GeV are of great interest. First, due to the violation of the mass hierarchy it is implausible that they could be a pure conventional $q\bar{q}$ states. In addition, there are some clear indications of the non-ordinary nature of such mesons. The $\sigma/f_0(500)$ and $\kappa/K^*(700)$ mesons, appearing as resonances in $\pi\pi \to \pi\pi$ and $\pi K \to \pi K$ processes, respectively, serve as a prime example. As a matter of course, any claims regarding the non-ordinary or *exotic* nature invoke some controversies surrounding

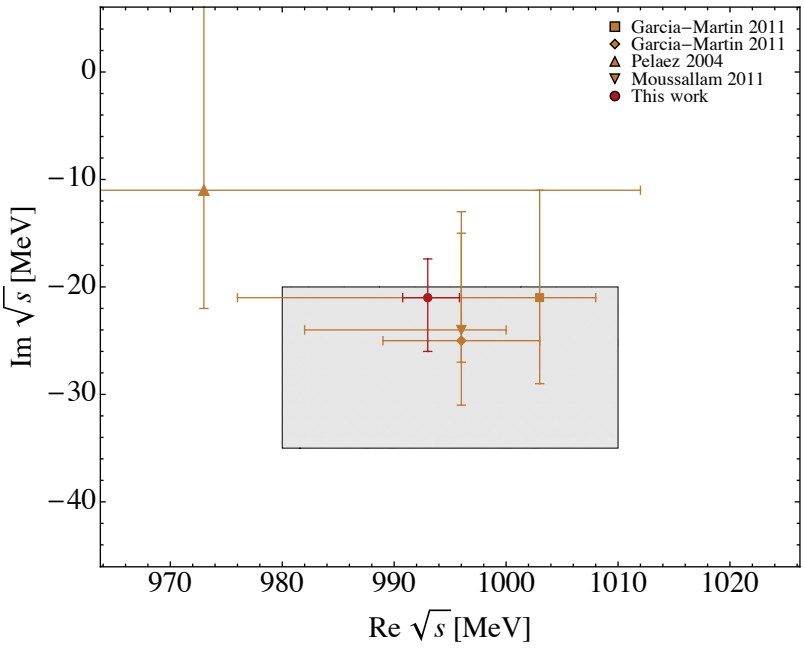

Figure 3.2: $f_0(980)$ pole positions included in the PDG (2021) [83] listings. The gray band covers the PDG estimate, which includes also other analyses on mass and width. Orange points show the most accurate dispersive predictions from [86–88]. The red point shows the result of the coupled-channel analysis of the $\{\pi\pi, K\bar{K}\}$ system presented in the present Chapter.

these mesons today.

The $\sigma/f_0(500)$ resonance enjoyed its peculiar position for quite a long time. For a comprehensive review on the history of combined theoretical and experimental effort in searching $\sigma/f_0(500)$ we refer to [97] and also to Fig. 3.1, where all the relevant findings from PDG listings are included, together with the results of the work presented in this Chapter. At the same time, there are considerably fewer results for the $\kappa/K^*(700)$ (see Fig. 3.3). As for the $f_0(980)$ resonance, there is only a handful of studies available (see Fig. 3.2). Rather than directly targeting the questions of their nature, in this Chapter we mainly aim to study the properties such as pole positions and couplings.

To correctly identify resonance parameters one has to search for poles in the complex plane. This is particularly important when there is an interplay between several inelastic channels or when the pole is lying very deep in the complex plane. In these cases, the structure of the resonance is quite different from a typical Breit-Wigner behaviour. In order to determine the pole position of the resonance, one has to analytically continue the amplitude to the unphysical Riemann sheets. At this stage, the right theoretical framework has to be applied. The latter should satisfy the main principles of the S-matrix theory, namely unitarity, analyticity, and crossing symmetry. These constraints were successfully incorporated in the set of Roy or Roy-Steiner equations [98, 99]. In a practical application, however, the rigorous implementation of these equations is almost impossible, since it requires experimental knowledge of all partial waves in the direct channel and all channels related by crossing. Therefore, the current precision studies of $\pi\pi$ [84–86, 97, 100–103] and πK [89, 91, 104, 105] scattering are based on a finite truncation, which in turn limits the results to a given kinematic region, and require a large experimental data basis. Furthermore, applying Roy-like equations for coupled-channel cases is quite complicated and has not been achieved in the literature so far. Because of the above-mentioned difficulties, in the experimental analyses, it is a common practice to ignore

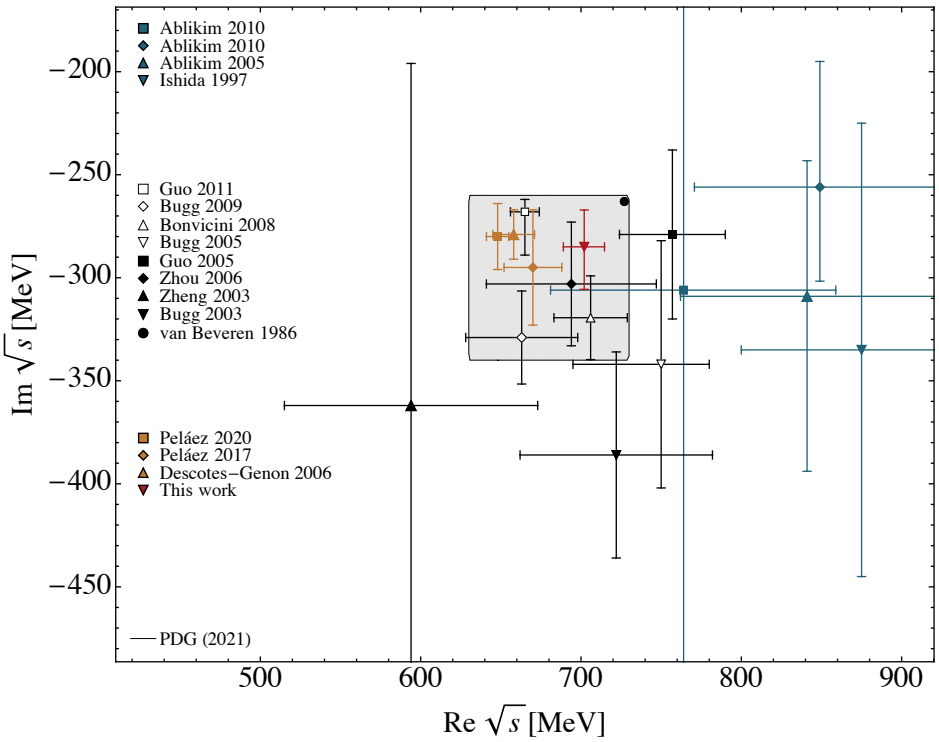

Figure 3.3: $\kappa/K^*(700)$ pole positions from various analyses included in PDG (2021) [83] listings. Blue points denote the results of the Breit-Wigner analyses, orange points - the most accurate dispersive predictions from [89–91]. The gray shaded area covers the PDG estimate. Finally, the red point shows the result of the analysis of the $\pi K \to \pi K$ system presented in the present Chapter.

the S-matrix constraints and rely on simple parameterizations. The most used ones are a superposition of Breit-Wigner resonances or the K-matrix approach. The latter implements unitarity, but ignores the existence of the left-hand cut and often leads to spurious poles in the complex plane. A good alternative to the K-matrix approach and a complementary method to Roy analysis is the so-called N/D technique [49], which is based on the partial-wave dispersion relations. In this method, the dominant constraints of resonance scattering, such as unitarity and analyticity are implemented exactly. Since the time it was introduced by Chew and Mandelstam [49], the N/D method has been extensively studied for different processes [51–54, 106–110]. The required input to solve the N/D equation are the discontinuities along the left-hand cut, which are typically approximated one way or another using chiral perturbation theory (χPT). In our approach we extend the ideas of [107–110], where the left-hand cut contributions were approximated using an expansion in powers of a suitably chosen conformal variable. In contrast to [53, 54], however, we follow here a data-driven approach and adjust the unknown coefficients in the expansion scheme to empirical data directly. In this way, the model dependence is avoided, and the method can also be applied to the reactions which do not include Goldstone bosons, like for instance the $J/\psi J/\psi$ scattering [92].

In this Chapter, we apply the N/D method to both resonant and non-resonant $\pi\pi$ and πK scattering in the S-wave. There are three main reasons for this choice.

First, the system of two pions (or pion and kaon) shows up very often as a part of the final state of many hadronic interactions and therefore serves as input in various theoretical or experimental data analyses, like e.g. $\eta \to 3\pi$ [111–115] , $\eta' \to \pi\pi\eta$ [116–118], $\gamma\gamma \to \pi\pi$ [119–121], $e^+e^- \to J/\psi(\psi')\,\pi\pi$ [122–124] (see also Chapter 4) or $D \to K\pi\pi$ [125, 126].

Second, even though the $\pi\pi \to \pi\pi$ (and to a lesser extent $\pi K \to \pi K$ and $\pi\pi \to K\bar{K}$) amplitudes are known very well from the Roy (Roy-Steiner) analyses [84–86, 89–91, 100–105, 127], in the practical dispersive applications the final state interactions (FSI) are implemented with the help of the so-called Omnès function, which does not have left-hand cuts. Indeed, the left-hand cuts are different for each production/decay mechanism, while the unitarity makes a connection between the production/decay and the scattering amplitudes only on the right-hand cut. In the N/D ansatz, the Omnès functions come out naturally, as the inverse of the D-functions.

Third, recently, it has become possible to calculate $\pi\pi$ and πK scattering using lattice QCD with almost physical masses [40, 128–135]. Since, both the $\sigma/f_0(500)$ and $\kappa/K_0^*(700)$ states lie deep in the complex plane, the reliable extraction of their properties requires the use of the formalism that goes beyond the simple K-matrix parametrization and incorporates in addition the analyticity constraint.

3.2 Dispersive formalism

In this section, we further develop the formalism outlined in the Sec. 2.2. While the main ideas of unitarity and analyticity encoded in the dispersion relation stand the same, their implementation in the case of the coupled-channel systems requires an additional discussion. The N/D equations discussed in Sec. 2.2.4 transform into a $(n \times n)$ system of equations, with each element requiring a proper left-hand cut input. Typically it is not always the case that the required data is available in each channel, and therefore it is necessary to resort to other types of constraints to describe the dynamics of the partial-wave amplitudes. In addition, when an integral equation comes into play, the purely technical question of the fitting procedure and error analysis arises naturally. This question appears to be unavoidable considering that the study of resonances requires an analytical continuation of the scattering amplitude into the complex s-plane and the complications related to it.

This section is organized as follows. We first present the extension of the N/D system to the coupled-channel case. In Sec. 3.2.2, we discuss the importance of the left-hand cuts and how they can be accounted for elegantly by employing the expansion in the conformal mapping variable. The coefficients of this expansion will serve as the parameters of our model, and hence, we will answer the question of how to determine them in a data-driven fashion while respecting the constraints dictated by chiral perturbation theory in the low energy region. Finally, we will focus on the fitting strategy and the nuances of the error analysis by implementing the bootstrap approach. We will also address the systematic uncertainties arising mainly from the parametrization of left-hand cuts and their effect on the analytical continuation of the scattering amplitude into the complex s-plane.

3.2.1 Dispersion relations for the $\pi\pi$ and πK systems

The main object of our study is the s-channel partial-wave amplitude t_{ab} , which for $2 \to 2$ process is given by the following decomposition:

$$T_{ab}(s,t) = \mathcal{N}_{ab} \sum_{J=0}^{\infty} (2J+1)\, t_{ab}^{(J)}(s)\, P_J(\cos\theta)\,, \tag{3.1}$$

where θ is the c.m. scattering angle and ab are the coupled-channel indices with a and b standing for the initial and final state, respectively. For the following discussion, we focus only on the S-wave ($J = 0$) and therefore will suppress the label (J). As it was mentioned in Sec. 2.2.4, the different normalization factors ($\mathcal{N}_{\pi\pi\pi\pi} = 2$, $\mathcal{N}_{\pi\pi K\bar{K}} = \sqrt{2}$ and $\mathcal{N}_{K\bar{K}K\bar{K}} =$

$\mathcal{N}_{\pi K\pi K} = 1$) are needed to ensure that the unitarity condition for identical and non-identical two-particle states are the same and can be written in the matrix form as

$$\begin{aligned} \text{Disc}\, t_{ab}(s) &\equiv \frac{1}{2i}\left(t_{ab}(s+i\epsilon) - t_{ab}(s-i\epsilon)\right) \\ &= \sum_c t_{ac}(s)\,\rho_c(s)\,t^*_{cb}(s)\,, \end{aligned} \tag{3.2}$$

where the sum goes over all intermediate states. The phase space factor $\rho_c(s)$ in Eq. (3.2) is given by

$$\rho_c(s) = \frac{1}{8\pi}\frac{p_c(s)}{\sqrt{s}}\,\theta(s - s_{th})\,, \tag{3.3}$$

with $p_c(s)$ and s_{th} being the center-of-mass three momentum and threshold of the corresponding two-meson system. Within the maximal analyticity assumption [46, 47], the partial-wave amplitudes satisfy the dispersive representation

$$t_{ab}(s) = \int_{-\infty}^{s_L} \frac{ds'}{\pi}\frac{\text{Disc}\; t_{ab}(s')}{s'-s} + \int_{s_{th}}^{\infty}\frac{ds'}{\pi}\frac{\text{Disc}\; t_{ab}(s')}{s'-s}\,, \tag{3.4}$$

where s_L is the position of the closest left-hand cut singularity and the discontinuity along the right-hand cut is given by (3.2). For unequal masses, as in πK scattering, the left-hand singularities of the partial-wave amplitude do not all lie on the real axis and the integration in the first term in Eq. (3.4) goes partly along the circle. We note, that the separation into left and right-hand cuts given in (3.4) is only possible for the systems where no anomalous thresholds are present [136, 137].

Again, we can subtract the dispersion relation given above in accordance with the unitarity condition

$$t_{ab}(s) = U_{ab}(s) + \frac{s - s_M}{\pi}\int_{s_{th}}^{\infty}\frac{ds'}{s'-s_M}\frac{\text{Disc}\; t_{ab}(s')}{s'-s}\,, \tag{3.5}$$

where we combined the subtraction constant together with the left-hand cut contributions into the function $U_{ab}(s)$. The choice of the subtraction point s_M will be discussed later. Just as in the single-channel case (see Sec. 2.2.4) the solution to (3.5) can be written using the N/D ansatz

$$t_{ab}(s) = \sum_c D^{-1}_{ac}(s)\,N_{cb}(s)\,, \tag{3.6}$$

which leads to a system of linear integral equations in a matrix form [138, 139]

$$\begin{aligned} N_{ab}(s) &= U_{ab}(s) + \frac{s-s_M}{\pi}\sum_c\int_{s_{th}}^{\infty}\frac{ds'}{s'-s_M}\frac{N_{ac}(s')\,\rho_c(s')\,(U_{cb}(s') - U_{cb}(s))}{s'-s}\,. \\ D_{ab}(s) &= \delta_{ab} - \frac{s-s_M}{\pi}\int_{s_{th}}^{\infty}\frac{ds'}{s'-s_M}\frac{N_{ab}(s')\rho_b(s')}{s'-s}\,. \end{aligned} \tag{3.7}$$

The integral equation for $N_{ab}(s)$ can be solved numerically given the input of $U_{ab}(s)$. Knowing the $N_{ab}(s)$ function on the right-hand cut, the $D_{ab}(s)$ function is calculated by (3.7) and finally the partial-wave amplitude is produced with Eq. (3.6). In other words, if the discontinuities across all the left-hand cuts were known[1] the exact solution can be obtained by the N/D method. An important property of Eq. (3.7) is that the input of $U(s)$ is only needed on the right-hand cut. In the case of many channels, both the diagonal and off-diagonal t-matrix

[1] in that case the subtraction constant is probably unnecessary to introduce.

elements have a right-hand cut starting at the lowest threshold s_{th}. However, only the input of the off-diagonal $U_{ab}(s)$ is required outside the physical region, while in order to solve (3.7), the input of the diagonal $U_{aa}(s)$ is needed in the physical region due to the phase space factor. It has a direct relevance for the $\{\pi\pi, K\bar{K}\}$ case, where in the $K\bar{K} \to K\bar{K}$ channel the overlap of left- and right-hand cuts happens, but only in the non-physical region, $4m_\pi^2 < s < 4(m_K^2 - m_\pi^2)$, and therefore does not require any modifications of the dispersion integrals. We also emphasize that by means of Eq. (3.6), the scattering amplitude can be rigorously continued into the complex plane, where one can determine pole parameters of the resonances. In our convention the scattering amplitude in the vicinity of the poles on the unphysical Riemann sheets (or physical Riemann sheet in the case of the bound state) is given by,

$$\mathcal{N}_{ab}\, t_{ab}(s) \simeq \frac{g_{pa}\, g_{pb}}{s_p - s}\,, \tag{3.8}$$

where the normalization factor $\mathcal{N}_{ab}$ comes from Eq. (3.1) and g_{pi} denotes the coupling of the pole at $s = s_p$ to the channel $i = a, b$.

We wish to comment on the case when there is a bound state in the system, since it happens for the relatively large unphysical pion masses. In the coupled-channel case to find the binding energy s_B, one searches for a zero of the determinant of the D_{ab} matrix for energies below threshold,

$$\det(D_{ab}(s_B)) = 0, \quad s_B < s_{th}\,. \tag{3.9}$$

In this case, the solution obtained using the set of N/D equations (3.6) with input from (3.16) satisfies the dispersion relation (3.5) combined with the bound state term,

$$t_{ab}(s) = U_{ab}(s) + \frac{s - s_M}{s_B - s_M}\frac{g_{Ba}\, g_{Bb}}{s_B - s} + \frac{s - s_M}{\pi}\int_{s_{th}}^{\infty}\frac{ds'}{s' - s_M}\frac{\text{Disc}\; t_{ab}(s')}{s' - s}\,. \tag{3.10}$$

At the same time, it is straightforward to show that including such a bound state term into the definition of $U_{ab}(s)$ does not change the solution of (3.6) or the integral equation (3.7), provided that the residues $g_{Ba}\, g_{Bb}$ are dialed properly using the $\det(D_{ab}(s_B)) = 0$ condition. The derivation for the single-channel case is given in Sec. 2.2.4.

The unitarity connects the partial-wave amplitudes in production (or decay) and scattering processes. Therefore, the reactions like $\gamma p \to \pi\pi p$, $\gamma\gamma \to \pi\pi$, $J/\psi \to \pi\pi\gamma$, $\eta \to 3\pi$, etc. are very sensitive to the FSI. In a dispersive formalism, FSI are typically implemented with the help of the so-called Omnès function [58, 140], $\Omega_{ab}(s)$, that fulfills the following unitarity relation on the right-hand cut

$$\text{Disc}\,\Omega_{ab}(s) = \sum_c t^*_{ac}(s)\,\rho_c(s)\,\Omega_{cb}(s)\,, \tag{3.11}$$

and analytic everywhere else in the complex plane, i.e. it satisfies a once-subtracted dispersion relation

$$\Omega_{ab}(s) = \delta_{ab} + \frac{s - s_M}{\pi}\int_{s_{th}}^{\infty}\frac{ds'}{s' - s_M}\frac{\text{Disc}\,\Omega_{ab}(s')}{s' - s}\,. \tag{3.12}$$

Therefore, for the case of no bound states or CDD poles, the $D_{ab}(s)$ function obtained in (3.7) can be easily related to the Omnès function as

$$\Omega_{ab}(s) = D^{-1}_{ab}(s)\,. \tag{3.13}$$

As we showed in Sec. 2.2.4, for the single-channel case, the Omnès function can be expressed in the analytic form in terms of the phase shift $\delta(s)$,

$$\Omega(s) = D^{-1}(s) = \exp\left(\frac{s - s_M}{\pi}\int_{s_{th}}^{\infty}\frac{ds'}{s' - s_M}\frac{\delta(s')}{s' - s}\right), \tag{3.14}$$

with the convention that $\delta(s_{th}) = 0$. Therefore, in single-channel approximations, the Omnès function is frequently computed directly from the existing parametrizations of the phase-shift data and various assumptions about its asymptotic behavior at infinity. The latter constrains the asymptotic behavior of the Omnès function: for $\delta(\infty) \to \alpha\pi$ one obtains $\Omega(\infty) \to 1/s^{\alpha}$. In our approach, the phase shift curves are obtained from fits to the data using the N/D method. The high-energy asymptotic of the phase shift is coming from the approximation of the left-hand cut by conformal expansion and subsequent solution of the once-subtracted dispersion relation. As a result, in this scheme, the obtained Omnès function (or its inverse) is always asymptotically bounded, if there is no bound state or CDD pole in the system. When there is a bound state in the system, the relation between the Omnès function and the $D(s)$ function given in Eq. (3.14) changes,

$$\Omega(s) = \left(\frac{s - s_B}{s_M - s_B}\right) D^{-1}(s) = \exp\left(\frac{s - s_M}{\pi}\int_{s_{th}}^{\infty}\frac{ds'}{s' - s_M}\frac{\delta(s')}{s' - s}\right), \tag{3.15}$$

where the extra factor $(s-s_B)/(s_M-s_B)$ removes the zero of $D(s)$. Due to this extra factor, the obtained Omnès function grows linearly at infinity and satisfies the twice-subtracted version of the dispersion relation given in Eq. (3.12). This can also be seen from the Levinson's theorem, which relates the contribution from the number of bound states n_B to the phase shift at infinity as $\delta(\infty) \to -n_B\,\pi$ (using the convention $\delta(s_{th}) = 0$).

For the multi-channel case, the Muskhelishvili-Omnès equations (3.12) do not have analytic solutions [141, 142], and one needs to find a numerical solution, by employing for instance a Gauss-Legendre procedure [142]. In order to achieve that, however, one needs to know the off-diagonal scattering amplitude in the unphysical region and again make the assumption about the high-energy asymptotics. On the other side, with the N/D method, both the scattering amplitude and the Omnès function are obtained simultaneously from the fit to the available data. Additional information about the off-diagonal scattering amplitude in the unphysical region can be used as a constraint and not as a necessary requirement to obtain the Omnès matrix. Also, as discussed above, in most of the cases the obtained Omnès function (or its inverse) is asymptotically bounded. Therefore, this approach is useful in many practical applications.

As a check of our numerical calculations, we verified that the Omnès functions obtained using Eqs. (3.7) and (3.13) satisfy Eq. (3.12). All results presented below have been checked to fulfill the partial-wave dispersion relation given in Eq. (3.5) or Eq. (3.10) in the case when there is a physical bound state in the system. In addition we checked that there are no spurious poles in the considered cases. For the non-resonant channels ($I = 2, I = 3/2$) we found out that sometimes $D(s)$ has an unphysical zero far away from the threshold on the first Riemann sheet. To avoid this spurious bound state, we will impose in the fit the fulfilment of p.w. dispersion relation which does not contain the bound state.

3.2.2 Left-hand cuts

With the construction of the N/D system a natural question arises on what input is required to solve the integral equation for the N-function and consequently reconstruct the D-function and the scattering amplitude. In fact, the D-function and in cases of no bound state, Omnés

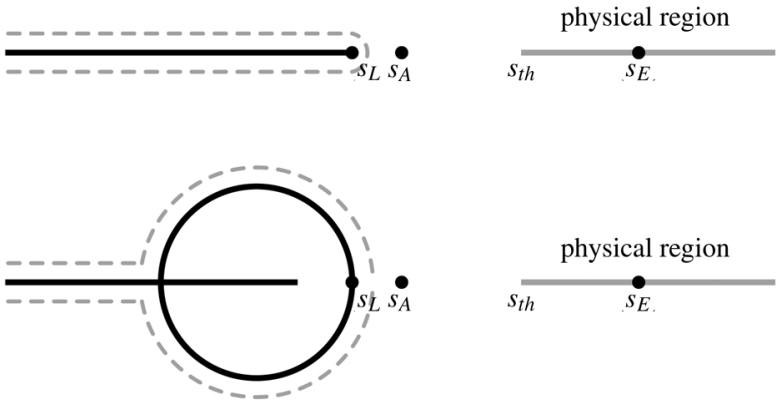

Figure 3.4: Left-hand cut singularities (solid black curves) in the complex s-plane for the $\pi\pi \to \pi\pi$ (a) and $\pi K \to \pi K$ (b) scattering. In the plot we schematically show the position of the closest left-hand cut singularity (s_L), Adler zero (s_A), threshold (s_{th}) and the expansion point (s_E). Dashed lines determine the specific form of the conformal map and subsequently the domain of convergence of the conformal expansion in Eq. (3.16).

function is universal for every reaction involving the same final states. However, each reaction differs by its left-hand cuts, the proper determination or parametrization of which are the core problem for the whole partial-wave dispersion analysis. In a general scattering problem, little is known about the left-hand cuts, except their analytic structure in the complex plane. The progress has been made in [107–110], by considering an analytic continuation of $U_{ab}(s)$ to the physical region, which is needed as input to Eq. (3.7), by means of an expansion in a suitably contracted conformal mapping variable $\xi(s)$,

$$U(s) = \sum_{n=0}^{\infty} C_n \, \xi^n(s) \,, \tag{3.16}$$

which is chosen such that it maps the left-hand cut plane onto the unit circle [143]. The form of $\xi(s)$ depends on the cut structure of the reaction (i.e. $\{ab\}$) and specified by the position of the closest left-hand cut branching point (s_L) and an expansion point (s_E) around which the series is expanded, $\xi(s_E) = 0$. Since for the $\{\pi\pi, K\bar{K}\}$ system all the left-hand cuts lie on the real axis, $-\infty < s < s_L$, one can use a simple function

$$\xi(s) = \frac{\sqrt{s - s_L} - \sqrt{s_E - s_L}}{\sqrt{s - s_L} + \sqrt{s_E - s_L}} \,, \tag{3.17}$$

where $s_L(\pi\pi \to \pi\pi) = s_L(\pi\pi \to K\bar{K}) = 0$ and $s_L(K\bar{K} \to K\bar{K}) = 4\,(m_K^2 - m_\pi^2)$. For the case of $\pi K \to \pi K$, the left-hand cut structure is a bit more complicated (see Fig. 3.4). In addition to the left-hand cut lying on the real axis $-\infty < s < (m_K - m_\pi)^2$, there is a circular cut at $|s| = m_K^2 - m_\pi^2$. The conformal map that meets these requirements is defined as

$$\xi(s) = -\frac{(\sqrt{s} - \sqrt{s_E})(\sqrt{s}\sqrt{s_E} + s_L)}{(\sqrt{s} + \sqrt{s_E})(\sqrt{s}\sqrt{s_E} - s_L)} \,, \tag{3.18}$$

where $s_L(\pi K \to \pi K) = m_K^2 - m_\pi^2$. The behavior of $\xi(s)$ is shown in Fig. 3.5, where we used the values of s_E, discussed in Sec. 3.2.4. We note that, given the forms of $\xi(s)$ in Eqs. (3.17)

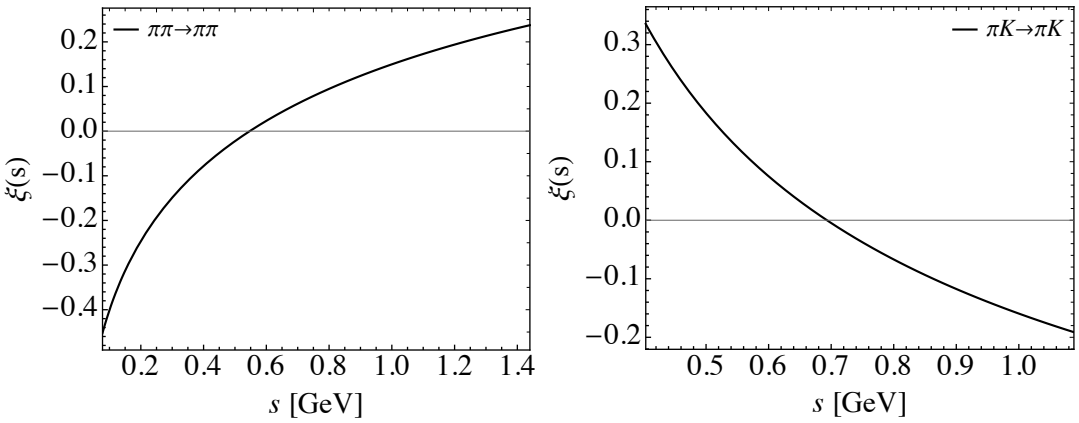

Figure 3.5: The behavior of the conformal variable $\xi(s)$ for the $\pi\pi \to \pi\pi$ (left panel) and $\pi K \to \pi K$ (right panel) scattering from Eqs. (3.17) and (3.18), respectively.

and (3.18), the series (3.16) truncated at any finite order is bounded asymptotically. This is consistent with the assigned asymptotic behavior of $U(s)$ in the once-subtracted dispersion relation (3.5).

In principle the coefficients of the conformal expansion (3.16) can be determined in several ways, for instance, by matching the function to the χPT results. However, this approach leads to the additional model dependency which we aim to avoid. Instead, we determine the unknown C_n in Eq. (3.16) and the optimal positions of s_E directly from the data and use χPT results only as constraints for the scattering lengths, slope parameters, and Adler zero values, which will be discussed in the next section.

With the given form of the conformal expansion a natural question arises, of how many terms are sufficient for the description of each particular process. The first answer comes from the data analysis consideration. Once the χ^2 becomes sufficiently close to 1, there is no need to introduce any additional parameters. However, another argument stems from the conformal expansion itself, by taking into account how fast it converges. For the problems considered here, we find that there is no need to consider more than 4 terms in the expansion.

3.2.3 χPT input

For reactions involving Goldstone bosons, in principle, χPT allows to calculate the amplitude over a finite portion of the closest left-hand cut and can be used to estimate C_n in (3.16) as it has been done for other processes in [53, 54, 107–110]. However, it is not clear at which point χPT calculated to a given order still represents a good approximation. In addition to that, in order to merge the conformal expansion with the chiral expansion, the expansion point s_E should lie within the region where χPT can be computed safely. For instance, for the elastic $\pi\pi \to \pi\pi$ scattering the natural choice would be to identify s_E with the two-pion threshold. However in that case, the last data point, which can be described with the elastic unitarity, corresponds to $\xi(s_{max}^{1/2} = 0.7\,\text{GeV}) \simeq 0.45$. On the other side, the faster convergence of the sum in Eq. (3.16) can be achieved for the choice of s_E in between the threshold and s_{max}, i.e. in the regions where χPT is at the limit of its applicability. Besides, for the coupled-channel case, one needs to rely on $SU(3)$ χPT, which converges slower than the SU(2) version of it.

In order to be consistent with χPT in the threshold region, we employ the effective range

expansion

$$\frac{2}{\sqrt{s}}\,\mathrm{Re}\left(\frac{t(s)}{16\,\pi}\right) \simeq a + b\,p^2(s) + \ldots\,, \tag{3.19}$$

where a is the scattering length and b is the slope parameter. For the $\pi\pi$ and πK scattering both a and b have been calculated at NNLO in χPT [84, 144]. As expected, for the πK scattering, the chiral convergence is a bit worse than for the $\pi\pi$ scattering [144], however the results for the scattering length and slope parameter do not show large discrepancies with the Roy-Steiner results [89, 91, 104, 105]. As for the Adler zero, we have checked that its position does not acquire large higher order corrections, and for simplicity one can take the LO result. In all numerical fits, however, we take the NLO result [59, 145, 146] as a central value, with the uncertainties from the omitted higher orders as |NLO − LO|, which should provide a conservative estimate. The NLO values for the low-energy constants are taken from [147]. For the case of non-physical pion masses with $m_\pi = 236$ MeV and $m_\pi = 239$ MeV, we only use Adler zero positions as a constraint, while for $m_\pi = 391$ MeV, where $\sigma/f_0(500)$ shows up as a bound state, no constraints are imposed.

We note that the latter brings a stringent constraint on the scattering amplitude, since for both $\pi\pi$ and πK scattering the Adler zero is located very close to the left-hand cut (see Fig. 3.4), and cannot be determined precisely from the fit to the data. However, once the Adler zero is imposed as a constraint, it improves drastically the convergence of (3.16) in the threshold region.

3.2.4 The choice of s_M and s_E

Before entering the discussion of the results of the fits, we would like to briefly comment on the freedom of the choice of the subtraction point s_M in the dispersion relation (3.4). The common choice in the application of the Omnès functions is $s_M = 0$, due to its relation to scalar form factors and matching to χPT. On the other side, one can fix s_M at the threshold, $s_M = s_{th}$, and then relate $\sum_{n=0}^{n_{max}} C_n\,\xi^n(s_{th})$ to the scattering length. Similarly, one can fix s_M at the Adler zero[2], $s_M = s_A$, which would imply that $\sum_{n=0}^{n_{max}} C_n\,\xi^n(s_A) = 0$. The last two choices can therefore reduce the number of fitted parameters by one. Eventually different choices of s_M redefine the fitted coefficients C_n in the $U_{ab}(s)$ function and the results of the N/D method are immune to that (after computing the D-function, it can be re-normalized to any other point below threshold). Since not in all the fits we impose threshold or Adler zero constraints, we decided to make the choice

$$s_M = 0\,, \tag{3.20}$$

in all the cases for simplicity. As for the expansion point s_E, we choose it in the middle between the threshold and the energy of the last data point that is fitted,

$$\sqrt{s_E} = \frac{1}{2}\,\left(\sqrt{s_{th}} + \sqrt{s_{max}}\right)\,. \tag{3.21}$$

Note, that in the coupled channel case, s_{th} in Eq. (3.21) denotes the physical threshold for the diagonal terms $U_{ab}(s)$, while for the off-diagonal terms it is the lowest threshold. We emphasize, that this particular choice guarantees a fast convergence of the conformal expansion (3.16) in the region where the scattering amplitude is fitted to the data and also where it is needed as input to Eq. (3.7).

[2] On the technical level, it may look that Adler zero could be accounted for as a CDD pole in the D-function [148, 149]. However, every CDD pole physically corresponds to the genuine QCD state, while the existence of the Adler zero is the property of the chiral symmetry. Therefore we encode it as a zero in the N-function and not as a pole in the D-function.

3.2.5 Fitting procedure and error analysis

The free parameters in our approach are the conformal coefficients in (3.16), which determine the form of the left-hand cut contribution $U_{ab}(s)$ in Eq. (3.5). Apart from the standard χ^2 criteria, the number of parameters is chosen in a way to ensure that the series (3.16) converges. In several cases, however, we will be fitting Roy (Roy-Steiner) solutions, which are smooth functions and their errors are fully correlated from one point to another. In these cases, $\chi^2/d.o.f$ loses its statistical meaning and can be < 1. In our fits, this scenario will simply indicate that we obtained the N/D solution which is consistent with the Roy (Roy Steiner) solutions, and we just make sure that the obtained uncertainty is consistent with that from Roy analyses.

Unlike the physical region, where the reaction models are typically fitted to data, the pole extraction may carry significant systematic uncertainties, especially if the pole lies deep in the complex plane [150, 151]. To assess these, we vary the parameter s_E around its central value fixed to (3.21). We allow for a conservative variation by 25% of the difference $\sqrt{s_{max}} - \sqrt{s_{th}}$, in order to have a compromise between $\sqrt{s_{th}}$ and $\sqrt{s_{max}}$. Note, that the extreme choice of 50% would correspond to $s_E = s_{th}$ or $s_E = s_{max}$, which we clearly want to avoid, since it would bias the fit towards one or the other region. As it will be seen later, the $\sigma/f_0(500)$ and $\kappa/K_0^*(700)$ poles acquire noticeable systematic errors which are of the size of statistical ones. However, even if we go to the extreme case of 50%, the statistical error will grow only by a factor of two, compared to the case of 25%. This is different from the K-matrix fits (see for instance [150]), which cannot extract accurately the pole parameters. We remind, that in our approach, as opposed to K-matrix models, the obtained amplitudes satisfy p.w. dispersion relations, which is an additional constraint on the amplitude both on the real axis and in the complex plane.

As for the statistical uncertainty, our approach requires solving an integral equation and searches for the pole in the complex s-plane. These facts make the traditional error analysis via uncertainty propagation inconvenient or even not-applicable. Therefore, we opt for the Monte-Carlo based technique namely *parametric bootstrap* to properly dial the statistical uncertainties in our analysis. Its main principle relies on the idea of generating many artificial measurements, using the assumed probabilty distribution of underlying data (or pseudo-data), which in turns allows to extract the uncertainties of the derived quantities like pole positions and couplings in a straightforward manner by applying the statistical criteria. The details about this method as well as the simple application example can be found in App. 3.B.

In the following results, the first error will indicate the statistical uncertainty (*i*.e. reflect the errors of the data and χPT input), while the second one will be associated with a variation of s_E. We admit that s_E variation only accounts for the dominant part of the systematic uncertainty and therefore only provides a lower bound on the systematic error.

3.3 Results for the $\pi\pi \to \pi\pi$ scattering

In this section we present the results of data-driven analysis of the S-wave $\pi\pi \to \pi\pi$ reaction using the partial-wave dispersion relation approach. The $I = 0$ channel accommodates two resonances: $\sigma/f_0(500)$ and $f_0(980)$. The data in this channel is relatively abundant [152–158], however, some datasets are conflicting and have to be selected carefully [159]. Moreover, most of the data has a large systematic uncertainty which may hinder the precision of the theoretical analyses. Only recently the Roy-like analyses has reached an unprecedented precision in the determination of the σ resonance with an input including the most recent and reliable data on K_{l4} decays [155]. While the $f_0(980)$ resonance has also been studied thoroughly within this framework, no proper coupled channel analysis, accounting for the intermediate $K\bar{K}$

	$\sqrt{s_E}$, MeV	C_0	C_1	C_2	C_3	χ^2/d.o.f
$\pi\pi \to \pi\pi, I = 0$ single-channel						
Exp.	740	9.5(5)	38.0(1.4)	55.2(1.2)	31.1(2.9)	2.7
Roy		15.9(7)	51.8(1.7)	58.2(1.4)	24.4(3.0)	0.5

Table 3.1: Fit parameters entering Eq. (3.16) which were adjusted to reproduce available experimental data or Roy-like results for $\pi\pi \to \pi\pi\,, I = 0$ scattering in the single channel approach.

	$\sqrt{s_A}$, MeV	$m_\pi a$	$m_\pi^3 b$	$\sqrt{s_A}^{\rm NLO}$, MeV	$m_\pi a^{\rm NNLO}$	$m_\pi^3 b^{\rm NNLO}$
$\pi\pi \to \pi\pi, I = 0$ single-channel						
Exp.	90(9)	0.219(5)	0.275(6)	90(9)	0.220(5) [84]	0.276(6) [84]
Roy	90(9)	0.220(5)	0.276(6)			

Table 3.2: Fit results for the threshold parameters a and b defined in Eq. (3.19) and the Adler zeros s_A for $\pi\pi \to \pi\pi\,, I = 0$ scattering in the single channel approach (left) compared to χPT values (right).

interaction has been implemented so far.

This section is organized as following. First, we concentrate on the single-channel $\pi\pi$ scattering. We compare the outcomes by fitting the available experimental data directly and by using the Roy-like results as a pseudo-data in Sec. 3.3.1. Then in Sec. 3.3.2 we analyse the lattice data for $m_\pi = 236$ and 391 MeV, which is available in the elastic region only. Afterwards, in Sec. 3.2.1 we proceed with an analysis of the coupled-channel $\{\pi\pi, K\bar{K}\}$ system, which requires input from several channels. In some cases, the available input is very limited or, in case of Roy-analyses, even conflicting. Finally, we present the results for the non-resonant $I = 2$ channel, which is necessary for the analysis of the $\gamma\gamma \to \pi\pi$ process in Chapter 4.

3.3.1 $I = 0$ single channel approach

As a first step, we consider only the elastic $\pi\pi$ scattering, which should be enough to get a realistic estimate of the resonance position of $\sigma/f_0(500)$, which is known to be connected almost exclusively to the pion sector. The reason for that is twofold. In many practical applications it is convenient to remove the $K\bar{K}$ (or $f_0(980)$) effects, which do not influence much the $\sigma/f_0(500)$ pole parameters, but at the same time require a proper coupled-channel treatment. Additionally, the current lattice QCD result for $m_\pi = 236$ MeV covers only the elastic region [40]. Therefore, as a necessary prerequisite of a meaningful $\sigma/f_0(500)$ pole extraction for unphysical pion masses, one has to test the N/D formalism first for physical quark mass values, where the position of $\sigma/f_0(500)$ has already been obtained from the sophisticated Roy analyses [84–86, 97, 100–103]. The inclusion of the $K\bar{K}$ channel (or $f_0(980)$ resonance) will allow for a slightly more precise evaluation of $\sigma/f_0(500)$ parameters and will be given in the next subsection.

Relying only on the available data up to $\sqrt{s_{max}} = 0.7$ GeV, where a strong influence of the $K\bar{K}$ threshold is not yet expected, we obtain a decent fit even without imposing chiral constraints. The pole occurs at $\sqrt{s_\sigma} = 463(8)^{+6}_{-7} - i\,217(6)^{+8}_{-9}$ MeV. The scattering length and slope parameters turn out to be compatible with those of χPT due to the presence of K_{l4} data. As we discussed above, this is not the case for the Adler zero, which is located too close to the

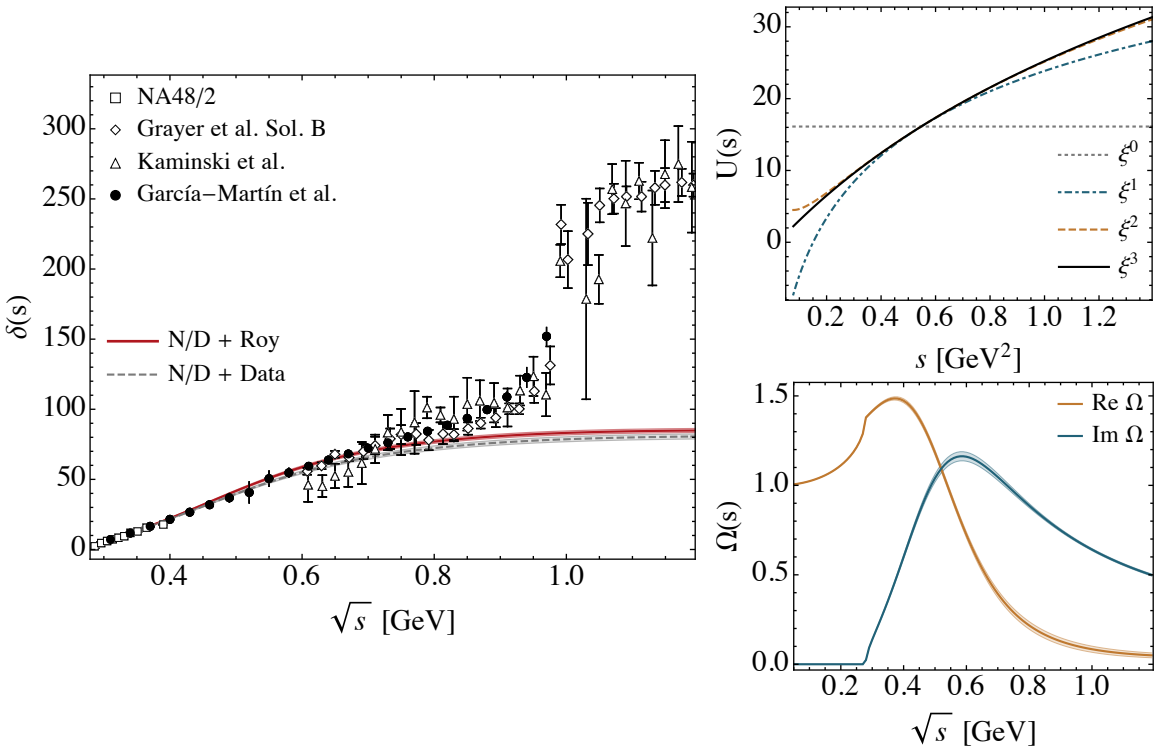

Figure 3.6: Results for the $\pi\pi \to \pi\pi$ scattering with $J = 0, I = 0$ in the single-channel case. Left panel shows the comparison with the data, right upper panel shows the convergence of the conformal expansion in Eq. (3.16), and right lower panel show the corresponding Omnès function. In the phase shift plot two curves are shown: fit to the experimental data [153–156] (dashed curve) and fit to the pseudo data from Roy analysis [86, 97, 100, 101]. For the sake of comparison with the coupled channel case (see Sec. 3.3.3), we adopted s_E based on $\sqrt{s_{max}} = 1.2$ GeV, as discussed in the text.

left hand cut,

$$s_A(\chi\mathrm{PT}_{\mathrm{LO}}) = m_\pi^2/2\,, \tag{3.22}$$

i.e. where the series (5.9) simply converges too slow. With the additional constraints for the scattering length, slope parameter and Adler zero, the best fit result contains four parameters and leads to $\sqrt{s_\sigma} = 435(7)^{+6}_{-8} - i\,250(5)^{+6}_{-8}$ MeV. This result is compatible with the value $\sqrt{s_\sigma} = 446(5)^{+6}_{-9} - i\,230(5)^{+7}_{-9}$ MeV, obtained by replacing the experimental data with the pseudo data from the Roy-like analysis [86, 100, 101]. As it is shown in Fig. 3.6 both N/D fits are consistent within the error. This provides a proof for our expectation, that even in the case where there is no available Roy analyses (like lattice QCD data), we can rely on the N/D approximation. For our final result of the single-channel Omnès function with physical pion mass, we opt for fitting the result of the Roy analysis [86, 100, 101], as the best representation of the data. The values of the fitted parameters are collected in Table 3.1, which result in the fast convergence of the conformal expansion (3.16) as shown in the left panel of Fig. 3.6. Note, that in order to use these fit parameters as the starting values of the more complicated coupled-channel fit, we have chosen s_E here to be the same as for the coupled-channel case, where we aim to describe the data up to $\sqrt{s_{max}} = 1.2$ GeV. Also, this choice slightly improves the obtained $\sigma/f_0(500)$ pole positions, since it pushes s_E further away from the threshold region, which is constrained accurately from χPT. In Table 3.2 we compare threshold parameters and

m_π, MeV	$\sqrt{s_E}$, MeV	C_0	C_1	C_2	C_3	χ^2/d.o.f
$\pi\pi \to \pi\pi, I = 0$ single-channel, lattice data						
236	646	13.3(2.9)	64.4(1.6)	64.5(5.6)	-	1.2
391	896	65.5(14.5)	-293.7(47.8)	409.2(35.7)	-	1.2

Table 3.3: Fit parameters entering Eq. (5.9) which were adjusted to reproduce the lattice data from [40].

m_π, MeV	$\sqrt{s_A}$, MeV	$m_\pi a$	$m_\pi^3 b$	$\sqrt{s_A}^{\rm NLO}$, MeV	$m_\pi a^{\rm NNLO}$	$m_\pi^3 b^{\rm NNLO}$
$\pi\pi \to \pi\pi, I = 0$ single-channel, lattice data						
236	187(35)	0.98(19)	0.89(43)	150(18)	$0.75 - 0.87$ [84]	-
391	-	-4.07(36)	67.0(19.0)	-	-	-

Table 3.4: Fit results for the threshold parameters a and b defined in Eq. (3.19) and the Adler zeros s_A for $\pi\pi \to \pi\pi\,, I = 0$ scattering in the single channel approach (left) compared to χPT values (right).

Adler zeros to χPT values, while in Table 3.7 poles and couplings are collected. Overall we achieve a good description of the Roy analyses results. In Fig. 3.6 we also show phase shift and Omnès function. Note, that a similar result for the Omnès function can be obtained by using the phase shift from the single-channel modified Inverse Amplitude Method (mIAM) [149, 160–162] and Eq. (3.14). In this method, the dispersion relation is written for the inverse amplitude, while the left-hand cut and subtraction constants are approximated by the chiral expansion. The result closest to the Roy analysis for the $\sigma/f_0(500)$ pole is achieved by performing two-loop mIAM fit [163]. In elastic N/D and mIAM approaches the $K\bar{K}$ channel is separated naturally from the $\pi\pi$ channel, which is beneficial for the practical applications.

3.3.2 $I = 0$: analysis of the lattice data

Apart from the experimental data, the recent lattice analysis [40] provided the results for the energy levels for pion mass values of $m_\pi = 236$ MeV and $m_\pi = 391$ MeV. While the former case is much closer to the physical pion mass, the lattice result for the larger mass deserves special attention, since in that case $\sigma/f_0(500)$ shows up as a bound state. In the lattice QCD analysis, the discrete energy spectrum in a finite volume is related to the infinite-volume scattering amplitude through the Lüscher formalism [164, 165], which was extended in [166–169] to the case of moving frames. In the case of elastic scattering at low energies it gives a one-to-one relation to $p\,\cot\delta$. The lattice results for $p\,\cot\delta$ with $m_\pi = 236$ MeV and $m_\pi = 391$ MeV were shown in [40]. To fit these data, we analytically continue $p\,\cot\delta$ below threshold, such that it does not produce any cusp behaviour at the threshold,

$$p(s)\,\cot\delta(s) = \frac{\sqrt{s}}{2}\left(\frac{1}{t(s)} + i\,\rho_0(s)\right) 16\pi\,, \tag{3.23}$$

where ρ_0 is the same as ρ in Eq. (3.3), but without the Heaviside step function.

For both $m_\pi = 236$ MeV and $m_\pi = 391$ MeV, we find that the three-parameter fit covers the data quite well (see left panel of Fig. 3.7). Similar to the K-matrix fits performed in [40], we found $\sigma/f_0(500)$ as a deep pole on the second Riemann sheet for $m_\pi = 236$ MeV and as a bound state for $m_\pi = 391$ MeV. In our approach, however, the obtained scattering amplitudes

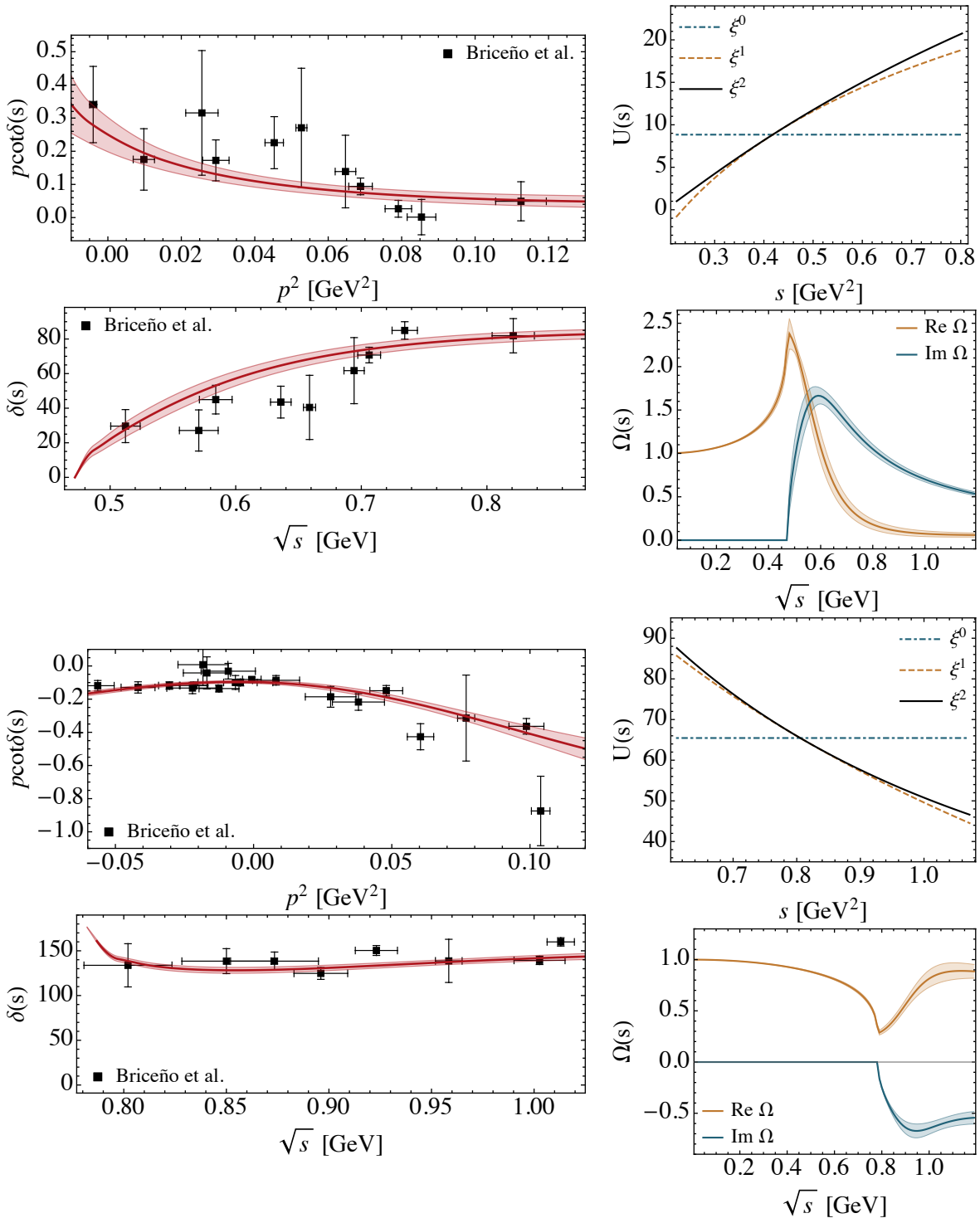

Figure 3.7: Results for the $\pi\pi \to \pi\pi$ scattering with $J = 0$, $I = 0$ in the single-channel case for the $m_\pi = 236$ MeV (upper plots) and $m_\pi = 391$ (lower plots). Left panels show the comparison with the lattice data from [40] for $p \cot \delta(s)$ function and its mapping onto the $\delta(s)$ function above threshold, right upper panels show the convergence of the conformal expansion in Eq. (3.16), and right lower panels show the corresponding Omnès functions.

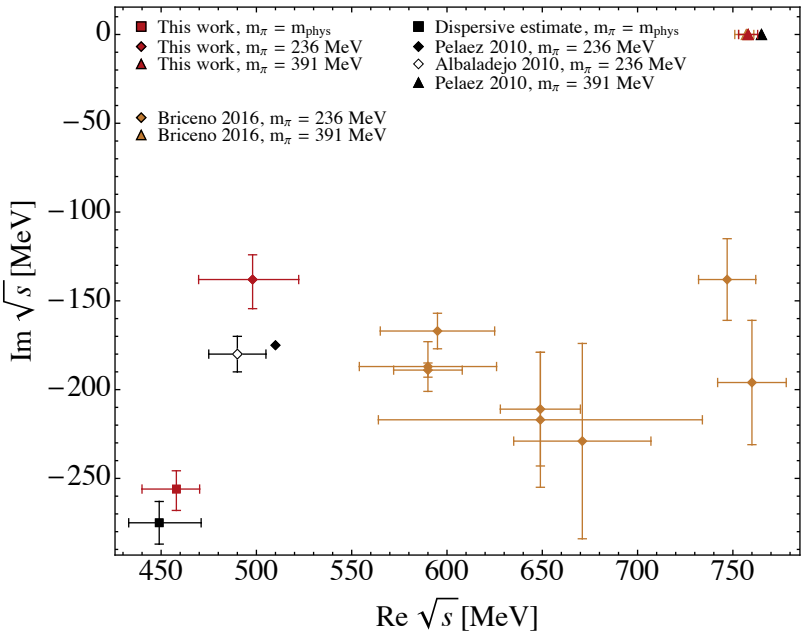

Figure 3.8: The comparison between the different $\sigma/f_0(500)$ positions for different pion masses. In red, the results of the present work are shown. Yellow points show the various K-matrix analyses of the lattice data. Black points show the predictions from mIAM [40].

satisfy p.w. dispersion relations, which is a stringent constraint on the real part of the inverse of the amplitude. As a result, the pole position is determined much more precisely, see Table 3.7. We also checked that the obtained scattering length $m_\pi\, a = 0.98(19)$ for $m_\pi = 236$ MeV is consistent with the chiral extrapolation result $m_\pi\, a_{\rm NNLO} = 0.75 - 0.87$ of [84] and therefore including such additional constraint in the fit barely affects the results of the $\sigma/f_0(500)$ pole and coupling.

It is instructive to compare the obtained pole positions of $\sigma/f_0(500)$ for non-physical pion masses with the predictions of unitarized chiral perturbation theory (UχPT). The most popular are two approaches: mIAM [163] and Bethe-Salpeter equation (BSE) [170]. Both observe the same qualitative behaviour of the $\sigma/f_0(500)$ pole. With increasing pion mass values the imaginary part of the pole decreases, then $\sigma/f_0(500)$ becomes a virtual bound state and as m_π increases further, one of the virtual states moves towards threshold and jumps onto the first Riemann sheet and becomes a real bound state. For $m_\pi = 236$ MeV, the extracted value from lattice data is consistent with UχPT predictions for the real part, but somewhat lower for the width,

$$\begin{aligned}
&\sqrt{s_\sigma} = 498(21)^{+12}_{-19} - i\,138(13)^{+5}_{-10} && (\text{lattice} + N/D),\\
&\sqrt{s_\sigma} = 510 - i\,175 && (\text{mIAM}_{\rm NNLO}, \text{fit D}),\\
&\sqrt{s_\sigma} = 490(15) - i\,180(10) && (\text{BSE}_{\rm NLO}),
\end{aligned} \tag{3.24}$$

all in units of MeV. For $m_\pi = 391$ MeV the situation is a bit different. Since it is on the edge of the applicability of χPT, the results of UχPT are very sensitive to the chiral order. Both mIAM [161] and BSE [170] at one loop found $\sigma/f_0(500)$ as a virtual bound state for $m_\pi = 391$ MeV. However, including the higher-order corrections (two loop) in mIAM [163] predicted the

	$\sqrt{s_E}$, MeV	C_0	C_1	C_2	C_3	χ^2/d.o.f
			$\pi\pi \to \pi\pi, I = 0$, coupled-channel			
Exp., U_{11}	740	17.5(1.1)	52.5(2.5)	50.6(2.6)	16.8(4.8)	t_{11} : 1.0
U_{12}		−7.8(4.5)	−14.7(4.3)	2.9(7.1)	–	$\lvert t_{12}\rvert$: 1.2
U_{22}	1095	65.2(21.1)	−230.6(46.6)	337.9(34.7)	–	δ_{12} : 1.7
Roy, U_{11}	740	17.1(9)	52.1(2.0)	51.1(2.2)	17.2(3.6)	t_{11} : 3.4
U_{12}		11.2(1.2)	12.6(2.5)	–	–	$\lvert t_{12}\rvert$: 2.4
U_{22}	1095	70.0(6.5)	−216.2(58.0)	321.0(53.9)	–	δ_{12} : 1.8

Table 3.5: Fit parameters entering Eq. (3.16) which were adjusted to reproduce available experimental (whenever possible replaced by the most recent Roy-like results) or lattice data. SC and CC stand for single-channel and coupled-channel analyses, respectively. See text for more details.

	$\sqrt{s_A}$, MeV	$m_\pi a$	$m_\pi^3 b$	$\sqrt{s_A}_{\rm SC}^{\rm NLO}$, MeV	$m_\pi a_{\rm SC}^{\rm NNLO}$	$m_\pi^3 b_{\rm SC}^{\rm NNLO}$
			$\pi\pi \to \pi\pi, I = 0$ coupled-channel			
Exp.	91(16)	0.219(10)	0.277(12)	90(9)	0.220(5) [84]	0.276(6) [84]
Roy	90(15)	0.218(9)	0.278(11)			

Table 3.6: Fit results for the threshold parameters a and b defined in Eq. (3.19) and the Adler zeros s_A for $\pi\pi \to \pi\pi\,, I = 0$ scattering in the single channel approach (left) compared to χPT values (right).

	$\sqrt{s_p}$, MeV	$\lvert g_{pa}\rvert/\sqrt{\mathcal{N}_{aa}}$	$\sqrt{s_p}$, MeV	$\lvert g_{pa}\rvert/\sqrt{\mathcal{N}_{aa}}$
		$\sigma/f_0(500)$		
Roy, SC	$458(7)^{+4}_{-10} - i\,245(6)^{+7}_{-10}$	$\pi\pi : 3.15(5)^{+0.11}_{-0.20}$	$449^{+22}_{-16} - i\,275(15)$	$\pi\pi : 3.45^{+0.25}_{-0.29}$ [97]
Roy, CC	$458(10)^{+7}_{-15} - i\,256(9)^{+5}_{-8}$	$\pi\pi : 3.33(8)^{+0.12}_{-0.20}$ $K\bar{K} : 2.11(17)^{+0.27}_{-0.11}$	[97]	$K\bar{K}$: –
Latt., 236	$498(21)^{+12}_{-19} - i\,138(13)^{+5}_{-10}$	$\pi\pi : 2.96(5)^{+0.05}_{-0.06}$		
Latt., 391	758(5)(0)	$\pi\pi : 3.91(26)(0)$		
		$f_0(980)$		
Roy, CC	$993(2)^{+2}_{-1} - i\,21(3)^{+2}_{-4}$	$\pi\pi : 1.93(15)^{+0.07}_{-0.12}$ $K\bar{K} : 5.31(24)^{+0.04}_{-0.24}$	$996^{+7}_{-14} - i\,25^{+11}_{-6}$ [86, 87, 100, 101]	$\pi\pi : 2.3(2)$ [86, 100, 101] $K\bar{K}$: –

Table 3.7: Poles and couplings of the $\sigma/f_0(500)$ and $f_0(980)$ resonances calculated in data-driven N/D approach compared with the results of Roy-like analyses. In our results, the first error is the statistical one, while the second one comes from a variation of s_E and has a systematic nature.

conventional bound state very close to the lattice results

$$\begin{aligned} &\sqrt{s_\sigma} = 758(5)(0)\ \text{MeV} && (\text{lattice} + N/D), \\ &\sqrt{s_\sigma} = 765\ \text{MeV} && (\text{mIAM}_{\rm NNLO}, \text{fit D}), \end{aligned} \tag{3.25}$$

confirming the proposed trajectory. In addition, another analysis of the same lattice data for $m_\pi = 236, 391$ MeV has been performed in [171]. For $m_\pi = 391$ MeV, it was found that

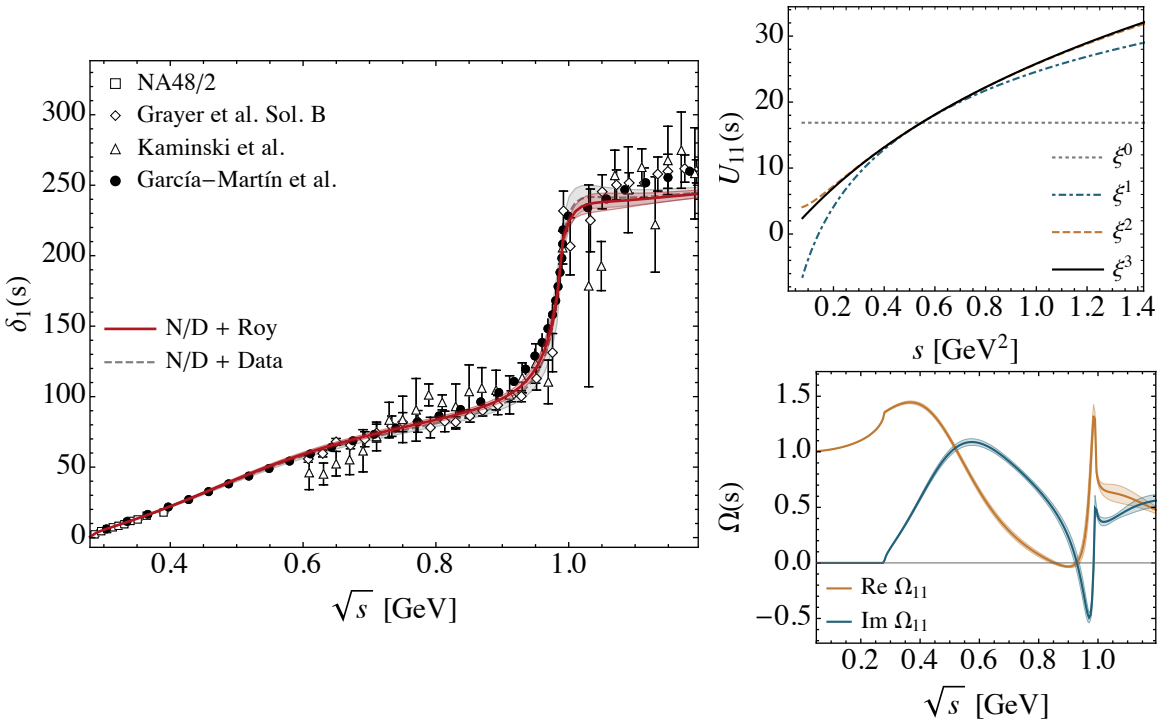

Figure 3.9: Results for the $\pi\pi \to \pi\pi$, $K\bar{K}$ scattering with $J = 0$, $I = 0$ in the coupled-channel case for the 11 matrix element with $1 = \pi\pi$. Left panel shows the comparison with the data, right upper panel show the convergence of the conformal expansion in Eq. (3.16), right lower panels show the elements of the Omnès matrix. In the left plot two curves are shown: fit to the experimental data [153–156] (dashed curve) and fit to the pseudo-data from Roy analyses [86, 97, 100, 101] (thick curve).

the fit quality improves with the inclusion of a bound state and a virtual bound state with $\sqrt{s_\sigma} = 774 \pm 6$ MeV and $\sqrt{s_\sigma} = 716 \pm 28$ MeV respectively. In [172], however, it was noted that the the existence of a pair of two poles on the real axis could be merely an artefact of a single-channel approach. Over this controversy, we do not include the results of [171] into further comparison.

All in all, as pointed out in [40], it would be useful to perform lattice calculations between 236 and 391 MeV, to see what really happens in the transition region between a resonance lying deep in the second Riemann sheet and the bound state. The comparison of the pole positions from different studies for $m_\pi = m_\pi^{\rm phys}, 236, 391$ MeV is given in Fig. 3.8.

We leave the coupled-channel study of the existing lattice data on $\{\pi\pi, K\bar{K}\}$ [41] with $m_\pi = 391$ MeV for a future work. In our opinion, this channel has to be analysed together with $\{\pi\eta, K\bar{K}\}$ lattice data [66], to shed more light onto the differences between the light scalar resonances $f_0(980)$ and $a_0(980)$.

3.3.3 $I = 0$: coupled channel approach

While the single-channel analysis allows us to reproduce the low-energy behavior of the phase shifts and gives very reasonable values of the $\sigma/f_0(500)$ pole parameters, a comprehensive study of the region up to $\sqrt{s} = 1.2$ GeV should account for the interplay between $\pi\pi$ and $K\bar{K}$ channels. In our normalization (see Eqs. (3.1-3.3)), the two-dimensional t-matrix, with

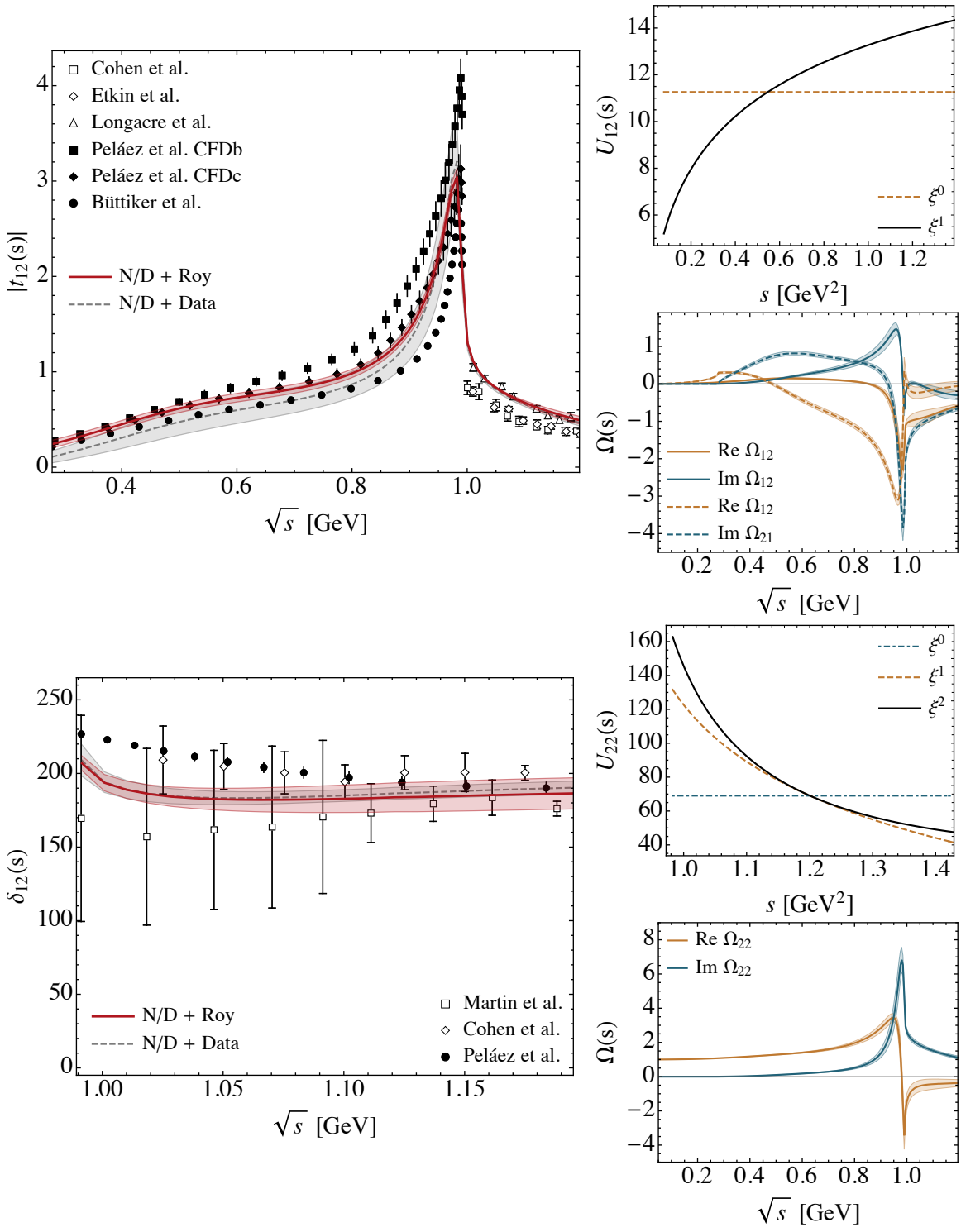

Figure 3.10: Results for the $\pi\pi \to \pi\pi, K\bar{K}$ scattering with $J = 0, I = 0$ in the coupled-channel case. Top and bottom panels correspond to 12 and 22 matrix elements, respectively, with $1 = \pi\pi$ and $2 = K\bar{K}$. Left panels show the comparison with the data, right upper panel in each set show the convergence of the conformal expansion in Eq. (3.16), right lower panels of each set show the elements of the Omnès matrix.

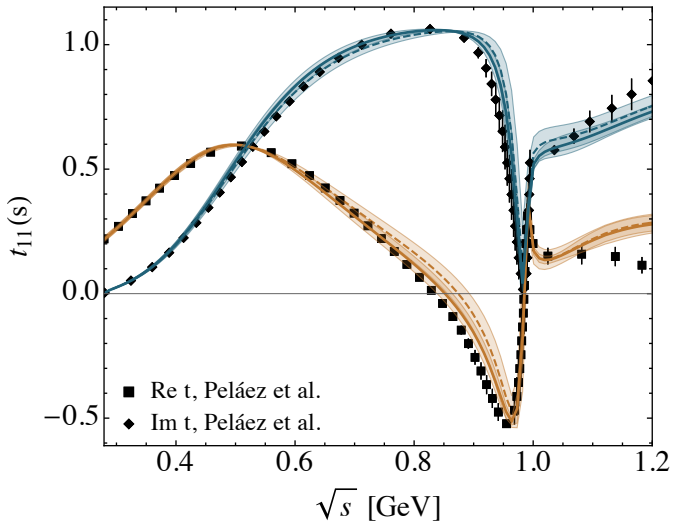

Figure 3.11: Comparison between the coupled-channel N/D fits and the Roy-like solution from [86, 100, 101]. The dashed curves are the fit solely to the experimental data, while the solid curves take advantage of both the experimental data and the results of Roy (Roy-Steiner) analyses on $\pi\pi \to \pi\pi$ ($\pi\pi \to K\bar{K}$).

channels denoted by $1 = \pi\pi$ and $2 = K\bar{K}$, is given by

$$t(s) = \begin{pmatrix} \frac{\eta(s)\, e^{2\,i\,\delta_1(s)} - 1}{2\,i\,\rho_1(s)} & |t_{12}(s)|\, e^{\delta_{12}(s)} \\ |t_{12}(s)|\, e^{\delta_{12}(s)} & \frac{\eta(s)\, e^{2\,i\,\delta_2(s)} - 1}{2\,i\,\rho_2(s)} \end{pmatrix} . \tag{3.26}$$

Under assumption of two-channel unitarity, the inelasticity is related to $|t_{12}(s)|$ as

$$\eta(s) = \sqrt{1 - 4\,\rho_1(s)\,\rho_2(s)\,|t_{12}(s)|^2}\,, \tag{3.27}$$

and due to Watson's theorem,

$$\delta_{12}(s) = \delta_1(s) + \delta_2(s)\,\theta(s > 4m_K^2)\,. \tag{3.28}$$

In the physical region the t-matrix is fully described by experimental information on the $\pi\pi$ phase shift $\delta_1(s)$ [152–156] , the inelasticity $\eta(s)$ (or $|t_{12}(s)|$ for $s > 4m_K^2$ [173–175]) and the $\pi\pi \to K\bar{K}$ phase $\delta_{12}(s)$ [173, 174, 176].

Similar to the single-channel analysis, we first fit the available experimental data supplemented with constraints for scattering length, slope parameter and Adler zero from χPT in the $\pi\pi \to \pi\pi$ channel. As for the $\pi\pi \to K\bar{K}$ channel, the complication stems from two facts. Firstly, the experimental data exist only in the physical region above $K\bar{K}$ threshold. Therefore, in order to stabilize the fits, we make sure that the obtained $|t_{12}(s)|$ stays small around[3] $s = 0$ as a manifestation of χPT. Secondly, the existing experimental data for both $|t_{12}(s)|$ and $\delta_{12}(s)$ contains incompatible data sets and requires to make some choice. Since the phase $\delta_{12}(s)$ is fully defined below $K\bar{K}$ threshold by means of Watson's theorem, we discard the data from [174] as it suggests that $\pi\pi \to K\bar{K}$ phase goes much lower than it is forced by the presence of $f_0(980)$ resonance. Therefore, we fit the data from [173] and [176] which are consistent due to the large error bars of the latter set. As for $|t_{12}(s)|$, the two data sets from [175] and [173, 174] should in principle be treated separately. However, only the data

[3]Specifically, at $s = m_\pi^2/2$ we impose NLO χPT with a conservative error that covers LO χPT result.

	$\sqrt{s_E}$, MeV	C_0	C_1	C_2	C_3	χ^2/d.o.f
$\pi\pi \to \pi\pi, I = 2$ single-channel						
Exp.	740	-16.6(5)	-28.0(1.0)	21.1(1.9)	36.4(3.6)	1.2
Roy		-17.4(4)	-30.1(9)	22.8(1.4)	41.5(2.9)	1.7

Table 3.8: Fit parameters entering Eq. (3.16) which were adjusted to reproduce available experimental data or Roy-like results for $\pi\pi \to \pi\pi\,, I = 2$ scattering.

	$\sqrt{s_A}$, MeV	$m_\pi a$	$m_\pi^3 b$	$\sqrt{s_A}^{\rm NLO}$, MeV	$m_\pi a^{\rm NNLO}$	$m_\pi^3 b^{\rm NNLO}$
$\pi\pi \to \pi\pi, I = 2$ single-channel						
Exp.	196(1)	-0.044(1)	-0.080(1)	197(0)	-0.044(1) [84]	-0.080(1) [84]
Roy	193(1)	-0.044(1)	-0.081(1)			

Table 3.9: Fit results for the threshold parameters a and b defined in Eq. (3.19) and the Adler zeros s_A for $\pi\pi \to \pi\pi\,, I = 2$ scattering in the single channel approach (left) compared to χPT values (right).

from [175] is compatible with the $\pi\pi$ inelasticity around the $K\bar{K}$ threshold. In order to describe the data from [173, 174], most likely one has to include the four-pion channel, which is beyond the scope of the present paper. The best fit with $(4, 4, 3)$ parameters in $(11, 12, 22)$ channels [175], provides $\sigma/f_0(500)$ and $f_0(980)$ poles at $\sqrt{s_\sigma} = 454(12)^{+6}_{-7} - 262(12)^{+8}_{-12}\,i$ MeV and $\sqrt{s_{f_0}} = 990(7)^{+2}_{-4} - 17(7)^{+4}_{-1}\,i$ MeV. These results are remarkably close to the Roy (for $\pi\pi \to \pi\pi$) and Roy-Steiner solutions for $(\pi\pi \to K\bar{K})$ as shown in Figs. 3.11, 3.9 and 3.10. The large error bars arise from scarce experimental data around $K\bar{K}$ threshold and almost unconstrained $|t_{12}|$ in the unphysical region.

On the other hand, we have at our disposal very precise $\pi\pi \to \pi\pi$ Roy-like analyses from [86, 100, 101] and $\pi\pi \to K\bar{K}$ Roy-Steiner analyses from [89, 91, 104, 105, 127]. Unfortunately, they do not come from the coupled-channel Roy-Steiner analyses and may display some inconsistencies between each other. In particularly, the Roy results on the real and imaginary parts of the $t_{11}(s)$ amplitude can constrain $\delta_1(s)$ and $\eta(s)$. The latter, in the two-channel approximation, is related to $|t_{12}(s)|$ by Eq. (3.27) and turns out to be inconsistent with any available Roy-Steiner solution on $\pi\pi \to K\bar{K}$ [89, 91, 104, 105, 127]. Therefore in order to avoid possible conflict in fitting two independent analyses, we impose $\pi\pi \to K\bar{K}$ Roy-Steiner solution only as constraint on $|t_{12}(s)|$ in the unphysical region $4m_\pi^2 < s < 4m_K$. Currently, there are three competing solutions: one from Büttiker et al. [104] and two (CFDc and CFDb) from Peláez et al. [91, 105]. We let the fit decide which solution to choose. As for the δ_{12}, we take advantage of experimental data of Cohen et al. [173] in the fit, which are quite precise. The good description of the data can be achieved with as low as $(4, 2, 3)$ parameters in $(11, 12, 22)$ channels, respectively. The results of the fit are collected in Tables 3.5, 3.6 and 3.7 and shown in Figs. 3.9, 3.10. As expected, the values for the fit parameters in the 11-channel do not deviate much from the single-channel analysis in Sec. 3.3.1. In the coupled-channel analysis the $\sigma/f_0(500)$ pole position comes a bit closer to the Roy analysis value, than in the single-channel study. Moreover, we are now in a position to calculate its coupling to the $K\bar{K}$ channel, which we include in Table 3.7. By inspecting Table 3.5, one can also see the striking similarity between the fit parameters in the 22 channel and the fit to lattice $\pi\pi \to \pi\pi$ data with $m_\pi = 391$ MeV, for which there is a bound state. Similarly, $f_0(980)$ will be a bound state

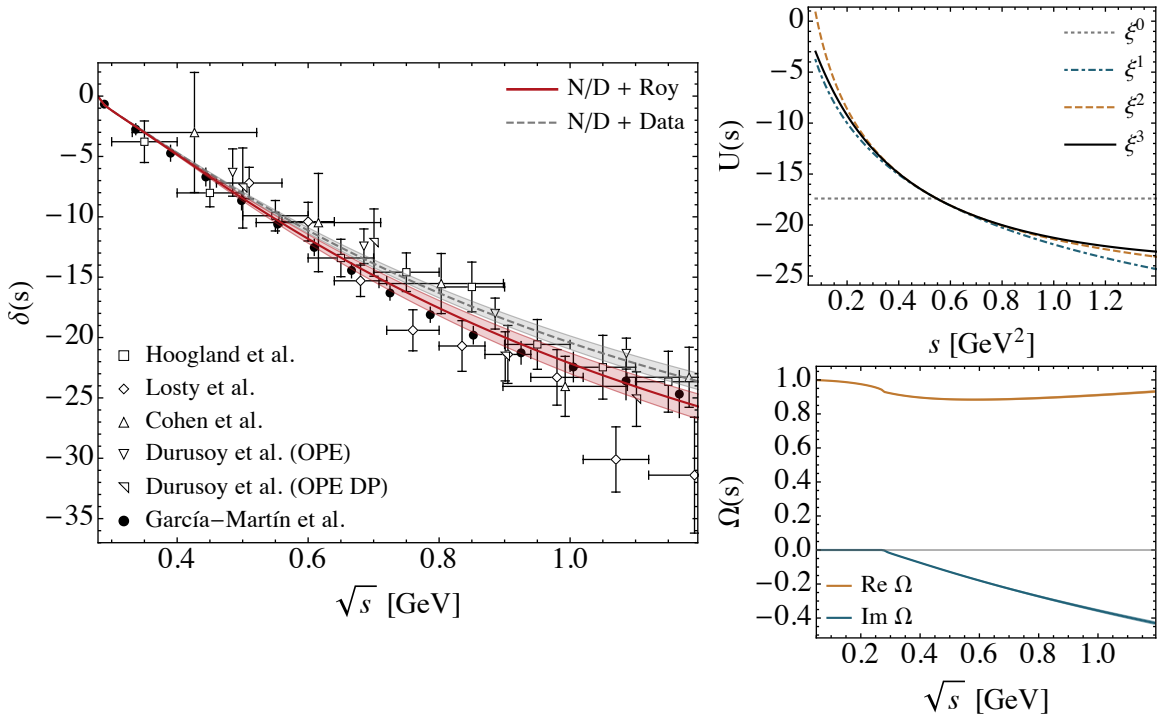

Figure 3.12: Results for the $\pi\pi \to \pi\pi$ $I = 2$ scattering. Left panel shows the comparison with the data, right upper panel shows the convergence of the conformal expansion in Eq. (3.16), and right lower panel show the corresponding Omnés function. In the phase shift plot two curves are shown: fit to the experimental data [173, 179–181] (dashed curve) and fit to the pseudo-data from Roy-Steiner analysis [97] (thick curve).

in the 22 channel, if we eliminate its connection to the 11 channel, i.e. by putting $U_{12} = 0$. This feature is not new and has already been observed in UχPT calculations, see for instance [177]. As for the 12 channel, the fit clearly favours CFDc solution of [91, 105]. This is also consistent with our previous "free" fit to to the experimental data, as shown by the dashed curves in Fig. 3.10. On the left lower panels of Figs. 3.9 and 3.10 we show the elements of the Omnès matrix calculated using Eq. (3.13). The previous version of them, with the fit to [104, 127] has already been successfully applied for the dispersive coupled-channel study of $\gamma^{(*)}\gamma^* \to \pi\pi(K\bar{K})$ [1, 4, 178] and $e^+e^- \to J/\psi\pi\pi(K\bar{K})$ [124].

3.3.4 $I = 2$ channel

We now turn to the partial wave dispersion relation analysis of the non-resonant $I = 2$ $\pi\pi \to \pi\pi$ scattering. The overall strategy remains the same for this channel, where we first fit the available experimental data and then the pseudo-data from the Roy-like analysis and compare the outcome. In fact, the data for the phase shift between the threshold and 1.2 GeV could be described with as few as two parameters, yet to satisfy to satisfy the χPT constraints mentioned before, it is necessary to introduce additional parameters. However, we notice that by fitting either experimental data or the Roy analysis results, supplemented with χPT constraints, we obtain an unphysical zero of $D(s)$ far away from the threshold on the first Riemann sheet. To avoid this artificial bound state, we impose in the fit the exact fulfilment of the partial-wave dispersion relation given by Eq. (5.2). With these constraints, we obtain the four-parameter fits with a good description of both experimental data and Roy-like analysis results. The fit

	$\sqrt{s_E}$, MeV	C_0	C_1	C_2	C_3	χ^2/d.o.f
$\pi K \to \pi K, I = 1/2$ single-channel						
Exp.	833	17.8(2.5)	-41.9(6.7)	27.5(7.7)	-10.5(12.6)	6.2
Roy		16.1(8)	-37.8(3.5)	32.9(2.7)	-18.6(6.0)	1.2

Table 3.10: Fit parameters entering Eq. (3.16) which were adjusted to reproduce available experimental data or Roy-like results for $\pi K \to \pi K\,, I = 1/2$ scattering in the single channel approach.

	$\sqrt{s_A}$, MeV	$m_\pi a$	$m_\pi^3 b$	$\sqrt{s_A}^{\rm NLO}$, MeV	$m_\pi a^{\rm NNLO}$	$m_\pi^3 b^{\rm NNLO}$
$\pi K \to \pi K, I = 1/2$ single-channel						
Exp.	480 (6)	0.220(12)	0.128(23)	480(6)	0.220 [144]	0.130 [144]
Roy	480(6)	0.219(10)	0.113(10)			

Table 3.11: Fit results for the threshold parameters a and b defined in Eq. (3.19) and the Adler zeros s_A for $\pi K \to \pi K\,, I = 1/2$ scattering in the single channel approach (left) compared to χPT values (right).

parameters are collected in Table 3.8, the threshold parameters and Adler zero in Table 3.9 and the resulting phase shifts, convergence and Omnès function are shown in Fig. 3.13.

Finally, having both $I = 0$ and $I = 2$ components of the $\pi\pi \to \pi\pi$ final state interaction, we are able to produce the amplitudes and consequently, the cross sections of the $\gamma^*\gamma^* \to \pi\pi$ process. We will come back to these results in Chapter 4 .

3.4 Results for the $\pi K \to \pi K$ scattering

In this section we first concentrate on the resonant $I = 1/2$ $\pi K \to \pi K$ scattering in which the $\kappa/K^*(700)$ resonance resides. This resonance presents a comparable enigma to the $\sigma/f_0(500)$, especially considering the fact that the $SU(3)$ χPT converges much slower than the $SU(2)$ version of it and hence less reliable predictions can be made. We will describe the single channel $\pi K \to \pi K$ scattering based both on the experimental data and the results of the Roy analyses. We will apply our method to the analysis of the lattice data for $m_\pi = 239$ MeV. Finally, we will comment on the non-resonant $I = 3/2$ scattering.

3.4.1 $I = 1/2$ channel

For the $\pi K \to \pi K$ single channel analysis we begin by fitting the experimental data and imposing constraints from χPT for the scattering length, slope parameter, and Adler zero. The latter at LO is given by a simple relation,

$$s_A(\chi\mathrm{PT}_{\rm LO}) = \frac{1}{5}\left(m_\pi^2 + m_K^2 + 2\sqrt{4\,m_\pi^4 - 7\,m_\pi^2\,m_K^2 + 4\,m_K^4}\right)\,. \tag{3.29}$$

The most precise calculation of the scattering length and slope parameter in χPT has been performed at NNLO in [144]. While the result for the scattering length $m_\pi\,a = 0.22$ is consistent with the recent Roy-Steiner predictions $m_\pi\,a = 0.223(9)$ [91, 105], it seems that there is a small tension in the slope parameter value $m_\pi^3\,b = 0.13$ compared to $m_\pi^3\,b = 0.108(8)$ from [91, 105]. The calculation of uncertainties is a bit cumbersome at NNLO and has not been

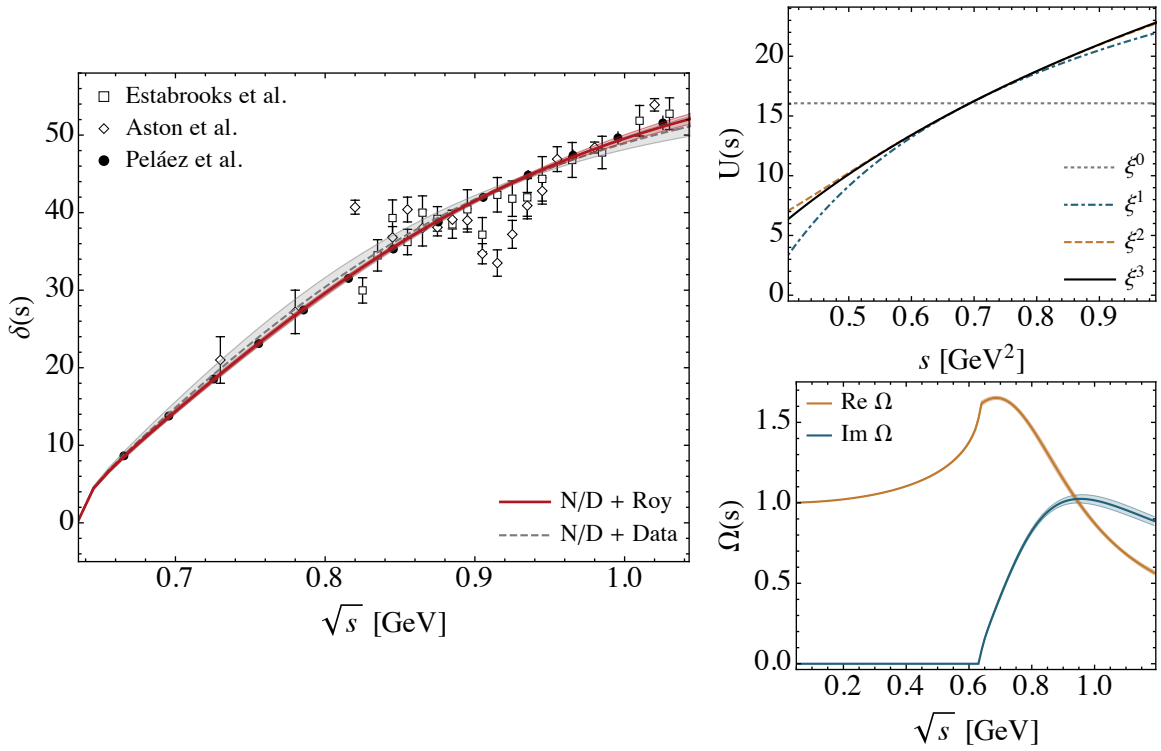

Figure 3.13: Results for the $\pi K \to \pi K$ scattering with $J = 0$, $I = 1/2$ in the single-channel approximation. Left show the comparison with the data, right upper panel show the convergence of the conformal expansion in Eq. (3.16), lower right panel shows the corresponding Omnès function. In the phase shift plot two curves are shown: fit to the experimental data [157, 158] (dashed curve) and fit to the pseudo-data from Roy-Steiner analysis [91, 105] (thick curve).

presented in [144]. Therefore in our fits we take NNLO χPT values as central results, but include the conservative error-bar, such that it covers the recent Roy-Steiner results [91, 105]. As for the Adler zero, we take the NLO value, as explained at the beginning of Sec. 3.3. The available experimental data for this process is scarce in the region close to the πK threshold, and often contains the discrepancies even within one dataset [157]. Since we consider only the single-channel approximation, we perform the fit till ηK threshold of the data from [157, 158]. In this way we also exclude the influence of the $K_0^*(1430)$ resonance. We observe a similar situation as for the $\pi\pi \to \pi\pi$ single-channel analysis, that fitting the experimental data [157, 158] or Roy-Steiner analysis of [91, 105] provides equivalent four parameter fits with $\kappa/K_0^*(700)$ pole positions at $689(24)^{+3}_{-2} - i\,263(33)^{+5}_{-8}$ MeV and $702(12)^{+4}_{-5} - i\,285(16)^{+8}_{-13}$ MeV, respectively. In general, these results compare well with the Roy-Steiner pole position $653^{+18}_{-12} - i\,280(16)$ MeV which we take as a conservative average between [89, 104] and [91, 105]. The one-sigma difference in the resonance mass can be attributed to the fact, that we are fitting Roy-Steiner solution only in the elastic region. The results are collected in Tables 3.10, 3.11, 3.14 and in Fig. 3.13.

We also look forward to the results of the KLF Collaboration, which plans to study πK scattering using a secondary K_L beam at Jefferson Lab [182]. It will further improve the position of the $\kappa/K_0^*(700)$ resonance.

m_π, MeV	$\sqrt{s_E}$, MeV	C_0	C_1	C_2	C_3	χ^2/d.o.f
$\pi K \to \pi K, I = 1/2$ single-channel, lattice data						
239	884	16.8(3.6)	−49.1(2.5)	28.2(7.5)	–	0.2

Table 3.12: Fit parameters entering Eq. (3.16) which were adjusted to reproduce available lattice data for $m_\pi = 239$ MeV, $\pi K \to \pi K\,, I = 1/2$ scattering in the single channel approach.

m_π, MeV	$\sqrt{s_A}$, MeV	$m_\pi a$	$m_\pi^3 b$	$\sqrt{s_A}^{\rm NLO}$, MeV	$m_\pi a^{\rm NNLO}$	$m_\pi^3 b^{\rm NNLO}$
$\pi K \to \pi K, I = 1/2$ single-channel, lattice data						
239	472(8)	0.426(71)	0.277(68)	472(9)	–	–

Table 3.13: Fit results for the threshold parameters a and b defined in Eq. (3.19) and the Adler zeros s_A for $\pi K \to \pi K\,, I = 1/2$ scattering in the single channel analysis of the lattice data with $m_\pi = 239$ MeV (left) compared to χPT values (right).

	$\sqrt{s_p}$, MeV	$\lvert g_{pa}\rvert/\sqrt{\mathcal{N}_{aa}}$	$\sqrt{s_p}$, MeV	$\lvert g_{pa}\rvert/\sqrt{\mathcal{N}_{aa}}$
	$\kappa/K_0^*(700)$			
Roy, SC	$702(12)^{+4}_{-5} - i\,285(16)^{+8}_{-13}$	$\pi K : 4.12(14)^{+0.13}_{-0.18}$	$653^{+18}_{-12} - i\,280(16)$ [89, 91, 104, 105]	$\pi K : 3.81(9)$ [91, 105]
Latt., 239	$747(39)^{+2}_{-0} - i\,265(16)^{+7}_{-6}$	$\pi K : 4.19(18)^{+0.07}_{-0.06}$		

Table 3.14: Poles and couplings of the $\kappa/K_0^*(700)$ resonance calculated in data-driven N/D approach compared with the results of Roy-like analyses. Roy, SC and Latt., 239 stand for single-channel analysis of the Roy data and the lattice data for $m_\pi = 239$ MeV, respectively. In our results, the first error is the statistical one, while the second one comes from a variation of s_E and has a systematic nature.

3.4.2 $I = 1/2$: analysis of the lattice data

For the unphysical pion mass, we again use recent lattice data from the Hadron Spectrum Collaboration [134]. We analyse the data for $m_\pi = 239$ MeV, where an evidence of $\kappa/K_0^*(700)$ was observed in the $p\cot\delta$ distribution. Due to large uncertainties, the pole position was not determined by the lattice collaboration, calling for more sophisticated approaches that include in addition to unitarity also the analyticity constraint. By employing the data-driven N/D approach, the present data can be easily described with the two-parameter fit, leading to $\chi^2/d.o.f = 0.4$. In this case, however, the Adler zero of the amplitude is located relatively far from the χPT value, since the lattice data in the low p^2 region suffers from the large uncertainties. Also, as we discussed before, in the Adler zero region the conformal expansion (3.16) does not converge well by construction and one has to impose Adler zero as a constraint, which effectively calls for one additional parameter. In this way, the impact of two points with prominently small errors at $p^2 \sim 0.09$ and ~ 0.11 GeV^2 is balanced out. The results of the fit are collected in Tables 3.12, 3.13, 3.14 and Fig. 3.14.

Again we would like to compare our results for the pole position and coupling with predictions of mIAM. According to [162], at $m_\pi = 239$ MeV, the imaginary part of the pole decreases by $\sim 17\%$, while the real part and coupling slowly increase by $\sim 4\%$ and $\sim 8\%$ respectively.

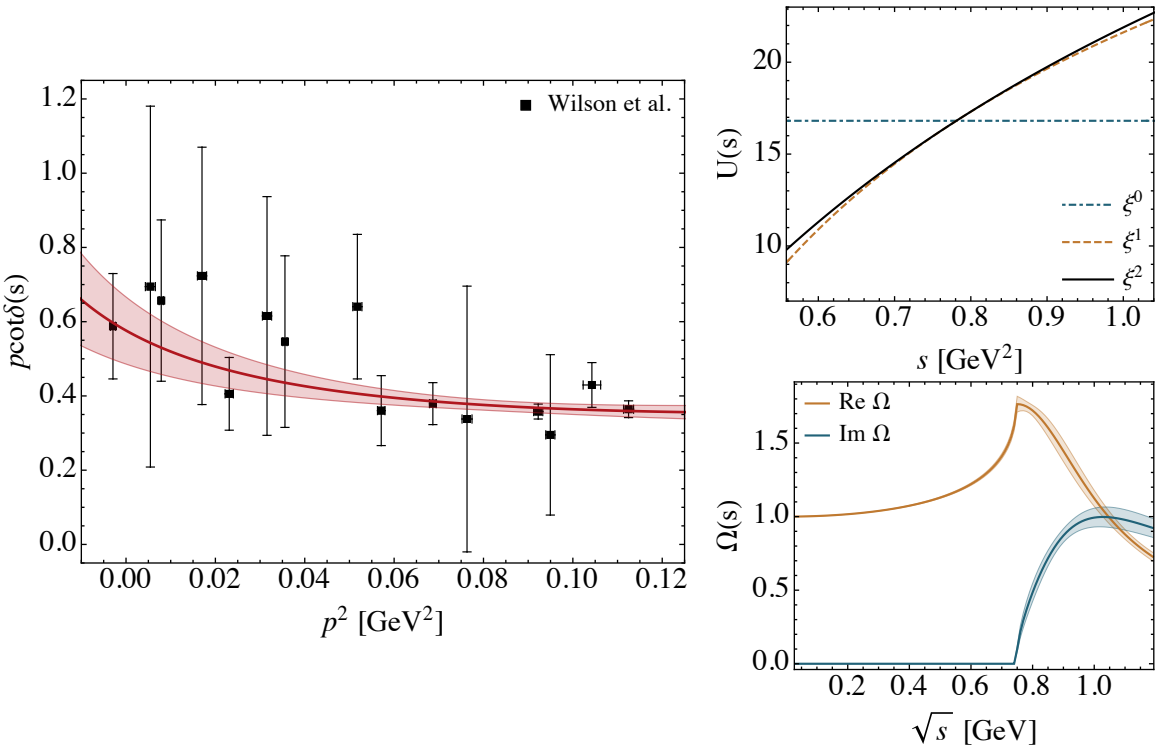

Figure 3.14: Results for the $\pi K \to \pi K$ scattering with $J = 0$, $I = 1/2$ of the lattice data [134] with the mass $m_\pi = 239$ MeV. Left panel shows the comparison with the data, right upper panel show the convergence of the conformal expansion in Eq. (3.16), and right lower panel shows the corresponding Omnès function.

Our values extracted from the lattice data show a similar behavior, with the decrease in the imaginary part of 7.0(7.7)%, increase in the real part and coupling of 6.4(5.8)% and 1.6(6.4)%, respectively.

3.4.3 $I = 3/2$ channel

The situation for the non-resonant $I = 3/2$, πK scattering resembles the $I = 2$, $\pi\pi$ scattering. Again, by fitting either experimental or Roy-Steiner pseudo-data we obtain an unphysical bound state far away from the threshold. Hence, we impose in the fit the exact fulfilment of p.w. dispersion relation given by Eq. (5.2) as an additional constraint and obtain the four-parameter fits. The fit to experimental data give us the result consistent with Roy-Steiner analysis [91, 105] including the slope parameter, which tends towards the value $m_\pi^3\, b^{\text{Roy-Steiner}} = -0.0471(49)$ (see Table 3.16). To minimize the uncertainties we also fitted directly the pseudo-data from Roy-Steiner analysis. The phase shifts and Omnès function obtained from these fits are shown in Fig. 3.15. The values of the fitted parameters, threshold parameters and Adler zeros are collected in Tables 3.15 and 3.16 .

3.5 Summary and Outlook

In this Chapter, we presented a data-driven analysis of the S-wave $\pi\pi \to \pi\pi$ and $\pi K \to \pi K$ reactions using the partial-wave dispersion relation. In this approach unitarity and analyticity constraints are implemented exactly. We accounted for the contributions from the left-hand cuts using the Taylor expansion in a conformal variable, which maps the left-hand cut plane

	$\sqrt{s_E}$, MeV	C_0	C_1	C_2	C_3	χ^2/d.o.f
			$\pi K \to \pi K, I = 3/2$			
Exp.	818	−20.7(8)	34.8(3.0)	25.7(8.0)	−52.0(11.3)	5.64
Roy		−19.8(2)	34.0(1.6)	21.1(1.9)	−46.4(4.5)	0.21

Table 3.15: Fit parameters entering Eq. (5.9) which were adjusted to reproduce the experimental data (denoted Exp.) and the most recent Roy-like results (Roy).

	$\sqrt{s_A}$, MeV	$m_\pi a$	$m_\pi^3 b$	$\sqrt{s_A^{\rm NLO}}$, MeV	$m_\pi a^{\rm NNLO}$	$m_\pi^3 b^{\rm NNLO}$
			$\pi K \to \pi K, I = 3/2$			
Exp.	522(11)	−0.048(5)	−0.056(4)	526(11)	−0.047[144]	−0.027[144]
Roy	524(9)	−0.047(4)	−0.053(1)			

Table 3.16: Fit results for the threshold parameters a and b and the Adler zeros s_A (left columns) compared to χPT values (right columns). The uncertainties on NLO Adler zero positions we estimated as |NLO − LO|, as explained in the text.

onto the unit circle. Then, the once subtracted p.w. dispersion relation was solved numerically by means of the N/D method.

Using existing experimental information and threshold constraints from χPT we tested the single-channel N/D formalism for the physical pion mass, where the positions of $\sigma/f_0(500)$ and $\kappa/K_0^*(700)$ have already been obtained from the sophisticated Roy and Roy-Steiner analyses. We demonstrated that the results for the pole parameters are stable and almost do not change if we replace the existing experimental data with the very precise pseudo-data generated by Roy and Roy-Steiner solutions in the physical region. Moreover, in our approach no spurious poles appear, in contrast to the K-matrix approach (see Fig. 3.16).

As a next step, we performed the fits to the lattice data of the Hadron Spectrum Collaboration for $m_\pi = 236, 391$ MeV in the case of $\pi\pi \to \pi\pi$ and for $m_\pi = 239$ MeV in the case of $\pi K \to \pi K$. We provided an improved determination of the $\sigma/f_0(500)$ and $\kappa/K_0^*(700)$ pole parameters compared to the simplistic K-matrix approach and also compared them with UχPT predictions.

An important feature of the N/D method is that the Omnès function comes out naturally, as the inverse of the D-function. The knowledge of the Omnès function, in turn, allows employing the Muskhelishvili-Omnès representation for the vast majority of production/decay reactions involving two pions (or pion and kaon) in the final state. While for the single-channel case, the Omnès function can be obtained analytically from the parametrisation of the phase shift, this is not the case for the coupled-channel case. In order to cover the $f_0(980)$ region we extended our analysis for the coupled-channel $\{\pi\pi, K\bar{K}\}$ case and extracted the corresponding Omnès matrix. In our construction it is asymptotically bounded (i.e. it satisfies once-subtracted dispersion relation) and therefore useful in many dispersive applications. The unknown coefficients from the conformal expansion were adjusted to reproduce existing Roy and Roy-Steiner analyses. The obtained Omnès matrix serves as an important building block, which allows for the dispersive calculation of the isoscalar two pion/kaon contribution to the hadronic light-by-light part [80, 183–185] of the anomalous magnetic moment of the muon $(g-2)_\mu$ [7, 71]. In particularly, with the input from $\gamma^*\gamma^* \to \pi\pi, KK$ [1, 4, 178] one can estimate dispersively the contribution from the $f_0(980)$ resonance, and compare it with narrow

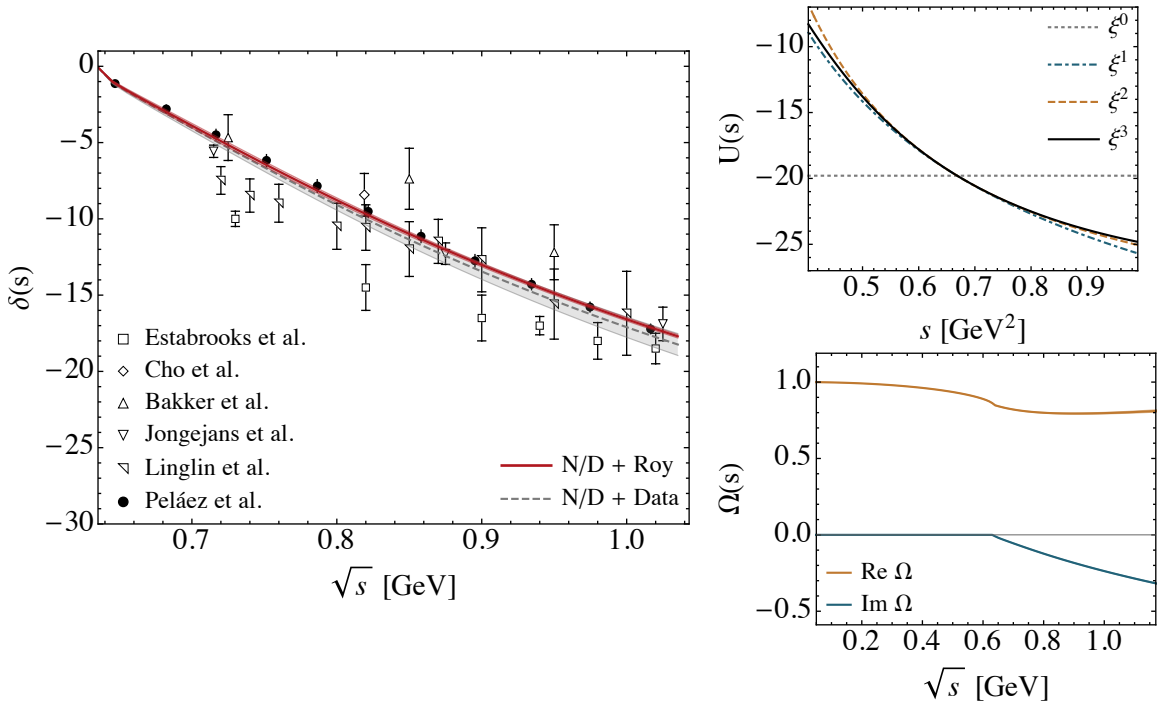

Figure 3.15: Results for the $\pi K \to \pi K$ scattering with $J = 0$, $I = 3/2$. Left panel show the comparison with the data, upper right panel shows the convergence of the conformal expansion in Eq. (3.16), and right lower panel show the corresponding Omnès function. In the phase shift plot for the physical pion mass two curves are shown: fit to the experimental data [157, 158] (dashed curve) and fit to the pseudo-data from Roy-Steiner analysis [91, 105] (thick curve).

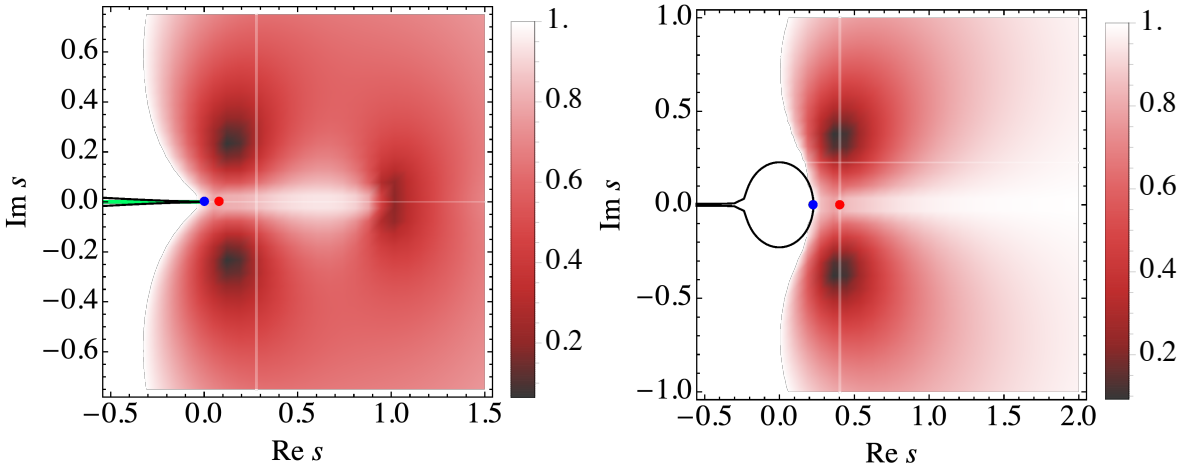

Figure 3.16: $\pi\pi \to \pi\pi$ coupled-channel (left panel) and $\pi K \to \pi K$ single-channel (right panel) scattering amplitudes in the complex s-plane. The red dots show the corresponding thresholds and blue dots show the closest l.h.c.. On the left plot there are $\sigma/f_0(500)$ and $f_0(980)$ resonances and on the right plot there is $\kappa/K^*(700)$ resonance. Note that the additional spurious poles do not appear within this method.

resonance results [186]. In the next Chapter, we will consider the two-photon fusion process with two pion in the final state, where the obtained hadronic part will be used to determine

the two-photon couplings of $\sigma/f_0(500)$ and $f_0(980)$ resonance.

The proposed method is not only limited to the $\pi\pi$ and πK scattering. We considered these reactions first because they show up as building blocks in many hadronic reactions/decays and have been calculated recently using lattice QCD. In principle, the N/D method combined with the conformal expansion for the left-hand cuts can be applied to any hadronic reaction where there is data (experimental or lattice) which possesses a broad (or coupled-channel) resonance that does not have a genuine QCD nature. For the latter (like for instance ρ or K^* resonances) one needs to extend the formalism to allow for CDD poles. Also, it has to be modified in the presence of anomalous thresholds. We will come back to this method in Chapter 5 to study the $D\bar{D}$ scattering.

Appendices

3.A Kinematics and Mandelstam vabiables

In $2 \to 2$ process, for the initial particles with masses m_1, m_2 and four-momenta q_1, q_2 respectively, in the *center-of-mass* (c.m.) frame, it holds:

$$\begin{aligned} q_1^\mu &= \{E_{q_1}, 0, 0, q_{\rm cm}\}\,, \quad E_{q_1} = \sqrt{q_{\rm cm}^2 + m_1^2}\,, \\ q_2^\mu &= \{E_{q_2}, 0, 0, -q_{\rm cm}\}\,, \quad E_{q_2} = \sqrt{q_{\rm cm}^2 + m_2^2}\,, \end{aligned} \tag{3.30}$$

and for final particles, with masses m_3, m_4 and four-momenta p_1, p_2:

$$\begin{aligned} p_1 &= \{E_{p_1}, p_{\rm cm}\sin\theta\cos\phi, p_{\rm cm}\sin\theta\sin\phi, p_{\rm cm}\cos\theta\}\,, \quad E_{p_1} = \sqrt{p_{\rm cm}^2 + m_3^2}\,, \\ p_2 &= \{E_{p_2}, -p_{\rm cm}\sin\theta\cos\phi, -p_{\rm cm}\sin\theta\sin\phi, -p_{\rm cm}\cos\theta\}\,, \quad E_{p_2}\sqrt{p_{\rm cm}^2 + m_4^2}\,, \end{aligned} \tag{3.31}$$

where θ is the scattering angle in the c.m. frame (see Fig. 3.17), $q_{\rm cm}$ and $p_{\rm cm}$ are the momenta of the initial and final state. If the scattering plane is chosen to be azimuthal plane, i.e. $\phi = 0$, the relation (3.31) simplifies as

$$\begin{aligned} p_1 &= \{E_{p_1}, p_{\rm cm}\sin\theta, 0, p_{\rm cm}\cos\theta\}\,, \\ p_2 &= \{E_{p_2}, -p_{\rm cm}\sin\theta, 0, -p_{\rm cm}\cos\theta\}\,, \end{aligned} \tag{3.32}$$

It is often convenient to work with Lorenz-invariant *Mandelstam variables* [46], which are defined as (see also Sec. 2.2.1):

$$\begin{aligned} s &= (q_1 + q_2)^2 = (p_1 + p_2)^2\,, \\ t &= (p_2 - q_2)^2 = (p_1 - q_1)^2\,, \\ u &= (p_2 - q_1)^2 = (p_1 - q_2)^2\,, \end{aligned} \tag{3.33}$$

and satisfy the relation

$$s + t + u = m_1^2 + m_2^2 + m_3^2 + m_4^2\,. \tag{3.34}$$

The c.m. three momenta $q_{\rm cm}$ and $p_{\rm cm}$ can then be expressed in terms of the total energy $\sqrt{s}$ as

$$\begin{aligned} q_{\rm cm} &= \sqrt{\frac{(s-(m_1+m_2)^2)(s-(m_1-m_2)^2)}{4s}} = \frac{1}{2\sqrt{s}}\lambda^{1/2}(s, m_1^2, m_2^2)\,, \\ p_{\rm cm} &= \sqrt{\frac{(s-(m_3+m_4)^2)(s-(m_3-m_4)^2)}{4s}} = \frac{1}{2\sqrt{s}}\lambda^{1/2}(s, m_3^2, m_4^2)\,, \end{aligned} \tag{3.35}$$

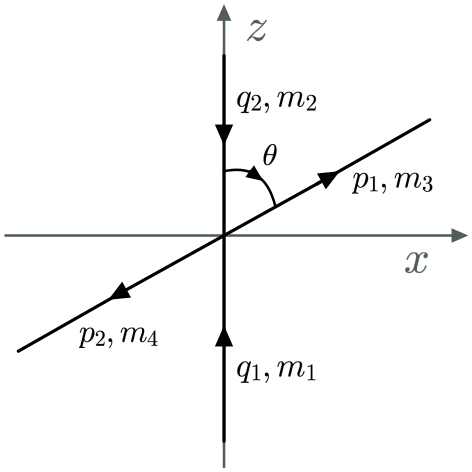

Figure 3.17: Definition of the scattering angle θ in the c.m. frame. The scattering plane is chosen to be azimuthal plane.

where $\lambda(x,y,z) \equiv x^2+y^2+z^2-2xy-2yz-2zx$ is a *Källén triangle* function [187]. In terms of the c.m. angle the Mandelstam variables have the following form:

$$\begin{aligned} t(s,z) &= \frac{1}{2}\left(m_1^2+m_2^2+m_3^2+m_4^2-s-\frac{(m_2^2-m_1^2)(m_4^2-m_3^2)}{s}\right)+2zp_{\rm cm}(s)q_{\rm cm}(s)\,, \\ u(s,z) &= \frac{1}{2}\left(m_1^2+m_2^2+m_3^2+m_4^2-s+\frac{(m_2^2-m_1^2)(m_4^2-m_3^2)}{s}\right)-2zp_{\rm cm}(s)q_{\rm cm}(s)\,, \end{aligned} \tag{3.36}$$

where $z \equiv \cos\theta$ can be written as

$$z = \frac{t-u-\frac{1}{s}(m_3^2-m_4^2)(m_2^2-m_1^2)}{4p_{\rm cm}(s)q_{\rm cm}(s)}\,. \tag{3.37}$$

While the processes described in this Chapter only include the spinless particles, it is instructive to consider $2\to 2$ scattering involving photons. In this case, the polarization vectors $\epsilon^\mu(k,\lambda)$, where k is a momentum and λ is a helicity for a spin-one particles are defined as

$$\begin{aligned} \epsilon^\mu(p_1,\pm1) &= \begin{pmatrix} 0 \\ \frac{\mp\cos\theta}{\sqrt{2}} \\ \frac{-i}{\sqrt{2}} \\ \frac{\pm\sin\theta}{\sqrt{2}} \end{pmatrix}\,, \quad \epsilon^\mu(p_1,0) = \begin{pmatrix} \frac{p_{\rm cm}}{m_3} \\ \frac{E_{p_1}}{m_3}\sin\theta \\ 0 \\ \frac{E_{p_1}}{m_3}\cos\theta \end{pmatrix}\,, \\ \epsilon^\mu(p_2,\pm1) &= \begin{pmatrix} 0 \\ \frac{\pm\cos\theta}{\sqrt{2}} \\ \frac{-i}{\sqrt{2}} \\ \frac{\mp\sin\theta}{\sqrt{2}} \end{pmatrix}\,, \quad \epsilon^\mu(p_2,0) = \begin{pmatrix} \frac{p_{\rm cm}}{m_4} \\ -\frac{E_{p_2}}{m_4}\sin\theta \\ 0 \\ -\frac{E_{p_2}}{m_4}\cos\theta \end{pmatrix}\,, \end{aligned} \tag{3.38}$$

for the final particles, while for the initial particles:

$$\epsilon^\mu(q_1,\pm1) = \begin{pmatrix} 0 \\ \frac{\mp1}{\sqrt{2}} \\ \frac{-i}{\sqrt{2}} \\ 0 \end{pmatrix}, \quad \epsilon^\mu(q_1,0) = \begin{pmatrix} \frac{q_{\rm cm}}{m_1} \\ 0 \\ 0 \\ \frac{E_{q_1}}{m_1} \end{pmatrix},$$
$$\epsilon^\mu(q_2,\pm1) = \begin{pmatrix} 0 \\ \frac{\pm1}{\sqrt{2}} \\ \frac{-i}{\sqrt{2}} \\ 0 \end{pmatrix}, \quad \epsilon^\mu(q_2,0) = \begin{pmatrix} \frac{q_{\rm cm}}{m_2} \\ 0 \\ 0 \\ -\frac{E_{q_2}}{m_2} \end{pmatrix}, \tag{3.39}$$

3.B Bootstrap method

"All models are wrong, but some are useful."

George Box, 1976

The ultimate goal of any fitting procedure is obtaining the maximum amount of helpful information from the available data. In practice, for the theoretical model $f(\mathbf{C})$ under consideration, this translates to the problem of extracting the best estimates of its parameters $\mathbf{C} = \{C_1 \dots C_N\}$ and consequently, assessing the validity of the result by means of the error analysis. Most often, it is done by maximizing the likelihood function given the underlying probability distribution of the data uncertainties. In case when the Gaussian distribution is obeyed, it is equivalent to minimizing the sum of the square residuals, weighted inversely by uncertainties σ_i in the individual measurements $\{x_i, y_i\}$, or χ^2 function:

$$\chi^2(\mathbf{C}) = \sum_i \left(\frac{y_i - f(x_i;\mathbf{C})}{\sigma_i} \right)^2 . \tag{3.40}$$

The uncertainties in the estimation of the best parameters $\hat{\mathbf{C}} = \{\hat{C}_1 \dots \hat{C}_N\}$ are collected in the *error* or *covariance matrix*, which also includes the effects of the parameters correlations. Within the least-square method it is usually defined as

$$\mathrm{cov}(\hat{C}_i, \hat{C}_j) = \left[\frac{1}{2} \frac{\partial^2 \chi^2}{\partial C_i \partial C_j} \bigg|_{\mathbf{C}=\hat{\mathbf{C}}} \right]^{-1} = \left[H^{-1} \right]_{ij}, \tag{3.41}$$

where H stands for the *hessian matrix*, which is symmetric and related to the curvature of χ^2 function in parameter space at its minimum. In general, for nonlinear models, the χ^2 hypersurface is essentially nonparabolic, hence H depends on the parameters.

While being relatively simple and straightforward to implement, the standard least square method suffers from several drawbacks. For instance, Eq. (3.40) assumes that only statistical errors are present in the given dataset. However, the systematic uncertainties $\sigma_{\rm syst}$ inherent to the actual experimental data can skew the results of the fit significantly. In the simplest case, they can be attributed to the common scale factor ξ and the χ^2 function can be modified accordingly [188]

$$\tilde{\chi}^2(\mathbf{C}) = \sum_i \left(\frac{\xi y_i - f(x_i;\mathbf{C})}{\xi \sigma_i} \right)^2 + \left(\frac{\xi - 1}{\sigma_{\rm syst}} \right)^2 , \tag{3.42}$$

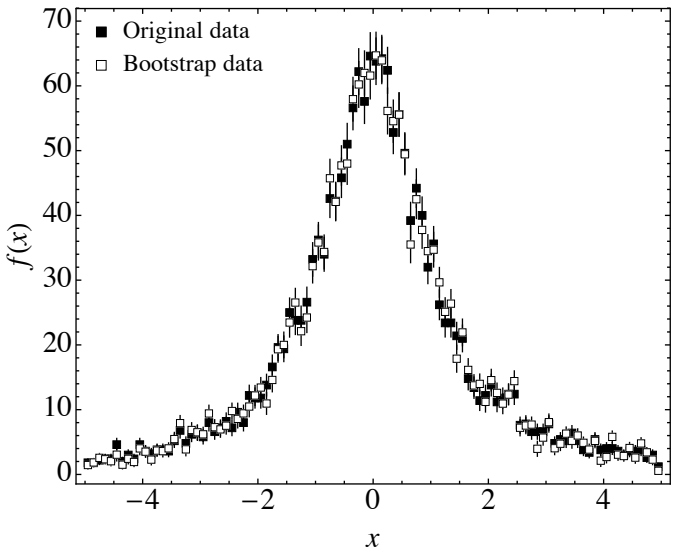

Figure 3.18: Simulated data from Cauchy distribution for $\mu = 0, \Gamma = 1, I = 200$.

where ξ is an additional parameter to be fitted. In general, this method fails numerically to describe the multiple datasets with different systematics, hence different normalization factors. Beyond the simplest case, the assumption of the common normalization factor is also not applicable due to the systematic uncertainties varying from point to point or the presence of correlation.

Another problem that stands before the standard least-square procedure is uncertainty propagation. Once the optimal set of parameters is obtained as the result of the minimization procedure, the uncertainties of any derived quantities $\boldsymbol{\eta}(\mathbf{C}) = \{\eta_1(\mathbf{C}) \dots \eta_M(\mathbf{C})\}$, including the fitting function itself, can be estimated by implementing the error propagation formula for the covariance matrix:

$$\operatorname{cov}(\hat{\eta}_i, \hat{\eta}_j) \approx \sum_{l,k} \frac{\partial \eta_i}{\partial C_l} \frac{\partial \eta_j}{\partial C_k}\bigg|_{\mathbf{C}=\hat{\mathbf{C}}} \operatorname{cov}(\hat{C}_l, \hat{C}_k)\,, \tag{3.43}$$

where $\hat{\boldsymbol{\eta}} \equiv \boldsymbol{\eta}(\hat{\mathbf{C}})$. This approximation fails, however, if the theoretical model is significantly non-linear. In this case, the calculation of the partial derivatives is quite challenging, even with modern numerical techniques.

These and other complications can be addressed within a framework of various *Monte-Carlo techniques*, a statistical tool for studying the problems based on the use of random numbers[4], which has made it possible to solve easily several estimation problems that would have been far more difficult by other means. In physics, these methods are frequently used to evaluate the complex integrals [189] or make simulations; however, the underlying concept of randomness can be applied to a broader class of problems requiring drawing the estimates from some probability distribution.

Among these, the *bootstrap* technique is widely used for fitting. For example, the *nonparametric* bootstrap [190] employs the idea of random sampling with the replacement to infer the variability in a statistic of interest. In this case, the main advantage is that all essential information can be estimated from the sample on hand, without the requirement to perform additional experiments or making assumptions on the underlying distribution [191]. In contrast, the *parametric bootstrap* assumes that each point of the original data is a realization

[4]In actual simulations, mainly the pseudo-random generators are used; however, the implied prefix "pseudo" will be omitted for clarity hereafter.

	χ^2/d.o.f	$\hat{I}$	$\hat{\mu} \times 10^{-2}$	$\hat{\Gamma} \times 10^{-1}$
Eq. (3.40)	0.99	197.9 ± 2.2	0.9×1.4	9.9 ± 0.2
$N_B = 10^2$	1.01	197.6 ± 2.2	0.9×1.2	9.9 ± 0.2
$N_B = 10^4$	0.99	197.9 ± 2.2	0.9×1.4	9.9 ± 0.2

Table 3.17: Comparison of the standard least squares fitting (3.40) with bootstrap technique with different number of cycles ($N_B = 10^2, 10^4$). For the bootstrap result we show $\chi^2/\text{d.o.f} = \chi^2_B/\text{d.o.f} - 1$ for the comparison only, see text for the details.

of a random sample from an unknown probability distribution of a specific parametric type approximated by the probability distribution of the measured value $p(x_i, y_i)$.

Knowing the distribution for y_i, new sample $\{x_i, y_i^B\}_m$ of the same size as an initial dataset can be generated according to $p(x_i, y_i)$. The *bootstrap cycle* is then each k-th generated dataset, for which the best parameters $\hat{\mathbf{C}}_k^B$ are estimated by the standard χ^2-minimization procedure and the resulting derived values $\boldsymbol{\eta}^B(\mathbf{C})$ are stored. This cycle is then repeated over the large number N_B of times resulting in a set $\hat{\mathbf{C}}_1^B \cdots \hat{\mathbf{C}}_{N_B}^B$ which contains the information on the probability distribution of each parameter, where the mean and the covariance matrix are given as

$$\hat{\mathbf{C}}^B = \frac{1}{N_B}\sum_{k=1}^{N_B} \mathbf{C}_k^B\,, \quad \operatorname{cov}(\hat{C}_i^B, \hat{C}_j^B) = \frac{1}{N_B - 1}\sum_{k=1}^{N_B} (\hat{C}_{i,k}^B - \hat{C}_i^B)(\hat{C}_{j,k}^B - \hat{C}_j^B)\,. \tag{3.44}$$

The bootstrap technique requires a generation of large numbers of random samples from specific probability distribution. For arbitrary distribution, one of the most common Monte Carlo algorithm for random number sampling is *inverse transformation method*. It is based on the fact that by inverting the *cumulative distribution function* (CDF), which is uniformly distributed on $[0, 1]$, the samples from the distribution itself can be obtained. However, for most of the continuous distributions, there is no analytical expression for CDF, and hence, other methods may be preferred. For the normally distributed data, there is a more computationally efficient alternative - *Box-Muller transformation* [192]. If applied to the real data points, the modified version of this transformation takes a pair of uniformly distributed random numbers $U_1, U_2 \in [0, 1]$ and produces numbers from the Gaussian distribution with non-unit variance δy_i and non-zero mean y_i:

$$y_i^B = \delta y_i \sqrt{-2 \ln U_1} \cos 2\pi U_2 + y_i\,, \tag{3.45}$$

where the $\cos 2\pi U_2$ varies the data between $y_i \pm \sigma_i$ and $\sqrt{-2 \ln U_1}$ is a weight function.

The advantage of the bootstrap method is that it can be applied in an automatic way to any situation regardless of the complexity. However, to illustrate the concept, we follow [193, 194] and consider a simple toy model based on the Cauchy distribution with the following *probability density function* (PDF):

$$f(x; I, \mu, \Gamma) = \frac{I}{\pi\Gamma} \frac{\Gamma^2}{(x - \mu)^2 + \Gamma^2}\,, \tag{3.46}$$

where I is an overall scale factor, μ is a peak position and Γ is half-width at half-maximum. In physics, it appears as the Breit-Wigner distribution, which is appropriate for describing the data corresponding to resonant behaviour (see App. 5.A). For this distribution, the CDF and

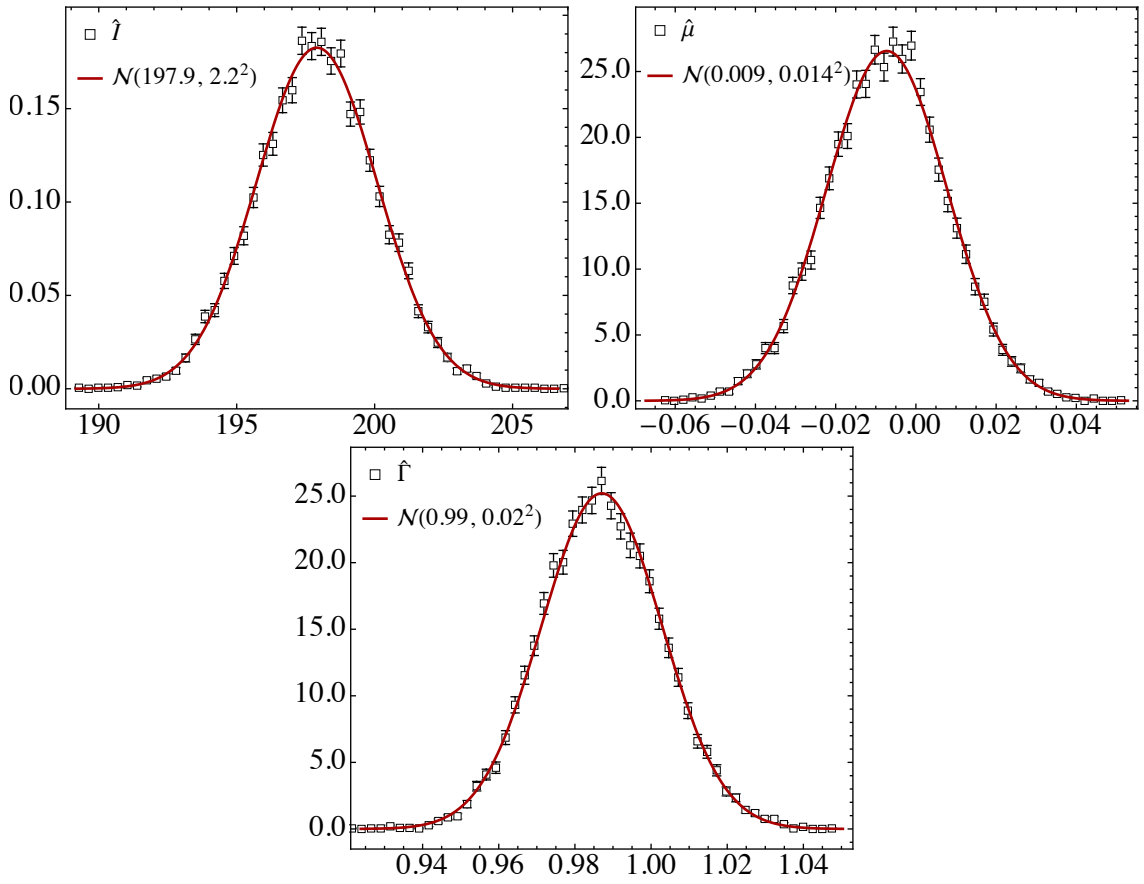

Figure 3.19: Bootstrap result ($N_B = 10^4$) for the probability distribution of the fitted parameters $\hat{I}, \hat{\mu}, \hat{\Gamma}$ compared to the Gaussian distribution $\mathcal{N}(x_0, \sigma^2)$ with corresponding parameters x_0, σ^2.

hence its inverse, the *quantile function*, are known analytically, so that x can be obtained[5] as:

$$x = \mu + \Gamma \tan\left[\pi\left(\xi - \frac{1}{2}\right)\right], \tag{3.47}$$

where ξ is randomly sampled from $[0, 1]$ and $I = 1$. In order to simulate the experimental data, we repeat this procedure 10^4 times with the peak located at $\mu = 0$, half width $\Gamma = 1$, collect the samples falling into [-5, 5] range and rescale the output to $I = 200$. The resulting 100-bin histogramm is then shown on Fig. 3.18 with y_i and σ_i as a height and uncertainty of each bin respectively.

We then treat this artificial data as an experimental output and, using Box-Muller transformation, generate bootstrap datasets, one of which is shown in Fig. 3.18. In general, the number of bootstrap cycles is situation-specific and is vaguely defined as very large. Table 3.17 shows the comparison of the standard fitting procedure and bootstrap for different number of runs. While the $N_B = 10^4$ is a commonly accepted choice, even $N_B = 10^2$ gives similar results in the case of the large statistics. As expected, with the statistical uncertainties only, the bootstrap output for the fit parameters coincides with the result of the minimization procedure in Eq. (3.40) given the suffiently high number of cycles.

[5]The Cauchy distribution is also known as normal ratio distribution since it comes about as the ratio of two normally distributed variables with zero mean. Therefore it is possible to generate samples using Box-Muller transform as well.

Each fit in Table 3.17 is characterized by the value χ^2/d.o.f., where d.o.f denotes the degrees of freedom. In case when there are no additional constraints, d.o.f=(number of data points)$-N$. In the case of the perfect fit hypothesis, each term in the sum in Eq. (3.40) will be of order unity. Therefore, the value χ^2/d.o.f. should be close to 1. Note that the pseudo-datasets generated under the bootstrap procedure are not Cauchy-distributed themselves but are randomly generated around the Cauchy-distributed original simulation. Therefore, the average χ^2_B/d.o.f. for fitting the pseudo-data should be close to 2. In Table 3.17 we show, when applicable, the value of $\chi^2/\text{d.o.f} = \chi^2_B/\text{d.o.f} - 1$ for the comparison only.

The advantage of the parametric bootstrap method is that the only assumption is made regarding the uncertainties distribution of the original dataset. However, the probability distribution of parameter is reconstructed as the result of sampling. The obtained results for I, Γ and μ compared to the normal distributions $\mathcal{N}(\mu, \sigma^2)$ with respective parameters are shown on Fig. 3.19. In more complicated cases, for instance, when the systematic uncertainties are included, the probability distribution of parameters is not expected to have Gaussian shape, illustrating the limitation of the standard least squares procedure. The detailed analysis of this scenario can be found in [193, 194].

To summarize, the bootstrap technique provides a powerful tool for the analysis of the available data without complex analytical evaluations. The parametric version allows to overcome additional complications, such as scarcity of data if the underlying distribution can be safely assumed. Moreover, for the complex models the analytic expressions are often not available and the bootstrap method serves as a simple yet rigorous tool for the error analysis. This is exactly the situation described in Chapters 3 and 5, as the N/D method requires the numerical solution of the integral equation and hence the standard error analysis for poles and couplings is hardly possible.

Chapter 4

Two photon fusion reaction with $\pi\pi$ final state

In the previous Chapter, we developed the approach required to describe the interaction of the light mesons pair, in particular the $\pi\pi \to \pi\pi$ process, which allowed us to extract valuable information regarding $\sigma/f_0(500)$ and $f_0(980)$ resonances. As we mentioned in Sec. 3.2, the resulting Omnès function is ubiquitous for processes where the $\pi\pi$ final state interaction arises since it contains only the right-hand cuts. We will take advantage of this universality by considering the prime example of the $\gamma\gamma \to \pi\pi$ process. Perpetuating the resonance subject, we note that the study of this reaction allows accessing the information regarding the $\sigma/f_0(500)$ and $f_0(980)$ coupling to photons, which in principle paves the way for deciphering their internal structure. Aside from this ambitious prospect, we also note that in the energy region from threshold to 1.5 GeV considered in this Chapter lies another resonance, $f_2(1270)$ in D-wave. While it can be safely considered a regular quark-model state, we will move further from the simplistic Breit-Wigner parametrization and attempt to describe it in a dispersive manner as well.

In Sec. 2.3 we brought up the importance of the two-photon fusion reaction with pseudoscalar mesons in the final state for the understanding of the anomalous magnetic moment of the muon problem. Providing a comparatively significant contribution to the theoretical uncertainty, the input from these reactions is rather vaguely estimated up to date. In recent years some progress has been achieved towards incorporating the $\pi\pi$ channel; however, the model-independent inclusion of the higher intermediate states approximated in terms of scalar, axial-vector and tensor resonances is still a work in progress. We note that the relevant input arises from the $\gamma^*\gamma^* \to \pi\pi$ reaction, where an off-shell photon carries a finite spacelike-virtuality. Naturally, both experiment and theory, including this work, first approached the special case of real photons in the initial state, which allowed to accumulate relatively abundant datasets and a large number of models designed to describe them. However, even for the single-virtual process, the available experimental data from the Belle Collaboration [195] is limited to the neutral pions pair in the final state and large photon virtualities. On other hand, BESIII Collabortation has already collected the data in both $\pi^0\pi^0$ and $\pi^+\pi^-$ channels for low photon virtuality [196], emphasizing the necessity of the theoretical framework able to provide a prediction for this data. Presenting such an approach in this Chapter, we, however, will refrain from the chronological pathway from real to single-virtual to double-virtual cases along which it has developed. Instead, we will present the general framework describing the double-virtual scenario and comment on the special cases when needed.

This Chapter is based on [1, 2, 4], and it is organized as follows. In the next section, we will expand on the importance of the $\gamma^*\gamma^* \to \pi\pi$ process in the view of the upcoming experimental data for low spacelike virtualities and the $(g-2)_\mu$ problem. We will also provide a brief overview of the existing theoretical approaches. In Sec. 4.2, we will extend the dispersive formalism given in the previous sections to the systems with two incoming photons. We will concentrate on the kinematic constraints of the partial wave amplitudes and discuss the peculiar analytical structure of the vector-meson exchange left-hand cuts. Finally, in Sec. 4.3 we will provide the numerical results for different combinations of photon virtualities: total

Contribution	Value $\times 10^{11}$
Experiment	116 592 061(41)
QED	116 584 718.931(104)
Electroweak	153.6(1.0)
HVP (e^+e^-, LO + NLO + NNLO)	6845(40)
HLbL (phenomenology + lattice + NLO)	92(18)
Total SM Value	116 591 810(43)
Difference: $\delta a_\mu := a_\mu^{\rm exp} - a_\mu^{\rm SM}$	251(59)

Table 4.1: Summary of the contributions to $a_\mu^{\rm SM}$ as compiled in [7] in comparison to the average experimental value of [76, 77]. See [6, 7] for the detailed explanation of each contribution.

and differential cross sections, pion dipole polarizabilities and the two-photon couplings of $\sigma/f_0(500)$ and $f_0(980)$ resonances. In App. 4.A we will provide an alternative approach to treat the anomalous threshold problem and in App. 4.B we will outline the connection between the general $e^+ + e^- \to e^+ + e^- + X$ cross section and the cross sections of the $\gamma^*\gamma^* \to \pi\pi$ reactions considered in this Chapter.

4.1 Introduction

As we mentioned in Sec. 2.3, the existing tension between the present high-precision $(g-2)_\mu$ measurements and the theoretical calculations amounts to 4.2σ difference. The current theoretical error entirely results from hadronic contributions (see Table 4.1). Forthcoming data from the high luminosity e^+e^- colliders, in particular from the BESIII and Belle-II Collaborations will further reduce the uncertainty in the HVP over the next years to make it commensurate with the experimental precision on $(g-2)_\mu$. The remaining hadronic uncertainty results from HLbL, where apart from the pseudo-scalar pole contribution, a further nontrivial contribution comes from the two-particle intermediate states such as $\pi\pi$, $\pi\eta$ and $K\bar{K}$ (see Table 4.2). The rescattering of $\pi\pi$ and $\pi\eta$ are responsible for the contribution from $f_0(500)$, $f_0(980)$, $f_2(1270)$ and $a_0(980)$ which can be taken into account in a dispersive framework. Among those, only $f_2(1270)$ can be interpreted within the quark model, as a state that does not originate from long-range interactions [197]. Given the fact that it is relatively narrow, its contribution to the $(g-2)_\mu$ can be accounted for in two ways: using a pole contribution as it is given in [198] (updated in [186] using recent data from the Belle Collaboration [195]), or through fully dispersive formalisms [80, 184, 199] and [185] with the input from $\gamma^*\gamma^* \to \pi\pi$. The comparison will shed light into the effective resonance description of other resonances such as axial-vector contributions [69, 198].

Experimentally, two-photon fusion reactions are studied at e^+e^- colliders. The most precise and comprehensive datasets for the $\gamma\gamma \to \pi^0\pi^0$, $\gamma\gamma \to \pi^+\pi^-$ and $\gamma\gamma \to \pi^0\eta$ processes involving quasi-real photons were obtained by the Belle Collaboration [200–202]. When both leptons in the process $e^+e^- \to X$ are detected in the final state, this reaction allows to access the two-photon process $\gamma^*\gamma^* \to X$ where both photons have a space like virtuality. The first measurement of the $\gamma\gamma^* \to \pi^0\pi^0$ process has been reported recently by the Belle Collaboration in [195] for Q^2 in the region from $3.5 - 30$ GeV^2. At small momentum transfers, the BESIII Collaboration is currently analyzing both $\pi^+\pi^-$ and $\pi^0\pi^0$ production in the 0.2 GeV$^2 \lesssim Q^2 \lesssim 2$ GeV^2 range [196], corresponding with the most relevant kinematical region for quantifying the

Contribution	Value $\times 10^{11}$
π^0, η, η'-poles	93.8(4.0)
π, K-loops/boxes	−16.4(2)
S-wave $\pi\pi$ rescattering	−8(1)
subtotal	69.4(4.1)
scalars	−1(3)
tensors	
axial vectors	6(6)
u, d, s-loops/short-distance	15(10)
c-loop	3(1)
total	92(19)

Table 4.2: Summary of constituents to the HLbL contribution to $a_\mu^{\rm SM}$ as compiled in [7]. See [6, 7] for the detailed explanation of each estimate.

HLbL contribution to $(g-2)_\mu$.

Very close to threshold, the $\gamma\gamma \to \pi\pi$ process has been studied in χPT up to two-loop accuracy [203, 204] as a tool to access pion polarizabilities. Such approaches however fail to describe the resonance region, which require resummation techniques to comply with exact unitarity [119–121, 205, 206]. Among those, the most established ones respect analyticity properties of the S-matrix [119, 120, 206–208]. The energy range of applicability of such dispersive techniques is typically limited by the inelastic contributions and inclusion of higher partial waves. Extending such dispersive techniques to the partial-wave helicity amplitudes of the single virtual $\gamma\gamma^* \to \pi\pi$ process is not straightforward, as in addition to the well-known low-energy constraints, partial-wave amplitudes exhibit kinematic constraints. For quite some time, the dispersive analyses of $\gamma\gamma^* \to \pi\pi$ have been limited to the S-wave and single-channel description [80, 183, 184, 209] which only covers the $\sigma/f_0(500)$ resonance region. In this Chapter we show the extension of the dispersive approach to the coupled-channel case by including $K\bar{K}$ intermediate states, where the D-wave contribution was first accounted in a full dispersive framework in [178]. This will allow for a validation of such approach by forthcoming BESIII data for the $\gamma^*\gamma^* \to \pi\pi$ reaction, which requires the careful uncertainty estimation.

In case of the double virtual process $\gamma^*\gamma^* \to \pi\pi$ the treatment of the kinematical constraints becomes even more cumbersome and there is an additional complication related to the anomalous threshold behavior as it was pointed out in [210]. We will show an alternative way of taking this contribution into account using an appropriate contour deformation.

4.2 Dispersive formalism

In this section, we are aiming to show the application of the dispersive formalism to the coupled-channel $\{\gamma\gamma, \pi\pi, K\bar{K}\}$ system. Since the intermediate states involving two photons are proportional to e^4 and therefore, suppressed, the expected (3×3) matrix dispersion relation can be reduced to the (2×1) form, which requires the previously obtained hadronic rescattering part as input. However, once we consider the processes involving a photon pair, the construction of dispersion relation becomes less straightforward. In particular, it requires careful handling of the kinematic constraints and singularities appearing in the partial-wave amplitudes.

This section is organized as follows. First, we define the helicity and partial-wave amplitudes

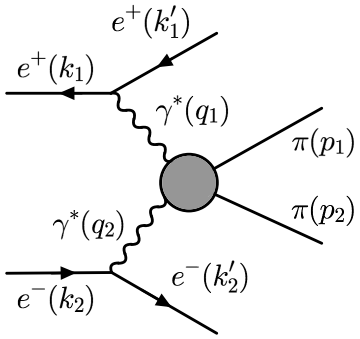

Figure 4.1: Feynman diagram for the two-photon production process with two pions in the final state.

of the $\gamma^*\gamma^* \to \pi\pi(K\bar{K})$ process. Then, in Sec. 4.2.2, we discuss the kinematic constraints and derive a new set of amplitudes, for which the dispersion relation can be written in Sec. 4.2.3. We devote particular attention to the left-hand cuts. While the generalization of the Born l.h.c. for the case with finite photon virtualities is relatively straightforward and only requires the proper parametrization of the pion and kaon form factors in the space-like region, the vector meson l.h.c. needed for the dispersive description of the $f_2(1270)$ resonance region, have a complicated analytical structure which should be treated carefully as we show in Sec. 4.2.6. The hadronic final state interaction in the S-wave is accounted for using the results of the Sec. 3.3 and hence, in Sec. 4.2.7 we only discuss the $J = 2$ Omnés function.

4.2.1 Helicity amplitudes

The two-photon fusion reaction $\gamma^*\gamma^* \to \pi\pi$ is a subprocess of the unpolarized double tagged process $e^+(k_1)e^-(k_2) \to e^+(k_1')e^-(k_2')\pi(p_1)\pi(p_2)$ (see Fig. 4.1) which in Lorenz gauge is given as

$$
\begin{aligned}
i\,\mathcal{M} &= \frac{i\,e^2}{q_1^2 q_2^2}\,[\bar{v}(k_1)\,\gamma_\mu\,v(k_1')]\,[\bar{u}(k_2')\,\gamma_\nu\,u(k_2)]\,H^{\mu\nu}\,, \\
H^{\mu\nu} &= i\int d^4x\, e^{-i\,q_1\cdot x}\langle\pi(p_1)\pi(p_2)|T(j^\mu_{em}(x)\,j^\nu_{em}(0))|0\rangle\,,
\end{aligned}
\tag{4.1}
$$

with $q_1 \equiv k_1 - k_1'$, where the momenta of leptons k_1' and k_2' are detected. This corresponds with the kinematical situation where the photons with momenta q_1 and q_2 have finite space-like virtualities, $q_1^2 = -Q_1^2$ and $q_2^2 = -Q_2^2$. In the single-virtual limit, the second lepton momentum k_1' goes undetected and therefore, the photon with momentum q_1 is quasi-real, i.e. $q_1^2 = -Q_1^2 \simeq 0$. By contracting the hadronic tensor $H^{\mu\nu}$ with polarization vectors, one defines helicity amplitudes $H_{\lambda_1\lambda_2}$ which can be further decomposed into partial waves

$$
\begin{aligned}
\epsilon_\mu(q_1,\lambda_1)\,\epsilon_\nu(q_2,\lambda_2)\,H^{\mu\nu} &\equiv e^{i\phi(\lambda_1-\lambda_2)}H_{\lambda_1\lambda_2} \\
&= e^{i\phi(\lambda_1-\lambda_2)}\mathcal{N}\sum_{J\,\text{even}}(2J+1)\,h^{(J)}_{\lambda_1\lambda_2}(s)\,d^{(J)}_{\Lambda,0}(\theta)\,,
\end{aligned}
\tag{4.2}
$$

where $\Lambda = \lambda_1 - \lambda_2$, $d^{(J)}_{\Lambda,0}(\theta)$ is a Wigner rotation function and θ is the c.m. scattering angle. The two-photon initial state implies that the C-parity quantum number of the final particles should be positive, which excludes the isospin $I = 1$ state in case of two pions, and due to Bose symmetry, only even-values of total angular momentum J are present in the p.w. expansion.

In Eq. (4.2), $\mathcal{N}=1$ for $\gamma^*\gamma^*\to\pi\pi$ and $\mathcal{N}=1/\sqrt{2}$ for $\gamma^*\gamma^*\to K\bar{K}$ to ensure the same unitarity relations for the identical and non-identical particles in the case of $I=0$ (see also Sec. 3.2). Further, we will work in the isospin limit, defining the helicity amplitudes $H_{I,\lambda_1,,\lambda_2}(K_{I,\lambda_1,\lambda_2})$ for $\gamma^{(*)}\gamma^{(*)}\to\pi\pi(K\bar{K})$, which imply the following relations for $I=0$ and $I=2$:

$$\begin{aligned}
H_{0,\lambda_1,\lambda_2} &= -\frac{2H^c_{\lambda_1\lambda_2}+H^n_{\lambda_1\lambda_2}}{\sqrt{3}}\,,\\
K_{0,\lambda_1,\lambda_2} &= -\frac{K^c_{\lambda_1\lambda_2}+K^n_{\lambda_1\lambda_2}}{\sqrt{2}}\,,\\
H_{2,\lambda_1,\lambda_2} &= \sqrt{\frac{2}{3}}\left(H^n_{\lambda_1\lambda_2}-H^c_{\lambda_1\lambda_2}\right)\,,
\end{aligned} \tag{4.3}$$

where $H^c_{\lambda_1\lambda_2}(K^c_{\lambda_1\lambda_2})$ and $H^n_{\lambda_1\lambda_2}(K^n_{\lambda_1\lambda_2})$ are the corresponding amplitude for charged or neutral pion (kaon) pairs.

4.2.2 Kinematic constraints

It is well known that p.w. amplitudes $h^{(J)}_{\lambda_1\lambda_2}$ may have kinematic singularities or obey kinematic constraints, such as zeros and singularities at threshold and pseudothreshold [107, 211, 212]. Therefore it is important to find a transformation to a new set of amplitudes which are more appropriate to use in partial-wave dispersion relations. The key step is to decompose the scattering amplitude into a complete set of invariant amplitudes F_i [213–215] (see also [216])

$$H^{\mu\nu}=\sum_{i=1}^{5}F_i\,L_i^{\mu\nu}\,, \tag{4.4}$$

where the structures $L_i^{\mu\nu}$ are defined as

$$\begin{aligned}
L_1^{\mu\nu} &= q_1^\nu\,q_2^\mu-(q_1,q_2)\,g^{\mu\nu}\,,\\
L_2^{\mu\nu} &= \left(\Delta^2\,(q_1,q_2)-2\,(q_1,\Delta)\,(q_2,\Delta)\right)g^{\mu\nu}-\Delta^2\,q_1^\nu\,q_2^\mu-2\,(q_1,q_2)\,\Delta^\mu\,\Delta^\nu\\
&\quad+2\,(q_2,\Delta)\,q_1^\nu\,\Delta^\mu+2(q_1,\Delta)\,q_2^\mu\,\Delta^\nu\,,\\
L_3^{\mu\nu} &= (t-u)\Big\{\Big(Q_1^2\,(q_2,\Delta)-Q_2^2\,(q_1,\Delta)\Big)\left(g^{\mu\nu}-\frac{q_1^\nu q_2^\mu}{(q_1,q_2)}\right)\\
&\quad-\left(\Delta^\nu-\frac{(q_2,\Delta)\,q_1^\nu}{(q_1,q_2)}\right)\Big(Q_1^2q_2^\mu+q_1^\mu\,(q_1,q_2)\Big)\\
&\quad+\left(\Delta^\mu-\frac{(q_1,\Delta)\,q_2^\mu}{(q_1,q_2)}\right)\Big(Q_2^2\,q_1^\nu+q_2^\nu\,(q_1,q_2)\Big)\Big\}\,,\\
L_4^{\mu\nu} &= Q_1^2\,Q_2^2\,g^{\mu\nu}+Q_1^2\,q_2^\mu\,q_2^\nu+Q_2^2\,q_1^\mu\,q_1^\nu+q_1^\mu\,q_2^\nu\,(q_1,q_2)\,,\\
L_5^{\mu\nu} &= \Big(Q_1^2\,\Delta^\mu+(q_1,\Delta)\,q_1^\mu\Big)\Big(Q_2^2\,\Delta^\nu+(q_2,\Delta)\,q_2^\nu\Big)\,,
\end{aligned} \tag{4.5}$$

with $\Delta\equiv p_1-p_2$ and each $L_i^{\mu\nu}$ satisfies a gauge invariance constraint, i.e. $q_{1\mu}\,L_i^{\mu\nu}=q_{2\nu}\,L_i^{\mu\nu}=0$. The numbering of the Lorentz structures is chosen such that in the single virtual case only $L^{\mu\nu}_{1,2,3}$ contribute to the process [178] while in the real photon case only $L^{\mu\nu}_{1,2}$ are relevant, which coincide with the tensor structures used in [65, 206, 217]. The invariant amplitudes F_i are free from kinematic singularities or constraints and depend on the Mandelstam variables for the $\gamma^*\gamma^*\to\pi\pi$ subprocess, which we choose as (see App. 3.A)

$$s=(q_1+q_2)^2\,,\quad t=(p_1-q_1)^2\,,\quad u=(p_1-q_2)^2\,. \tag{4.6}$$

The prefactor $(t-u)$ in front of the tensor $L_3^{\mu\nu}$ is chosen so as to make all five amplitudes F_i even under pion and photon crossing symmetry $(t \leftrightarrow u)$ [209, 216].

The generalization of the Born contribution to the case of off-shell photons is performed by multiplying the scalar QED result by the electromagnetic pion (kaon) form factors $f_i(Q^2)$ [216, 218] which lead to the following invariant amplitudes

$$\begin{aligned} F_1^{\rm Born} &= -\frac{e^2\,(4\,m_i^2+Q_1^2+Q_2^2)}{(t-m_i^2)\,(u-m_i^2)}\,f_i(Q_1^2)\,f_i(Q_2^2)\,, \\ F_2^{\rm Born} &= -\frac{e^2}{(t-m_i^2)\,(u-m_i^2)}\,f_i(Q_1^2)\,f_i(Q_2^2)\,, \\ F_3^{\rm Born} &= F_4^{\rm Born} = F_5^{\rm Born} = 0\,, \end{aligned} \tag{4.7}$$

where $i=\pi\,(K)$ for $\gamma^*\gamma^*\to\pi\pi\;(K\bar{K})$. As these Born terms coincide with the pion pole terms obtained in a dispersive derivation, there is a full agreement between the results of [216, 218]. We note that the Born terms possess a double pole structure in the soft-photon limit, as a manifestation of Low's theorem [219].

The kinematic constraints can be obtained by analyzing projected helicity amplitudes in terms of the quantities (for $i=1,\ldots,5$)

$$A_i^J(s) = \frac{1}{(p\,q)^J}\int_{-1}^{1}\frac{dz}{2}P_J(z)\,F_i(s,t)\,, \tag{4.8}$$

which are free of any singularities due to the properties of the Legendre polynomials [211, 212]. In Eq. (4.8), q and p are initial and final relative momenta in the c.m. frame. Due to specifics of our basis (4.5) all the results below are given for the Born subtracted p.w. amplitudes

$$\bar{h}^{(J)}_{\lambda_1\lambda_2} \equiv h^{(J)}_{\lambda_1\lambda_2} - h^{(J),Born}_{\lambda_1\lambda_2}, \tag{4.9}$$

where for S-wave it holds [80, 184, 199]

$$\begin{aligned} &\bar{h}^{(0)}_{++}(s) \pm \bar{h}^{(0)}_{00}(s) \sim (s - s^{(\mp)}_{\rm kin})\,, \\ &s^{(\pm)}_{\rm kin} \equiv -\,(Q_1 \pm Q_2)^2\,, \end{aligned} \tag{4.10}$$

with $Q_i \equiv \sqrt{Q_i^2}$ $(i=1,2)$ and $s^{(\pm)}_{\rm kin}$ are pseudo-thresholds (see App. 4.A). Note that in the single virtual or real photon cases these constraints are required by the soft-photon theorem [219] and have been implemented already in [120, 121, 209, 220, 221]. The kinematically uncorrelated amplitudes for the s-wave can be obtained by dividing left-hand side (l.h.s.) of Eq. (4.10) by its right-hand side (r.h.s.)

$$\bar{h}^{(0)}_{i=1,2}(s) = \frac{\bar{h}^{(0)}_{++}(s) \pm \bar{h}^{(0)}_{00}(s)}{s - s^{(\mp)}_{\rm kin}}\,. \tag{4.11}$$

In [178] the kinematically unconstrained basis of the partial wave amplitudes were derived

for the single virtual case. Below we extend this result for the double-virtual case for $J = 2$,

$$
\begin{aligned}
&(s + Q_1^2 + Q_2^2)\, \bar{h}^{(2)}_{+-} + 2\sqrt{2} Q_1^2 Q_2^2\, \bar{h}_- \sim \gamma_1(s)\,, \\
&\sqrt{2}\, \bar{h}^{(2)}_{+-} - \bar{h}_+ + \left(Q_1^2 + Q_2^2\right)\, \bar{h}_- \sim \gamma_1(s)\,, \\
&\sqrt{2}\, \bar{h}^{(2)}_{+-} + \left(s + Q_1^2 + Q_2^2\right)\, \bar{h}_- \sim \gamma_1(s)\,, \\
&\sqrt{6}\, s\, \bar{h}^{(2)}_{+-} - 2\sqrt{3}\, s\, \bar{h}_+ + 3\, s\, (s + Q_1^2 + Q_2^2)\, \bar{h}_0 + 6\, s\, \bar{h}^{(2)}_{++} \\
&\quad + \sqrt{3}\left(s^2 + 2\left(Q_1^2 + Q_2^2\right) s - \left(Q_1^2 - Q_2^2\right)^2\right)\, \bar{h}_- \sim \gamma_2(s)\,, \\
&6s\, (s + Q_1^2 + Q_2^2)\, \bar{h}^{(2)}_{++} + 12\, Q_1^2\, Q_2^2\, s\, \bar{h}_0 \\
&\qquad - \sqrt{6}\left(s\, (Q_1^2 + Q_2^2) + (Q_1^2 - Q_2^2)^2\right)\, \bar{h}^{(2)}_{+-} \\
&\qquad + 2\sqrt{3}\left(s\, (Q_1^2 + Q_2^2) + (Q_1^2 - Q_2^2)^2\right)\, \bar{h}_+ \\
&\qquad - 2\sqrt{3}\left(Q_1^2 - Q_2^2\right)^2\, (s + Q_1^2 + Q_2^2)\, \bar{h}_- \sim \gamma_2(s)\,,
\end{aligned}
\tag{4.12}
$$

with auxiliary factor $\gamma_n(s)$ defined as

$$
\gamma_n(s) \equiv \lambda^n(s, -Q_1^2, -Q_2^2)\, (s - 4\, m_\pi^2)\,, \tag{4.13}
$$

where λ is the Källén triangle function and $\bar{h}_{+,-,0}$ were introduced for convenience

$$
\begin{aligned}
\bar{h}_+(s) &\equiv \frac{\sqrt{s}}{Q_2}\, \bar{h}^{(2)}_{+0}(s) + \frac{\sqrt{s}}{Q_1}\, \bar{h}^{(2)}_{0+}(s), \\
\bar{h}_-(s) &\equiv \left(\frac{\sqrt{s}}{Q_2}\, \bar{h}^{(2)}_{+0}(s) - \frac{\sqrt{s}}{Q_1}\, \bar{h}^{(2)}_{0+}(s)\right) \frac{1}{Q_1^2 - Q_2^2}\,, \\
\bar{h}_0(s) &\equiv \frac{\bar{h}^{(2)}_{00}(s)}{Q_1\, Q_2}\,.
\end{aligned}
\tag{4.14}
$$

We emphasize that in addition to the $s^{(\pm)}_{\rm kin}$ points the p.w. amplitudes for $J \neq 0$ exhibit a so-called centrifugal barrier factor at $4\, m_\pi^2$, which comes from the properties of the Legendre polynomials entering p.w. expansion Eq. 4.2. The new set of amplitudes $\bar{h}^{(2)}_{i=1..5}(s)$ can be obtained similar to (4.11) by dividing l.h.s. of Eq. (4.12) by its r.h.s.[1] We emphasize, that Eq. (4.12) shows the correlation of the p.w helicity amplitudes explicitly, as compared to the result based on the Roy-Steiner equations [183, 210], where kinematic constraints are contained in the integral kernels. The full set of these off-diagonal kernels is given in [210], and the final solution is obtained by diagonalization of the kernel matrix.

4.2.3 Dispersion relations for the $\gamma^{(*)}\gamma^{(*)} \to \pi\pi$ system

The new set of amplitudes $\bar{h}^{(J)}_{1-5}$ contains only dynamical singularities. These are right and left-hand cuts and one can write a dispersion relation in the following form (modulo subtractions which will be discussed in Sec. 4.3)

$$
\bar{h}_i^{(J)}(s) = \int_{-\infty}^{0} \frac{ds'}{\pi} \frac{\mathrm{Disc}\, \bar{h}_i^{(J)}(s')}{s' - s} + \int_{4m_\pi^2}^{\infty} \frac{ds'}{\pi} \frac{\mathrm{Disc}\, h_i^{(J)}(s')}{s' - s}\,, \tag{4.15}
$$

[1] Note that when $Q_1^2 = Q_2^2$ (and pions in the final state) special care is required. In that case, $H_{+0} = -H_{0+}$ and only four Lorentz tensors in (4.5) are independent. Therefore one needs to reshuffle Eq. (4.12) in such a way that only four amplitudes $\bar{h}_i^{(J)}$ survive. We checked that numerically the results for $Q_1^2 \approx Q_2^2$ given by (4.12) are consistent with the strict $Q_1^2 = Q_2^2$ limit.

where we used that $\text{Disc}\,\bar{h}_i^{(J)}(s) = \text{Disc}\,h_i^{(J)}(s)$ along the right-hand cut. The latter is determined by the unitarity condition and in the elastic approximation is given by

$$\begin{aligned} \text{Disc}\,h_i^{(J)}(s) &= t^{(J)*}(s)\,\rho(s)\,h_i^{(J)}(s)\,, \\ \rho(s) &= \frac{p(s)}{8\,\pi\sqrt{s}}\,\theta(s-4\,m_\pi^2)\,, \end{aligned} \tag{4.16}$$

where $\rho(s)$ is a two-body phase space factor and $t^{(J)}(s)$ is the hadronic scattering amplitude, which is normalized as $\text{Im}(t^{(J)})^{-1} = -\rho$. For the energy region above 1 GeV, it is necessary to take into account the inelasticity. The first relevant inelastic channel is $K\bar{K}$ which is required to capture the dynamics of the $f_0(980)$ scalar meson (see Sec. 3.3.3). For the coupled-channel case, the phase-space function $\rho(s)$ and the amplitude $t^{(J)}(s)$ turn into (2×2) matrices, while $h_i^{(J)}$ will be written in the (2×1) form with elements $h_i^{(J)}$ and $k_i^{(J)}$ which correspond to $\gamma^*\gamma^* \to \pi\pi$ and $\gamma^*\gamma^* \to K\bar{K}$ amplitudes, respectively. The solution to Eq. (5.2) is given by the well known Muskhelishvili-Omnès (MO) method for treating the final-state interactions [58]. It is based on writing a dispersion relation for $\bar{h}_i^{(J)}(\Omega^{(J)})^{-1}$ [119], where the Omnès function $\Omega^{(J)}$ satisfies a similar unitarity constraint

$$\text{Disc}\,\Omega^{(J)}(s) = t^{(J)}(s)\,\rho(s)\,\Omega^{(J)*}(s)\,. \tag{4.17}$$

In result we obtain,

$$\begin{aligned} h_i^{(J)}(s) = h_i^{(J),\text{Born}}(s) + \Omega^{(J)}(s)\Big[&- \int_{4m_\pi^2}^{\infty} \frac{ds'}{\pi}\,\frac{\text{Disc}\,(\Omega^{(J)}(s'))^{-1}\,h_i^{(J),\text{Born}}(s')}{s'-s} \\ &+ \int_{-\infty}^{0} \frac{ds'}{\pi}\,\frac{(\Omega^{(J)}(s'))^{-1}\,\text{Disc}\,\bar{h}_i^{(J)}(s')}{s'-s}\Big]\,, \end{aligned} \tag{4.18}$$

which can be straightforwardly generalized for the coupled-channel case. The Born subtracted amplitudes along the left-hand cut (second term inside the brackets) are given by multi-pion exchanges in the t and u channels which in practice can be approximated by resonance (R) exchanges [119]. The dominant contribution is generated by vector mesons ω and ρ. The contribution from other heavier resonances will be absorbed in an effective way by allowing for a slight adjustment of the $VP\gamma$ coupling [178]. We also note that the double pole structure of the Born amplitudes does not bring an extra complication to Eq. (4.18), since its singularities lie outside of the physical region.

Here we note that there is a freedom of writing the dispersion relation. In principle, one could write a dispersion relation for the combination $(\bar{h}_i^{(J)} - h_i^{(J),V})(\Omega^{(J)})^{-1}$ as it was done for $\gamma\gamma^* \to \pi\pi$ in [209]. However, in this case one needs to make an assumption on the high-energy dependence of the real part of $h_i^{(J),V}$, as was explained in [210]. In the present work, we only take out the Born term in Eg. (4.18), and therefore only need to know the high-energy behavior of the imaginary part of the vector mesons exchange entering the left-hand cut, which does not have any polynomial ambiguities [119].

4.2.4 Left-hand cuts

The vector-meson exchange left-hand cuts are obtained by the effective Lagrangian which couples photon, vector (V) and pseudoscalar (P) meson fields,

$$\mathcal{L}_{VP\gamma} = e\,C_{VP\gamma}\,\epsilon^{\mu\nu\alpha\beta}\,F_{\mu\nu}\,\partial_\alpha P\,V_\beta\,, \tag{4.19}$$

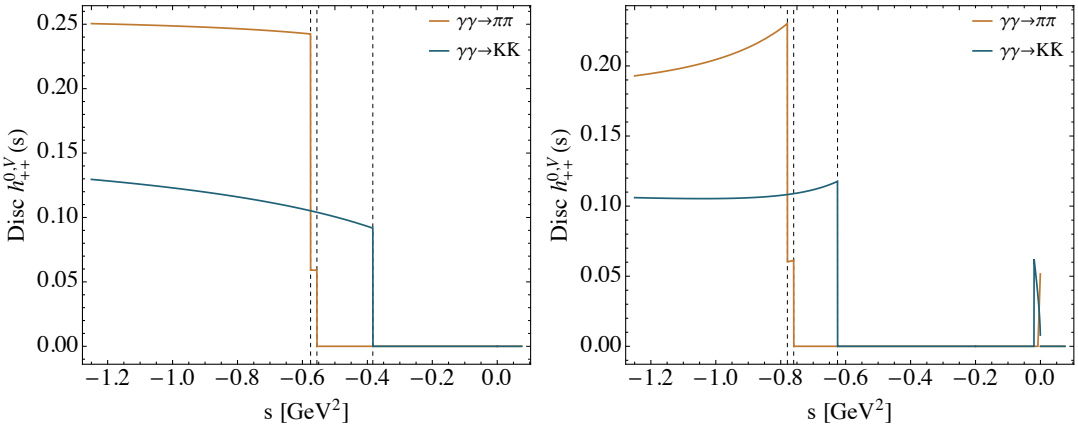

Figure 4.2: The behaviour of the vector-meson exchange amplitudes $h_{++}^{0,V}(s)$ and $k_{++}^{0,V}(s)$ for $\gamma\gamma^{(*)} \to \pi\pi(K\bar{K})$ process. Left panel: $Q_1^2 = Q_2^2 = 0$ GeV^2, right panel $Q_1^2 = 0, Q_2^2 = 0.2$ GeV^2. The dashed lines indicate the closest $s_L^{(-)}$ corresponding to ρ, ω and K^* meson masses. Note the additional l.h.c. piece close to zero for the single-virtual case.

where $F_{\mu\nu} = \partial_\mu A_\nu - \partial_\nu A_\mu$. This Lagrangian density implies

$$
\begin{aligned}
F_1^{V\text{exch}} &= -\sum_V \frac{e^2\, C_{VP\gamma}^2}{2} \left(\frac{4\,t + Q_1^2 + Q_2^2}{t - m_V^2} + \frac{4\,u + Q_1^2 + Q_2^2}{u - m_V^2} \right) \tilde{f}_{V,i}(Q_1^2, Q_2^2)\,, \\
F_2^{V\text{exch}} &= \sum_V \frac{e^2\, C_{VP\gamma}^2}{2} \left(\frac{1}{t - m_V^2} + \frac{1}{u - m_V^2} \right) \tilde{f}_{V,i}(Q_1^2, Q_2^2)\,, \\
F_3^{V\text{exch}} &= \sum_V \frac{e^2\, C_{VP\gamma}^2}{t - u} \left(\frac{1}{u - m_V^2} - \frac{1}{t - m_V^2} \right) \tilde{f}_{V,i}(Q_1^2, Q_2^2)\,, \\
F_4^{V\text{exch}} &= \sum_V e^2\, C_{VP\gamma}^2 \left(\frac{1}{t - m_V^2} + \frac{1}{u - m_V^2} \right) \tilde{f}_{V,i}(Q_1^2, Q_2^2)\,, \\
F_5^{V\text{exch}} &= 0\,,
\end{aligned}
\tag{4.20}
$$

where we defined

$$
\tilde{f}_{V,i}(Q_1^2, Q_2^2) \equiv f_{V,i}(Q_1^2)\, f_{V,i}(Q_2^2)\,, \tag{4.21}
$$

The couplings C_V can be extracted from the experimentaly measured width of vector meson radiative decays:

$$
\Gamma_{VP\gamma} = \frac{e^2 C_V^2 (m_V^2 - m_P^2)^3}{24\pi m_V^3}\,. \tag{4.22}
$$

In the following we will use the modulus of the radiative couplings arising from the SU(3) relations

$$
g_{VP\gamma} \simeq C_{\rho^{\pm,0}\pi^{\pm,0}\gamma} \simeq C_{\omega\pi^0\gamma}/3\,, \tag{4.23}
$$

as the only fit parameter, as discussed in [178], yielding $g_{VP\gamma} = 0.33$ GeV^{-1}. This value lies within 10% with the PDG average $g_{VP\gamma}^{\text{PDG}} = 0.37(2)$ GeV^{-1} [27], thus justifying the approximation of left-hand cuts by vector mesons. The slight difference accounts for the contribution from other heavier left-hand cuts, which in general should be taken into account by imposing Regge asymptotics. Such a study is however beyond the scope of the present analysis. In Eq. (4.21) $f_{V,\pi}(Q_i^2)$ are vector meson transition form factors, which will be discussed in the next section.

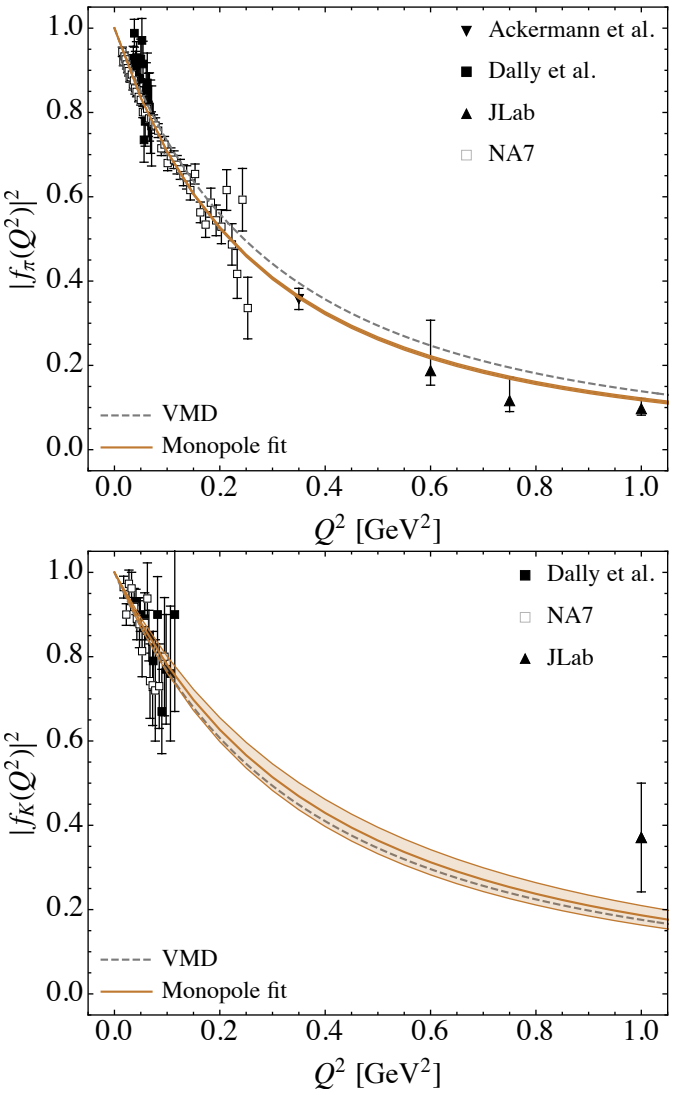

Figure 4.3: Comparison of the pion (upper panel) and kaon (lower panel) form factors from VMD prediction (dashed line) and simple monopole fits (solid line) to the available data from [222–224] and [225–227] respectively. See text for the details.

In Fig. 4.2 we illustrate the behaviour of the vector-meson exchange amplitude $h_{++}^{0,V}(s)$ for both real and a single-virtual case with $Q_2^2 = 0.2$ GeV^2. Note that in the single-virtual case, the additional piece appears close to the threshold. In the double-virtual case, the analytical structure of the vector-meson left-hand cuts is even more complicated. We will discuss it in details in Sec. 4.2.6 and App. 4.A.

4.2.5 Pion, kaon and vector mesons form factors

As mentioned in the previous section, in order to account for the finite virtuality of the photon, the Born l.h.c. should be multiplied by the electromagnetic pion (kaon) form factor. In the space-like region $q^2 = -Q^2 < 0$ pion and kaon form factors in the are defined as [218]

$$\begin{aligned}\langle \pi^+(p')|j_\mu(0)|\pi^+(p)\rangle &= e\,(p+p')_\mu\, f_\pi\left((p'-p)^2\right)\,,\\ \langle K^+(p')|j_\mu(0)|K^+(p)\rangle &= e\,(p+p')_\mu\, f_K\left((p'-p)^2\right)\,.\end{aligned} \tag{4.24}$$

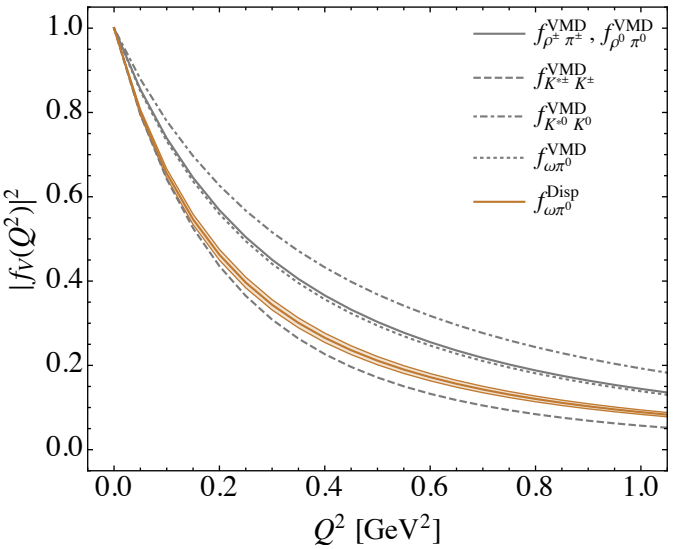

Figure 4.4: Comparison of the vector meson form factors from VMD predictions and the dispersive estimation of $\omega\pi^0$ form factor [228]. See text for the details.

To evaluate them in the region of $Q^2 \lesssim 1$ GeV^2 we improve the *vector meson dominance* (VMD) [229] prediction by performing the simple monopole fits

$$\begin{aligned} f_\pi(Q^2) &= \frac{1}{1+Q^2/m_\rho^2} \to \frac{1}{1+Q^2/\Lambda_\pi^2}\,, \\ f_K(Q^2) &= \frac{1/2}{1+Q^2/m_\rho^2} + \frac{1/6}{1+Q^2/m_\omega^2} + \frac{1/3}{1+Q^2/m_\phi^2} \to \frac{1}{1+Q^2/\Lambda_K^2}\,. \end{aligned} \tag{4.25}$$

to the available data from [222–224] and [225–227] respectively, with the following parameters $\Lambda_\pi = 0.727(5)$ GeV with $\chi^2/\text{d.o.f} = 1.22$ and $\Lambda_K = 0.872(47)$ GeV with $\chi^2/\text{d.o.f} = 0.69$ (see Fig. 4.3)

For the vector meson contribution the vertex function is given as

$$\langle V(k,\lambda)|j_\mu(0)|\pi(p)\rangle \;=\; 2\,e\,C_{VP\gamma}\,f_{V,\pi}(Q^2)\,\epsilon_{\mu\alpha\beta\gamma}\,k^\alpha\,p^\beta\,\epsilon^{\gamma*}(k,\lambda)\,, \tag{4.26}$$

and VMD predicts following transition form factors (TFF):

$$\begin{aligned} f_{\omega\pi^0}(Q^2) &= \frac{1}{1+Q^2/m_\rho^2}\,, \\ f_{\rho^0\pi^0}(Q^2) &= f_{\rho^\pm\pi^\pm}(Q^2) = \frac{1}{1+Q^2/m_\omega^2}\,, \\ f_{K^{*\pm}K^\pm}(Q^2) &= \frac{3/2}{1+Q^2/m_\rho^2} + \frac{1/2}{1+Q^2/m_\omega^2} + \frac{1}{1+Q^2/m_\phi^2}\,, \\ f_{K^{*0}K^0}(Q^2) &= \frac{3/4}{1+Q^2/m_\rho^2} + \frac{1/4}{1+Q^2/m_\omega^2} + \frac{1/2}{1+Q^2/m_\phi^2}\,. \end{aligned} \tag{4.27}$$

Unfortunately, for the vector meson TFF there is no data available in the spacelike region. For the transition form factor $f_{\omega,\pi}(Q^2)$ we use the dispersive analysis from [228] (see also [230]), while for the TFF $f_{\rho\pi}(Q^2)$ the VMD model from Eq. (4.27) is used. We note, that in the time-like region, $Q^2 < 0$, more complicated parametrizations are needed.

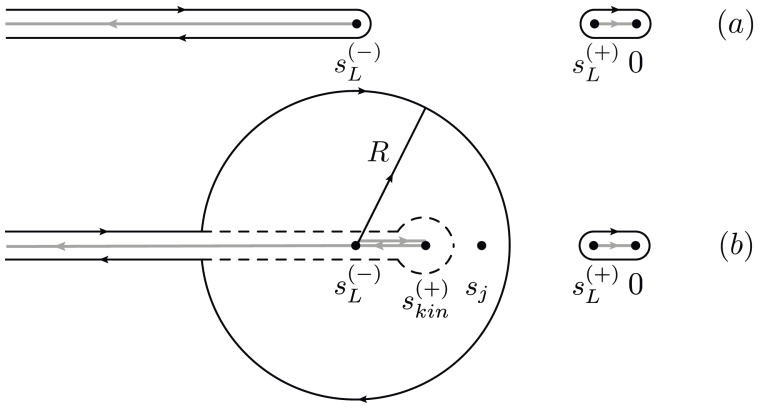

Figure 4.5: Left-hand cut singularities and the integration contour for non-anomaly case (a) and its deformation for the anomaly case (b). See text for details.

4.2.6 Analytic structure of the left-hand cuts

In order to find a solution of the dispersion relations given in (4.18), one needs to understand the singularity structure of the p.w. amplitudes $h_i^{(J)}$ as a function of the complex variable s. For the space-like photons the p.w. Born amplitudes are real functions above the threshold and do not bring any complexity. On the other hand, the vector-meson exchange left-hand cut is determined by four branching points: $s = 0$, $s = -\infty$ and

$$s_L^{(\pm)} = \frac{1}{2}(2m_\pi^2 - Q_1^2 - Q_2^2 - m_V^2 - \frac{(m_\pi^2+Q_1^2)(m_\pi^2+Q_2^2)}{m_V^2}) \\ \pm \frac{\lambda^{1/2}(m_V^2, m_\pi^2, -Q_1^2)\,\lambda^{1/2}(m_V^2, m_\pi^2, -Q_2^2)}{2\,m_V^2}\,. \tag{4.28}$$

When one photon is real, the cut consists of two pieces: $(-\infty, s_L^{(-)}]$ and $[s_L^{(+)}, 0]$. However, when both photons carry a space-like virtuality, one has to be careful, since for $Q_1^2\,Q_2^2 > (m_V^2 - m_\pi^2)^2$ the left-hand branch point $s_L^{(-)}$ moves to the right and reaches the pseudo-threshold point $s_{\rm kin}^{(+)}$ and only then moves to the left (see Fig. 4.5). In this case the integration along the cut acquires an additional piece $[s_L^{(-)}, s_{\rm kin}^{(+)}]$ which is related to an "anomalous" discontinuity [136, 231]. In addition, the integral around $s_{\rm kin}^{(+)}$, in general, is non-zero and requires a special care [210]. Indeed, according to (4.12), the $J = 2$ p.w. amplitude schematically

$$h^V(s) = \frac{1}{\left(s - s_{\rm kin}^{(+)}\right)^2} \int_{-1}^{1} \frac{z^4\,dz}{t(s,z) - m_V^2}\,, \tag{4.29}$$

behaves like $\left(s - s_{\rm kin}^{(+)}\right)^{-9/2}$. Splitting the contour path into an integral up to $s_{\rm kin}^{(+)} - \epsilon$ and a circular integral of radius ϵ around $s_{\rm kin}^{(+)}$ (dashed curve in Fig. 4.5) produces the cancellation of two singular pieces. In [210], this was solved by using a fit function (which consists of an appropriate square-root-like behavior and a polynomial) in the vicinity of the singular point. We follow here a different strategy and enlarge the contour around $s_{\rm kin}^{(+)}$ such that one stays away from possible numerical issues related to the anomaly piece (see Fig. 4.5). We propose

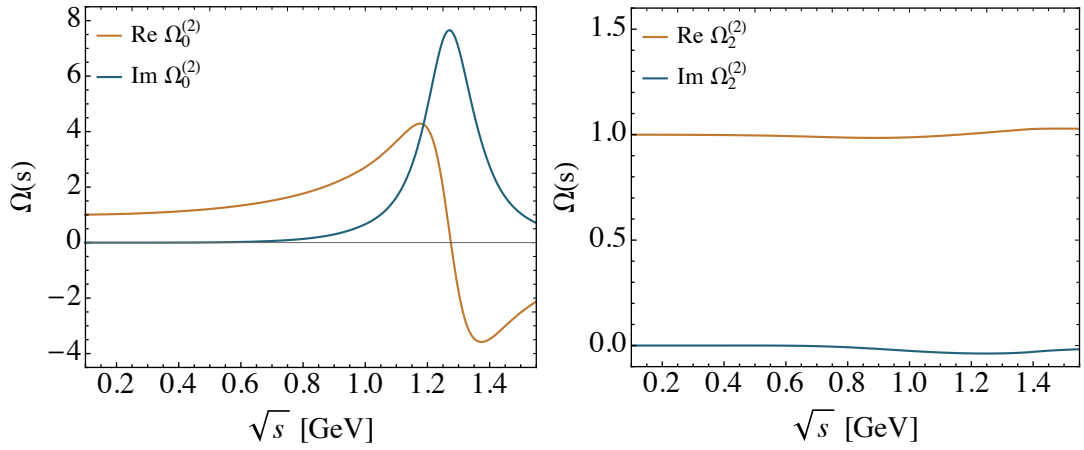

Figure 4.6: Omnès functions for $J = 2, I = 0$ (left panel) and $J = 2, I = 2$ (right panel) using the parametrization of Eq. (4.31). See text for the details.

to present $h^V(s)$ in the physical region as

$$h^V(s) = \int_{-\infty}^{s_L^{(-)}-R} \frac{d\,s'}{\pi} \frac{\mathrm{Disc}\, h^V(s')}{s'-s} + \int_{C_R} \frac{d\,s'}{2\pi i} \frac{h^V(s')}{s'-s} + \int_{s_L^{(+)}}^{0} \frac{d\,s'}{\pi} \frac{\mathrm{Disc}\, h^V(s')}{s'-s}\,, \tag{4.30}$$

where R is chosen such that $s_j = -Q_1^2 - Q_2^2 + 2\,m_\pi^2 - 2\,m_V^2$ lies inside the circle. The location of s_j is determined by the condition that the imaginary part of the logarithm in (4.29) changes sign and therefore requires a proper choice of the Riemann sheet which we want to avoid. The merit of (4.30) is such that it works for both anomaly and non-anomaly cases, so one can use it for any space-like Q_i including the "transition" line when $Q_1^2\,Q_2^2 = (m_V^2 - m_\pi^2)^2$. In addition, it is independent on the degree of singularity and can be used equally well for higher p.w. with $J > 2$. The generalization to the physical case with Omnès functions (4.18) is then straightforward since all of the quantities are well defined at complex energies.

We also propose an alternative approach of treating the anomalous threshold problem. The details of this approach and the anomalous threshold problem itself can be found in App. 4.A. For time-like virtualities (which are not of interest in the present work) we refer the reader to [209, 232] where different cases of overlapping left- and right-hand cuts are considered.

4.2.7 Hadronic input

For the hadronic input, we are implementing the results presented in the Chapter 3. For the S-wave isospin $I = 0$ amplitude, we use the coupled-channel Omnès function, discussed in Sec. 3.3.3 and for the $I = 2$ we use the single-channel result from Sec. 3.3.4. For the D-wave $I = 0, 2$ amplitudes we use the single-channel Omnès function in terms of the corresponding phase shifts,

$$\Omega_I^{(2)}(s) = \exp\left(\frac{s}{\pi}\int_{4m_\pi^2}^{\infty} \frac{ds'}{s'}\frac{\delta_I^{(2)}(s')}{s'-s}\right). \tag{4.31}$$

Its numerical evaluation requires a high-energy parametrization of the phase shifts. We use a recent Roy analysis [100] below 1.42 GeV, and let the phase smoothly approach π (0) for $I = 0$ ($I = 2$) respectively. The resulting Omnès functions are shown in Fig. 4.6

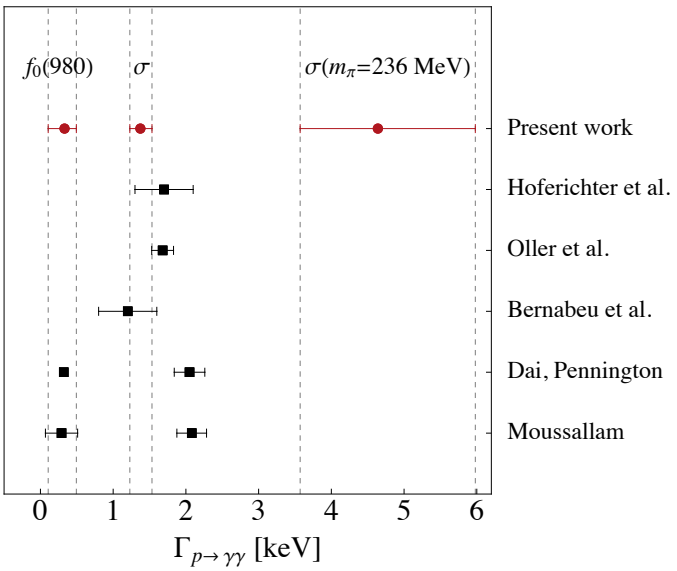

Figure 4.7: Two-photon decay width of $\sigma/f_0(500)$ and $f_0(980)$ compared to the recent dispersive estimations from [87, 120, 208, 221, 233].

4.3 Numerical results

The constructed set of dispersion relations allows us to evaluate many physical quantities of interest. Unfortunately, as we mentioned in Sec. 4.1 it is possible to confront the obtained results directly with the data only in a limited number of scenarios. In some other cases, the χPT calculations are readily available for comparison, but they have a minimal range of validity in terms of the photon virtuality. Therefore, the major part of this section is dedicated to the different predictions for the processes with virtualities not yet accesible by the experiment or other models.

This section is organized as following. We first consider the case when both photons are real, which allows to extract the two-photon couplings of the $\sigma/f_0(500)$ and $f_0(980)$ resonances. In Sec. 4.3.2 we discuss the pion dipole polarizabilities which are related to the subtraction constants in the dispersion relation. We will compare the S-wave results for unsubtracted and once-subtracted versions of the dispersion relation for real and single-virtual cases, and will try to understand the discrepancy between the obtained value for neutral pion dipole polarizability and the NLO χPT prediction. Finally, in Sec. 4.3.3 we will provide the total and differential cross sections. For the real case we will also compare the results to the available experimental data.

4.3.1 Two-photon couplings of $\sigma/f_0(500)$ and $f_0(980)$

As an application of the Omnès functions obtained in Sec. 3.3 and the $\gamma\gamma \to \pi\pi$ amplitude $h^{(0)}_{0,++}(s)$, we would like to extract the two-photon couplings of $\sigma/f_0(500)$ and $f_0(980)$. In principle, the coupling to the external currents has the potential to infer the scalar meson composition. Furthermore, it characterizes the interaction strength of $\sigma/f_0(500)$ and $f_0(980)$ in the two-photon channel. The latter is important for the light-by-light sum rule applications [186, 234–236] and serves as a key input to estimate the isoscalar two-pion (kaon) contribution to the HLbL scattering for $(g-2)_\mu$. The central result in this section will be obtained using a coupled-channel dispersive representation, however, for $\sigma/f_0(500)$ we will employ as well the single-channel representation both for physical and non-physical pion masses.

$\lvert g_{p\gamma\gamma}\rvert$, GeV		
$\sigma/f_0(500)$		
Exp., SC	$5.6(1)(0)\cdot 10^{-3}$	$6.1(7)\cdot 10^{-3}$ [120]
Exp., CC	$5.6(2)^{+0.1}_{-0.1}\cdot 10^{-3}$	
Latt., 236	$10.7(9)^{+0.1}_{-0.1}\cdot 10^{-3}$	
$f_0(980)$		
Exp., CC	$4.0(8)^{+0.3}_{-1.1}\cdot 10^{-3}$	$3.8(1.4)\cdot 10^{-3}$[87]

Table 4.3: Two photon couplings of the $\sigma/f_0(500)$ and $f_0(980)$ resonances calculated in the data-driven N/D approach compared with the result of Roy-like analyses. SC and CC stand for single- and coupled-channel analyses, respectively. In our results, the first error is the statistical one, while the second one comes from a variation of s_E and has a systematic nature (see Sec. 3.2 for the details).

The two-photon couplings are extracted by calculating the residue of $h^{(0)}_{0,++}(s)$ at the pole positions, s_p. Following [207, 237], in our convention it is given by

$$\frac{g^2_{p\gamma\gamma}}{g^2_{p\pi\pi}} = -\left(\rho_0(s_p)\, h^{(0)}_{0,++}(s_p)\right)^2 , \tag{4.32}$$

where $h^{(0)}_{0,++}(s)$ is evaluated on the first Riemann sheet for $p=\sigma/f_0(500)$, $f_0(980)$. An intuitive way of re-expressing the two-photon couplings, shown in Table 4.3, is by using the formal definition of the corresponding two-photon decay widths

$$\Gamma_{p\to\gamma\gamma} = \frac{|g_{p\gamma\gamma}|^2}{16\,\pi\,\mathrm{Re}\sqrt{s_p}} , \tag{4.33}$$

where the pole positions s_p for each case are listed in Sec. 3.3. Converted to (4.33), our results read

$$\begin{aligned} \Gamma_{\sigma\to\gamma\gamma} &= 1.37(13)^{+0.09}_{-0.06}\,\left[1.38(9)^{+0.01}_{-0.01}\right]\ \text{keV}, \\ \Gamma_{f_0(980)\to\gamma\gamma} &= 0.33(16)^{+0.04}_{-0.16}\,\text{keV}, \\ \Gamma^{m_\pi=236\,\text{MeV}}_{\sigma\to\gamma\gamma} &= 4.64(1.01)^{+0.88}_{-0.35}\,\text{keV}, \end{aligned} \tag{4.34}$$

where in square brackets the single-channel approximation is shown. As expected, its $\Gamma_{\sigma\to\gamma\gamma}$ is almost indistinguishable from the coupled-channel case. In Fig. 4.3 we compare our results with the recent dispersive estimates [87, 120, 208, 221, 233]. While the two-photon decay width of $f_0(980)$ is consistent with the coupled-channel amplitude analysis of [221] and the over-subtracted coupled-channel Muskhelishvili-Omnès analysis [87], the two-photon width of $\sigma/f_0(500)$ is about 25% smaller than their values. On the other hand, the obtained two-photon width of $\sigma/f_0(500)$ is consistent with the sophisticated Roy-Steiner analysis [120] and other dispersive analyses from [208, 233]. Finally, we also predicted $\sigma/f_0(500)$ two-photon coupling/width for the unphysical $m_\pi = 236$ MeV, which would be interesting to confront with the direct lattice calculations.

We note, that the errors quoted in Eq. (4.34) correspond solely to the uncertainties in the Omnès matrix. In principle, one can perform a more comprehensive study of the theoretical uncertainties, by the inclusion of more distant left-hand cuts in $\gamma\gamma\to\pi\pi(K\bar{K})$. This would

	$(\alpha_1-\beta_1)_{\pi^\pm}\times 10^4$, fm^3			$(\alpha_1-\beta_1)_{\pi^0}\times 10^4$, fm^3		
cut-off, GeV^2	$-\infty$	-10	-1	$-\infty$	-10	-1
π		4.8			7.9	
ρ	-4.5	-3.8	-1.4	-4.5	-3.8	-1.4
ω	-9.6	-7.6	-2.2	-21.7	-19.3	-7.8
total	-9.2	-6.5	1.3	-18.3	-15.2	-1.3
NLO χPT		6.0			-1.0	
Experiment		$4.0(1.2)_{\rm stat}(1.4)_{\rm syst}$				

Table 4.4: Different contributions to the dipole polarizabilities of pion extracted from the dispersive sum rule in comparison with the NLO χPT prediction and the recent COMPASS measurement for the charged case [238]. See text for the details.

require introducing subtraction constants which can be either fixed from the pion dipole polarizabilities or fitted directly to the cross-section data . We will discuss this choice in details in the next sections. Doing so would likely enlarge the error, but we do not expect a significant change of the central values, since the current description of the cross-section data, which is parameter-free in the S-wave (see Sec. 4.3.3), is quite impressive.

4.3.2 Pion dipole polarizabilities

The Born-subtracted S-wave amplitude of the process $\bar{h}^{(0)}_{I,++}$ is related to the generalized dipole polarizability of the pion $(\alpha_1-\beta_1)_\pi$ as

$$\bar{h}^{(0)}_{I,++}(s,Q^2) = 2\,\pi\, m_\pi (\alpha_1-\beta_1)^I_\pi\,(s+Q^2) + \dots\,. \tag{4.35}$$

Re-expressing Eq. (4.18) in terms of the helicity amplitudes leads to the following sum rule for the generalized dipole polarizability

$$(\alpha_1-\beta_1)^I_\pi = \frac{\Omega^{(0)}_I(-Q^2)}{2\,\pi\, m_\pi}\Big[\int_{-\infty}^{0}\frac{ds'}{\pi}\,\frac{(\Omega^{(0)}_I(s'))^{-1}\,\mathrm{Disc}\,\bar{h}^{(0)}_{I,++}(s')}{(s'+Q^2)^2} - \int_{4m_\pi^2}^{\infty}\frac{ds'}{\pi}\,\frac{\mathrm{Disc}\;(\Omega^{(0)}_I(s'))^{-1}\,h^{(0),\mathrm{Born}}_{I,++}(s')}{(s'+Q^2)^2}\Big]\,. \tag{4.36}$$

Similar to [80] we calculated the dipole polarizabilities of charged and neutral pions $(\alpha_1-\beta_1)_\pi$, as shown in (4.35). Unsubtracted dispersion relations allow us to extract the following charged pion dipole polarizability: $(\alpha_1-\beta_1)_{\pi^\pm} = 4.8\times 10^{-4}$ fm^3, which is consistent with NLO χPT $(\alpha_1-\beta_1)^{\chi\rm PT}_{\pi^\pm} = 6.0\times 10^{-4}$ fm^3 and with the recent COMPASS measurement: $(\alpha_1-\beta_1)^{\rm exp}_{\pi^\pm} = 4.0(1.2)_{\rm stat}(1.4)_{\rm syst}\times 10^{-4}$ fm^3 [238]. For the neutral pion dipole polarizability we obtain $(\alpha_1-\beta_1)_{\pi^0} = 7.9\times 10^{-4}$ fm^3, thus being far from the NLO χPT value of $(\alpha_1-\beta_1)^{\chi\rm PT}_{\pi^0} = -1.0\times 10^{-4}$ fm^3.

Even though the charged channel is the dominant one, the question might arise of how suitable the current input is when estimating $(g-2)_\mu$. The neutral pion dipole polarizability discrepancy may have origin in the correction from heavier l.h.c., i.e. the first term in Eq. (4.36). The dominant l.h.c beyond the pion pole comes from vector meson t- and u-channel exchanges. Since they are much stronger for the neutral channel due to ω-exchange, the π^0 polarizabilities are expected to get large corrections [80]. Even though the dispersive integral is formally convergent due to the asymptotically bounded behavior of our Omnès function and

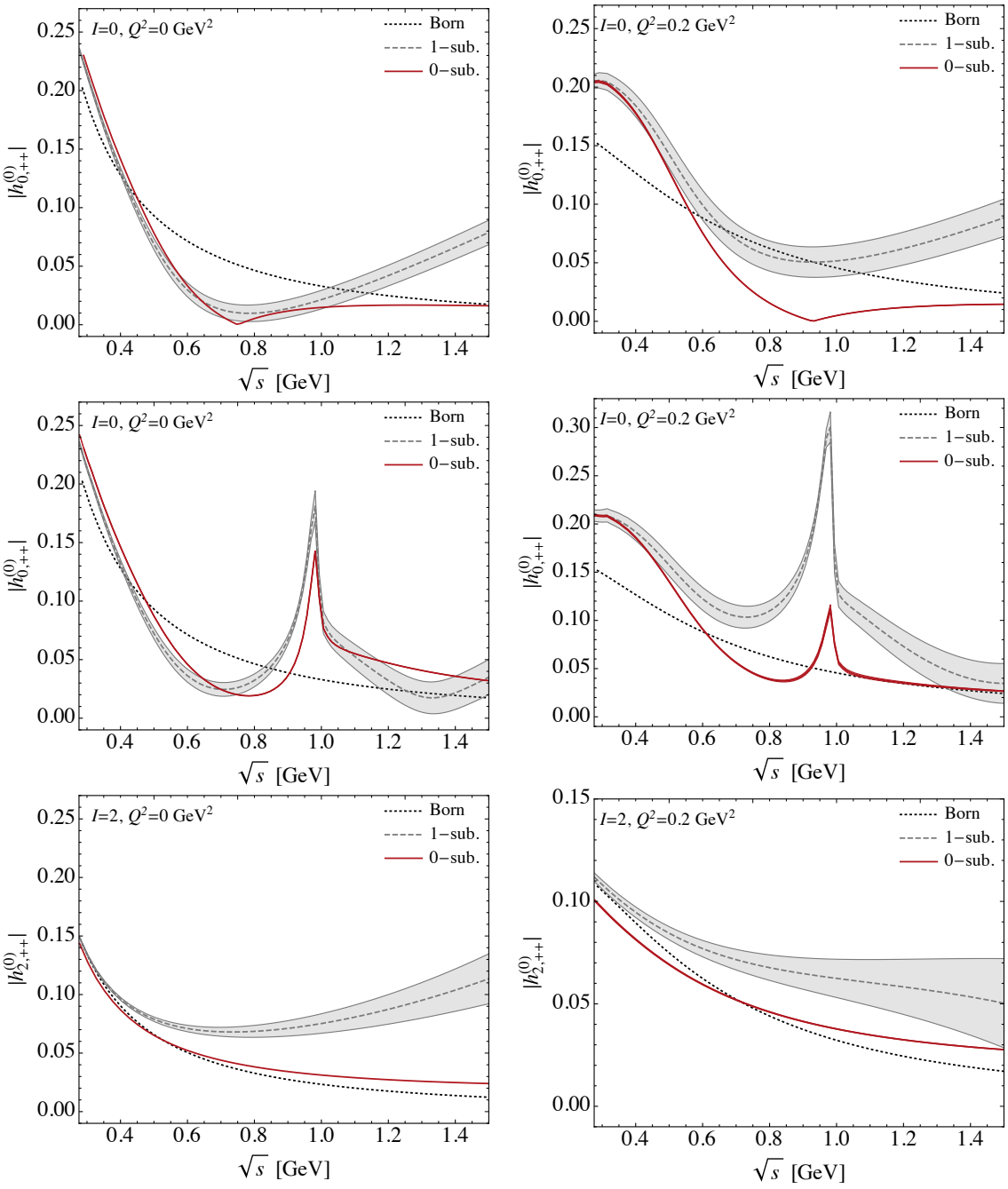

Figure 4.8: Comparison of the p.w. amplitudes $|h^{(0)}_{I,++}|$ for once-subtracted (dashed line) and unsubtracted (solid line) dispersion relations; Born results are shown by the dotted lines. First row: $I = 0$, single channel; second row: $I = 0$, coupled-channel; third row: $I = 2$, single channel.

the discontinuity of the amplitude $\bar{h}^0_{I,++}$, it acquires significant corrections from the integration over large negative s. In the Table 4.4 we show the contributions from π, ρ and ω to both charged and neutral pion polarizabilities. The second term in (4.36) corresponds to the pure π contribution. For the ρ and ω contributions we study also the dependence on the left-hand cut cut-off, or the integration limit in the first term in (4.18). If the cut-off is taken as -1 GeV^2, the result from combined contributions for the π^0 match the NLO χPT value and

the contribution from ω exchange is indeed, dominant. Therefore, the implementation of the dispersion relations with higher intermediate states beyond ρ and ω corresponds to introducing at least one subtraction, which can be fixed to the NLO χPT (with some adjustments as explained below) given by [239]:

$$
\begin{aligned}
(\alpha-\beta)_{\pi^\pm} &= \frac{e^2}{4\,\pi\,m_\pi}\left\{\frac{8\,(L_9^r+L_{10}^r)}{F_0^2}+\frac{-Q^2}{F_0^2}\left[\bar{J}'_\pi(-Q^2)+\frac{1}{2}\,\bar{J}'_K(-Q^2)\right]\right\}\,,\\
(\alpha-\beta)_{\pi^0} &= \frac{e^2}{2\,\pi\,m_\pi}\left\{\frac{-Q^2-m_\pi^2}{F_0^2}\,\bar{J}'_\pi(-Q^2)+\frac{-Q^2}{4\,F_0^2}\bar{J}'_K(-Q^2)\right\}\,,\\
(\alpha-\beta)_{K^\pm} &= \frac{e^2}{4\,\pi\,m_K}\left\{\frac{8\,(L_9^r+L_{10}^r)}{F_0^2}+\frac{-Q^2}{F_0^2}\left[\frac{1}{2}\bar{J}'_\pi(-Q^2)+\bar{J}'_K(-Q^2)\right]\right\}\,,\\
(\alpha-\beta)_{K^0} &= \frac{e^2}{8\,\pi\,m_K}\frac{-Q^2}{F_0^2}\left\{\bar{J}'_\pi(-Q^2)+\bar{J}'_K(-Q^2)\right\}\,,
\end{aligned}
\tag{4.37}
$$

with $F_0 \simeq F_\pi = 92.4$ MeV and the following loop function

$$
\bar{J}_i(s) = \frac{1}{16\pi^2}\left[2+\sigma_i(s)\log\left(\frac{\sigma_i(s)-1}{\sigma_i(s)+1}\right)\right]\,,\quad \sigma_i(s)=\sqrt{1-\frac{4\,m_i^2}{s}}\,. \tag{4.38}
$$

For $Q^2=0$ we fix $\pi^\pm$ polarizability to the COMPASS result [238] while for π^0 and K ($I=0$) we used $(L_9^r+L_{10}^r)=(0.84\pm0.64)\times10^{-3}$ taken from [240] similar to [119]. The Q^2 dependence is fully governed by (4.37), where in the single channel case we used the pion-loop contributions only. The comparison between unsubtracted and once-subtracted results is shown in Fig. 4.8. For $I=0$ the single channel descriptions coincide in the region of $f_0(500)$ both for $Q^2=0$, 0.2 GeV^2 cases. The coupled-channel description, in turn, shows a slight difference for $Q^2=0$, which becomes significant for the finite Q^2. This behaviour can be ascribed to the lack of experimental information on the kaon polarizabilities and the poor convergence of $SU(3)$ χPT. For $I=2$ we note the discrepancy of about 10%-25% ($\sqrt{s}<0.6$ GeV) at $Q^2=0.2$ GeV^2, which, however, does not affect strongly the total cross section. Since the NLO χPT is expected to be valid only in the region $Q^2\lesssim 0.2$ GeV^2, the introduction of the additional subtraction reduces the predictive power of the dispersion relations. In the future, the upcoming data from the BESIII Collaboration in the range $0.2\lesssim Q^2\lesssim 2.2$ GeV^2 [196] will allow to fix the subtraction constant directly from the data and hence, extract essential information on Q^2-dependence of the polarizabilities.

4.3.3 Total and differential cross sections

The cross sections for the double virtual process $\gamma^*\gamma^*\to\pi\pi$, which involve either two transverse (TT) photon polarizations or two longitudinal (LL) photon polarizations or one transverse and one longitudinal (TL) photon polarization are defined by

$$
\begin{aligned}
\frac{d\sigma_{TT}}{d\cos\theta} &= \frac{\beta_{\pi\pi}}{64\,\pi\,\lambda^{1/2}(s,-Q_1^2,-Q_2^2)}\left(|H_{++}|^2+|H_{+-}|^2\right)\,,\\
\frac{d\sigma_{TL}}{d\cos\theta} &= \frac{\beta_{\pi\pi}}{32\,\pi\,\lambda^{1/2}(s,-Q_1^2,-Q_2^2)}\,|H_{+0}|^2\,,\\
\frac{d\sigma_{LL}}{d\cos\theta} &= \frac{\beta_{\pi\pi}}{32\,\pi\,\lambda^{1/2}(s,-Q_1^2,-Q_2^2)}\,|H_{00}|^2\,,\\
\beta_{\pi\pi} &= \frac{2\,p}{\sqrt{s}}\,,
\end{aligned}
\tag{4.39}
$$

where for the neutral pions one has to include a symmetry factor of 1/2. The quantities σ_{TT}, σ_{TL}, σ_{LT} and σ_{LL} enter the cross section for the process $e^+e^- \to e^+e^-\pi\pi$ given in Refs. [235, 241] (see App. 4.B). It sets the convention for the virtual photon flux factor, while the convention for the wave functions of the longitudinally polarized photons is chosen as

$$\begin{aligned} \epsilon^\mu(q_1,0) &= \frac{1}{Q_1}\,(q,0,0,E_{q_1})\,, \\ \epsilon^\nu(q_2,0) &= \frac{1}{Q_2}\,(-q,0,0,E_{q_2})\,, \\ E_{q_i} &= \sqrt{q^2-Q_i^2}\,, \quad q = \frac{\lambda^{1/2}(s,-Q_1^2,-Q_2^2)}{2\sqrt{s}}\,. \end{aligned} \tag{4.40}$$

This convention reproduces the real photon limit continuously. Naturally, the processes involving real photons produce only the cross section σ_{TT} and the single-virtual process produces cross sections σ_{TT} and σ_{TL}.

We first start the discussion with the real case $\gamma\gamma \to \pi\pi$, for which the data is available both for charged [200, 242, 243] and neutral [201, 244] channels. We implement rescattering in S- and D-waves, while the partial waves beyond are approximated by the Born terms. Regarding the S-wave, we find that the unsubtracted dispersion relation in Eq. 4.18, including Born left-hand cuts alone, predicts a reasonable description of the $f_0(500)$ and $f_0(980)$ regions. However, to describe the $f_2(1270)$ region in the D-wave, it is necessary to include heavier left-hand cuts [119], which we approximate with only vector mesons exchanges and slightly adjust the coupling $g_{VP\gamma} = 0.33$ GeV^{-1} in Eq. (4.20) to reproduce the $f_2(1270)$ peak in the $\gamma\gamma \to \pi^0\pi^0$ cross-section. We emphasize that this is the only parameter we adjust to the real photon data. We also note that the convergence of the unsubtracted dispersive integrals for $J = 2$ is generally better than for $J = 0$ due to the centrifugal barrier factor. Therefore, including vector meson left-hand cuts in the S-wave requires adding at least one subtraction, which can be fixed from χPT. As we discussed in Sec. 4.3.2, for relatively small Q^2, the results of the two solutions are very similar. Since the finite Q^2 prediction from χPT is expected to get large corrections for $Q^2 > 0.25$ GeV^2 we opted to stay with the unsubtracted version of the dispersion relations.

In Fig. 4.9 it is shown that with this choice, we achieve a reasonable agreement for both charged and neutral channels. Note, that for the charged case the total result is below the sum of S- and D-waves due to the presence of the incoherent sum of amplitudes squared in total cross section (see App. 4.B.) The slight difference in the intermediate region in $\gamma\gamma \to \pi^+\pi^-$ total cross section, in principle, can be fixed by over-subtracting the dispersion relation and fitting this unknown subtraction constant to the data, similar to the analysis in [119]. However, our main goal in this approach is to have predictive power for the single and double virtual processes. Our prediction for the spacelike single virtual case using the unsubtracted dispersion relation is shown in Fig. 4.10 and 4.11 for σ_{TT} and σ_{TL} respectively. The latter is fully determined by helicity-1 contribution and increases with increasing Q_2^2 in the low Q_2^2 regime. We also notice that the angular distribution $d\sigma_{TL}/d\cos\theta$ is forward peaked due to the Born contribution. For the σ_{TT}, we emphasize the importance of the unitarization, which increases the pure Born prediction at low energy by a significant amount.

The obtained results have to be further confronted with data; therefore, we attempt to estimate the uncertainties of the given approach. For this purpose, we take into account the fitting error for the $g_{VP\gamma}$, which contributes to the D-wave. The uncertainties of the S-wave treatment mainly originate from the hadronic rescattering part since the Born terms are well known. Previously, in [4] we estimated the hadronic uncertainty rather conservatively and compared the results using two different data-driven coupled-channel Omnès functions:

from our N/D analysis and from [245]. However, using the bootstrap technique in our N/D analysis, which we discussed extensively in Sec. 3.2, we are now in a position to estimate the hadronic contribution to the overall $\gamma\gamma \to \pi\pi$ in a more controlled and model-independent manner. To further account for the uncertainties coming from the finite photon virtuality, we include the errors of the monopole fit for pion and kaon electromagnetic form factors. For the vector meson left-hand cuts, we include the dispersive estimation uncertainty of $f_{\omega\pi\gamma}(Q^2)$ and consider conservatively the error bar of the $f_{\rho\pi\gamma}(Q^2)$ at $Q^2 = 0.5$ GeV^2 in the VMD treatment to be at around 15%.

Finally, in Fig. 4.12 we present the σ_{TT}, σ_{TL} and σ_{LL} predictions for a fixed value $Q_1^2 = 0.5$ GeV^2 for one photon virtuality and different values $Q_2^2 = 0.25, 0.5, 0.75, 1.0$ GeV^2 for the second photon virtuality. The last two Q_2^2 points are above the anomaly point. Here for the σ_{TL}, we again notice that the helicity-1 contribution increases with increasing virtualities. It is also instructive to compare our approach with a dispersive study based on the Roy-Steiner equations. In [210], there is a different strategy for treating kinematic singularities and anomalous thresholds. Secondly, there is a coupling between S-wave and D-wave with strength related to the high-energy behaviour assumption. Thirdly, the extra subtraction in [210] leads to a $1/s$ singular behaviour, which is due to the truncation of the partial wave expansion. In our approach, we solve a partial wave dispersion relation under the assumption of maximal analyticity. For the S-wave and D-wave we perform a coupled-channel and single-channel dispersive analysis, respectively and present a simpler implementation of the anomalous thresholds. Furthermore, in the present approach, there is no coupling between S- and D-waves and no extra $1/s$ singularities. In [7], the comparison between [210] and our current results has been done. Both approaches agree well up to the details due to a different treatment of the vector-meson couplings, form factors, and the inclusion of the coupled-channel effects in the S-wave.

4.4 Summary and Outlook

In this Chapter, we have presented a dispersive analysis of the $\gamma^*\gamma^* \to \pi\pi$ reaction from the threshold up to 1.5 GeV in the $\pi\pi$ invariant mass for several values of the photon spacelike virtualities. For the S-wave, we used a coupled-channel dispersive approach in order to simultaneously describe the scalar $\sigma/f_0(500)$ and $f_0(980)$ resonances since the latter has a dynamical $\{\pi\pi, K\bar{K}\}$ origin. Since $f_2(1270)$ tensor resonance decays predominantly to two pions, for the D-wave, we adopted a single-channel dispersive approach that requires t- and u-channel vector-meson contributions to the left-hand cut. This contribution introduces the one parameter fixed to the real photon data - the $g_{VP\gamma}$ coupling, which lies well within the $SU(3)$ spread of the couplings determined from the experimental vector meson radiative decays.

Considering the S-wave resonances, we extracted their two-photon couplings and two-photon decay width. For the $\sigma/f_0(500)$ resonance we performed the calculations for the unphysical pion mass $m_\pi = 236$ MeV. The obtained results will serve as one of the relevant inputs to constrain the hadronic piece of the light-by-light scattering contribution to the muon's a_μ [80, 184, 185, 199]. Especially it allows to estimate the contributions from $f_0(500)$, $f_0(980)$ and $f_2(1270)$, where the latter can be compared with the narrow resonance result [186, 198] as it was recently done for $f_0(980)$ in [81] using the results of the present work.

While for the real photon processes $\gamma\gamma \to \pi^+\pi^-$ and $\gamma\gamma \to \pi^0\pi^0$, we have achieved a reasonable description of the total cross section in comparison with the most recent data from the Belle Collaboration [200, 201], there are still a few open issues before it can be fully implemented in a $(g-2)_\mu$ calculation. First, one needs to validate a current treatment of left-hand cuts by forthcoming BESIII data on the $\gamma\gamma^* \to \pi^+\pi^-$ and $\gamma\gamma^* \to \pi^0\pi^0$ reactions [196]. This is a prerequisite for a data-driven approach in quantifying the uncertainty of the HLbL contribution to a_μ. Second, for higher Q^2, one has to incorporate constraints from

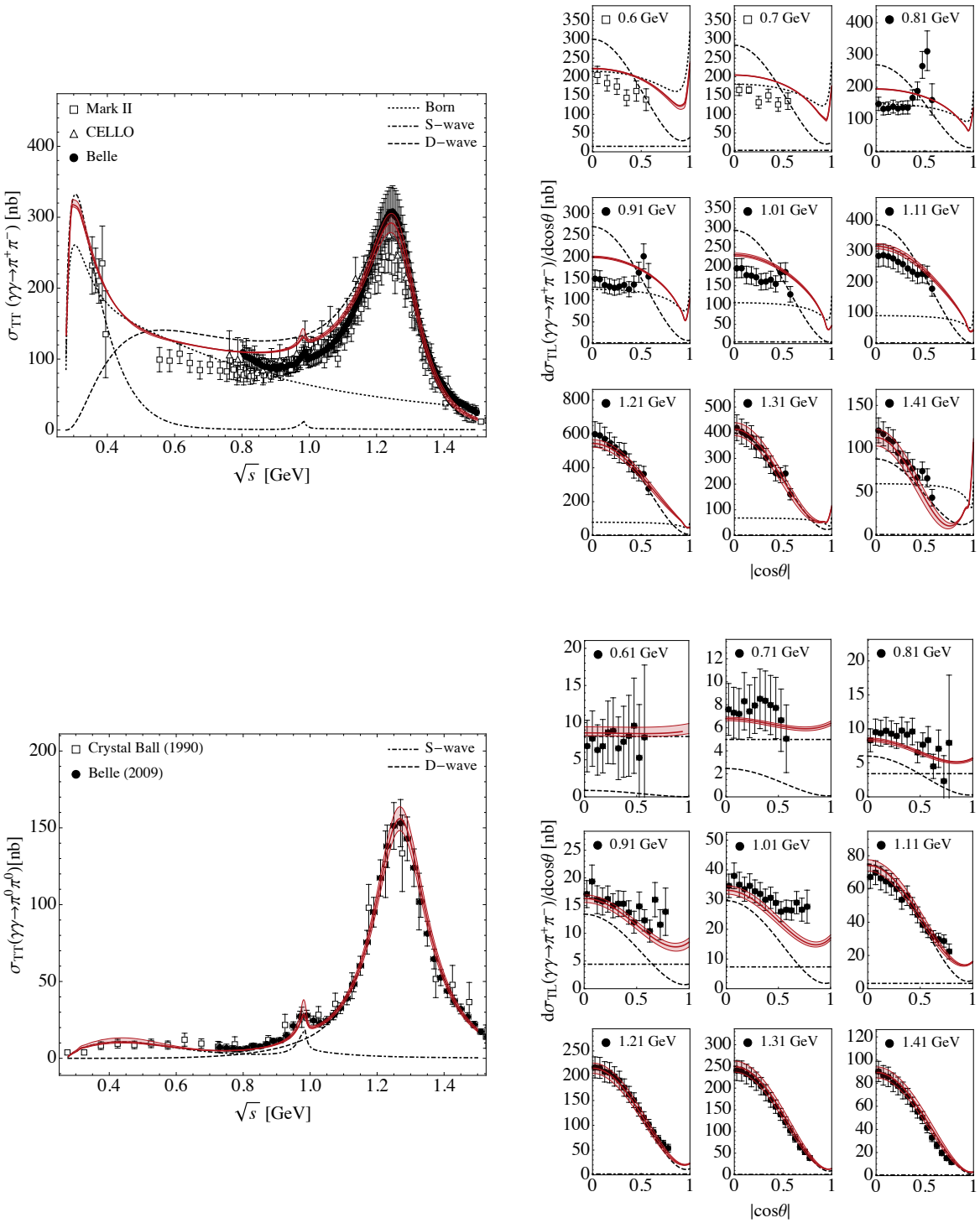

Figure 4.9: Total σ_{TT} (left panels) and differential $d\sigma_{TT}/d\cos\theta$ (right panels) cross sections for the $\gamma\gamma \to \pi\pi$ $Q_1^2 = Q_2^2 = 0$ GeV^2 case. Upper plots the results for the $\gamma\gamma \to \pi^+\pi^-$ scattering for angular coverage $|\cos\theta| \leq 0.6$ in comparison to the data from [200, 242, 243] and lower plots show the results for the $\gamma\gamma \to \pi^0\pi^0$ scattering for angular coverage $|\cos\theta| \leq 0.8$ in comparison to the data from [201, 244]. The Born results are shown by the dotted curve, the S- and D-wave contributions are shown by dot-dashed and dashed curves respectively.

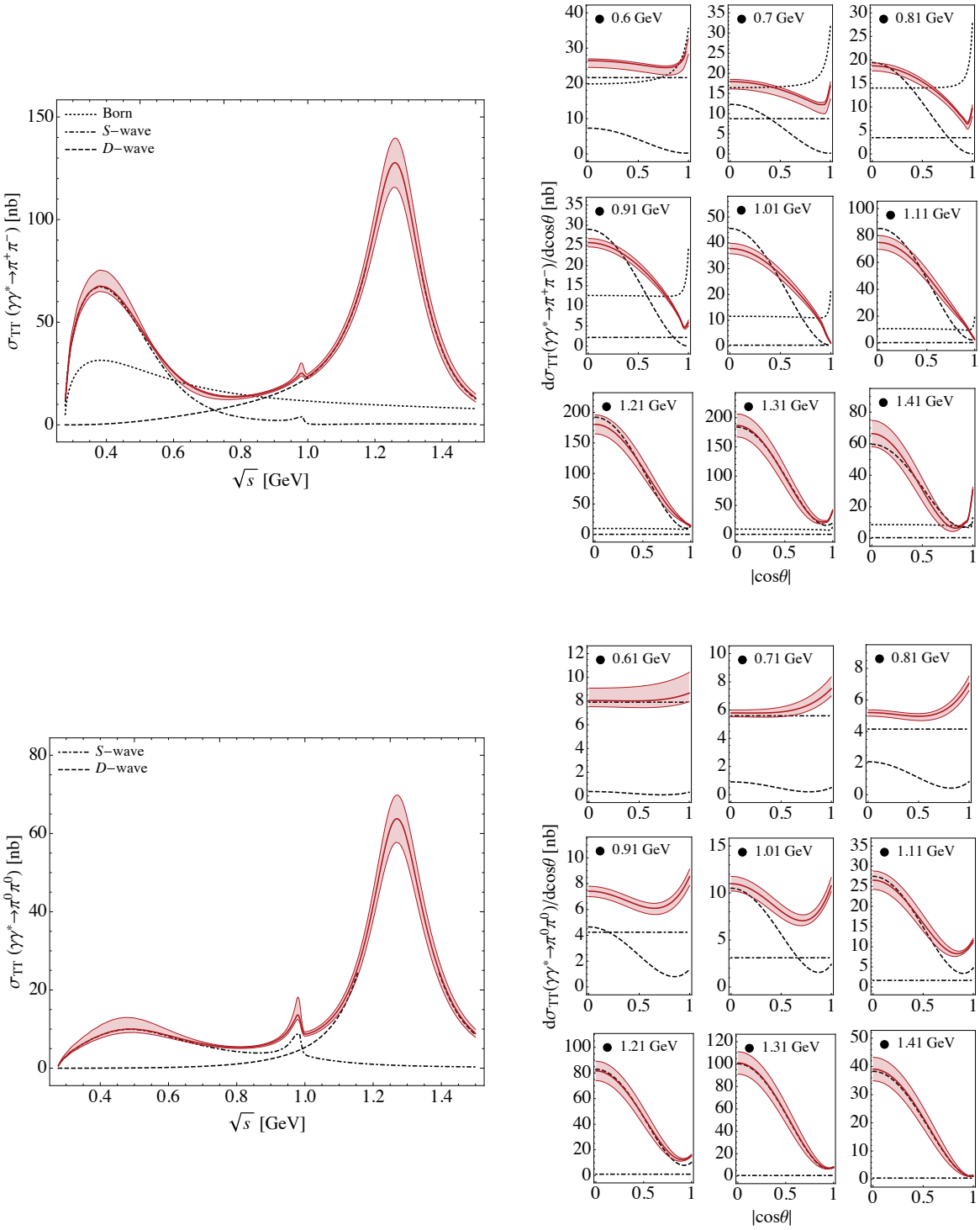

Figure 4.10: Total σ_{TT} (left panels) and differential $d\sigma_{TT}/d\cos\theta$ (right panels) cross sections for the $\gamma\gamma^* \to \pi\pi$ $Q_1^2 = 0, Q_2^2 = 0.5$ GeV^2 case and the full angular coverage $|\cos\theta| \leq 1$. The upper plots show the results for the $\gamma\gamma^* \to \pi^+\pi^-$ scattering and lower plots show the results for the $\gamma\gamma^* \to \pi^0\pi^0$. The Born results are shown by the dotted curve, the S- and D-wave contributions are shown by dot-dashed and dashed curves respectively.

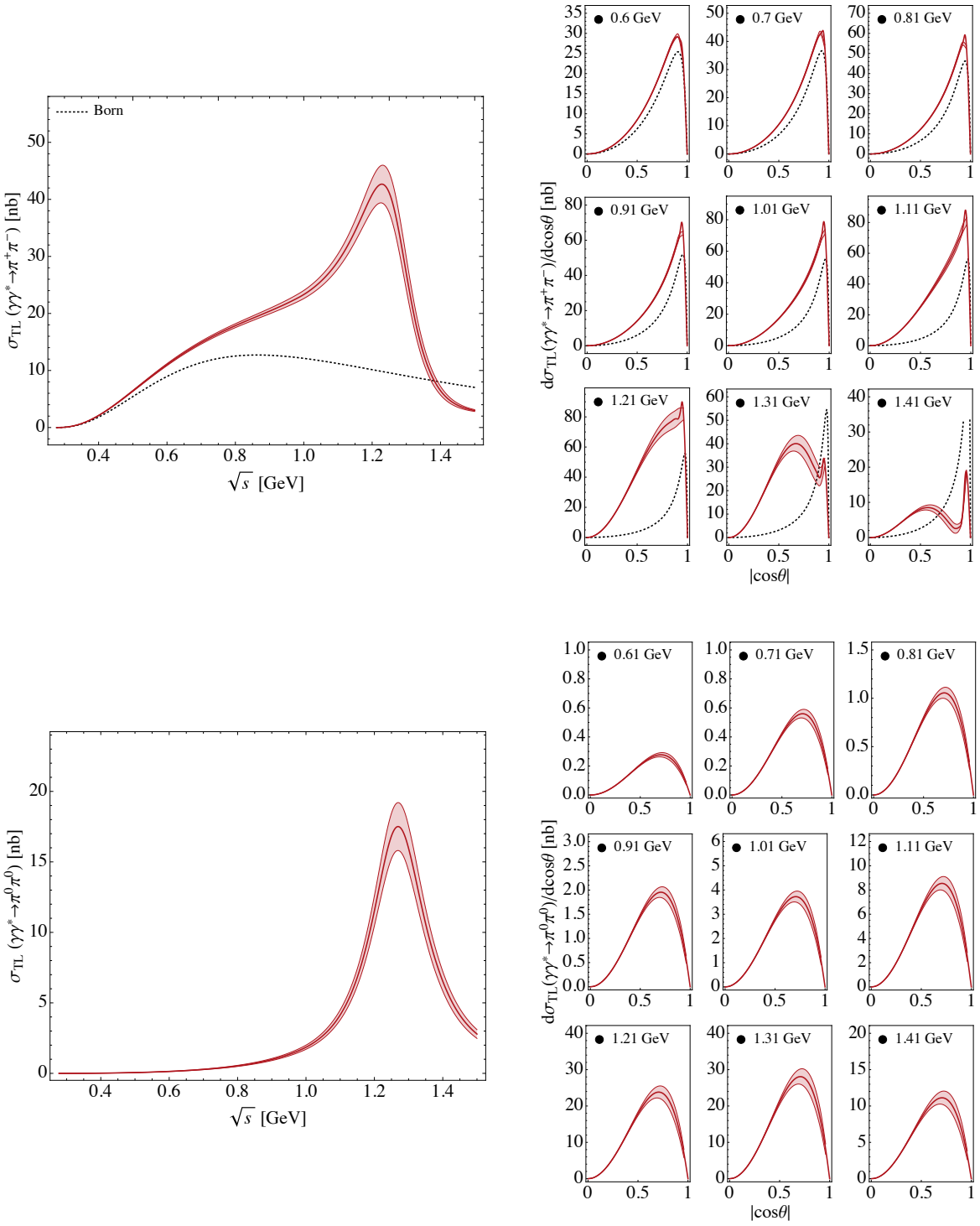

Figure 4.11: Total σ_{TL} (left panels) and differential $d\sigma_{TL}/d\cos\theta$ (right panels) cross sections for the $\gamma\gamma^* \to \pi\pi$ $Q_1^2 = 0, Q_2^2 = 0.5$ GeV^2 case and the full angular coverage $|\cos\theta| \leq 1$. The upper plots show the results for the $\gamma\gamma^* \to \pi^+\pi^-$ scattering and lower plots show the results for the $\gamma\gamma^* \to \pi^0\pi^0$. The Born results are shown by the dotted curve.

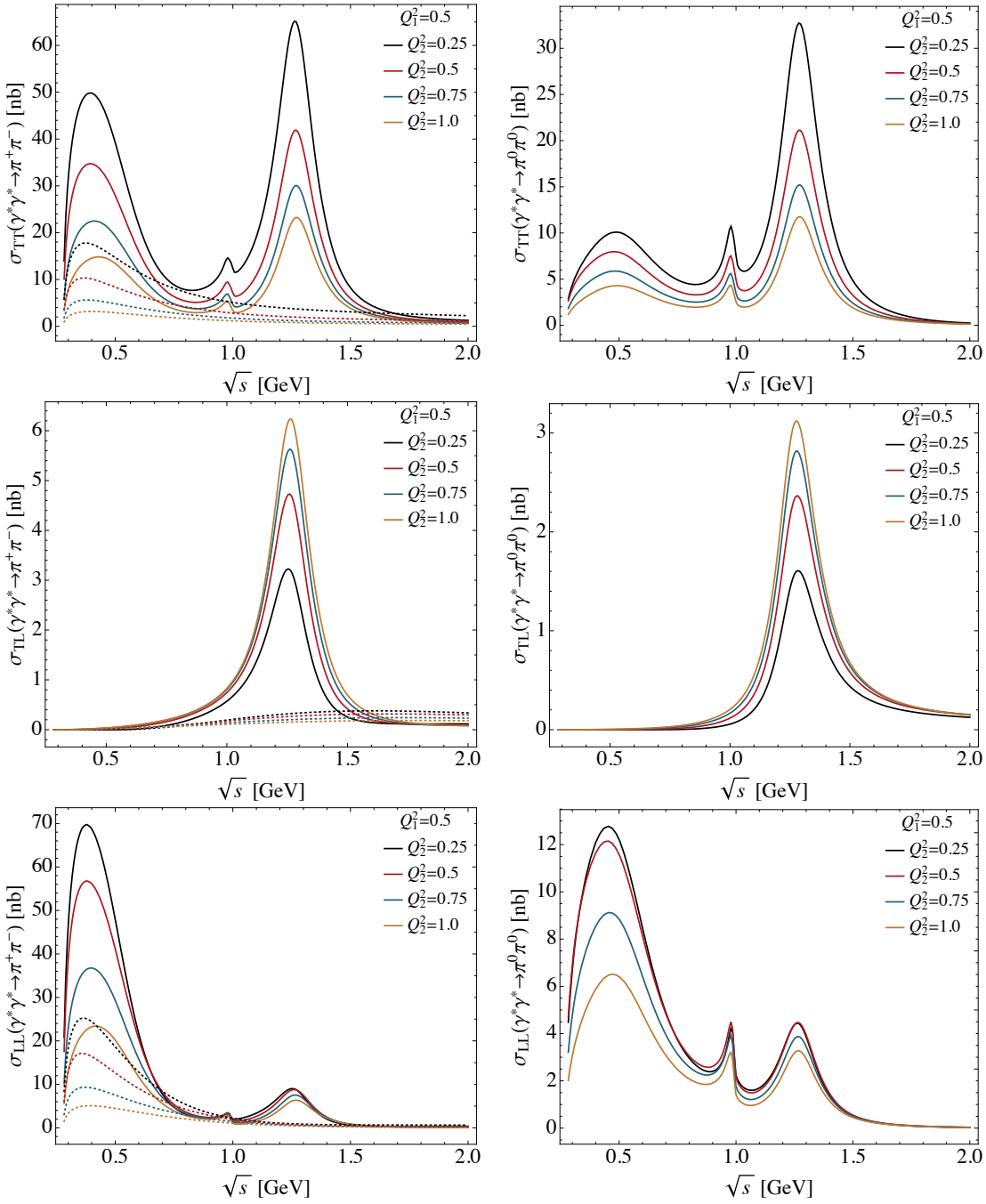

Figure 4.12: Predictions for σ_{TT}, σ_{TL}, σ_{LL} cross sections for $\gamma^*\gamma^* \to \pi^+\pi^-$ (left panels) and $\gamma^*\gamma^* \to \pi^0\pi^0$ (right panels) for $Q_1^2 = 0.5$ GeV^2 and $Q_2^2 = 0.25, 0.5, 0.75, 1.0$ GeV^2 and for full angular coverage $|\cos\theta| \leq 1$. The Born results for each set of Q_1^2, Q_2^2 are shown by the dotted curves in corresponding colors.

perturbative QCD for the vector transition from factors $f_{V,\pi}(Q^2)$ which is the driving force governing the Q^2 dependence of the $f_2(1270)$ resonance [71]. This will be investigated in future work.

Appendices

4.A Analytic structure of the left hand cuts

The analytical structure of the left hand cuts in the $\gamma^*(Q_1)\gamma^*(Q_2) \to \pi\pi$ process was discussed in Chapter 4. In this Appendix, we mainly aim to introduce an alternative approach to treating the *anomalous thresholds* problem, which appears when both photons carry non-zero spacelike virtuality. For this purpose, we remind that the vector-meson left hand cut is determined by four branching points, arising from the condition $t(s_L^{(\pm)}, \pm 1) - M^2 = 0$:

$$\begin{aligned} &s_L = 0\,, \quad s_L = -\infty\,, \\ &s_L^{(\pm)} = \frac{1}{2}\left(2m^2 - Q_1^2 - Q_2^2 - M^2 - \frac{(Q_1^2+m^2)(Q_2^2+m^2)}{M^2}\right) \\ &\qquad\qquad \pm \frac{\sqrt{\lambda(M^2, m^2-Q_1^2)}\sqrt{\lambda(M^2, m^2, -Q_2^2)}}{2M^2}\,, \end{aligned} \tag{4.41}$$

where M is the mass of the intermediate vector meson and $\lambda(x,y,z)$ is a Källén triangle function (see App. 3.A). In addition, there are two kinematic singularities:

$$q_{\rm cm}(s) \equiv \frac{\lambda^{1/2}(s, -Q_1^2, -Q_2^2)}{2\sqrt{s}} = 0 \quad \Longrightarrow \quad s_{\rm kin}^{(\pm)} = -(Q_1 \pm Q_2)^2\,. \tag{4.42}$$

The relative positions of these structures on the s-plane for the small photon virtualities are shown in Fig. 4.13.

The implementation of the dispersion relations requires the integration of the amplitudes over the left-hand cuts. If one of the photons is real, the cut consists of two pieces: $(-\infty, s_L^{(-)}]$ and $[s_L^{(+)}, 0]$. However, when both photons carry space-like virtuality, the left hand cut structure becomes more complicated depending on the values Q_1^2 and Q_2^2. To study this effect, we consider the following type of integrals, which naturally appear in the vector-meson exchange amplitudes:

$$L_n(s) \equiv \int\limits_{-1}^{1} dz \frac{z^n}{t(s,z) - M^2}\,. \tag{4.43}$$

It is convenient to work in the following notation:

$$\begin{aligned} &t(s,z) - M^2 \equiv \alpha(s) + \beta(s) z\,, \\ &\alpha(s) \equiv \frac{1}{2}(2m^2 - Q_1^2 - Q_2^2 - s) - M^2\,, \quad \beta(s) \equiv 2p_{\rm cm}(s) q_{\rm cm}(s)\,. \end{aligned} \tag{4.44}$$

In the absence of the anomalous thresholds, the integrals of this type for an arbitrary integer n can be expressed as a sum of two hypergeometric functions

$$L_n(s) = \frac{{}_2F_1\left(1, n+1, n+2; -\frac{\beta(s)}{\alpha(s)}\right) + (-1)^n {}_2F_1\left(1, n+1, n+2; \frac{\beta(s)}{\alpha(s)}\right)}{(n+1)\alpha(s)}\,. \tag{4.45}$$

The present analyses of the $\gamma^*(Q_1)\gamma^*(Q_2) \to \pi\pi$ reactions [1, 210] are limited to the S- and D-waves only. Therefore, for the practical applications, it is sufficient to consider the terms up to $n = 2\,, J = 4$:

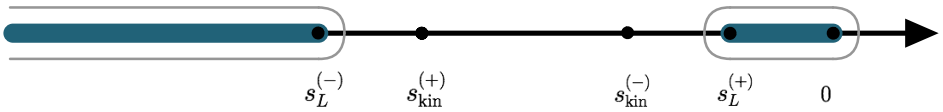

Figure 4.13: Relative positions of left hand cuts and kinematic points for small values of Q_1^2, Q_2^2. The integration contour is shown in grey.

$$
\begin{aligned}
L_0(s) &= -\frac{1}{\beta(s)} \log\left(\frac{X(s)+1}{X(s)-1}\right) , \\
L_1(s) &= \frac{1}{\beta(s)}(2-\alpha(s)L_0(s)) , \\
L_2(s) &= \frac{1}{\beta^2(s)}(-2\alpha(s)+\alpha^2(s)L_0(s)) , \\
L_3(s) &= \frac{1}{\beta^3(s)}\left(\frac{2}{3}\beta^2(s)+2\alpha^2(s)-\alpha^3(s)L_0(s)\right) , \\
L_4(s) &= \frac{1}{\beta^4(s)}\left(-\frac{2}{3}\alpha(s)\beta^2(s)-2\alpha^3(s)+\alpha^4(s)L_0(s)\right) .
\end{aligned} \tag{4.46}
$$

where we introduced the notation

$$
X(s) \equiv \frac{-2m^2+2M^2+s+Q_1^2+Q_2^2}{4p_{\rm cm}(s)q_{\rm cm}(s)} . \tag{4.47}
$$

The above expressions for $L_n(s)$ are given for the t-channel. For the u-channel, the integrals with even index have the same form, while the odd ones acquire an overall factor of (-1).

According to the Cauchy theorem (see Sec. 2.2.3), the analytical function can be reconstructed from its discontinuities along the branch cuts. Therefore, we introduce

$$
L_i^{\rm Disp}(s) \equiv \int_{-\infty}^{s_L^-} \frac{ds'}{\pi} \frac{\text{Im } L_i(s')}{s'-s} + \int_{s_L^+}^{0} \frac{ds'}{\pi} \frac{\text{Im } L_i(s')}{s'-s} , \tag{4.48}
$$

so that the correctness of the amplitude behavior along the left hand cut is ensured by requirement $L_i(s) = L_i^{\rm Disp}(s)$, i.e. the unsubtracted dispersion relation (4.48) is fulfilled. Whether it happens automatically or not, depends on the relative dynamics of the branching points $s_L^{\pm}$ and pseudo-thresholds $s_{\rm kin}^{(\pm)}$ with changing Q_1^2, Q_2^2.

First, when the photon virtualities are small, all special points are well separated, and the integration proceeds as normal. Then, with increasing values of Q_1^2, Q_2^2 the left-hand branch point $s_L^{(-)}$ moves to the right and reaches $s_{\rm kin}^{(+)}$ at

$$
s_{\rm kin}^{(+)} = s_L^{(-)} \quad \Longrightarrow \quad Q_1^2 Q_2^2 = (M^2-m^2)^2 . \tag{4.49}
$$

and only then moves to the left. Therefore, for the case of $Q_1^2 Q_2^2 \geq (M^2-m^2)^2$ an additional piece $[s_L^-, s_{\rm kin}^1]$ shown on Fig. 4.15, which is related to an *anomalous discontinuity* [136, 231], has to be considered.

The integrals $L_i(s)$ now diverge at the point $s = s_{\rm kin}^{(+)}$. Appart from the method, used in Sec. 4.2.6, it is also possible to deform the integration contour introducing the circle with small radius r centered around $s = s_{\rm kin}^{(+)}$ (see Fig. 4.15). To demonstrate how this contour

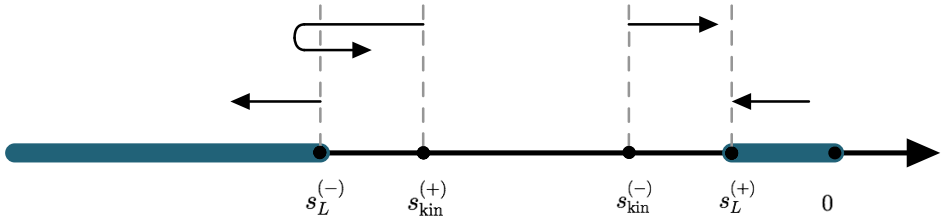

Figure 4.14: The dynamics of the branching points $s_L^{\pm}$ and pseudo-thresholds $s_{\rm kin}^{(\pm)}$ depending on photons virtualities. The arrows represent the direction in which every point moves with growing Q_1^2, Q_2^2 (see text for the details).

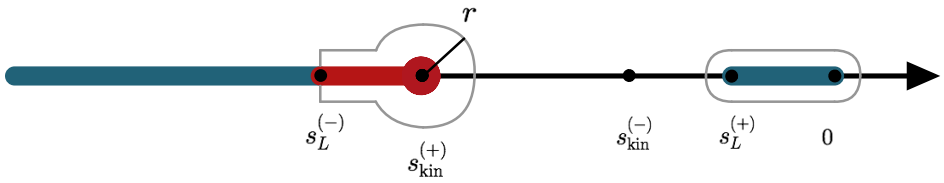

Figure 4.15: Integration contour for $L_n(s)$ in the case $Q_1^2 Q_2^2 \geq (M^2 - m^2)^2$, which accounts for the singularity at $s_{\rm kin}^{(+)}$.

deformation works we start by considering the simple case $L_0(s)$. The integration along the additional $[s_L^{(-)}, s_{\rm kin}^{(+)}]$ piece

$$\begin{aligned}\int_{s_L^{(-)}}^{s_{\rm kin}^{(+)}} \frac{ds'}{\pi} \frac{\text{Im}\,[L_0(s'+i\epsilon) - L_0(s'-i\epsilon)]}{s'-s} &= \int_{s_L^-}^{s_{\rm kin}^{(+)}} \frac{ds'}{\pi} \frac{\text{Im}\,[\text{Disc}\; L_0(s')]}{s'-s} \\ &= \int_{s_L^-}^{s_{\rm kin}^{(+)}} \frac{ds'}{\pi} \frac{\text{Im}\,[-\frac{i\pi}{p_{cm}(s')q_{cm}(s')}]}{s'-s}\,, \end{aligned} \tag{4.50}$$

brings a new term to $L_0^{\rm Disp}(s)$:

$$L_0^{\rm Disp}(s) = \int_{-\infty}^{s_L^-} \frac{ds'}{\pi} \frac{\text{Im}\; L_0(s')}{s'-s} + \int_{s_L^+}^{0} \frac{ds'}{\pi} \frac{\text{Im}\; L_0(s')}{s'-s} + \int_{s_L^-}^{s_{\rm kin}^{(+)}} \frac{ds'}{\pi} \frac{\text{Im}\,[-\frac{i\pi}{p_{cm}(s')q_{cm}(s')}]}{s'-s}\,. \tag{4.51}$$

The singularity in the last term is of a square root type $1/q_{cm}(s') \sim 1/\sqrt{s - s_{\rm kin}^{(+)}}$ and therefore is integrable, meaning that the integral over circle goes to zero, when $r \to 0$. It was checked numerically that the dispersion relation works for $s = (4m^2, \infty)$ and the result is shown in Fig. 4.16.

However, it is not the case for the further integrals. The same procedure for $L_2(s)$ leads to the anomalous piece of the form

$$\int_{s_L^-}^{s_{\rm kin}^{(+)}} \frac{ds'}{\pi} \frac{\text{Im}\,\left[\frac{\alpha^2(s')}{\beta^2(s')} \frac{-i\pi}{p_{cm}(s')q_{cm}(s')}\right]}{s'-s}\,, \tag{4.52}$$

The integral over the circle then adds:

$$\int_{s_L}^{s_{\rm kin}^{(+)}-r} ds' f(s'+i\epsilon) + \int_{s_{\rm kin}^{(+)}-r}^{s_L} ds' f(s'-i\epsilon) + \int_{\pi}^{-\pi} d\phi f(s_{\rm kin}^{(+)} + re^{i\phi})\,. \tag{4.53}$$

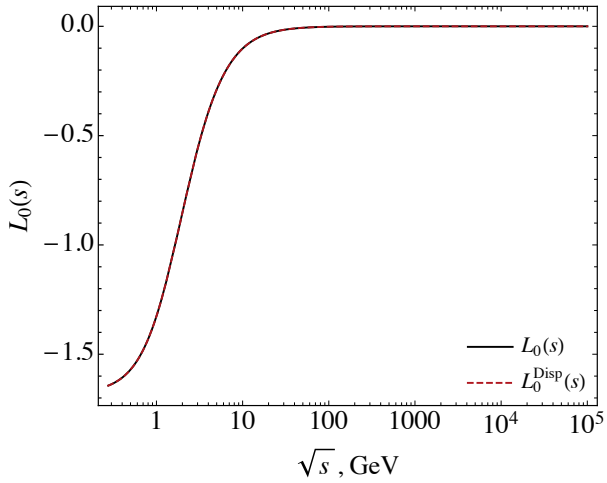

Figure 4.16: Linear-log comparison between $L_0(s)$ and $L_0^{\rm Disp}(s)$ from Eq. (4.51).

The circular part of $L_2(s)$ can be further evaluated as

$$\int_{\pi}^{-\pi} d\phi f(s_{\rm kin}^{(+)} + re^{i\phi}) = \int_{\pi}^{-\pi} \frac{ds'}{\pi} \frac{1}{s'-s} \frac{1}{2i} \frac{\alpha^2(s')(-i\pi)}{4p_{cm}^3(s')q_{cm}^3(s')}\Big|_{s'=s_{\rm kin}^{(+)}+re^{i\phi}}$$

$$\text{where } q_{cm}(s) = \frac{\sqrt{s-s_{\rm kin}^{(+)}}\sqrt{s-s_{\rm kin}^{(-)}}}{2\sqrt{s}} = \frac{\left|\sqrt{s-s_{\rm kin}^{(-)}}\right|}{2|\sqrt{s}|}\sqrt{s-s_{\rm kin}^{(+)}}$$

$$= \underbrace{\frac{1}{s_{\rm kin}^{(+)}-s} \frac{\alpha^2(s_{\rm kin}^{(+)})}{4|p_{cm}(s_{\rm kin}^{(+)})|^3} \left(\frac{\left|\sqrt{s_{\rm kin}^{(+)}-s_{\rm kin}^{(-)}}\right|}{2\left|\sqrt{s_{\rm kin}^{(+)}}\right|}\right)^{-3}}_{z\left(s,s_{\rm kin}^{(+)}\right)} \int_{\pi}^{-\pi} \frac{re^{i\phi}id\phi}{\pi} \frac{1}{2i} \frac{-i\pi}{i^3(re^{i\phi})^{3/2}}$$

$$= \frac{z\left(s,s_{\rm kin}^{(+)}\right)}{2\sqrt{r}} \int_{\pi}^{-\pi} e^{-i\phi/2}d\phi = -\frac{2z\left(s,s_{\rm kin}^{(+)}\right)}{\sqrt{r}}, \tag{4.54}$$

where $r << s_{\rm kin}^{(+)}$ is assumed. The total expression for $L_2^{\rm Disp}(s)$ is then

$$L_2^{\rm Disp}(s) = \int_{-\infty}^{s_L^-} \frac{ds'}{\pi} \frac{\text{Im } L_2(s')}{s'-s} + \int_{s_L^+}^{0} \frac{ds'}{\pi} \frac{\text{Im } L_2(s')}{s'-s}$$

$$+ \int_{s_L^-}^{s_{\rm kin}^{(+)}-r} \frac{ds'}{\pi} \frac{\text{Im}\left[\frac{\alpha^2(s')}{\beta^2(s')} \frac{-i\pi}{p_{cm}(s')q_{cm}(s')}\right]}{s'-s} - \frac{2z\left(s,s_{\rm kin}^{(+)}\right)}{\sqrt{r}}. \tag{4.55}$$

We keep only the leading order term to derive the singular component in Eq. (4.54), and the next-to-leading term $\propto \sqrt{r}$ is neglected. The numerical check is demonstrated in Fig. 4.17, where $\Delta L_2(s_0) = (L_2(s_0) - L_2^{\rm Disp}(s_0))/L_2(s_0)$ is plotted against the variation of r and we choose $s_0 = 1$ GeV^2. The obtained curve follows the square root dependence with high accuracy.

It can be seen from Fig. 4.17, that Eq. (4.55) give a rather good approximation for calculating $L_2(s)$. Therefore, a similar approach could be expected to be successfully applied to $L_4(s)$. However, in contrast to the $L_2(s)$ case, the next-to-leading term in the expansion for L_4 is also divergent. One possible solution is finding the optimal value of r, which would keep the

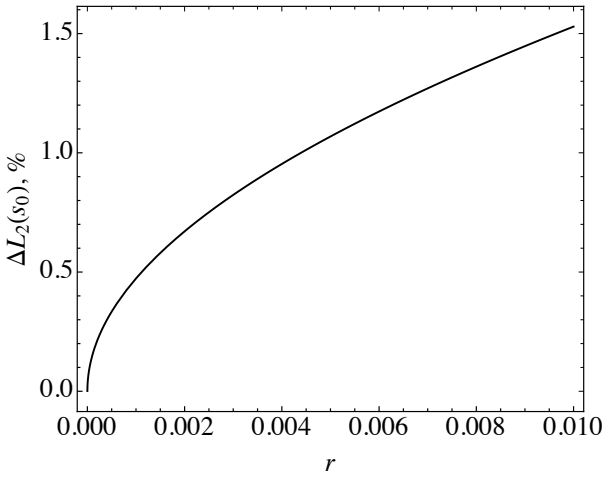

Figure 4.17: Percentage error of $L_2^{\text{Disp}}(s_0)$ calculated with Eq. 4.55 (see text for the details).

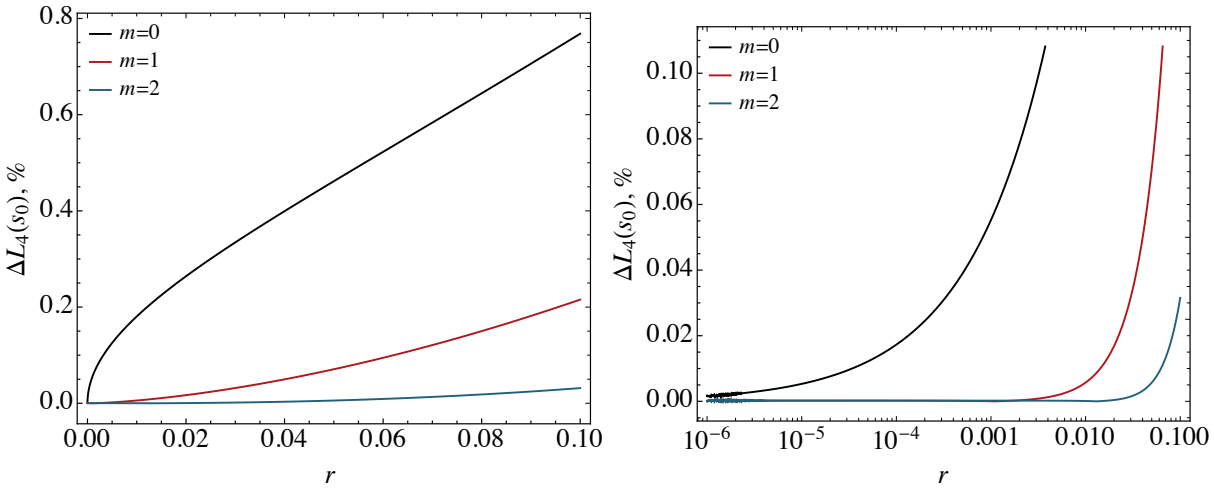

Figure 4.18: Percentage error of $L_4^{\text{Disp}}(s)$ calculated with Eq. (4.56) and the next terms in the expansion. Left panel: linear plot, right panel: linear-log plot.

next-to-leading order term $\propto r^{-1/2}$ small in comparison to the leading divergent term $\propto r^{-3/2}$ while simultaneously also making the non-divergent terms negligible. However, this choice will introduce the dependence on the value of r and make the integration procedure less flexible for higher $L_n(s)$.

In this approach, we prefer to control the errors by extending the described method to include the terms beyond the leading order. The general case for the integral over the circle can be easily derived as

$$\int_{\pi}^{-\pi} \frac{re^{i\phi}id\phi}{\pi} \frac{1}{2i} \frac{-i\pi}{i^{2n+1}(re^{i\phi})^{(2n+1)/2}} = \frac{(-1)^{n+1}}{2r^{n-1/2}} \int_{\pi}^{-\pi} d\phi e^{-i(n-1/2)\phi} = \frac{(-1)^{n+1}}{2r^{n-1/2}} \frac{4(-1)^n}{2n-1}$$
$$= -\frac{2}{2n-1} \frac{1}{r^{n-1/2}}. \quad (4.56)$$

The resulting accuracy depends then on the number of terms N in the expansion on the nominator of L_{2n}. The criteria for the optimal r and N are formulated as: in order to have accuracy $O(r^{1/2+m})$ we need to take $N = n + m$ terms.

The comparison between the number of terms in the expansion for $L_4^{\text{Disp}}(s)$ different values

of m is plotted on Fig. 4.18. It shows that the series converges quite fast, and the inclusion of large number of terms is excessive, considering the precision of the numerical integration procedure itself.

4.B General cross section of the $e^+ + e^- \to e^+ + e^- + X$ process

The cross section for the process $e(p_1)+e(p_2) \to e(p_1')+e(p_2')+X$, with X being the produced hadronic system, can be expressed in terms of the response functions for the $\gamma^*\gamma^* \to X$ process: four positive definite cross sections $\sigma_{TT}, \sigma_{LL}, \sigma_{TL}, \sigma_{LT}$, as well as four responses which can have either sign, $\tau_{TT}, \tau_{TL}, \tau^a_{TT}, \tau^a_{TL}$ (see [235] for the details), so that

$$\begin{aligned} d\sigma = & \frac{\alpha^2}{16\pi^4 Q_1^2 Q_2^2} \frac{2\sqrt{X}}{\tilde{s}(1-4m^2/\tilde{s})^{1/2}} \cdot \frac{d^3\vec{p'}_1}{E_1'} \frac{d^3\vec{p'}_2}{E_2'} \\ & \times \Big\{ 4\rho_1^{++}\rho_2^{++}\sigma_{TT} + \rho_1^{00}\rho_2^{00}\sigma_{LL} + 2\rho_1^{++}\rho_2^{00}\sigma_{TL} + 2\rho_1^{00}\rho_2^{++}\sigma_{TL} \\ & + 2(\rho_1^{++}-1)(\rho_2^{++}-1)\left(\cos 2\tilde{\phi}\right)\tau_{TT} + 8\left[\frac{(\rho_1^{00}+1)(\rho_2^{00}+1)}{(\rho_1^{++}-1)(\rho_2^{++}-1)}\right]^{1/2}\left(\cos\tilde{\phi}\right)\tau_{TL} \\ & + 4h_1h_2\left[(\rho_1^{00}+1)(\rho_2^{00}+1)\right]^{1/2}\tau^a_{TT} + 8h_1h_2\left[(\rho_1^{++}-1)(\rho_2^{++}-1)\right]^{1/2}\left(\cos\tilde{\phi}\right)\tau^a_{TL}\Big\}, \end{aligned} \tag{4.57}$$

where $h_1 = \pm 1$ and $h_2 = \pm 1$ are both lepton beam helicities, $\tilde{\phi}$ is the azimuthal angle between both lepton planes, in the $\gamma\gamma$ c.m. frame, and we defined

$$X \equiv (q_1 \cdot q_2)^2 - q_1^2 q_2^2. \tag{4.58}$$

The virtual photon density matrix elements have the following form:

$$\begin{aligned} \rho_1^{++} &= \frac{1}{2}\left\{1 - \frac{4m^2}{Q_1^2} + \frac{1}{X}(2p_1\cdot q_2 - q_1\cdot q_2)^2\right\}, \\ \rho_2^{++} &= \frac{1}{2}\left\{1 - \frac{4m^2}{Q_2^2} + \frac{1}{X}(2p_2\cdot q_1 - q_1\cdot q_2)^2\right\}, \\ \rho_1^{00} &= \frac{1}{X}(2p_1\cdot q_2 - q_1\cdot q_2)^2 - 1\,, \\ \rho_2^{00} &= \frac{1}{X}(2p_2\cdot q_1 - q_1\cdot q_2)^2 - 1\,. \end{aligned} \tag{4.59}$$

The eight response functions depend upon three kinematical variables: $s = (q_1+q_2)^2, Q_1^2$ and Q_2^2. In the convention of (4.57) the cross sections are defined as

$$\begin{aligned} \frac{d\sigma_{TT}}{d\cos\theta} &= \frac{\beta(s)}{128\pi\sqrt{X}}(|H_{++}|^2 + |H_{+-}|^2) \xrightarrow{Q_1^2=0} \frac{\beta(s)}{64\pi(s+Q_2^2)}(|H_{++}|^2 + |H_{+-}|^2)\,, \\ \frac{d\sigma_{TL}}{d\cos\theta} &= \frac{\beta(s)}{64\pi\sqrt{X}}|H_{+0}|^2 \xrightarrow{Q_1^2=0} \frac{\beta(s)}{32\pi(s+Q_2^2)}|H_{+0}|^2\,, \\ \frac{d\sigma_{LT}}{d\cos\theta} &= \frac{\beta(s)}{64\pi\sqrt{X}}|H_{0+}|^2 \xrightarrow{Q_1^2=0} 0\,, \\ \frac{d\sigma_{LL}}{d\cos\theta} &= \frac{\beta(s)}{64\pi\sqrt{X}|H_00|^2} \xrightarrow{Q_1^2=0} 0\,. \end{aligned} \tag{4.60}$$

where we showed also what happens in the single-virtual limit, i.e. when $Q_1^2 \to 0$ and used

$$\beta(s) = \sqrt{1 - \frac{4m_\pi^2}{s}}\,, \quad X = \frac{1}{4}(s + Q_1^2 + Q_2^2)^2 - Q_1^2 Q_2^2\,. \tag{4.61}$$

Using the partial-wave decomposition (4.2) and Eq. (4.57) and integrating over $\cos\theta \in [-1, 1]$ one can show that

$$\begin{aligned}
\sigma_{TT}(s) &= \frac{\beta(s)}{64\pi(s+Q^2)}\left(2|h^{(0)}_{I,++}|^2 + 10|h^{(2)}_{I,++}|^2 + 10|h^{(2)}_{I,+-}|^2\right)\,, \\
\sigma_{TL}(s) &= \frac{\beta(s)}{32\pi(s+Q^2)}\left(10|h^{(2)}_{I,+0}|^2\right)\,.
\end{aligned} \tag{4.62}$$

We emphasize that Eq. (4.57) is a physical observable and the choice of convention for the longitudinal polarization vector should not have any influence on it. However, the definition of σ_{TL} depends on the convention, since off-shell photons are not physical states. In order to have positive definite σ_{TL} cross section we use the following longitudinal polarization vectors

$$\begin{aligned}
\epsilon^\mu(q_1, 0) &= \frac{1}{Q_1}\left(q, 0, 0, q^0\right)\,, \\
\epsilon^\mu(q_2, 0) &= \frac{1}{Q_2}\left(-q, 0, 0, q^0\right)\,,
\end{aligned} \tag{4.63}$$

which implies the following normalization and completeness relation

$$\begin{aligned}
&\epsilon^\mu(q,\lambda)\epsilon^*_\mu(q,\lambda') = (-1)^\lambda \delta_{\lambda,\lambda'}\,, \\
&\sum_{\lambda=\pm1,0} (-1)^\lambda \epsilon^\mu(q,\lambda)\epsilon^{\nu *}(q,\lambda) = g^{\mu\nu} + \frac{q^\mu q^\nu}{Q^2}\,.
\end{aligned} \tag{4.64}$$

Note, the factor $(-1)^\lambda$ in the relation above, which implies an extra sign for the helicity amplitude involving longitudinal photon. For the case when one photon is virtual and one is real, Eq. (4.57) simplifies and experimentally one can access the quantity [195]

$$\sigma_{\rm tot} = \sigma_{TT} + \epsilon\sigma_{TL}\,, \quad \epsilon \equiv \frac{\rho_2^{00}}{2\rho_2^{++}} = \frac{1-x}{1-x+x^2/2}\,, \quad x \equiv \frac{q_1\cdot q_2}{p_1\cdot q_2}\,, \tag{4.65}$$

where the pre-factor ϵ lies in the region $0 < \epsilon < 1$ and depends on s, Q^2. For the case of $\epsilon \simeq 1$, the completeness relation (4.64) can be used to obtain $\sigma_{\rm tot}$ without going into the frame

$$\begin{aligned}
\sigma_{\rm tot}(\epsilon = 1) &\sim \sum_{\lambda_1=\pm1,\lambda_2=\pm1,0} |H_{\lambda_1,\lambda_2}|^2 \\
&= \sum_{\lambda_1=\pm1} \epsilon_\mu(q_1,\lambda_1)\epsilon^*_{\mu'}(q_1,\lambda_1) \sum_{\lambda_2=\pm1,0} \epsilon_\nu(q_2,\lambda_2)\epsilon^*_{\nu'}(q_2,\lambda_2) H^{\mu\nu}H^{\mu'\nu'}\,,
\end{aligned} \tag{4.66}$$

where the first sum can be safely replaced by $-g_{\mu\mu'}$, while in the second sum one has to take into account $(-1)^{\lambda_2}$ in order to use a completeness relation (4.64). As a result one obtains

$$\sigma_{\rm tot}(\epsilon = 1) \sim \left(2|h^{(0)}_{I,++}|^2 + 10|h^{(2)}_{I,++}|^2 + 10|h^{(2)}_{I,+-}|^2 + 10|h^{(2)}_{I,+0}|^2\right)\,. \tag{4.67}$$

Chapter 5

Dispersive analysis of the $\gamma\gamma \to D\bar{D}$ scattering data

In the previous chapters, we have shown that the partial-wave dispersive approach is a powerful tool that can be applied even in the cases when the data is scarce (see, for instance, Sec. 3.3.2). This feature proves to be particularly important when describing the interactions involving heavier particles and, consequently, the higher energies. It is rather typical for such reactions to have data with such low statistics that even the existence of a particular resonant state is called into question, not to mention the exact determination of its position and other properties.

In this Chapter, we venture into the charmonium region by studying the two-photon fusion reaction with a $D\bar{D}$ meson pair in the final state. In this reaction, it is expected to observe two charmonium-like states: $\chi_{c0}(2P)$ and $\chi_{c2}(2P)$. While the latter is unambiguously identified with the $X(3930)$ state found in several experimental setups, the former still raises controversies over its assignment. There are some indications that $\chi_{c0}(2P)$ can be identified with $X(3860)$, which appears as a broad S-wave resonance in the $\gamma\gamma \to D\bar{D}$ and $e^+e^- \to J/\psi D\bar{D}$ reactions, at first glance, similar to the $\sigma/f_0(500)$ resonance. However, other theoretical works suggest that the structure appearing in the cross section is caused by the bound state slightly below the $D\bar{D}$ threshold. By studying the $\pi\pi \to \pi\pi$ scattering from the lattice data with different pion masses in Sec. 3.3.2, we showed that the considered dispersive approach could easily distinguish between the bound state and the broad resonance. Therefore, the same technique applied to the data for the $\gamma\gamma \to D\bar{D}$ process can shed light on the structure observed in this reaction and its properties.

This Chapter is based on [3] and it is organized as follows. First, in Sec. 5.1 we provide an overview of the current experimental and theoretical results directed towards the identification of $\chi_{c0}(2P)$ and $\chi_{c2}(2P)$ states. In Sec. 5.2 we describe how the partial-wave dispersive formalism can be applied for the $\gamma\gamma \to D\bar{D}$ system and present the details of the tensor $\chi_{c2}(3930)$ resonance. We show our numerical results in Sec. 5.3, which included the analysis of the $\gamma\gamma \to D\bar{D}$ data and a post-diction to the $e^+e^- \to J/\psi D\bar{D}$ process. A summary and outlook are given in Sec. 5.4.

5.1 Introduction

In recent years, the growing interest in the charmonium mass region has been nourished with new experimental discoveries (see Fig. 5.1). Ever since the Belle Collaboration discovered the $X(3872)$ [246] extremely close to the $D^0\bar{D}^{*0}$ threshold, a plethora of new states has been observed. Nevertheless, only a few of them are unambiguously identified. For comprehensive reviews, we refer to [247–252].

The only unambiguosly identified radially excited P-wave charmonium state up to date is $\chi_{c2}(2P)$, associated with the resonance $X(3930)$. First it was discovered by Belle Collaboration [253] as a distinct peak near 3930 MeV in the $D\bar{D}$ invariant mass distribution of the $\gamma\gamma \to D\bar{D}$ reaction. This analysis obtained a mass of $M = 3929 \pm 5(\text{stat}) \pm 2(\text{syst})$ MeV and a total width of $\Gamma = 29 \pm 10(\text{stat}) \pm 2(\text{syst})$ with the preferred quantum numbers of $J^{PC} = 2^{++}$. Located between $D\bar{D}$ and $D^*\bar{D}^*$ thresholds, it decays predominantly into $D\bar{D}$ pair in a D-

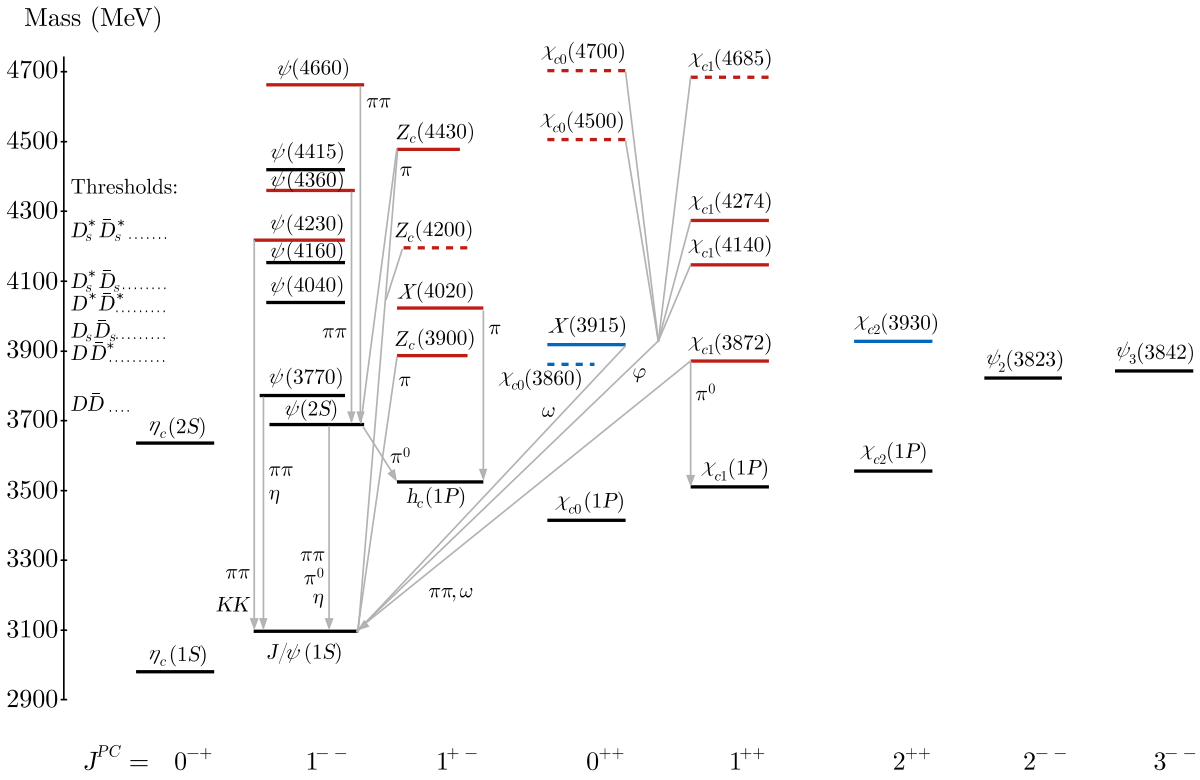

Figure 5.1: The level scheme of meson states containing a minimal quark content of $c\bar{c}$. States included in PDG (2022) Summary Tables [27] are shown with solid lines; selected states not in the Summary Tables, but with assigned quantum numbers, are shown with dashed lines. The conventional $q\bar{q}$ states are indicated with black lines, and the candidates for an exotic structure are shown in red. The arrows indicate the most dominant hadronic transitions. The states discussed in this Chapter are shown in blue. The figure is adapted from PDG [27].

wave. Later, in the same $\gamma\gamma \to D\bar{D}$ reaction the X(3930) resonance was observed with the mass and total width of $M = 3926.7 \pm 2.7(\text{stat}) \pm 1.1(\text{syst})$ MeV with $\Gamma = 21.3 \pm 6.8(\text{stat}) \pm 3.6(\text{syst})$ by the BaBar Collaboration [254]. Again, the analysis of the angular distribution favored a tensor over scalar interpretation. The obtained values for the mass, width and $\Gamma(X(3930) \to \gamma\gamma)\mathcal{B}(X(3930) \to D\bar{D})$ were consistent with the Belle results and with the expectations for the $\chi_{c2}(2P)$ state.

The $\chi_{c2}(3930)$ assignment was recently confirmed in completely different experiment, namely the LHCb Collaboration found this state using proton-proton collision data with the mass and width measured to be $M_{\chi_{c2}(3930)} = 3921.9 \pm 0.6(\text{stat}) \pm 0.2(\text{syst})$ MeV and $\Gamma_{\chi_{c2}(3930)} = 36.6 \pm 1.9(\text{stat}) \pm 0.9(\text{syst})$ MeV [255] and later in the amplitude analysis of the $B \to D^+D^-K+$ decay with $M_{\chi_{c2}(3930)} = 3926.8 \pm 2.4(\text{stat}) \pm 0.8(\text{syst})$ MeV and $\Gamma_{\chi_{c2}(3930)} = 34.2 \pm 6.6(\text{stat}) \pm 1.1(\text{syst})$ [256]. The current average for the $\chi_{c2}(2P)$ mass and width [27], including the Belle [253], BaBar [254] and LHCb [255, 256] results stands as

$$M_{\chi_{c2}(3930)} = 3922.2 \pm 1.0 \text{ MeV}, \quad \Gamma_{\chi_{c2}(2P)} = 35.3 \pm 2.8 \text{ MeV}. \tag{5.1}$$

The identification of $\chi_{c0}(2P)$ state, which is expected to exist roughly in the same mass region, however is still problematic. The first attempts of its assignment date back to 2010, when a possible candidate has been observed by Belle Collaboration as a near threshold $\omega J/\psi$ mass enhancement in the exclusive $B \to K\omega J/\psi$ decays [257], which was confirmed by BaBar

Collaboration [258, 259]. This structure was later identified to be the same as X(3915) state found by Belle Collaboration in $\gamma\gamma \to \omega J/\psi$ [260] process with the mass $M = 3915 \pm 3(\text{stat}) \pm 2(\text{syst})$ MeV and width $\Gamma = 17 \pm 10(\text{stat}) \pm (\text{syst})$ MeV. In [261] the $X(3915)$ assignment as $\chi_{c0}(2P)$ state was proposed and was later supported by the spin-parity analysis by the BaBar Collaboration [262]. However, as it was pointed out in several other works [263–265], $X(3915)$ is a problematic candidate for $\chi_{c0}(2P)$ due to its narrowness, dominant decay channels (which contradict the expectations for $\chi_{c0}(2P)$), and the small mass splitting with the well-established $\chi_{c2}(3930)$.

In principle, when the Belle Collaboration reported $X(3915)$ in [260], both assignments $J^{PC} = 0^{++}$ and 2^{++} were acceptable. Soon after, BaBar Collaboration [262] suggested that it has $J^{PC} = 0^{++}$ based on the helicity-2 dominance assumption, which originally comes from the quark model calculations. The later reanalysis [266] of both Belle and BaBar data showed that if $X(3915)$ has an exotic nature (also [267]), this assumption may be relaxed, and helicity-0 contribution may also be sizable. In this case, the $X(3915)$ being narrow $J^{PC} = 2^{++}$ resonance is preferred by data, which implicitly suggests that it might be the same tensor resonance as $X(3930)$ In [268] it was found, that if the $X(3915)$ is the $D^{(*)}\bar{D}^{(*)}$ hadronic molecule which should exist as a spin partner of the $X(3872)$, the data favors the scalar assignment. Still, other exotic explanation, like tetraquark state [249, 269], can not be discarded.

The alternative candidate for $\chi_{c0}(2P)$ state may have been already observed in the $\gamma\gamma \to D\bar{D}$ process by both Belle [253] and BaBar [254] Collaborations somewhere in an energy range from the $D\bar{D}$ threshold up to the $\chi_{c2}(2P)$ position. They fitted the $D\bar{D}$ invariant mass spectrum with a single Breit-Wigner function for the $\chi_{c2}(2P)$ and some background functions. In [267], $\gamma\gamma \to D\bar{D}$ data were reanalyzed using two Breit-Wigner functions under the assumption that the resonance structures dominate the invariant mass distribution. In other words, it was assumed that the broad bump located around ~ 3800 MeV, which was considered to be a background in experimental analyses, may hide the broad resonance. By fixing the mass and the width of $\chi_{c2}(2P)$ to its experimental values the fit to data predicted the existence of $\chi_{c0}(2P)$ with $M_{\chi_{c0}(2P)} = 3837.6 \pm 11.5$ MeV and $\Gamma_{\chi_{c0}(2P)} = 221 \pm 19$ MeV. The later result was reinforced by the Belle Collaboration [270], which in the analysis of $e^+e^- \to J/\psi D\bar{D}$ data found the new charmonium-like state $X(3860)$, that decays mainly to $D\bar{D}$ channel. With the mass 3862^{+26+40}_{-32-13} MeV, the width $201^{+154+88}_{-67-82}$MeV and $J^{PC} = 0^{++}$ this state is currently included in the PDG (2021) [27] as $\chi_{c0}(2P)$. This assignment is supported by the constituent quark model in [271], which also favors the hypothesis of $X(3915)$ and $X(3930)$ being the same tensor state.

However, it is still an open question of what has been seen in $\gamma\gamma \to D\bar{D}$ and $e^+e^- \to J/\psi D\bar{D}$ processes. First, the statistics of the Belle data [270] for the $e^+e^- \to J/\psi D\bar{D}$ process is rather low close to the threshold. Second, unlike simple Breit-Wigner parametrizations, the proper resonance analysis should account for the S-matrix constraints, such as unitarity and analyticity. In [272] a unitary approach based on the Bethe-Salpeter equation was used to describe the Belle data. No peak structure that justifies the claim for the $X(3860)$ state was found. The same observation was made in [273] regarding the $\gamma\gamma \to D\bar{D}$ data from the Belle [253] and BaBar [254] Collaborations. Instead, this analysis suggested that the behaviour around the threshold is consistent with the $D\bar{D}$ dynamics that encodes a bound state, previously predicted in [274]. On another side, the recent coupled-channel $\{D\bar{D}, D_s\bar{D}_s\}$ analysis performed on the lattice with $m_\pi = 280(3)$ MeV [275] suggests the existence of both: a shallow bound state slightly below $D\bar{D}$ threshold and the broad resonance, comparable to $X(3860)$. From the analysis at $m_\pi = 400$ MeV [276] the mass splitting between $\chi_{c0}(2P)$ and $\chi_{c2}(2P)$ can be extracted, which, using the experimental mass of $\chi_{c2}(2P)$ gives an estimation of $\chi_{c0}(2P)$ mass compatible with the value $X(3860)$. Moreover, the situation gets more puzzling

by the recent LHCb observation [256, 277] of two resonances, sitting at the same mass, the $\chi_{c0}(3930)$ and the $\chi_{c2}(3930)$, with widths around 17 MeV and 34 MeV, respectively, and no evidence of the broad $X(3860)$ state.

The present ambiguity regarding the existing data and the character of the structures present in $\gamma\gamma \to D\bar{D}$ cross sections and $e^+e^- \to J/\psi D\bar{D}$ calls for a theoretical approach that rigorously implements both the unitarity and analyticity constraints and does not make any assumption about underlying $D\bar{D}$ dynamics. Within the partial-wave dispersive approach, which was successfully used to analyze the $\pi\pi$ and πK scattering in Chapter 3, it is straightforward to perform the analytical continuation of the scattering amplitudes to the unphysical regions and identify the positions of the poles and bound states. Therefore, an application of this technique to the $D\bar{D}$ system can shed more light on the nature of the near-threshold enhancements seen in the experiment.

5.2 Dispersive formalism

In this section we again consider the formalism outlined in the Sec. 2.2.4. We have already applied this method extensively in Secs. 3.2 and 4.2, yet for the $\{\gamma\gamma, D\bar{D}\}$ system there are some details we are willing to discuss further. In contrast to the $\pi\pi$ and πK scattering considered in Chapter 3, there is no separate data for the DD scattering phase shifts. Instead, the available data is given for the cross sections of the $\gamma\gamma \to D^+D^-$ and $\gamma\gamma \to D^0\bar{D}^0$ processes. It is also important to note, that for this case we do not have any additional constraints similar to ones considered in 3.2 and rely on the data alone to establish the amplitudes. As for the D-wave, we take into account only the contribution from the isoscalar $\chi_{c2}(3930)$ resonance and approximate it by a simple Breit-Wigner form.

This section is organized as follows. First, we consider an N/D approach in application to the $\{\gamma\gamma, D\bar{D}\}$ system. Then, in Sec. 5.2.2 we specify the left-hand cut input. Finally, in 5.2.3 we show the approximation of the D-wave amplitude.

5.2.1 N/D approach for the $\{\gamma\gamma, D\bar{D}\}$ system

In the same manner as in Sec. 3.2 we consider a $2 \to 2$ process described by the partial wave amplitudes $t^{(J)}_{I,ab}$, where ab are the coupled-channel indices with a and b standing for the initial and final state, respectively. Again, we focus only on the S-wave, with isospin $I = 0$, and therefore will suppress the labels I, J. The once write once-subtracted dispersive representation is then (see Secs. 2.2.4 and 3.2.1)

$$t_{ab}(s) = U_{ab}(s) + \frac{s}{\pi}\sum_c \int_{s_{th}}^{\infty} \frac{ds'}{s'} \frac{t_{ac}(s')\,\rho_c(s')\,t^*_{cb}(s')}{s'-s}\,, \tag{5.2}$$

where $s_{\rm th}$ is the lowest threshold and s_L is the position of the closest left-hand cut singularity. As a consequence of the N/D ansatz, one needs to solve a system of linear integral equations

$$\begin{aligned} N_{ab}(s) &= U_{ab}(s) + \frac{s}{\pi}\sum_c \int_{s_{th}}^{\infty} \frac{ds'}{s'} \frac{N_{ac}(s')\,\rho_c(s')\,(U_{cb}(s') - U_{cb}(s))}{s'-s}\,, \\ D_{ab}(s) &= \delta_{ab} - \frac{s}{\pi}\int_{s_{th}}^{\infty} \frac{ds'}{s'} \frac{N_{ab}(s')\,\rho_b(s')}{s'-s}\,, \end{aligned} \tag{5.3}$$

where the input of $U_{ab}(s)$ is required for $s > s_{th}$ only.

We aim to extract the S-wave photon fusion amplitude $\gamma\gamma \to D\bar{D}$, which is the off-diagonal term of the coupled channel $\{1 = \gamma\gamma, 2 = D\bar{D}\}$ system. Note that for the S-wave, there is only one $\gamma(\lambda_1)\gamma(\lambda_2) \to D\bar{D}$ helicity amplitude with helicities $\lambda_1 = \lambda_2 = +1$. By neglecting $\gamma\gamma$

intermediate states in the unitary relation $\rho_1 = 0$, and putting $U_{11} = 0$ (which is proportional to e^4 and hence suppressed, see also Sec. 4.2), the coupled-channel N/D solution reduced down to the separate set of integral equations for the hadronic part

$$\begin{aligned} t_{22}(s) &= N_{22}(s)/D_{22}(s)\,, \\ N_{22}(s) &= U_{22}(s) + \frac{s}{\pi}\int_{4m_D^2}^{\infty} \frac{ds'}{s'}\frac{N_{22}(s')\,\rho_2(s')\,(U_{22}(s') - U_{22}(s))}{s'-s}\,, \\ D_{22}(s) &= 1 - \frac{s}{\pi}\int_{4m_D^2}^{\infty} \frac{ds'}{s'}\frac{N_{22}(s')\,\rho_2(s')}{s'-s}\,, \end{aligned} \tag{5.4}$$

and for the $\gamma\gamma \to D\bar{D}$ part

$$t_{12}(s) = U_{12}(s) + D_{22}^{-1}(s)\left(-\frac{s}{\pi}\int_{4m_D^2}^{\infty}\frac{ds'}{s'}\frac{\mathrm{Disc}(D_{22}(s'))U_{12}(s')}{s'-s}\right). \tag{5.5}$$

The latter requires as input the hadronic D_{22} function given in Eq. (5.4) as well as the $\gamma\gamma \to D\bar{D}$ left-hand cuts, U_{12}.

For the case when there is no bound state in the system, Eq. (5.5) can be obtained from writing the once-subtracted dispersion relation for the quantity $\Omega_{22}^{-1}\,(t_{12} - U_{12})$ [119, 121, 221], where $\Omega_{22} = D_{22}^{-1}$ is the Omnès function. However, it is important to emphasize that Eqs. (5.4) and (5.5) are universal also for the case when there is a bound state in the system. It is straightforward to show that adding a bound state into $U_{ab}(s)$,

$$\tilde{U}_{ab}(s) = U_{ab}(s) + \frac{s}{s_B}\frac{g_{ab}^2}{s_B - s}\,, \tag{5.6}$$

does not change Eqs. (5.4) and (5.5) provided that the binding energy $s = s_B$ is determined by

$$D_{22}(s_B) = 1 - \frac{s_B}{\pi}\int_{4m_D^2}^{\infty}\frac{ds'}{s'}\frac{N_{22}(s')\,\rho_2(s')}{s'-s_B} = 0\,. \tag{5.7}$$

For the case when there is a bound state in the system, Eq. (5.5) is equivalent to the once-subtracted dispersion relation for the quantity $\Omega_{22}^{-1}\left(t_{12} - \tilde{U}_{12}\right)$, where the Omnès function is now related to the D-function as $\Omega_{22} = \left(\frac{s_B}{s_B - s}\right) D_{22}^{-1}$.

5.2.2 Left-hand cuts

To evaluate the dispersion relations in Eqs. (5.4) and (5.5), we need to specify the left-hand cuts. For the photon-fusion process $\gamma\gamma \to D\bar{D}$ the left-hand cuts can be well approximated by the exactly calculable Born contribution (see also Sec. 4.2),

$$\begin{aligned} U_{12}(s) &= -\frac{2\sqrt{2}\,e^2 m_D^2}{s\,\beta(s)}\log\frac{1+\beta(s)}{1-\beta(s)}\,, \\ \beta(s) &\equiv \frac{2\,p(s)}{\sqrt{s}} = \sqrt{1 - \frac{4\,m_D^2}{s}}\,. \end{aligned} \tag{5.8}$$

Heavier left-hand cuts exchanges start farther away from the physical region and typically suppressed for the S-wave contribution [178]. Note, that the choice of the subtraction point in Eq. (5.2) and consequently in Eq. (5.5) is motivated by the soft-photon theorem [219], which

states that the Born term subtracted photon fusion amplitude must vanish at $s = 0$. As for the $D\bar{D} \to D\bar{D}$ left-hand cuts, little is known about them, except their analytic structure in the complex plane. Since we need the input for $U_{22}(s)$ only in the physical region, one can approximate $U_{22}(s)$ by means of a model independent conformal expansion [107–110]

$$U_{22}(s) = \sum_{n=0}^{\infty} C_n \, \xi^n(s) \,, \tag{5.9}$$

where the conformal mapping variable $\xi(s)$

$$\xi(s) = \frac{\sqrt{s - s_L} - \sqrt{s_E - s_L}}{\sqrt{s - s_L} + \sqrt{s_E - s_L}} \,, \tag{5.10}$$

maps the left-hand cut plane $-\infty < s < s_L$ onto the unit circle [143]. The position of the closest left-hand cut branching point $s_L = 4(m_D^2 - m_\pi^2)$ is determined by the $t-$ and $u-$ channel exchange of two pions. The expansion point s_E (at which $\xi(s_E) = 0$) is chosen in the middle of the region where we expect the S-wave contribution to dominate

$$\sqrt{s_E} = \frac{1}{2} \left(\sqrt{s_{\rm th}} + \sqrt{s_{\rm max}} \right) \,, \tag{5.11}$$

with $\sqrt{s_{\rm max}} = 3.86$ GeV. We note that, given the form of $\xi(s)$ in Eq. (5.10), the series (5.9) truncated at any finite order is bounded asymptotically. This is consistent with the assigned asymptotic behavior of $U_{22}(s)$ in the once-subtracted dispersion relation (5.2). In the next section, we will determine the unknown C_n in Eq. (5.9) directly from the data.

Hereafter, to distinguish the amplitudes involving photons from the pure hadronic amplitude, for the $\gamma\gamma \to D\bar{D}$ p.w. amplitudes we adopt the notation of Sec. 4.2: $h^{(J)}_{I,\lambda_1\lambda_2}(s)$, where $\lambda_{1,2} = \pm 1$ are photon helicities, so that

$$h^{(0)}_{0,++}(s) \equiv t_{12}(s) \,. \tag{5.12}$$

While it is natural to associate any resonant structure with the dynamics in the $I = 0$ channel, the $I = 1$ amplitude does not have known direct channel resonances and we approximate it by the Born amplitude

$$h^{(0)}_{1,++}(s) = -\frac{2\sqrt{2}\, e^2 m_D^2}{s\, \beta(s)} \log \frac{1 + \beta(s)}{1 - \beta(s)} \,. \tag{5.13}$$

We note, however, that taking into account the $I = 1$ contribution is absolutely necessary to obtain nonequal cross sections for the $\gamma\gamma \to D^+D^-$ and $\gamma\gamma \to D^0\bar{D}^0$ channels. For instance, Eq. (5.13) combined with Eq. (5.8) gives a zero direct Born term for $\gamma\gamma \to D^0\bar{D}^0$, leaving only contributions via rescattering.

5.2.3 D-wave parametrization

For the D-wave in the $\gamma\gamma \to D\bar{D}$ process we take into account only the contribution from the isoscalar $\chi_{c2}(3930)$ resonance, which is a radially excited P-wave charmonium state. We approximate it by a simple Breit–Wigner form, similar to how it was done for $f_2(1270)$ in the $\gamma\gamma \to \pi\pi$ process in [120, 278] and for $a_2(1320)$ in the $\gamma\gamma \to \pi^0\eta$ process in [65, 217]. Is it based on the effective Lagrangians of the following form

$$\begin{aligned} \mathcal{L}_{R\gamma\gamma} &= e^2 \, g_{R\gamma\gamma} \, \Phi_{\mu\nu} \, F^{\mu\lambda} \, F_\lambda{}^\nu \,, \\ \mathcal{L}_{RD\bar{D}} &= g_{RD\bar{D}} \, \Phi^{\mu\nu} \, \partial_\mu D \, \partial_\nu D \,, \end{aligned} \tag{5.14}$$

where $F^{\mu\nu}$ is an electromagnetic tensor and $\Phi^{\mu\nu}$ is a massive spin-2 field. In the first line of Eq. (5.14) it is assumed that the $\chi_{c2}(3930)$ resonance is predominantly produced in a state with helicity-2. The D-wave amplitude is then given by

$$h^{(2)}_{0,+-}(s) = -\frac{e^2\, g_{R\gamma\gamma}\, g_{RD\bar{D}}}{10\sqrt{6}} \frac{s^2\, \beta^2(s)}{s - M_R^2 + i\, M_R\, \Gamma_R(s)}\,, \tag{5.15}$$

where $g_{R\gamma\gamma}, g_{RD\bar{D}}$ denote $\chi_{c2}(3930)$ couplings to $\gamma\gamma$ and $D\bar{D}$ channels, respectively. The energy-dependent decay width of the resonance is parametrized as [202]

$$\Gamma(s) = \Gamma_R \left(\frac{p(s)}{p(M_R^2)} \right)^5\,, \tag{5.16}$$

with Γ_R being the width of the resonance at rest. Note, that for simplicity we have not included Blatt-Weisskopf factors in Eqs. (5.15) and (5.16), which only slightly change the cross section in the considered region but introduce additional dependence on the unknown interaction radius, which cannot be fixed given the quality of the present data. While for the mass and the width of $\chi_{c2}(3930)$ we use PDG 2021 values $M_R = 3922.2 \pm 1.0$ MeV, $\Gamma_R = 35.3 \pm 2.8$ [27], the couplings $g_{R\gamma\gamma}$, $g_{RD\bar{D}}$ cannot be fixed due to unknown branching fractions and will be absorbed into the unknown normalisation parameter (see Sec. 5.3.2). More details on the derivation of the amplitude in Eq. 5.15 and a discussion regarding the Blatt-Weisskopf factor can be found in App. 5.A.

5.3 Numerical results and interpretation

This section concentrates on the numerical results for the $\gamma\gamma \to D\bar{D}$ process. We start by discussing the quality of experimental data in Sec. 5.3.1 and the possible issues caused by it. Then, in Sec. 5.3.2 we first show the results for the combined $\gamma\gamma \to D\bar{D}$ fit. We then also show the fit to $\gamma\gamma \to D^0\bar{D}^0$ and $\gamma\gamma \to D^+D^-$ channels and discuss the difference between the results. In Sec. 5.3.3 we show the postdiction for the $e^+e^- \to J/\psi D\bar{D}$ process. Finally, in Sec. 5.3.4 we discuss the analogies between the $\gamma\gamma \to D\bar{D}$ and $\gamma\gamma \to K\bar{K}$ cases.

5.3.1 Experimental input

Before implementing the dispersive approach, we would like to comment on the quality of data that serves as an input to our analysis. The statistics in both Belle [253] and BaBar [254] $\gamma\gamma \to D\bar{D}$ experiments are relatively low, and therefore the combined sum of charged and neutral production modes was presented as the main result. In this way, the interference between $I = 0$ and $I = 1$ contributions cancels out, and since the $I = 1$ amplitude is expected to be smooth, it is natural to associate any structure in the combined data with the $I = 0$ resonances. However, it will become apparent that the separate treatment of the neutral and charged channels is necessary to obtain the correct result for the $I = 0$, $D\bar{D}$ dynamics. Since the Born term contribution enters the $D^0\bar{D}^0$ channel only via rescattering, one can expect more events in the D^+D^- channel, which is not the case for the data on hand. In [273] this discrepancy was attributed to the fact that more decay modes were analyzed for the neutral channel in both experiments, and the additional artificial factor of 1/3 was included to compensate for it. We, however, refrain from making any assumptions regarding the nature of the difference and proceed with the given data in a standard way.

While the Belle data [253] is not efficiency corrected, the efficiency decreases by only 10% for the invariant mass region between 3.8 and 4.2 GeV, and therefore, this effect is expected to be negligible considering the resolution of the data itself. In addition, the data is provided

	C_0	C_1	C_2	$\frac{N_2}{N_0} \times 10^2$	$\tilde{\chi}^2_{\text{comb}}$	$\tilde{\chi}^2_{\text{c}}$	$\tilde{\chi}^2_{\text{n}}$
Fit I comb. Belle	−64.5(16.1)	167.7(18.9)	–	2.9(0.9)	0.91	9.84	2.88
Fit II c, n Belle	888.1(16.0)	−2315.1(0.5)	1613.5(11.9)	1.3(0.4)	1.08	0.96	0.98
Fit III c, n BaBar	996.3(103.8)	−2336.1(208.4)	1552.6(118.1)	0.6(0.2)	3.29	2.26	3.24

Table 5.1: Fit parameters entering Eqs. (5.9) and (5.19). Fit I is a fit to a combined $\sigma_c(s) + \sigma_n(s)$ data from the Belle Collaboration [253], while Fit II and Fit III are the fits to the charged and neutral channel data from Belle [253] and BaBar Collaborations [254], respectively. The individual $\bar{\chi}^2_{\text{comb/c/n}} \equiv \chi^2_{\text{comb/c/n}}/\text{d.o.f.}$ show how good each fit describe the combined, charged or neutral data-sets.

in terms of the events distribution, and to compare it with the cross sections, an additional normalization factor has to be introduced as a fitting parameter. This fact limits the possibility of extracting the meaningful two-photon couplings of the resonances or bound states. Even though BaBar Collaboration provides efficiency corrected data, it is given only for the sum of neutral and charged channels. Since the information in each channel separately is essential for our analysis, we opt to use the non-efficiency corrected version of the data in each channel, which, however, suffers from even lower resolution.

5.3.2 $\gamma\gamma \to D\bar{D}$ cross sections

In the analysis of the $\gamma\gamma \to D\bar{D}$ data, we limit ourselves to the region below 4.0 GeV, where the leading contribution is coming from the S and D-wave amplitudes. The cross-sections for individual partial waves in charged (c) or neutral (n) channels are given by

$$\sigma^{(J)}_{c/n,\lambda_1\lambda_2}(s) = (2J+1)\,\frac{\beta(s)}{32\,\pi\,s}\,|h^{(J)}_{c/n,\lambda_1\lambda_2}(s)|^2\,, \tag{5.17}$$

where the following relation between the isospin and particle basis holds

$$\begin{aligned} h^{(J)}_{c,\lambda_1\lambda_2}(s) &= -\frac{1}{\sqrt{2}}\,(h^{(J)}_{0,\lambda_1\lambda_2}(s) + h^{(J)}_{1,\lambda_1\lambda_2}(s))\,, \\ h^{(J)}_{n,\lambda_1\lambda_2}(s) &= -\frac{1}{\sqrt{2}}\,(h^{(J)}_{0,\lambda_1\lambda_2}(s) - h^{(J)}_{1,\lambda_1\lambda_2}(s))\,. \end{aligned} \tag{5.18}$$

As it was mentioned in Sec. 5.3.1, to fit $\gamma\gamma \to D\bar{D}$ data we need to introduce the normalization factor to convert the theoretical cross-section to the number of events from the experimental plot and a factor N_2, which accounts for the $\chi_{c2}(3930)$ couplings. The total cross-section for the charged or neutral channels is then given by

$$\sigma_{c/n}(s) \approx N_0\,\sigma^{(0)}_{c/n,++}(s) + N_2\,\sigma^{(2)}_{c/n,+-}(s)\,, \tag{5.19}$$

where we neglected the helicity-0 component of the D-wave. In addition to the free parameters N_0, N_2, there are also coefficients of the conformal expansion (5.9), which determine the form of the left-hand cuts in (5.2) and have to be fitted to the data. Apart from the standard χ^2 criteria, their number is chosen in a way to ensure that the series (5.9) converges in the physical region. The statistical uncertainties are then propagated using the parametric bootstrap technique (see App. 3.B) for all parameters and derived quantities like pole positions.

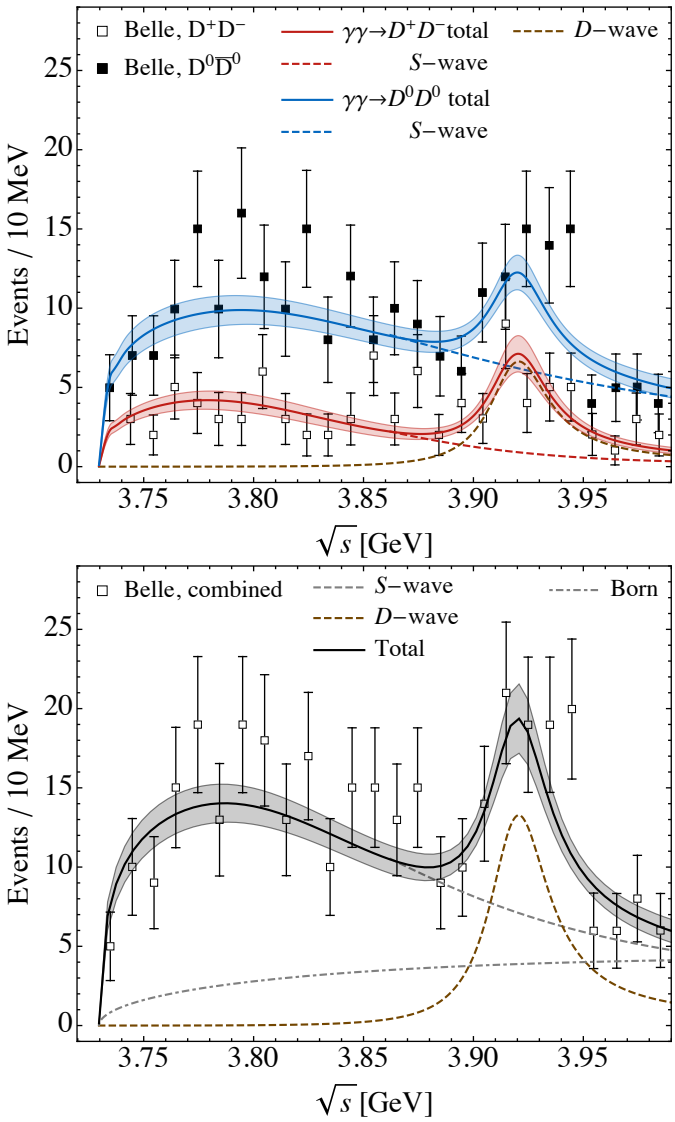

Figure 5.2: Fit results compared to the data from the Belle Collaboration [253]. The top panel shows the charged and neutral cross sections. For comparison, in the bottom panel the sum of both is presented.

As the first step, we consider the combined $\gamma\gamma \to D\bar{D}$ data

$$\sigma_c(s) + \sigma_n(s) \tag{5.20}$$

from the Belle Collaboration [253] alone as an input, similarly as it was done in [267]. We find that the fit to this data is already saturated with only two conformal expansion parameters and $\chi^2_{\rm comb}/\text{d.o.f.} = 0.91$. Their values are listed in Table 5.1 (Fit I). For this fit we find a pole located at the second Riemann sheet with $\sqrt{s_P} = 3765.3(11.4) - i\,57.3(9.5)$ MeV, which is around 100 MeV lower than the estimated values for the $X(3860)$ in [267] and significantly narrower. However, these results can not be directly compared, as the parameterization used in [267] does not establish the pole position in the complex s-plane, and only the mass and the width of the Breit-Wigner resonance are given. However, this fit can be misleading, since it may not describe charged and neutral channels separately. In order to include this additional information, apart from the standard $\chi^2_{\rm comb}/\text{d.o.f.}$ we introduce $\chi^2_{\rm c}/\text{d.o.f.}$ and $\chi^2_{\rm n}/\text{d.o.f.}$ tests,

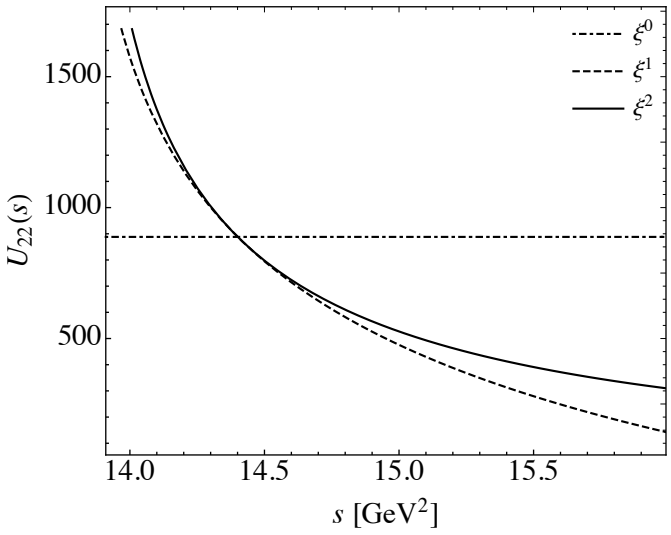

Figure 5.3: Convergence of the conformal expansion in Eq. (5.9) for C_i values from Fit II.

describing how well the given set of parameters reproduce the data in charged and neutral channels, respectively. We find, that even though Fit I accurately describes the combined data, it completely fails to account for the differences in separated data sets with $\chi^2_{\rm c}/\text{d.o.f.} = 9.84$ and $\chi^2_{\rm n}/\text{d.o.f.} = 2.88$.

As a natural continuation, we perform a fit aiming to describe neutral and charged channels simultaneously. The best results are obtained with three conformal expansion parameters leading to $\chi^2_{\rm c}/\text{d.o.f.} = 0.96$ and $\chi^2_{\rm n}/\text{d.o.f.} = 0.98$. If compared to the combined data, this fit gives $\chi^2_{\rm comb}/\text{d.o.f.} = 1.08$. The values of parameters are collected in Table 5.1 (Fit II) and the resulting curves are shown in Fig. 5.2. For this fit, instead of the pole in the complex plane, we find a bound state located under the $D\bar{D}$ threshold at

$$\sqrt{s_B} = 3695(4)\,\text{MeV}\,. \tag{5.21}$$

This bound state is stable against the variation of the s_E parameter leading to negligible systematic uncertainties. We also checked explicitly that adding one more term in the conformal expansion barely changes the χ^2. Note that even though the convergence of U_{22} (see Fig. 5.3) and consequently N_{22} is limited to energies $s > s_L$, the applicability domain of D_{22} (which does not have a left-hand cut) is the whole complex plane and Eq. (5.7) is valid for energies sufficiently lower than the threshold.

From the Fit I we found, that fitting the combined data can lead to wrong results. Therefore, we do not consider the combined dataset of the BaBar data [254], which is efficiency corrected. Instead, we perform an auxiliary fit to the charged and neutral channels, which are not efficiency corrected, to show that even in case of very low data resolution we are able to obtain the aforementioned bound state with $\sqrt{s_{\rm B}} = 3669.4(18.0)$ MeV. The resulting parameters are again tabulated in Table 5.1 (Fit III) and shown in Fig. 5.2.

Regarding the energy region around $\chi_{c2}(3930)$ resonance, all fits provide similar results. While the resonance structure itself is governed by the Breit-Wigner-like parametrization (5.15), the height of the peak is partially defined by the tail of the S-wave contribution. This interplay between S- and D-waves can be studied on the level of angular distribution, for which the data from Belle Collaboration is provided in the region $\sqrt{s} = [3.91 - 3.95]$ GeV. Adopting the parameters of Fit II, we find a good agreement with the data (see Fig. 5.6), showing that for these energies the angular distribution has a characteristic D-wave behavior with a constant shift from the S-wave contribution. Given the quality of the data, one cannot exclude

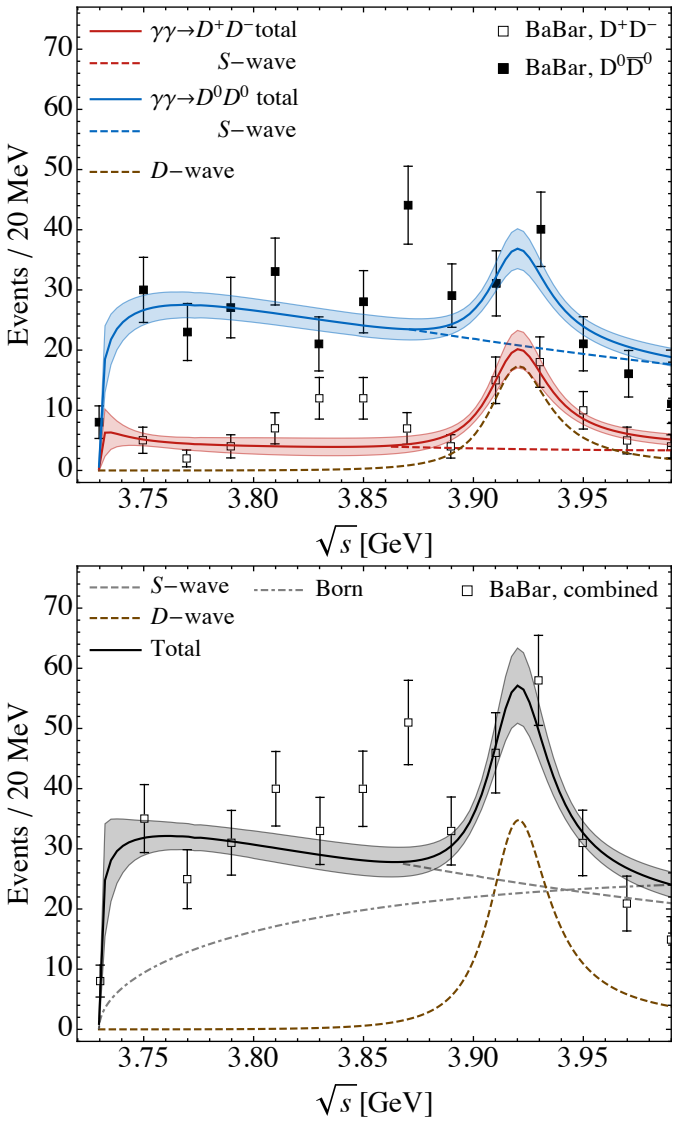

Figure 5.4: Fit results compared to the data from the BaBar Collaboration [254]. The top panel shows the charged and neutral cross sections. For comparison, in the bottom panel the sum of both is presented.

that in the $\chi_{c2}(3930)$ region there is an additional small S-wave contribution from $\chi_{c0}(3930)$, which was recently claimed by the LHCb Collaboration [256, 277] in the $B^+ \to D^+D^-K^+$ decays. However, we refrain from including it (as opposed to [279]), since the $\gamma\gamma \to D\bar{D}$ data will not be able to constrain it.

5.3.3 $e^+e^- \to J/\psi D\bar{D}$ process

By considering only S-wave rescattering in the $D\bar{D}$ channel, the differential cross-section for the process $e^+e^- \to J/\psi D\bar{D}$ can be written as (see App. 5.B for the derivation)

$$\frac{d\sigma}{d\sqrt{s}} = N \frac{\lambda^{1/2}(s, q^2, m_{J/\psi}^2)\, \lambda^{1/2}(s, m_D^2, m_D^2)}{q^6 \sqrt{s}} \left| D_{22}^{-1}(s) \right|^2 , \tag{5.22}$$

where q is the e^+e^- center of mass energy, with λ the Källén function. In Eq.(5.22), similar to Eq.(5.5), the $D\bar{D}$ final state interaction is accounted for through the D_{22} function. In this

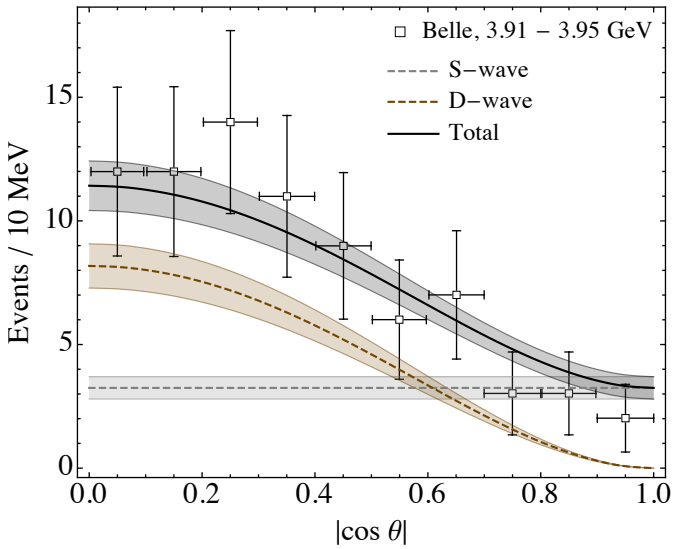

Figure 5.5: Angular distribution of the combined $\gamma\gamma \to D\bar{D}$ data from the Belle Collaboration [253] in the energy range $3.91 - 3.95$ GeV compared to the theoretical curve calculated using the Fit II parameters.

case, however, we use a simple model which only preserves unitarity in the direct s-channel and neglects possible contributions from the crossed channels (i.e. left-hand cuts). The latter are typically suppressed for the three-body decays, but at the same require solving a set of Khuri-Treiman-type equations [111, 112, 228, 280, 281]. This study goes far beyond the scope of this paper and requires precise Dalitz plot data.

With the limitations listed in Sec. 5.3.1, i.e. only a few available experimental points in the near-threshold region, the data from [270] alone is not constraining enough to provide a unique and meaningful solution without introducing additional assumptions. The same observation has been made in [272]. Therefore, we only check the consistency with the $\gamma\gamma \to D\bar{D}$ results by taking the best set of conformal expansion parameters given by Fit II and adjusting only the normalisation constant N in Eq. (5.22). Note, that we excluded the point $\sqrt{s} \sim 3930$ MeV, where we expect a significant $\chi_{c2}(3930)$ contribution. The results for the invariant mass distribution are shown in Fig. 5.6, where we choose the value of the e^+e^- c.m. energy in the middle of the experimental region $9.46-10.87$ GeV. The data is described with $\chi^2/\text{d.o.f} = 1.57$, indicating a very good agreement.

It is worth noting that both the analysis presented in this section and in [272] perform a one-dimensional fit of the binned data without efficiency corrections. However, for the extraction of $X(3860)$ in [270], a multidimensional unbinned amplitude analysis with the generally non-trivial angular distribution was used. Therefore, to determine what structure can be observed in the $e^+e^- \to J/\psi D\bar{D}$ reaction, the amplitudes given in this section need to be checked with complete unbinned data in the fit performed by the experiment itself. For instance, it could be done in the upcoming Belle-II analysis [282].

5.3.4 Analogy to the $\gamma\gamma \to K\bar{K}$ scattering

It is instructive to compare the obtained results for the $\gamma\gamma \to D\bar{D}$ process with a relatively well-known case of $\gamma\gamma \to K\bar{K}$. In the low-lying isoscalar S-wave sector, there are two resonances: $\sigma/f_0(500)$ and $f_0(980)$. While $\sigma/f_0(500)$ is known to be connected almost exclusively to the pion sector, $f_0(980)$ is a quasi-bound $K\bar{K}$ state. If we eliminate the connection to the $\pi\pi$ channel in the coupled-channel $\{\pi\pi, K\bar{K}\}$ dispersive analysis of [2], then $f_0(980)$ resonance

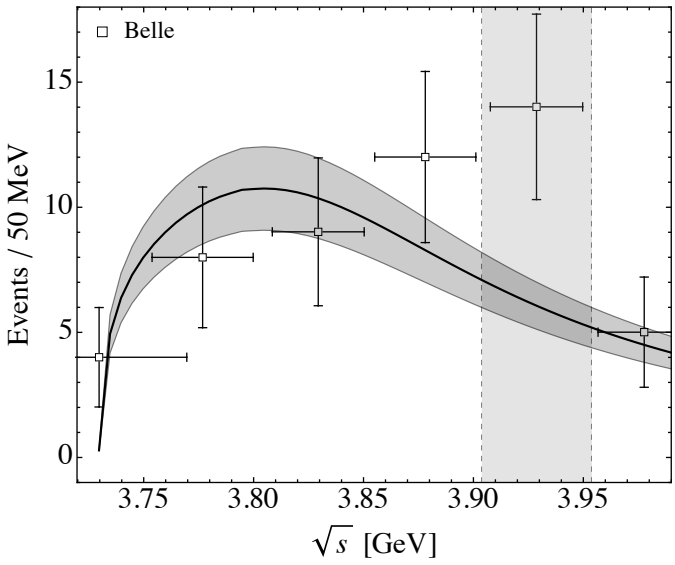

Figure 5.6: The invariant $D\bar{D}$ mass distribution of the $e^+e^- \to J/\psi D\bar{D}$ process measured by the Belle Collaboration [270] compared to the S-wave dispersive result calculated using the Fit II parameters. The gray area covers the region where we expect a significant $\chi_{c2}(3930)$ contribution.

originally located at $\sqrt{s_p} = 993(2)^{+2}_{-1} - i\,21(3)^{+2}_{-4}$ MeV becomes a pure $K\bar{K}$ bound state with a binding energy of $\sqrt{s_B} = 961$ MeV. A similar feature was also observed in unitarized chiral perturbation theory calculations, see for instance [177]. On the level of cross-sections, if we treat $\gamma\gamma \to K\bar{K}\,(I=1)$ case on the same footing as the $\gamma\gamma \to D\bar{D}\,(I=1)$ process by taking only the Born terms[1], then we observe a very similar pattern (compare Fig. 5.7 with upper panels of Fig. 5.2). While in the neutral channel the Born terms enter only via rescattering, it shows up stronger than the charged channel, due to destructive interference of the rescattering contribution with a pure Born amplitude at the level of the cross-section.

Similar to $f_0(980)$, one can also expect that the bound state $\sqrt{s_B} = 3695(4)$ MeV found in the single-channel $\{D\bar{D}\}$ approximation will become a pole on the unphysical Riemann sheet once the channels $\{\pi\pi, K\bar{K}, \eta\eta, ...\}$ will be switched on. However, the couplings to these channels are expected to be strongly suppressed due to their distant location [274].

5.4 Summary and outlook

In this Chapter, we presented a theoretical analysis of the reaction $\gamma\gamma \to D\bar{D}$ from threshold up to 4.0 GeV. In order to account for the $D\bar{D}$ rescattering in the S-wave, we used a partial wave dispersive representation, which implements constraints from analyticity and exact unitarity. The left-hand cut contributions were accounted for by performing a model independent conformal mapping expansion, whose coefficients were fitted to the experimental data. On top of the S-wave, the well-established narrow D-wave resonance $\chi_{c2}(3930)$ was taken into account explicitly in the s-channel.

In the analysis of the data from the Belle [253] and BaBar [254] Collaborations, we found that it is crucial to simultaneously describe both charged $\gamma\gamma \to D^+D^-$ and neutral $\gamma\gamma \to D^0\bar{D}^0$ channels. Within our approach, we found no broad resonance $X(3860)$ currently associated with $\chi_{c0}(2P)$ in PDG (2021) [27]. Instead, we found a bound state, located below $D\bar{D}$ threshold

[1] In the "real" world $\gamma\gamma \to K\bar{K}\,(I=1)$ channel has also a significant contribution from the $a_0(980)$ resonance through the $\{\gamma\gamma, \pi\eta, K\bar{K}\}$ coupled channels.

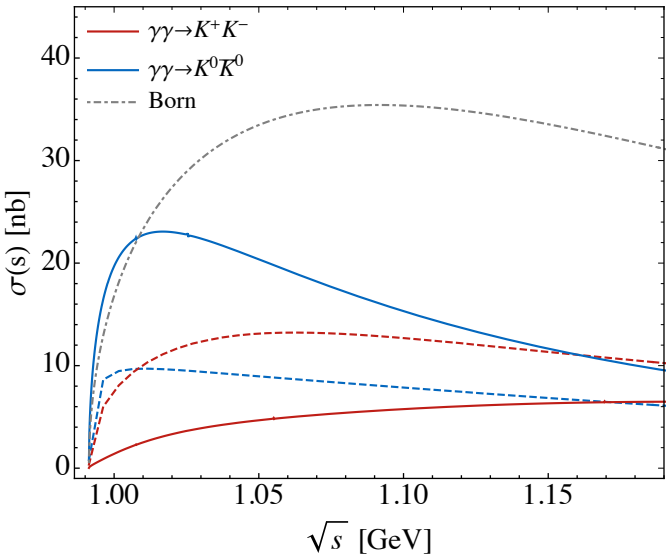

Figure 5.7: The S-wave cross-sections for the reactions $\gamma\gamma \to K^+K^-$ (red) and $\gamma\gamma \to K^0\bar{K}^0$ (blue) under the assumption that $I = 1$ contribution is dominated by the Born terms. Solid curves correspond to the hypothetical situation when there is no coupling to the $\pi\pi$ channel and $f_0(980)$ is a pure bound state just below $K\bar{K}$ threshold, while dashed curves come from the $I = 0$ $\{\gamma\gamma, \pi\pi, K\bar{K}\}$ coupled-channel analysis [2]. The Born contribution is shown as a dot-dashed curve.

at $\sqrt{s_B} = 3695(4)$ MeV. The dataset for the invariant $D\bar{D}$ mass distribution of the $e^+e^- \to J/\psi D\bar{D}$ reaction, in which the $X(3860)$ resonance was reported [270], confirms the consistency of our results. Using the S-wave $D\bar{D}$ final state interaction, we described the $e^+e^- \to J/\psi D\bar{D}$ process reasonably well, by adjusting only the overall normalization.

The bound state in the dispersive analysis without CDD poles qualifies for a molecular state. It is also consistent with other theoretical predictions [274, 275, 283–289] and the absence of the broad near-threshold resonance was recently observed by experimental analysis of the LHCb Collaboration [256, 277]. The detailed study of the properties of the found bound state $X(3695)$, however, requires more refined experimental input which can be achieved at Belle II. For this purpose it may be promising to search for the radiative decay $\psi(3770) \to \gamma X(3695)$, in analogy with $\psi(3770) \to \gamma\chi_{c0}$ radiative decay measurement at BESIII [290]. Furthermore, the existence such state $X(3695)$ may be tested in direct production at PANDA@FAIR.

Appendices

5.A Breit-Wigner approximation for the $\chi_{c2}(3930)$ resonance

The unitarity and analyticity properties of the S-matrix are essential for studying the broad resonances. In general, searching for the poles in the complex s-plane requires a proper analytical continuation of the scattering amplitude (see Sec. 2.2.6). However, the narrow, isolated resonances located far from the relevant thresholds [27] can be approximated employing a standard Breit-Wigner parametrization [291], which is widely used in experimental analyses. Some D-wave resonances in two-photon fusion reactions serve as relevant examples: $a_2(1320)$ in $\gamma\gamma \to \pi\eta$, and $\chi_{c2}(3930)$ in $\gamma\gamma \to D\bar{D}$ (see. Chapter 5). They can be described as the intermediate resonance state process $\gamma\gamma \to R \to MM$, where R is a spin-2 resonance and MM is a meson pair (Fig. 5.8).

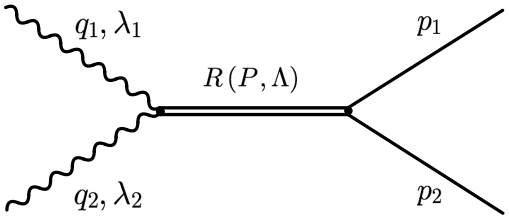

Figure 5.8: The tree-level diagram for the $\gamma\gamma \to R \to MM$ process.

The partial wave amplitudes are then derived from the effective $\Lambda = 2$ Lagrangian for each of the vertices [278]:

$$\begin{aligned} \mathcal{L}_{R\gamma\gamma} &= e^2 g_{R\gamma\gamma} T_{\mu\nu} F^{\mu\lambda} F^{\nu}_{\lambda} \,, \\ \mathcal{L}_{RMM} &= g_{RMM} T^{\mu\nu} \partial_\mu M \partial_\nu M \,, \end{aligned} \tag{5.23}$$

where g_{RMM} and $g_{R\gamma\gamma}$ denote the resonance coupling constants to meson and photon pair respectively. The propagator for the tensor particle with mass m_R has the form [292]:

$$i\mathcal{D}^{\mu\nu\alpha\beta} = i \frac{\sum_\Lambda \varepsilon^{*\mu\nu}(P,\Lambda)\varepsilon^{\alpha\beta}(P,\Lambda)}{P^2 - m_R^2} \,, \tag{5.24}$$

where $\epsilon^{\mu\nu}(P,\Lambda)\,(\Lambda = -2,-1,0,1,2)$ is a symmetric and traceless polarization tensor for which the following completness relation holds:

$$\begin{aligned} \sum_\Lambda \varepsilon^{\mu\nu}(P,\Lambda)\left[\varepsilon^{\alpha\beta}(P,\Lambda)\right]^* &= \frac{1}{2}\left(K^{\mu\alpha}K^{\nu\beta} + K^{\mu\beta}K^{\nu\alpha} - \frac{2}{3}K^{\mu\nu}K^{\alpha\beta}\right) \,, \\ K^{\mu\nu} &= -g^{\mu\nu} + \frac{P^\mu P^\nu}{m_R^2} \,. \end{aligned} \tag{5.25}$$

Using the notation of Fig. 5.8, the invariant amplitude of the s-channel process is given by

$$\begin{aligned} \mathcal{M} = -2ie^2 g_{R\gamma\gamma} g_{RMM} p_{1\mu} p_{2\nu} &\frac{\frac{1}{2}\left(K^{\mu\alpha}K^{\nu\beta} + K^{\mu\beta}K^{\nu\alpha} - \frac{2}{3}K^{\mu\nu}K^{\alpha\beta}\right)}{s - m^2} \\ &\times (p_{1\alpha}\epsilon_1^\lambda - p_1^\lambda \epsilon_{1\lambda})(p_{2\lambda}\epsilon_{2\beta} - p_{2\beta}\epsilon_{2\lambda}) \,, \end{aligned} \tag{5.26}$$

where $\epsilon_i^\lambda \equiv \epsilon(p_i, \lambda_i)$. In the center-of-mass (c.m.) system (see App. 3.A) for this choice of Lagrangian the physical amplitude with equal photon helicities $(\Lambda = 0)$[2] vanishes and the resonance contributes only in case of opposite photon helicities $(\Lambda = 2)$:

$$\begin{aligned} \mathcal{M}_{++} &= 0 \,, \\ \mathcal{M}_{+-} &= -ie^2 g_{R\gamma\gamma} g_{RMM} \frac{1}{8} \frac{s^2\beta^2(s)\sin^2(\theta)}{s - m_R^2} \,, \end{aligned} \tag{5.27}$$

where $\beta(s) = 2p(s)/\sqrt{s}$, $p(s)$ is a c.m. momentum and θ is a scattering angle. The $J = 2$ resonance amplitude is derived from the above equation using the inverse Wiegner transformation:

$$h^{(2)}_{+-}(s) = -e^2 g_{R\gamma\gamma} g_{RMM} \frac{1}{10\sqrt{6}} \frac{s^2\beta^2(s)}{s - m_R^2} \,. \tag{5.28}$$

[2] In general, $\mathcal{M}_{++} \neq 0$, but is strongly suppressed.

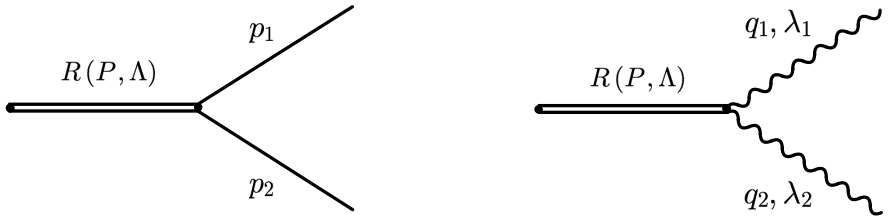

Figure 5.9: The $R \to MM$ (left) and $R \to \gamma\gamma$ (right) decay processes.

Therefore, when additional mechanisms are absent, the total D-wave cross section has a following form

$$\sigma^{(2)}(s) = \frac{e^4 g^2_{RMM} g^2_{R\gamma\gamma}}{1920\pi s} \frac{s^4 \beta^5(s)}{(s - m_R^2)^2}\,, \tag{5.29}$$

where the threshold factors appear automatically.

In general, the absolute values of couplings g_{RMM} and $g_{R\gamma\gamma}$ can be extracted from the radiative decay widths of the resonance in question to correponding channels.
The amplitudes for these decays, using the notations of Fig. 5.9 are

$$\begin{aligned} \mathcal{M}_{RMM} &= g_{RMM} p_1^\mu p_2^\nu \varepsilon_{\mu\nu}(P,\Lambda)\,, \\ \mathcal{M}_{R\gamma\gamma} &= -2ie^2 g_{R\gamma\gamma} \varepsilon_{\mu\nu}(P,\Lambda) \left(p_1^\mu \epsilon_1^{\lambda *} - p_1^\lambda \epsilon_1^{\mu *}\right) \left(p_{2\lambda} \epsilon_2^{\nu *} - p_2^\nu \epsilon^*_{2\lambda}\right)\,. \end{aligned} \tag{5.30}$$

Then the partial can be calculated, performing a sum over polarizations:

$$\begin{aligned} \Gamma_{RMM} &= \frac{1}{2} \int \frac{d^3\bar{p}_1}{(2\pi)^3 2E_{p_1}} \int \frac{d^3\bar{p}_2}{(2\pi)^3 2E_{p_2}} (2\pi)^4 \delta^4(P - p_1 - p_2) \frac{1}{5} \sum_\Lambda |\mathcal{M}_{RMM}|^2 = \frac{g^2_{RMM}}{60\pi} \frac{p^5(m_R)}{m_R^2}\,, \\ \Gamma_{R\gamma\gamma} &= \frac{1}{2} \int \frac{d^3\bar{q}_1}{(2\pi)^3 (2|\bar{q}_1|)^2} 2\pi \delta(M_R - 2|\bar{q}_1|) \frac{1}{5} \sum_\Lambda |\mathcal{M}_{R\gamma\gamma}|^2 = \frac{e^4 m_R^3}{80\pi} g^2_{R\gamma\gamma}\,, \end{aligned} \tag{5.31}$$

and the couplings can be extracted given the experimental values of Γ_{RMM} and $\Gamma_{R\gamma\gamma}$. For the $\chi_{c2}(3930)$ resonance the numerical values of $\Gamma_{\chi_{c2}(3930)D\bar{D}}$ and $\Gamma_{\chi_{c2}(3930)\gamma\gamma}$ have not been measured and the product of correspondimg couplings is absorbed into the cross section normalization parameter (see Chapter 5).

The Lagrangian-based result for the cross section in Eq. 5.29 needs to be modified, since the physical resonances have the finite width Γ_R, which then enters the denominator:

$$\sigma^{(2)}(s) = \frac{e^4 g^2_{RMM} g^2_{R\gamma\gamma}}{1920\pi s} \frac{s^4 \beta^5(s)}{(s - m_R^2)^2 + m_R^2 \Gamma_R^2}\,. \tag{5.32}$$

With a constant width, however, the cross section grows with energy due to the factor $\beta^5(s) \sim p^5(s)$ in the numerator. In general, the factor $p^{2L+1}(s)$ in Breit-Wigner parametrization ensures a proper threshold behaviour and is often introduced manually if there is a relevant threshold nearby, together with an energy-dependent expression for the width in denominator

$$\Gamma_R \longrightarrow \Gamma(s) = \Gamma_R \left(\frac{p(s)}{p(M_R^2)}\right)^{2L+1}\,. \tag{5.33}$$

Among the different methods to supress the rapid growth of the width itself, the phenomenological *Blatt-Weisskopf form factor* $B_L(s)$ is commonly used [293]. In the D-wave, for instance, it has the following form:

$$B_2(s) = \frac{F_2(p(s)r)}{F_2(p(m_R^2)r)}, \quad F_2(x) = \frac{1}{9 + 3x^2 + x^4}\,, \tag{5.34}$$

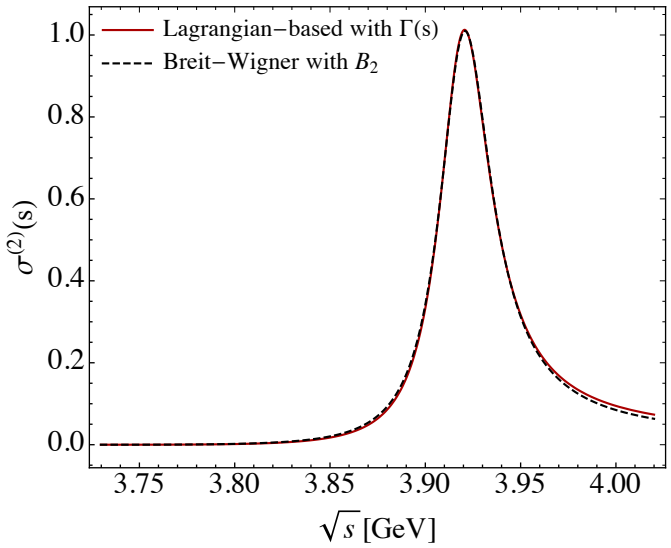

Figure 5.10: Comparison between Lagrangian-based cross section with energy-dependend width and Breit-Wigner parametrization including Blatt-Weisskopf factor for the $\chi_{c2}(3930)$ resonance in $\gamma\gamma \to D\bar{D}$ scattering, both normalized to 1 at the resonance peak position. Here interaction radius is taken as $r = 1.5$ GeV^{-1}.

where r is an effective interaction radius, which gives out the asymmetry of the resonance line shape. The numerical values of this parameter vary around several GeV^{-1} in different hadronic reactions. While the presence of Blatt-Weisskopf barrier factor both in the numerator of the cross section and in the width can improve the data description, it adds an additional uncertainty since the value of interaction radius can not be precisely defined for all resonances.

The Breit-Wigner parametrization with Blatt-Weisskopf factor [254] for a resonance, decaying predominantly in one channel has a following form:

$$\begin{aligned} \mathrm{BW}(s) &= \left(\frac{p(s)}{p(m_R^2)}\right)^{2L+1} \frac{m_R}{\sqrt{s}} \frac{B_L^2(s)}{(s-m_R^2)^2 + m_R^2 \Gamma_{\mathrm{BL}}^2(s)}\,, \\ \Gamma_{\mathrm{BL}}(s) &= \Gamma_R \left(\frac{p(s)}{p(m_R^2)}\right)^{2L+1} \frac{m_R}{\sqrt{s}} B_L^2(s)\,, \end{aligned} \tag{5.35}$$

where the factor $m_R/\sqrt{s} \approx 1$ scales the resonance effect on the energies far from the peak. In case of multiple relevant channels Eq. (5.35) can be generalized by taking the sum of the respective widths.

For the $\chi_{c2}(3930)$ resonance on the level of cross section the difference between the Lagrangian-based result (5.29) with energy dependent width (5.33) and the Breit-Wigner parametrization (5.35) is negligible (see Fig. 5.10), therefore, the Blatt-Weisskopf factor can be omitted.

5.B Cross section of the $e^+e^- \to J/\psi D\bar{D}$ process

The process $e^+e^- \to J/\psi D\bar{D}$ can be described by the diagram in Fig. 5.11 assuming that the $D\bar{D}$ pair comes from the resonance X. The cross section for this reaction is given by an

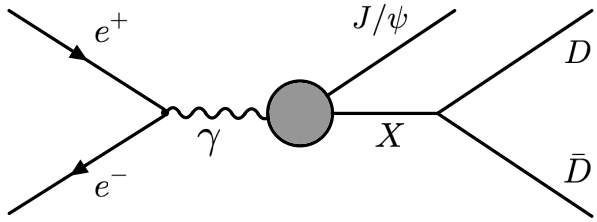

Figure 5.11: Feynman diagram for the process $e^+e^- \to J/\psi D\bar{D}$ assuming that the $D\bar{D}$ pair comes from the resonance X.

integral over the phase space of the three particles in final state

$$\sigma = \frac{1}{2q^2}\int\left(\frac{d^3\vec{p}_{J/\psi}}{(2\pi)^3 2E_{J/\psi}}\right)^{\text{c.m.}}\int\left(\frac{d^3\vec{p}_D}{(2\pi)^3 2E_D}\right)^{\text{r.f.}}\int\left(\frac{d^3\vec{p}_{\bar{D}}}{(2\pi)^3 2E_{\bar{D}}}\right)^{\text{r.f.}} \times (2\pi)^4\delta^4\left(q - p_{J/\psi} - p_D - p_{\bar{D}}\right)^{\text{r.f.}}|\mathcal{M}_{e^+e^-\to J/\psi D\bar{D}}|^2\,, \tag{5.36}$$

where c.m. denotes the e^+e^- center of mass frame, r.f denotes the $X(D\bar{D})$ rest frame (see Fig. 5.12) and $\mathcal{M}_{e^+e^-\to J/\psi D\bar{D}}$ is the amplitude of the $e^+e^- \to J/\psi D\bar{D}$ process; here $q = p_{e^+} + p_{e^-}$. The integration over $d\phi_{J/\psi}$ in this case is trivial and brings an overall factor of 2π and the integration over $d^3\vec{p}_{\bar{D}}$ gives

$$\sigma = \frac{1}{2q^2}\frac{1}{(2\pi)^4}\int\left(\frac{|\vec{p}_{J/\psi}|^2 d|\vec{p}_{J/\psi}|d\cos\theta_{J/\psi}}{2E_{J/\psi}}\right)^{\text{c.m.}}\int\left(\frac{d^3\vec{p}_D}{2E_D}\right)^{\text{r.f.}}\left(\frac{1}{2E_{\bar{D}}}\right)^{\text{r.f.}} \times \delta\left(\sqrt{s} - 2\sqrt{\vec{p}_D^{\,2} + m_D^2}\right)^{\text{r.f.}}|\mathcal{M}_{e^+e^-\to J/\psi D\bar{D}}|^2\,, \tag{5.37}$$

where we introduce $\sqrt{s} = (q^0 - E_{J/\psi})^{\text{r.f.}}$. From the energy conserving δ-function in Eq. (5.37) follows that $\sqrt{s} = (E_D + E_{\bar{D}})^{\text{r.f.}} = (2E_D)^{\text{r.f.}}$. We note, that in arbitrary frame $s = (p_D + p_{\bar{D}})^2$. To perform the integration over $d|\vec{p}_D|$, we use

$$\delta\left(\sqrt{s} - 2\sqrt{\vec{p}_D^{\,2} + m_D^2}\right) = \frac{\delta\left(|\vec{p}_D| - \frac{1}{2\sqrt{s}}\lambda^{1/2}(s, m_D^2, m_D^2)\right)}{2\frac{|\vec{p}_D|}{\sqrt{\vec{p}_D^{\,2}+m_D^2}}} = \frac{2E_{\bar{D}}}{4|\vec{p}_D|}\delta\left(|\vec{p}_D| - \frac{1}{2\sqrt{s}}\lambda^{1/2}(s, m_D^2, m_D^2)\right)\,, \tag{5.38}$$

where $\lambda(x, y, z)$ is a standard Källén function (see cf. App. 3.A). Therefore,

$$\begin{aligned}\sigma &= \frac{1}{2q^2}\frac{1}{(2\pi)^4}\int\left(\frac{|\vec{p}_{J/\psi}|^2 d|\vec{p}_{J/\psi}|d\cos\theta_{J/\psi}}{2E_{J/\psi}}\right)^{\text{c.m}}\int\left(\frac{|\vec{p}_D|^2 d|\vec{p}_D|d\Omega_D}{2E_D}\right)^{\text{r.f}} \\ &\quad\times\frac{1}{4|\vec{p}_D|}\delta\left(|\vec{p}_D| - \frac{1}{2\sqrt{s}}\lambda^{1/2}(s, m_D^2, m_D^2)\right)|\mathcal{M}_{e^+e^-\to J/\psi D\bar{D}}|^2 \\ &= \frac{1}{2q^2}\frac{1}{(2\pi)^4}\frac{1}{\sqrt{s}}\left(\frac{|\vec{p}_{J/\psi}|^2 d|\vec{p}_{J/\psi}|d\cos\theta_{J/\psi}}{2E_{J/\psi}}\right)^{\text{c.m.}}\left(\frac{|\vec{p}_D|d\Omega_D}{4}\right)^{\text{r.f.}}|\mathcal{M}_{e^+e^-\to J/\psi D\bar{D}}|^2\,.\end{aligned} \tag{5.39}$$

where we imply $|\vec{p}_D| = \frac{1}{2\sqrt{s}}\lambda^{1/2}(s, m_D^2, m_D^2)$. In the end we are aiming to obtain the differential cross section $d\sigma/d\sqrt{s}$, therefore, using:

$$s = (q - p_{J/\psi})^2 = q^2 - 2\sqrt{q^2}E_{J\psi} + m_{J/\psi}^2\,, \quad d\sqrt{s} = -\frac{\sqrt{q^2}}{\sqrt{s}}\frac{|\vec{p}_{J/\psi}|}{E_{J/\psi}}d|\vec{p}_{J/\psi}|\,, \tag{5.40}$$

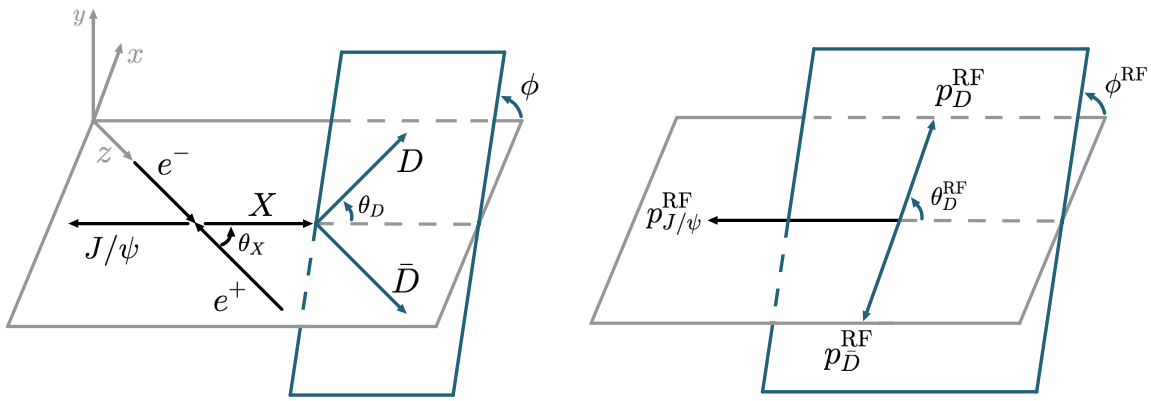

Figure 5.12: Kinematics of the $e^+e^- \to J/\psi D\bar{D}$ process. Left panel: e^+e^- center-of-mass frame; right panel: $D\bar{D}$ pair rest frame. Here $\phi^{\mathrm{RF}} = \phi$.

the differential cross section yields

$$\frac{d\sigma}{d\Omega_D d\cos\theta_{J/\psi} d\sqrt{s}} = \frac{1}{16q^2\sqrt{q^2}} \frac{1}{(2\pi)^4} |\vec{p}_{J/\psi}|^{\mathrm{c.m.}} |\vec{p}_D|^{\mathrm{r.f.}} |\mathcal{M}_{e^+e^-\to J/\psi D\bar{D}}|^2 \,. \tag{5.41}$$

In the c.m. frame for the J/ψ momentum holds

$$|\vec{p}_{J/\psi}|^{\mathrm{c.m.}} = \frac{1}{2\sqrt{q^2}} \lambda^{1/2}(s, q^2, m_{J/\psi}^2) \,, \tag{5.42}$$

and Eq. 5.41 transforms to

$$\frac{d\sigma}{d\Omega_D d\cos\theta_{J/\psi} d\sqrt{s}} = \frac{\lambda^{1/2}(s, m_D^2, m_D^2)\lambda^{1/2}(s, q^2, m_{J/\psi}^2)}{(2\pi)^4 64 q^4 \sqrt{s}} |\mathcal{M}_{e^+e^-\to J/\psi D\bar{D}}|^2 \,. \tag{5.43}$$

Now we want to put the amplitude $\mathcal{M}_{e^+e^-\to J/\psi D\bar{D}}$ under closer inspection. First, for the ultra-relativistic e^+e^- pair we can neglect their masses, so that

$$\mathcal{M}_{e^+e^-\to J/\psi D\bar{D}} = \bar{v}(p_{e^+}, s_{e^+})(ie\gamma^\mu)u(p_{e^-}, s_{e^-}) \left(\frac{-i}{q^2} g_{\mu\mu'}\right) (-ie) J^{\mu'}_{\gamma^*\to J/\psi D\bar{D}} \,. \tag{5.44}$$

The averaging over the initial states and summing over the final states reads as

$$\begin{aligned} \overline{\sum_i} \sum_f |\mathcal{M}_{e^+e^-\to J/\psi D\bar{D}}|^2 = \frac{1}{2}\sum_{s_{e^-}} \frac{1}{2}\sum_{s_{e^+}} \sum_{\lambda_{J/\psi}} \frac{e^4}{q^4} \\ \times \bar{v}(p_{e^+}, s_{e^+})\gamma^\mu u(p_{e^-}, s_{e^-}) g_{\mu\mu'} J^{\mu'}_{\gamma^*\to J/\psi D\bar{D}} \\ \times \bar{u}(p_{e^-}, s_{e^-})\gamma^\nu v(p_{e^+}, s_{e^+}) g_{\nu\nu'} J^{\nu'}_{\gamma^*\to J/\psi D\bar{D}} \,, \end{aligned} \tag{5.45}$$

where $\lambda_{J/\psi}$ denotes J/ψ helicity. Using $\sum\limits_{s_{e^-}} u(p_{e^-}, s_{e^-})\bar{u}(p_{e^-}, s_{e^-}) = \not{p}_{e^-}$, we obtain

$$\begin{aligned} \overline{\sum_i} \sum_f |\mathcal{M}_{e^+e^-\to J/\psi D\bar{D}}|^2 &= \frac{e^4}{q^4}\frac{1}{4}\mathrm{Tr}\left\{\not{p}_{e^+}\gamma^\mu \not{p}_{e^-}\gamma^\nu\right\} g_{\mu\mu'}g_{\nu\nu'} \sum_{\lambda_{J/\psi}} J^{\mu'}_{\gamma^*\to J/\psi D\bar{D}} J^{\nu'*}_{\gamma^*\to J/\psi D\bar{D}} \\ &= \frac{e^4}{q^4}\left(p^\mu_{e^+}p^\nu_{e^-} + p^\nu_{e^+}p^\mu_{e^-} - (p_{e^-}\cdot p_{e^+})g^{\mu\nu}\right)\left(g_{\mu\mu'} - \frac{q_\mu q_{\mu'}}{q^2}\right) \\ &\quad \times \left(g_{\nu\nu'} - \frac{q_\nu q_{\nu'}}{q^2}\right) \sum_{\lambda_{J/\psi}} J^{\mu'}_{\gamma^*\to J/\psi D\bar{D}} J^{\nu'*}_{\gamma^*\to J/\psi D\bar{D}} \,, \end{aligned} \tag{5.46}$$

since $\mathrm{Tr}\{\gamma^\mu\gamma^\nu\gamma^\rho\gamma^\sigma\} = 4(g^{\mu\nu}g^{\rho\sigma} - g^{\mu\rho}g^{\nu\sigma} + g^{\mu\sigma}g^{\nu\rho})$. We inserted the terms $\sim q_\mu q_{\mu'}, q_\nu q_{\nu'}$ as they give zero upon the contraction with the leptonic tensor and for which holds:

$$g_{\mu\mu'} - \frac{q_\mu q_{\mu'}}{q^2} = \sum_{\lambda_\gamma=-1,0,+1} \epsilon_\mu(q,\lambda_\gamma)\epsilon^*_{\mu'}(q,\lambda_\gamma)\,. \tag{5.47}$$

Therefore, we can rewrite Eq. 5.46:

$$\begin{aligned}\overline{\sum_i}\sum_f |\mathcal{M}_{e^+e^-\to J/\psi D\bar{D}}|^2 &= \frac{e^4}{q^4}\left(p^\mu_{e^+}p^\nu_{e^-} + p^\nu_{e^+}p^\mu_{e^-} - \frac{q^2}{2}g^{\mu\nu}\right)\sum_{\lambda_\gamma}\sum_{\lambda'_\gamma}\epsilon_\mu(q,\lambda_\gamma)\epsilon^*_\nu(q,\lambda'_\gamma) \\ &\quad\times\sum_{\lambda_{J/\psi}}\left(\epsilon_{\mu'}(q,\lambda_\gamma)J^{\mu'}_{\gamma^*\to J/\psi D\bar{D}}\right)\left(\epsilon_{\nu'}(q,\lambda'_\gamma)J^{\nu'}_{\gamma^*\to J/\psi D\bar{D}}\right)^* \\ &= \frac{e^4}{q^4}\left(p^\mu_{e^+}p^\nu_{e^-} + p^\nu_{e^+}p^\mu_{e^-} - \frac{q^2}{2}g^{\mu\nu}\right) \\ &\quad\times\sum_{\lambda_\gamma}\sum_{\lambda'_\gamma}\epsilon_\mu(q,\lambda_\gamma)\epsilon^*_\nu(q,\lambda'_\gamma)\sum_{\lambda_{J/\psi}}H_{\lambda_\gamma\lambda_{J/\psi}}H^*_{\lambda'_\gamma\lambda_{J/\psi}}\,,\end{aligned} \tag{5.48}$$

where $H_{\lambda_\gamma\lambda_{J/\psi}}$ denotes the helicity amplitude. In the c.m. system

$$\begin{aligned} p_{e^-} &= \left(\frac{\sqrt{q^2}}{2},0,0,+\frac{\sqrt{q^2}}{2}\right), \quad \epsilon^\mu(q,\lambda_\gamma=+1) = \left(0,-\frac{1}{\sqrt{2}},-\frac{i}{\sqrt{2}},0\right), \\ p_{e^+} &= \left(\frac{\sqrt{q^2}}{2},0,0,-\frac{\sqrt{q^2}}{2}\right), \quad \epsilon^\mu(q,\lambda_\gamma=+1) = \left(0,+\frac{1}{\sqrt{2}},-\frac{i}{\sqrt{2}},0\right), \\ q &= \left(\sqrt{q^2},0,0,0\right), \qquad\qquad \epsilon^\mu(q,\lambda_\gamma=0) = (0,0,0,1)\,, \end{aligned} \tag{5.49}$$

so that we can evaluate the following expression

$$\left(p^\mu_{e^+}p^\nu_{e^-} + p^\nu_{e^+}p^\mu_{e^-} - \frac{q^2}{2}g^{\mu\nu}\right)\epsilon_\mu(q,\lambda_\gamma)\epsilon^*_\nu(q,\lambda'_\gamma) = -\frac{q^2}{2}\delta_{\lambda_\gamma 0}\delta_{\lambda'_\gamma 0} - \frac{q^2}{2}(-\delta_{\lambda_\gamma\lambda'_\gamma})\,. \tag{5.50}$$

Therefore, for $\lambda_\gamma = \lambda'_\gamma = 0$

$$\left(p^\mu_{e^+}p^\nu_{e^-} + p^\nu_{e^+}p^\mu_{e^-} - \frac{q^2}{2}g^{\mu\nu}\right)\epsilon_\mu(q,\lambda_\gamma)\epsilon^*_\nu(q,\lambda'_\gamma) = 0\,, \tag{5.51}$$

and for $\lambda_\gamma = \lambda'_\gamma = +1$ or $\lambda_\gamma = \lambda'_\gamma = -1$

$$\left(p^\mu_{e^+}p^\nu_{e^-} + p^\nu_{e^+}p^\mu_{e^-} - \frac{q^2}{2}g^{\mu\nu}\right)\epsilon_\mu(q,\lambda_\gamma)\epsilon^*_\nu(q,\lambda'_\gamma) = \frac{q^2}{2}\,. \tag{5.52}$$

Since due to parity $H_{+1\lambda_{J/\psi}} = H_{-1\lambda_{J/\psi}}$ in the unpolarized case,

$$\overline{\sum_i}\sum_f |\mathcal{M}_{e^+e^-\to J/\psi D\bar{D}}|^2 = \frac{e^4}{q^2}\sum_{\lambda_{J/\psi}}|H_{+1\lambda_{J/\psi}}|^2\,, \tag{5.53}$$

and the resulting differential cross section is

$$\frac{d\sigma}{d\Omega_D d\cos\theta_{J/\psi} d\sqrt{s}} = \frac{e^4}{(2\pi)^4 64 q^6\sqrt{s}}\lambda^{1/2}(s,m_D^2,m_D^2)\lambda^{1/2}(s,q^2,m^2_{J/\psi})|H_{+1\lambda_{J/\psi}}|^2\,, \tag{5.54}$$

where $H_{+1\lambda_{J/\psi}}$ is helicity amplitude in e^+e^- c.m., where the resonance X is emitted at angle θ_X and X decays in plane with azimuthal angle $\phi^*_{J/\psi}$. We assume, that close to threshold this amplitude depends only on the $D\bar{D}$ invariant mass so that the integration over $d\Omega_D$ gives 4π and over $d\cos\theta_{J/\psi}$ gives 2, resulting in

$$\frac{d\sigma}{d\sqrt{s}} = \frac{e^4}{(2\pi)^3 32 q^6 \sqrt{s}} \lambda^{1/2}(s, m_D^2, m_D^2)\lambda^{1/2}(s, q^2, m_{J/\psi}^2)|H_{+1\lambda_{J/\psi}}|^2 \,. \tag{5.55}$$

Following the arguments from Sec. 5.3.3, the production of the resonance X in $D\bar{D}$ final state interaction can be described by the inverse of the D_{22} function. Finally, by absorbing all numerical prefactors into the normalisation constant N and obtain the cross section from Eq. 5.22:

$$\frac{d\sigma}{d\sqrt{s}} = N \frac{\lambda^{1/2}(s, q^2, m_{J/\psi}^2)\lambda^{1/2}(s, m_D^2, m_D^2)}{q^6\sqrt{s}} |D_{22}^{-1}(s)|^2 \,. \tag{5.56}$$

Chapter 6

Thesis summary and outlook

In this thesis, we have analysed various hadronic processes using the dispersive approach, which comprises the analyticity and unitarity constraints of the S-matrix. Here, we summarise the obtained results and provide a brief overview of the prospects for future work.

First, we presented the results of the data-driven dispersive analysis of the S-wave $\pi\pi \to \pi\pi$ and $\pi K \to \pi K$ reactions aimed primarily to study the properties of $\sigma/f_0(500)$, $f_0(980)$ and $\kappa/K^*(700)$ resonances. For the πK system, we performed the single-channel, and for the $\pi\pi$ system, both single and coupled-channel analyses of the existing experimental data were performed. In addition, we supplemented the data input by the threshold constraints and Adler zeros from χPT for physical pion mass. By replacing the experimental data with the pseudo data of high precision generated from the sophisticated Roy and Roy-Steiner analyses, we found that the obtained pole parameters are stable, thus justifying the proposed treatment. We also note that our approach does not suffer from the spurious poles in contrast to the K-matrix approach commonly used for the resonance analysis. This advantage manifested itself in the analysis of the lattice $\pi\pi$ data for $m_\pi = 236, 391$ MeV and πK data for $m_\pi = 239$ MeV, which allowed to extact the $\sigma/f_0(500)$ and $\kappa/K^*(700)$ pole parameters in contrast to the simple K-matrix parametrisation. We compared the results for the unphysical pion masses with existing UχPT predictions, which allows to shed light on the structure and dynamics of $\sigma/f_0(500)$ resonance, which for the large pion mass appears as the $\pi\pi$ bound state.

We then utilised the obtained coupled-channel Omnès function, which characterises two pions final state interaction in the two-photon fusion processes. The coupled-channel treatment in the S-wave allowed us to simultaneously reproduce the $\sigma/f_0(500)$ and $f_0(980)$ resonances, resulting in reasonable agreement with the experimental data for the real photon case. In addition, we calculated the two-photon couplings and decay width of $\sigma/f_0(500)$ and $f_0(980)$ resonances, with obtained results being consistent with other theoretical analyses. We also calculated the pion dipole polarizabilities, which show some tension with the current χPT prediction for the neutral pion case, indicating the importance of ω left-hand cut contribution. For the tensor resonance $f_2(1270)$, we adopted the single-channel dispersive approach supplemented by the vector-meson exchange left-hand cuts contribution. This D-wave treatment introduced the coupling of the photon, vector and pseudoscalar meson fields $g_{VP\gamma}$, which is the only parameter in our approach fitted to the real photon data. In this manner, we predicted the cross sections for the single- and double-virtual $\gamma^{(*)}\gamma^* \to \pi\pi$ processes in the low spacelike virtuality regime. The single virtual results have yet to be confronted with the upcoming data from the BESIII Collaboration to confirm the validity of the dispersive technique further to ensure the correctness of the input to the HLbL scattering part of the $(g-2)_\mu$ and to further improve on the theoretical precision.

Third, we considered the $\gamma\gamma \to D\bar{D}$ reaction, which is expected to produce two charmonium-like resonances $\chi_{c0}(2P)$ and $\chi_{c2}(2P)$. We described the narrow tensor $\chi_{c2}(3930)$ resonance using the Breit-Wigner parametrisation, while for the S-wave, we implemented a partial-wave dispersion representation to account for the $D\bar{D}$ rescattering. The simultaneous treatment of the charged and neutral channel appears crucial to establishing the absence of the broad

resonance $X(3860)$, currently associated with $\chi_{c0}(2P)$. Instead, we have found a $D\bar{D}$ bound state, located slightly below the threshold, which may qualify for the $D\bar{D}$ molecule. This finding was further reinforced by the description of the related $e^+e^- \to J/\psi D\bar{D}$ process.

For all processes considered in this thesis, we established that provided sufficient data input from the left-hand cuts; we are able to predict the stable results for several observables.

As an outlook of our research, we would like to outline several prospects.

Regarding the $\pi\pi$ and πK scattering, we mentioned that the current formalism has to be extended to allow for the CDD poles, for instance, ρ or K^*. In addition, the slight discrepancy between our $\kappa/K^*(700)$ pole position and the result obtained in the Roy-like framework indicates that the proper coupled-channel treatment is needed for the πK scattering as well. As for the $\pi\pi$ scattering, we note that currently, the coupled-channel data from lattice is available only for pion mass value $m_\pi = 391$ MeV; however, we anticipate that once the result for the lower pion masses is achieved, the application of our approach will be relatively straightforward. On the other hand, for the $D\bar{D}$ system, the lattice results are available from the coupled-channel system, and hence, we are motivated to extend our current framework to the coupled $\{D\bar{D}, D_s\bar{D}_s\}$ scattering as well. Currently, the quality of experimental data leaves no realistic opportunity to go beyond the single-channel final-state interaction for the $\gamma\gamma \to D\bar{D}$. In addition, the question of the χ_{c0} presence in this reaction remains open. We believe that with more refined experimental input, which is achievable at Belle II, we could study the properties of obtained bound state $X(3695)$ in more detail. The nature of this state can also be tested by the future PANDA@FAIR experiment. On the subject of already existing data, we consider the study of the $J/\psi J/\psi$ scattering, recently measured by LHCb [92] quite promising. The developed approach can be further extended to study other charmonium and even bottomonium systems.

As a natural continuation of our two-photon project we consider the $\gamma\gamma \to \pi^0\eta, K\bar{K}$ scattering. We have already described both real and single-virtual $\gamma\gamma^{(*)} \to \pi^0\eta$ process in our earlier works [65, 217], resulting in a reasonable description of the real photon data from Belle [202]. However, in order to provide a data-driven input from $a_0(980)$ resonance to HLbL part of $(g-2)_\mu$ in the same manner as it was done for $f_0(980)$ resonance in [81], the coupled-channel $\{\pi^0\eta, K\bar{K}\}$ treatment has to be modified. Since there is no experimental data for the $\pi^0\eta$ phase shifts currently available, we can follow the approach used in our $\gamma\gamma \to D\bar{D}$ study and fit the conformal expansion coefficients directly to the cross section data. The cross sections for the single-virtual case with modified hadronic rescattering part are then to be confronted with the upcoming data from BESIII.

Overall, we want to emphasise that among all physical interplays, the most important one is the interaction between theory and experiment. Any theoretical prediction or analysis is immaterial until confronted with experimental data, and therefore, we look forward to further testing our approach in the light of growing experimental capabilities. Meanwhile, the partial-wave dispersive approach developed in this work provides a very powerful tool for forthcoming resonance analysis by both experimental as well as lattice collaborations.

Bibliography

[1] I. Danilkin, O. Deineka, and M. Vanderhaeghen, "Dispersive analysis of the $\gamma^*\gamma^* \to \pi\pi$ process", Phys. Rev. D **101**, 054008 (2020), arXiv:1909.04158 [hep-ph].

[2] I. Danilkin, O. Deineka, and M. Vanderhaeghen, "Data-driven dispersive analysis of the $\pi\pi$ and πK scattering", Phys. Rev. D **103**, 114023 (2021), arXiv:2012.11636 [hep-ph].

[3] O. Deineka, I. Danilkin, and M. Vanderhaeghen, "Dispersive analysis of the $\gamma\gamma \to D\bar{D}$ data and the confirmation of the $D\bar{D}$ bound state", Phys. Lett. B **827**, 136982 (2022), arXiv:2111.15033 [hep-ph].

[4] O. Deineka, I. Danilkin, and M. Vanderhaeghen, "On the Importance of Left-hand Cuts in the $\gamma\gamma^* \to \pi\pi$ Process", Acta Phys. Polon. B **50**, 1901–1910 (2019).

[5] O. Deineka, I. Danilkin, and M. Vanderhaeghen, "Dispersive analysis of the $\pi\pi$ and πK scattering data", in 10th International workshop on Chiral Dynamics (Mar. 2022), arXiv:2203.02215 [hep-ph].

[6] G. Colangelo et al., "Prospects for precise predictions of a_μ in the Standard Model", (2022), arXiv:2203.15810 [hep-ph].

[7] T. Aoyama et al., "The anomalous magnetic moment of the muon in the Standard Model", Phys. Rept. **887**, 1–166 (2020), arXiv:2006.04822 [hep-ph].

[8] S. Weinberg, "A Model of Leptons", Phys. Rev. Lett. **19**, 1264–1266 (1967).

[9] S. L. Glashow, "Partial Symmetries of Weak Interactions", Nucl. Phys. **22**, 579–588 (1961).

[10] A. Salam and J. C. Ward, "Electromagnetic and weak interactions", Phys. Lett. **13**, 168–171 (1964).

[11] G. 't Hooft and M. J. G. Veltman, "Regularization and Renormalization of Gauge Fields", Nucl. Phys. B **44**, 189–213 (1972).

[12] M. E. Peskin and D. V. Schroeder, *An Introduction to quantum field theory* (Addison-Wesley, Reading, USA, 1995).

[13] J. F. Donoghue, E. Golowich, and B. R. Holstein, *Dynamics of the standard model*, Vol. 2 (CUP, 2014).

[14] G. Aad et al., "Observation of a new particle in the search for the Standard Model Higgs boson with the ATLAS detector at the LHC", Phys. Lett. B **716**, 1–29 (2012), arXiv:1207.7214 [hep-ex].

[15] S. Chatrchyan et al., "Observation of a New Boson at a Mass of 125 GeV with the CMS Experiment at the LHC", Phys. Lett. B **716**, 30–61 (2012), arXiv:1207.7235 [hep-ex].

[16] P. W. Higgs, "Broken symmetries, massless particles and gauge fields", Phys. Lett. **12**, 132–133 (1964).

[17] F. Englert and R. Brout, "Broken Symmetry and the Mass of Gauge Vector Mesons", Phys. Rev. Lett. **13**, edited by J. C. Taylor, 321–323 (1964).

[18] G. S. Guralnik, C. R. Hagen, and T. W. B. Kibble, "Global Conservation Laws and Massless Particles", Phys. Rev. Lett. **13**, edited by J. C. Taylor, 585–587 (1964).

[19] G. Arnison et al., "Experimental Observation of Isolated Large Transverse Energy Electrons with Associated Missing Energy at $\sqrt{s} = 540$ GeV", Phys. Lett. B **122**, 103–116 (1983).

[20] T. Aaltonen et al., "Precise measurement of the W-boson mass with the CDF II detector", Phys. Rev. Lett. **108**, 151803 (2012), arXiv:1203.0275 [hep-ex].

[21] D. J. Gross and F. Wilczek, "Ultraviolet Behavior of Nonabelian Gauge Theories", Phys. Rev. Lett. **30**, edited by J. C. Taylor, 1343–1346 (1973).

[22] H. D. Politzer, "Reliable Perturbative Results for Strong Interactions?", Phys. Rev. Lett. **30**, edited by J. C. Taylor, 1346–1349 (1973).

[23] H. Yukawa, "On the Interaction of Elementary Particles I", Proc. Phys. Math. Soc. Jap. **17**, 48–57 (1935).

[24] C. M. G. Lattes, G. P. S. Occhialini, and C. F. Powell, "Observations on the Tracks of Slow Mesons in Photographic Emulsions. 2", Nature **160**, 486–492 (1947).

[25] G. D. Rochester and C. C. Butler, "Evidence for the Existence of New Unstable Elementary Particles", Nature **160**, 855–857 (1947).

[26] R. Aaij et al., "Observation of a narrow pentaquark state, $P_c(4312)^+$, and of two-peak structure of the $P_c(4450)^+$", Phys. Rev. Lett. **122**, 222001 (2019), arXiv:1904.03947 [hep-ex].

[27] P. A. Zyla et al., "Review of Particle Physics", PTEP **2020**, 083C01 (2020).

[28] B. Kubis, "An Introduction to chiral perturbation theory", in Workshop on Physics and Astrophysics of Hadrons and Hadronic Matter (Mar. 2007), arXiv:hep-ph/0703274.

[29] S. Weinberg, "Phenomenological Lagrangians", Physica A **96**, edited by S. Deser, 327–340 (1979).

[30] H. Leutwyler, "On the foundations of chiral perturbation theory", Annals Phys. **235**, 165–203 (1994), arXiv:hep-ph/9311274.

[31] E. D'Hoker and S. Weinberg, "General effective actions", Phys. Rev. D **50**, R6050–R6053 (1994), arXiv:hep-ph/9409402.

[32] R. Machleidt and D. R. Entem, "Chiral effective field theory and nuclear forces", Phys. Rept. **503**, 1–75 (2011), arXiv:1105.2919 [nucl-th].

[33] K. G. Wilson, "Confinement of Quarks", Phys. Rev. D **10**, edited by J. C. Taylor, 2445–2459 (1974).

[34] R. P. Feynman, "Space-time approach to nonrelativistic quantum mechanics", Rev. Mod. Phys. **20**, 367–387 (1948).

[35] G. C. Wick, "Properties of Bethe-Salpeter Wave Functions", Phys. Rev. **96**, 1124–1134 (1954).

[36] M. Wagner, S. Diehl, T. Kuske, and J. Weber, "An introduction to lattice hadron spectroscopy for students without quantum field theoretical background", in (Oct. 2013), arXiv:1310.1760 [hep-lat].

[37] C. Gattringer and C. B. Lang, *Quantum chromodynamics on the lattice*, Vol. 788 (Springer, Berlin, 2010).

[38] J. J. Dudek, R. G. Edwards, P. Guo, and C. E. Thomas, "Toward the excited isoscalar meson spectrum from lattice QCD", Phys. Rev. D **88**, 094505 (2013), arXiv:1309.2608 [hep-lat].

[39] M. Luscher, "Volume Dependence of the Energy Spectrum in Massive Quantum Field Theories. 2. Scattering States", Commun. Math. Phys. **105**, 153–188 (1986).

[40] R. A. Briceno, J. J. Dudek, R. G. Edwards, and D. J. Wilson, "Isoscalar $\pi\pi$ scattering and the σ meson resonance from QCD", Phys. Rev. Lett. **118**, 022002 (2017), arXiv:1607.05900 [hep-ph].

[41] R. A. Briceno, J. J. Dudek, R. G. Edwards, and D. J. Wilson, "Isoscalar $\pi\pi, K\overline{K}, \eta\eta$ scattering and the σ, f_0, f_2 mesons from QCD", Phys. Rev. D **97**, 054513 (2018), arXiv:1708.06667 [hep-lat].

[42] W. Heisenberg, "Die „beobachtbaren größen"in der theorie der elementarteilchen", Zeitschrift für Physik **120**, 513–538 (1943).

[43] R. J. Eden, P. V. Landshoff, D. I. Olive, and J. C. Polkinghorne, *The analytic S-matrix* (Cambridge Univ. Press, Cambridge, 1966).

[44] V. N. Gribov, *Strong interactions of hadrons at high emnergies: Gribov lectures on Theoretical Physics*, edited by Y. L. Dokshitzer and J. Nyiri (Cambridge University Press, Oct. 2012).

[45] A. Martin and T. Spearman, *Elementary particle theory* (North-Holland Publishing Company, 1970).

[46] S. Mandelstam, "Determination of the pion - nucleon scattering amplitude from dispersion relations and unitarity. General theory", Phys. Rev. **112**, 1344–1360 (1958).

[47] S. Mandelstam, "Analytic properties of transition amplitudes in perturbation theory", Phys. Rev. **115**, 1741–1751 (1959).

[48] D. I. Olive, "Unitarity and the evaluation of discontinuities", Il Nuovo Cimento (1955-1965) **26**, 73–102 (1962).

[49] G. F. Chew and S. Mandelstam, "Theory of low-energy pion pion interactions", Phys. Rev. **119**, 467–477 (1960).

[50] L. Castillejo, R. H. Dalitz, and F. J. Dyson, "Low's scattering equation for the charged and neutral scalar theories", Phys. Rev. **101**, 453–458 (1956).

[51] A. P. Szczepaniak, P. Guo, M. Battaglieri, and R. De Vita, "P-wave pi pi amplitude from dispersion relations", Phys. Rev. D **82**, 036006 (2010), arXiv:1005.5562 [hep-ph].

[52] P. Guo, R. Mitchell, and A. P. Szczepaniak, "The Role of P-wave inelasticity in $J/\psi to \pi^+\pi^-\pi^0$", Phys. Rev. D **82**, 094002 (2010), arXiv:1006.4371 [hep-ph].

[53] I. V. Danilkin, L. I. R. Gil, and M. F. M. Lutz, "Dynamical light vector mesons in low-energy scattering of Goldstone bosons", Phys. Lett. B **703**, 504–509 (2011), arXiv:1106.2230 [hep-ph].

[54] I. V. Danilkin and M. F. M. Lutz, "Chiral dynamics with vector fields: an application to $\pi\pi$ and πK scattering", EPJ Web Conf. **37**, edited by A. Wronska, R. Skibinski, C. Guaraldo, S. Kistryn, and H. Stroeher, 08007 (2012), arXiv:1208.2568 [hep-ph].

[55] J. A. Oller, "Coupled-channel approach in hadron–hadron scattering", Prog. Part. Nucl. Phys. **110**, 103728 (2020), arXiv:1909.00370 [hep-ph].

[56] J. A. Oller and D. R. Entem, "The exact discontinuity of a partial wave along the left-hand cut and the exact N/D method in non-relativistic scattering", Annals Phys. **411**, 167965 (2019), arXiv:1810.12242 [hep-ph].

[57] Z.-H. Guo, J. A. Oller, and G. Ríos, "Nucleon-Nucleon scattering from the dispersive N/D method: next-to-leading order study", Phys. Rev. C **89**, 014002 (2014), arXiv:1305.5790 [nucl-th].

[58] R. Omnes, "On the Solution of certain singular integral equations of quantum field theory", Nuovo Cim. **8**, 316–326 (1958).

[59] J. Gasser and H. Leutwyler, "Chiral Perturbation Theory to One Loop", Annals Phys. **158**, 142 (1984).

[60] R. E. Cutkosky, "Singularities and discontinuities of Feynman amplitudes", J. Math. Phys. **1**, 429–433 (1960).

[61] B. Hyams et al., "$\pi\pi$ Phase Shift Analysis from 600-MeV to 1900-MeV", Nucl. Phys. B **64**, 134–162 (1973).

[62] M. Fujikawa et al., "High-Statistics Study of the tau- —> pi- pi0 nu(tau) Decay", Phys. Rev. D **78**, 072006 (2008), arXiv:0805.3773 [hep-ex].

[63] C. Hanhart, "A New Parameterization for the Pion Vector Form Factor", Phys. Lett. B **715**, 170–177 (2012), arXiv:1203.6839 [hep-ph].

[64] G. Calucci, L. Fonda, and G. C. Ghirardi, "Correspondence between unstable particles and poles in S matrix theory", Phys. Rev. **166**, 1719 (1968).

[65] I. Danilkin, O. Deineka, and M. Vanderhaeghen, "Theoretical analysis of the $\gamma\gamma \to \pi^0\eta$ process", Phys. Rev. D **96**, 114018 (2017), arXiv:1709.08595 [hep-ph].

[66] J. J. Dudek, R. G. Edwards, and D. J. Wilson, "An a_0 resonance in strongly coupled $\pi\eta$, $K\overline{K}$ scattering from lattice QCD", Phys. Rev. D **93**, 094506 (2016), arXiv:1602.05122 [hep-ph].

[67] M. R. Pennington, "Hadronic structure from two photon collisions", in KLOE-2 Physics Workshop '09 (June 2009), arXiv:0906.1072 [hep-ph].

[68] A. Keshavarzi, K. S. Khaw, and T. Yoshioka, "Muon $g-2$: current status", (2021), arXiv:2106.06723 [hep-ex].

[69] F. Jegerlehner, *The Anomalous Magnetic Moment of the Muon*, Vol. 274 (Springer, Cham, 2017).

[70] F. Jegerlehner and A. Nyffeler, "The Muon g-2", Phys. Rept. **477**, 1–110 (2009), arXiv:0902.3360 [hep-ph].

[71] I. Danilkin, C. F. Redmer, and M. Vanderhaeghen, "The hadronic light-by-light contribution to the muon's anomalous magnetic moment", Prog. Part. Nucl. Phys. **107**, 20–68 (2019), arXiv:1901.10346 [hep-ph].

[72] P. A. M. Dirac, "The Quantum theory of electron. 2.", Proc. Roy. Soc. Lond. A **118**, 351 (1928).

[73] J. S. Schwinger, "On Quantum electrodynamics and the magnetic moment of the electron", Phys. Rev. **73**, 416–417 (1948).

[74] D. Hanneke, S. Fogwell, and G. Gabrielse, "New Measurement of the Electron Magnetic Moment and the Fine Structure Constant", Phys. Rev. Lett. **100**, 120801 (2008), arXiv:0801.1134 [physics.atom-ph].

[75] S. Eidelman, M. Giacomini, F. V. Ignatov, and M. Passera, "The tau lepton anomalous magnetic moment", Nucl. Phys. B Proc. Suppl. **169**, edited by F. Cei, I. Ferrante, and A. Lusiani, 226–231 (2007), arXiv:hep-ph/0702026.

[76] G. W. Bennett et al., "Final Report of the Muon E821 Anomalous Magnetic Moment Measurement at BNL", Phys. Rev. D **73**, 072003 (2006), arXiv:hep-ex/0602035.

[77] B. Abi et al., "Measurement of the Positive Muon Anomalous Magnetic Moment to 0.46 ppm", Phys. Rev. Lett. **126**, 141801 (2021), arXiv:2104.03281 [hep-ex].

[78] S. Borsanyi et al., "Leading hadronic contribution to the muon magnetic moment from lattice QCD", Nature **593**, 51–55 (2021), arXiv:2002.12347 [hep-lat].

[79] M. Hoferichter, B.-L. Hoid, B. Kubis, S. Leupold, and S. P. Schneider, "Pion-pole contribution to hadronic light-by-light scattering in the anomalous magnetic moment of the muon", Phys. Rev. Lett. **121**, 112002 (2018), arXiv:1805.01471 [hep-ph].

[80] G. Colangelo, M. Hoferichter, M. Procura, and P. Stoffer, "Rescattering effects in the hadronic-light-by-light contribution to the anomalous magnetic moment of the muon", Phys. Rev. Lett. **118**, 232001 (2017), arXiv:1701.06554 [hep-ph].

[81] I. Danilkin, M. Hoferichter, and P. Stoffer, "A dispersive estimate of scalar contributions to hadronic light-by-light scattering", Phys. Lett. B **820**, 136502 (2021), arXiv:2105.01666 [hep-ph].

[82] M. Lindner, M. Platscher, and F. S. Queiroz, "A Call for New Physics : The Muon Anomalous Magnetic Moment and Lepton Flavor Violation", Phys. Rept. **731**, 1–82 (2018), arXiv:1610.06587 [hep-ph].

[83] P. Zyla et al., "Review of Particle Physics", PTEP **2020**, and 2021 update, 083C01 (2020).

[84] G. Colangelo, J. Gasser, and H. Leutwyler, "$\pi\pi$ scattering", Nucl. Phys. B **603**, 125–179 (2001), arXiv:hep-ph/0103088.

[85] I. Caprini, G. Colangelo, and H. Leutwyler, "Mass and width of the lowest resonance in QCD", Phys. Rev. Lett. **96**, 132001 (2006), arXiv:hep-ph/0512364.

[86] R. Garcia-Martin, R. Kaminski, J. R. Pelaez, and J. Ruiz de Elvira, "Precise determination of the f0(600) and f0(980) pole parameters from a dispersive data analysis", Phys. Rev. Lett. **107**, 072001 (2011), arXiv:1107.1635 [hep-ph].

[87] B. Moussallam, "Couplings of light I=0 scalar mesons to simple operators in the complex plane", Eur. Phys. J. C **71**, 1814 (2011), arXiv:1110.6074 [hep-ph].

[88] J. R. Pelaez, "Light scalars as tetraquarks or two-meson states from large N(c) and unitarized chiral perturbation theory", Mod. Phys. Lett. A **19**, 2879–2894 (2004), arXiv:hep-ph/0411107.

[89] S. Descotes-Genon and B. Moussallam, "The K*0 (800) scalar resonance from Roy-Steiner representations of pi K scattering", Eur. Phys. J. C **48**, 553 (2006), arXiv:hep-ph/0607133.

[90] J. R. Peláez, A. Rodas, and J. Ruiz de Elvira, "Strange resonance poles from $K\pi$ scattering below 1.8 GeV", Eur. Phys. J. C **77**, 91 (2017), arXiv:1612.07966 [hep-ph].

[91] J. R. Peláez and A. Rodas, "Determination of the lightest strange resonance $K_0^*(700)$ or κ, from a dispersive data analysis", Phys. Rev. Lett. **124**, 172001 (2020), arXiv:2001.08153 [hep-ph].

[92] R. Aaij et al., "Observation of structure in the J/ψ -pair mass spectrum", Sci. Bull. **65**, 1983–1993 (2020), arXiv:2006.16957 [hep-ex].

[93] R. Aaij et al., "Observation of $J/\psi p$ Resonances Consistent with Pentaquark States in $\Lambda_b^0 \to J/\psi K^- p$ Decays", Phys. Rev. Lett. **115**, 072001 (2015), arXiv:1507.03414 [hep-ex].

[94] C. Adolph et al., "Odd and even partial waves of $\eta\pi^-$ and $\eta'\pi^-$ in $\pi^- p \to \eta^{(\prime)}\pi^- p$ at 191 GeV/c", Phys. Lett. B **740**, [Erratum: Phys.Lett.B 811, 135913 (2020)], 303–311 (2015), arXiv:1408.4286 [hep-ex].

[95] R. A. Briceno, J. J. Dudek, and R. D. Young, "Scattering processes and resonances from lattice QCD", Rev. Mod. Phys. **90**, 025001 (2018), arXiv:1706.06223 [hep-lat].

[96] M. R. Shepherd, J. J. Dudek, and R. E. Mitchell, "Searching for the rules that govern hadron construction", Nature **534**, 487–493 (2016), arXiv:1802.08131 [hep-ph].

[97] J. R. Pelaez, "From controversy to precision on the sigma meson: a review on the status of the non-ordinary $f_0(500)$ resonance", Phys. Rept. **658**, 1 (2016), arXiv:1510.00653 [hep-ph].

[98] S. M. Roy, "Exact integral equation for pion pion scattering involving only physical region partial waves", Phys. Lett. B **36**, 353–356 (1971).

[99] G. E. Hite and F. Steiner, "New dispersion relations and their application to partial-wave amplitudes", Nuovo Cim. A **18**, 237–270 (1973).

[100] R. Garcia-Martin, R. Kaminski, J. R. Pelaez, J. Ruiz de Elvira, and F. J. Yndurain, "The Pion-pion scattering amplitude. IV: Improved analysis with once subtracted Roy-like equations up to 1100 MeV", Phys. Rev. D **83**, 074004 (2011), arXiv:1102.2183 [hep-ph].

[101] J. R. Pelaez, A. Rodas, and J. Ruiz De Elvira, "Global parameterization of $\pi\pi$ scattering up to 2 GeV", Eur. Phys. J. C **79**, 1008 (2019), arXiv:1907.13162 [hep-ph].

[102] B. Ananthanarayan, G. Colangelo, J. Gasser, and H. Leutwyler, "Roy equation analysis of pi pi scattering", Phys. Rept. **353**, 207–279 (2001), arXiv:hep-ph/0005297.

[103] H. Leutwyler, "Model independent determination of the sigma pole", AIP Conf. Proc. **1030**, edited by G. Rupp, E. Van Beveren, P. Bicudo, B. Hiller, and F. Kleefeld, 46–55 (2008), arXiv:0804.3182 [hep-ph].

[104] P. Buettiker, S. Descotes-Genon, and B. Moussallam, "A new analysis of pi K scattering from Roy and Steiner type equations", Eur. Phys. J. C **33**, 409–432 (2004), arXiv:hep-ph/0310283.

[105] J. R. Peláez and A. Rodas, "Dispersive $\pi K \to \pi K$ and $\pi\pi \to K\bar{K}$ amplitudes from scattering data, threshold parameters and the lightest strange resonance κ or $K_0^*(700)$", (2020), arXiv:2010.11222 [hep-ph].

[106] J. A. Oller and E. Oset, "N/D description of two meson amplitudes and chiral symmetry", Phys. Rev. D **60**, 074023 (1999), arXiv:hep-ph/9809337.

[107] A. Gasparyan and M. F. M. Lutz, "Photon- and pion-nucleon interactions in a unitary and causal effective field theory based on the chiral Lagrangian", Nucl. Phys. A **848**, 126–182 (2010), arXiv:1003.3426 [hep-ph].

[108] I. V. Danilkin, A. M. Gasparyan, and M. F. M. Lutz, "On causality, unitarity and perturbative expansions", Phys. Lett. B **697**, 147–152 (2011), arXiv:1009.5928 [hep-ph].

[109] A. M. Gasparyan, M. F. M. Lutz, and B. Pasquini, "Compton scattering from chiral dynamics with unitarity and causality", Nucl. Phys. A **866**, 79–92 (2011), arXiv:1102.3375 [hep-ph].

[110] A. M. Gasparyan, M. F. M. Lutz, and E. Epelbaum, "Two-nucleon scattering: Merging chiral effective field theory with dispersion relations", Eur. Phys. J. A **49**, 115 (2013), arXiv:1212.3057 [nucl-th].

[111] P. Guo, I. V. Danilkin, D. Schott, C. Fernández-Ramírez, V. Mathieu, and A. P. Szczepaniak, "Three-body final state interaction in $\eta \to 3\pi$", Phys. Rev. D **92**, 054016 (2015), arXiv:1505.01715 [hep-ph].

[112] P. Guo, I. V. Danilkin, C. Fernández-Ramírez, V. Mathieu, and A. P. Szczepaniak, "Three-body final state interaction in $\eta \to 3\pi$ updated", Phys. Lett. B **771**, 497–502 (2017), arXiv:1608.01447 [hep-ph].

[113] G. Colangelo, S. Lanz, H. Leutwyler, and E. Passemar, "$\eta \to 3\pi$: Study of the Dalitz plot and extraction of the quark mass ratio Q", Phys. Rev. Lett. **118**, 022001 (2017), arXiv:1610.03494 [hep-ph].

[114] G. Colangelo, S. Lanz, H. Leutwyler, and E. Passemar, "Dispersive analysis of $\eta \to 3\pi$", Eur. Phys. J. C **78**, 947 (2018), arXiv:1807.11937 [hep-ph].

[115] M. Albaladejo and B. Moussallam, "Extended chiral Khuri-Treiman formalism for $\eta \to 3\pi$ and the role of the $a_0(980)$, $f_0(980)$ resonances", Eur. Phys. J. C **77**, 508 (2017), arXiv:1702.04931 [hep-ph].

[116] T. Isken, B. Kubis, S. P. Schneider, and P. Stoffer, "Dispersion relations for $\eta' \to \eta\pi\pi$", Eur. Phys. J. C **77**, 489 (2017), arXiv:1705.04339 [hep-ph].

[117] S. Gonzàlez-Solís and E. Passemar, "$\eta' \to \eta\pi\pi$ decays in unitarized resonance chiral theory", Eur. Phys. J. C **78**, 758 (2018), arXiv:1807.04313 [hep-ph].

[118] L. Gan, B. Kubis, E. Passemar, and S. Tulin, "Precision tests of fundamental physics with η and η' mesons", Phys. Rept. **945**, 1–105 (2022), arXiv:2007.00664 [hep-ph].

[119] R. Garcia-Martin and B. Moussallam, "MO analysis of the high statistics Belle results on $\gamma\gamma \to \pi^+\pi^-, \pi^0\pi^0$ with chiral constraints", Eur. Phys. J. C **70**, 155–175 (2010), arXiv:1006.5373 [hep-ph].

[120] M. Hoferichter, D. R. Phillips, and C. Schat, "Roy-Steiner equations for gamma gamma -> pi pi", Eur. Phys. J. C **71**, 1743 (2011), arXiv:1106.4147 [hep-ph].

[121] L.-Y. Dai and M. R. Pennington, "Comprehensive amplitude analysis of $\gamma\gamma \to \pi^+\pi^-, \pi^0\pi^0$ and $\overline{K}K$ below 1.5 GeV", Phys. Rev. D **90**, 036004 (2014), arXiv:1404.7524 [hep-ph].

[122] D. A. S. Molnar, I. Danilkin, and M. Vanderhaeghen, "The role of charged exotic states in $e^+e^- \to \psi(2S)\,\pi^+\pi^-$", Phys. Lett. B **797**, 134851 (2019), arXiv:1903.08458 [hep-ph].

[123] Y.-H. Chen, L.-Y. Dai, F.-K. Guo, and B. Kubis, "Nature of the $Y(4260)$: A light-quark perspective", Phys. Rev. D **99**, 074016 (2019), arXiv:1902.10957 [hep-ph].

[124] I. Danilkin, D. A. S. Molnar, and M. Vanderhaeghen, "Simultaneous description of the $e^+e^- \to J/\psi\,\pi\pi\,(K\bar{K})$ processes", Phys. Rev. D **102**, 016019 (2020), arXiv:2004.13499 [hep-ph].

[125] F. Niecknig and B. Kubis, "Dispersion-theoretical analysis of the $D^+ \to K^-\pi^+\pi^+$ Dalitz plot", JHEP **10**, 142 (2015), arXiv:1509.03188 [hep-ph].

[126] F. Niecknig and B. Kubis, "Consistent Dalitz plot analysis of Cabibbo-favored $D^+ \to \bar{K}\pi\pi^+$ decays", Phys. Lett. B **780**, 471–478 (2018), arXiv:1708.00446 [hep-ph].

[127] J. R. Pelaez and A. Rodas, "$\pi\pi \to K\bar{K}$ scattering up to 1.47 GeV with hyperbolic dispersion relations", Eur. Phys. J. C **78**, 897 (2018), arXiv:1807.04543 [hep-ph].

[128] C. B. Lang, L. Leskovec, D. Mohler, and S. Prelovsek, "K pi scattering for isospin 1/2 and 3/2 in lattice QCD", Phys. Rev. D **86**, 054508 (2012), arXiv:1207.3204 [hep-lat].

[129] S. Prelovsek, T. Draper, C. B. Lang, M. Limmer, K.-F. Liu, N. Mathur, and D. Mohler, "Lattice study of light scalar tetraquarks with I=0,2,1/2,3/2: Are \sigma and \kappa tetraquarks?", Phys. Rev. D **82**, 094507 (2010), arXiv:1005.0948 [hep-lat].

[130] L. Liu et al., "Isospin-0 $\pi\pi$ s-wave scattering length from twisted mass lattice QCD", Phys. Rev. D **96**, 054516 (2017), arXiv:1612.02061 [hep-lat].

[131] Z. Fu and X. Chen, "$I = 0$ $\pi\pi$ s-wave scattering length from lattice QCD", Phys. Rev. D **98**, 014514 (2018), arXiv:1712.02219 [hep-lat].

[132] D. Guo, A. Alexandru, R. Molina, M. Mai, and M. Döring, "Extraction of isoscalar $\pi\pi$ phase-shifts from lattice QCD", Phys. Rev. D **98**, 014507 (2018), arXiv:1803.02897 [hep-lat].

[133] M. Mai, C. Culver, A. Alexandru, M. Döring, and F. X. Lee, "Cross-channel study of pion scattering from lattice QCD", Phys. Rev. D **100**, 114514 (2019), arXiv:1908.01847 [hep-lat].

[134] D. J. Wilson, R. A. Briceno, J. J. Dudek, R. G. Edwards, and C. E. Thomas, "The quark-mass dependence of elastic πK scattering from QCD", Phys. Rev. Lett. **123**, 042002 (2019), arXiv:1904.03188 [hep-lat].

[135] G. Rendon, L. Leskovec, S. Meinel, J. Negele, S. Paul, M. Petschlies, A. Pochinsky, G. Silvi, and S. Syritsyn, "$I = 1/2$ S-wave and P-wave $K\pi$ scattering and the κ and K^* resonances from lattice QCD", Phys. Rev. D **102**, 114520 (2020), arXiv:2006.14035 [hep-lat].

[136] S. Mandelstam, "Unitarity Condition Below Physical Thresholds in the Normal and Anomalous Cases", Phys. Rev. Lett. **4**, 84–87 (1960).

[137] M. F. M. Lutz and C. L. Korpa, "On coupled-channel dynamics in the presence of anomalous thresholds", Phys. Rev. D **98**, 076003 (2018), arXiv:1808.08695 [hep-ph].

[138] M. Luming, "Application of N/D and determinantal methods to Yukawa potential scattering", Phys. Rev. **136**, B1120–B1133 (1964).

[139] P. W. Johnson and R. L. Warnock, "Solution of the unitarity equation with overlapping left and right cuts: a tool for study of the s* and similar systems", J.Math.Phys. **22**, 385 (1981).

[140] N. I. Muskhelishvili, "Singular Integral Equations", Singular Integral Equations, Wolters-Noordhoff Publishing, Groningen (1953).

[141] J. F. Donoghue, J. Gasser, and H. Leutwyler, "The Decay of a Light Higgs Boson", Nucl. Phys. B **343**, 341–368 (1990).

[142] B. Moussallam, "N(f) dependence of the quark condensate from a chiral sum rule", Eur. Phys. J. C **14**, 111–122 (2000), arXiv:hep-ph/9909292.

[143] W. R. Frazer, "Applications of Conformal Mapping to the Phenomenological Representation of Scattering Amplitudes", Phys. Rev. **123**, 2180–2182 (1961).

[144] J. Bijnens, P. Dhonte, and P. Talavera, "pi K scattering in three flavor ChPT", JHEP **05**, 036 (2004), arXiv:hep-ph/0404150.

[145] V. Bernard, N. Kaiser, and U. G. Meissner, "Threshold parameters of pi K scattering in QCD", Phys. Rev. D **43**, 2757–2760 (1991).

[146] A. Gomez Nicola and J. R. Pelaez, "Meson meson scattering within one loop chiral perturbation theory and its unitarization", Phys. Rev. D **65**, 054009 (2002), arXiv:hep-ph/0109056.

[147] J. Bijnens and G. Ecker, "Mesonic low-energy constants", Ann. Rev. Nucl. Part. Sci. **64**, 149–174 (2014), arXiv:1405.6488 [hep-ph].

[148] D.-L. Yao, L.-Y. Dai, H.-Q. Zheng, and Z.-Y. Zhou, "A review on partial-wave dynamics with chiral effective field theory and dispersion relation", Rept. Prog. Phys. **84**, 076201 (2021), arXiv:2009.13495 [hep-ph].

[149] A. Salas-Bernárdez, F. J. Llanes-Estrada, J. Escudero-Pedrosa, and J. A. Oller, "Systematizing and addressing theory uncertainties of unitarization with the Inverse Amplitude Method", SciPost Phys. **11**, 020 (2021), arXiv:2010.13709 [hep-ph].

[150] I. Caprini, "Finding the sigma pole by analytic extrapolation of pi pi scattering data", Phys. Rev. D **77**, 114019 (2008), arXiv:0804.3504 [hep-ph].

[151] I. Caprini, P. Masjuan, J. Ruiz de Elvira, and J. J. Sanz-Cillero, "Uncertainty estimates of the σ-pole determination by Padé approximants", Phys. Rev. D **93**, 076004 (2016), arXiv:1602.02062 [hep-ph].

[152] S. D. Protopopescu, M. Alston-Garnjost, A. Barbaro-Galtieri, S. M. Flatte, J. H. Friedman, T. A. Lasinski, G. R. Lynch, M. S. Rabin, and F. T. Solmitz, "Pi pi Partial Wave Analysis from Reactions pi+ p —> pi+ pi- Delta++ and pi+ p —> K+ K- Delta++ at 7.1-GeV/c", Phys. Rev. D **7**, 1279 (1973).

[153] G. Grayer et al., "High Statistics Study of the Reaction pi- p –> pi- pi+ n: Apparatus, Method of Analysis, and General Features of Results at 17-GeV/c", Nucl. Phys. B **75**, 189–245 (1974).

[154] R. Kaminski, L. Lesniak, and K. Rybicki, "Separation of S wave pseudoscalar and pseudovector amplitudes in pi- p (polarized) —> pi+ pi- n reaction on polarized target", Z. Phys. C **74**, 79–91 (1997), arXiv:hep-ph/9606362.

[155] J. R. Batley et al., "New high statistics measurement of K(e4) decay form factors and pi pi scattering phase shifts", Eur. Phys. J. C **54**, 411–423 (2008).

[156] J. R. Batley et al., "Precise tests of low energy QCD from K(e4)decay properties", Eur. Phys. J. C **70**, 635–657 (2010).

[157] P. Estabrooks, R. K. Carnegie, A. D. Martin, W. M. Dunwoodie, T. A. Lasinski, and D. W.G. S. Leith, "Study of K pi Scattering Using the Reactions K+- p —> K+- pi+ n and K+- p —> K+- pi- Delta++ at 13-GeV/c", Nucl. Phys. B **133**, 490–524 (1978).

[158] D. Aston et al., "A Study of K- pi+ Scattering in the Reaction K- p —> K- pi+ n at 11-GeV/c", Nucl. Phys. B **296**, 493–526 (1988).

[159] R. Kaminski, J. R. Pelaez, and F. J. Yndurain, "The pion-pion scattering amplitude. II. Improved analysis above bar K anti-K threshold", Phys. Rev. D **74**, [Erratum: Phys.Rev.D 74, 079903 (2006)], 014001 (2006), arXiv:hep-ph/0603170.

[160] A. Gomez Nicola, J. R. Pelaez, and G. Rios, "The Inverse Amplitude Method and Adler Zeros", Phys. Rev. D **77**, 056006 (2008), arXiv:0712.2763 [hep-ph].

[161] C. Hanhart, J. R. Pelaez, and G. Rios, "Quark mass dependence of the rho and sigma from dispersion relations and Chiral Perturbation Theory", Phys. Rev. Lett. **100**, 152001 (2008), arXiv:0801.2871 [hep-ph].

[162] J. Nebreda and J. R. Pelaez., "Strange and non-strange quark mass dependence of elastic light resonances from SU(3) Unitarized Chiral Perturbation Theory to one loop", Phys. Rev. D **81**, 054035 (2010), arXiv:1001.5237 [hep-ph].

[163] J. R. Pelaez and G. Rios, "Chiral extrapolation of light resonances from one and two-loop unitarized Chiral Perturbation Theory versus lattice results", Phys. Rev. D **82**, 114002 (2010), arXiv:1010.6008 [hep-ph].

[164] M. Luscher, "Signatures of unstable particles in finite volume", Nucl. Phys. B **364**, 237–251 (1991).

[165] M. Luscher and U. Wolff, "How to Calculate the Elastic Scattering Matrix in Two-dimensional Quantum Field Theories by Numerical Simulation", Nucl. Phys. B **339**, 222–252 (1990).

[166] K. Rummukainen and S. A. Gottlieb, "Resonance scattering phase shifts on a nonrest frame lattice", Nucl. Phys. B **450**, 397–436 (1995), arXiv:hep-lat/9503028.

[167] C. h. Kim, C. T. Sachrajda, and S. R. Sharpe, "Finite-volume effects for two-hadron states in moving frames", Nucl. Phys. B **727**, 218–243 (2005), arXiv:hep-lat/0507006.

[168] N. H. Christ, C. Kim, and T. Yamazaki, "Finite volume corrections to the two-particle decay of states with non-zero momentum", Phys. Rev. D **72**, 114506 (2005), arXiv:hep-lat/0507009.

[169] L. Leskovec and S. Prelovsek, "Scattering phase shifts for two particles of different mass and non-zero total momentum in lattice QCD", Phys. Rev. D **85**, 114507 (2012), arXiv:1202.2145 [hep-lat].

[170] M. Albaladejo and J. A. Oller, "On the size of the sigma meson and its nature", Phys. Rev. D **86**, 034003 (2012), arXiv:1205.6606 [hep-ph].

[171] X.-L. Gao, Z.-H. Guo, Z. Xiao, and Z.-Y. Zhou, "Scrutinizing $\pi\pi$ scattering in light of recent lattice phase shifts", (2022), arXiv:2202.03124 [hep-ph].

[172] E. van Beveren and G. Rupp, "Comment on "Scrutinizing pion-pion scattering in light of recent lattice phase shifts"", (2022), arXiv:2202.08809 [hep-ph].

[173] D. H. Cohen, D. S. Ayres, R. Diebold, S. L. Kramer, A. J. Pawlicki, and A. B. Wicklund, "Amplitude Analysis of the K- K+ System Produced in the Reactions pi- p —> K- K+ n and pi+ n —> K- K+ p at 6-GeV/c", Phys. Rev. D **22**, 2595 (1980).

[174] A. Etkin et al., "Amplitude Analysis of the K0(s) K0(s) System Produced in the Reaction pi- p —> K0(s) K0(s) n at 23-GeV/c", Phys. Rev. D **25**, 1786 (1982).

[175] R. S. Longacre et al., "A Measurement of $\pi^- p \to K^0(s)\ K^0(s)\ n$ at 22-GeV/c and a Systematic Study of the 2++ Meson Spectrum", Phys. Lett. B **177**, 223–227 (1986).

[176] A. D. Martin and E. N. Ozmutlu, "Analyses of $K\bar{K}$ Production and Scalar Mesons", Nucl. Phys. B **158**, 520–545 (1979).

[177] J. A. Oller and E. Oset, "Chiral symmetry amplitudes in the S wave isoscalar and isovector channels and the σ, $f_0(980)$, $a_0(980)$ scalar mesons", Nucl. Phys. A **620**, [Erratum: Nucl.Phys.A 652, 407–409 (1999)], 438–456 (1997), arXiv:hep-ph/9702314.

[178] I. Danilkin and M. Vanderhaeghen, "Dispersive analysis of the $\gamma\gamma^* \to \pi\pi$ process", Phys. Lett. B **789**, 366–372 (2019), arXiv:1810.03669 [hep-ph].

[179] M. J. Losty, V. Chaloupka, A. Ferrando, L. Montanet, E. Paul, D. Yaffe, A. Zieminski, J. Alitti, B. Gandois, and J. Louie, "A Study of pi- pi- scattering from pi- p interactions at 3.93-GeV/c", Nucl. Phys. B **69**, 185–204 (1974).

[180] N. B. Durusoy, M. Baubillier, R. George, M. Goldberg, A. M. Touchard, N. Armenise, M. T. Fogli Muciaccia, and A. Silvestri, "Study of the i=2 pi pi scattering from the reaction pi- d —> pi- pi- p(s) p at 9.0 gev/c", Phys. Lett. B **45**, 517–520 (1973).

[181] W. Hoogland et al., "Measurement and Analysis of the pi+ pi+ System Produced at Small Momentum Transfer in the Reaction pi+ p —> pi+ pi+ n at 12.5-GeV", Nucl. Phys. B **126**, 109–123 (1977).

[182] M. Amaryan et al., "Strange Hadron Spectroscopy with Secondary KL Beam in Hall D", (2020), arXiv:2008.08215 [nucl-ex].

[183] G. Colangelo, M. Hoferichter, M. Procura, and P. Stoffer, "Dispersive approach to hadronic light-by-light scattering", JHEP **09**, 091 (2014), arXiv:1402.7081 [hep-ph].

[184] G. Colangelo, M. Hoferichter, M. Procura, and P. Stoffer, "Dispersion relation for hadronic light-by-light scattering: two-pion contributions", JHEP **04**, 161 (2017), arXiv:1702.07347 [hep-ph].

[185] V. Pauk and M. Vanderhaeghen, "Anomalous magnetic moment of the muon in a dispersive approach", Phys. Rev. D **90**, 113012 (2014), arXiv:1409.0819 [hep-ph].

[186] I. Danilkin and M. Vanderhaeghen, "Light-by-light scattering sum rules in light of new data", Phys. Rev. D **95**, 014019 (2017), arXiv:1611.04646 [hep-ph].

[187] G. Källén, *Elementary particle physics* (Addison-Wesley, Reading, MA, 1964).

[188] G. D'Agostini, "On the use of the covariance matrix to fit correlated data", Nucl. Instrum. Meth. A **346**, 306–311 (1994).

[189] P. Bevington and D. Robinson, *Data reduction and error analysis for the physical sciences* (McGraw-Hill Education, 2003).

[190] B. Efron, "Bootstrap Methods: Another Look at the Jackknife", Annals Statist. **7**, 1–26 (1979).

[191] A. C. Davison and D. V. Hinkley, *Bootstrap methods and their application*, Cambridge Series in Statistical and Probabilistic Mathematics (Cambridge University Press, 1997).

[192] G. E. P. Box and M. E. Muller, "A Note on the Generation of Random Normal Deviates", The Annals of Mathematical Statistics **29**, 610 –611 (1958).

[193] P. Pedroni and S. Sconfietti, "A new Monte Carlo-based fitting method", J. Phys. G **47**, 054001 (2020), arXiv:1909.03885 [physics.data-an].

[194] S. Sconfietti, "Nucleon polarizabilities from Compton scattering data", PhD thesis (Universita' Di Pavia, Pavia U., 2020).

[195] M. Masuda et al., "Study of π^0 pair production in single-tag two-photon collisions", Phys. Rev. D **93**, 032003 (2016), arXiv:1508.06757 [hep-ex].

[196] C. F. Redmer, "The two-photon physics program at BESIII", Nucl. Part. Phys. Proc. **287-288**, edited by C. Yuan, X. Mo, and L. Wang, 99–102 (2017).

[197] S. C. Frautschi, "Regge poles and s-matrix theory", Regge poles and S-matrix theory, Frontiers in physics, W.A. Benjamin (1963).

[198] V. Pauk and M. Vanderhaeghen, "Single meson contributions to the muon's anomalous magnetic moment", Eur. Phys. J. C **74**, 3008 (2014), arXiv:1401.0832 [hep-ph].

[199] G. Colangelo, M. Hoferichter, B. Kubis, M. Procura, and P. Stoffer, "Towards a data-driven analysis of hadronic light-by-light scattering", Phys. Lett. B **738**, 6–12 (2014), arXiv:1408.2517 [hep-ph].

[200] T. Mori et al., "High statistics measurement of the cross-sections of gamma gamma —> pi+ pi- production", J. Phys. Soc. Jap. **76**, 074102 (2007), arXiv:0704.3538 [hep-ex].

[201] S. Uehara et al., "High-statistics study of neutral-pion pair production in two-photon collisions", Phys. Rev. D **79**, 052009 (2009), arXiv:0903.3697 [hep-ex].

[202] S. Uehara et al., "High-statistics study of eta pi0 production in two-photon collisions", Phys. Rev. D **80**, 032001 (2009), arXiv:0906.1464 [hep-ex].

[203] J. Gasser, M. A. Ivanov, and M. E. Sainio, "Low-energy photon-photon collisions to two loops revisited", Nucl. Phys. B **728**, 31–54 (2005), arXiv:hep-ph/0506265.

[204] J. Gasser, M. A. Ivanov, and M. E. Sainio, "Revisiting gamma gamma —> pi+ pi- at low energies", Nucl. Phys. B **745**, 84–108 (2006), arXiv:hep-ph/0602234.

[205] J. A. Oller and E. Oset, "Theoretical study of the gamma gamma —> meson - meson reaction", Nucl. Phys. A **629**, 739–760 (1998), arXiv:hep-ph/9706487.

[206] I. V. Danilkin, M. F. M. Lutz, S. Leupold, and C. Terschlusen, "Photon-fusion reactions from the chiral Lagrangian with dynamical light vector mesons", Eur. Phys. J. C **73**, 2358 (2013), arXiv:1211.1503 [hep-ph].

[207] J. A. Oller, L. Roca, and C. Schat, "Improved dispersion relations for gamma gamma —> pi0 pi0", Phys. Lett. B **659**, 201–208 (2008), arXiv:0708.1659 [hep-ph].

[208] J. A. Oller and L. Roca, "Two photons into pi0 pi0", Eur. Phys. J. A **37**, 15–32 (2008), arXiv:0804.0309 [hep-ph].

[209] B. Moussallam, "Unified dispersive approach to real and virtual photon-photon scattering at low energy", Eur. Phys. J. C **73**, 2539 (2013), arXiv:1305.3143 [hep-ph].

[210] M. Hoferichter and P. Stoffer, "Dispersion relations for $\gamma^*\gamma^* \to \pi\pi$: helicity amplitudes, subtractions, and anomalous thresholds", JHEP **07**, 073 (2019), arXiv:1905.13198 [hep-ph].

[211] M. F. M. Lutz and I. Vidana, "On Kinematical Constraints in Boson-Boson Systems", Eur. Phys. J. A **48**, 124 (2012), arXiv:1111.1838 [hep-ph].

[212] Y. Heo and M. F. M. Lutz, "On kinematical constraints in the hadrogenesis conjecture for the baryon resonance spectrum", Eur. Phys. J. A **50**, 130 (2014), arXiv:1405.1597 [hep-ph].

[213] W. A. Bardeen and W. K. Tung, "Invariant amplitudes for photon processes", Phys. Rev. **173**, [Erratum: Phys.Rev.D 4, 3229–3229 (1971)], 1423–1433 (1968).

[214] R. Tarrach, "Invariant Amplitudes for Virtual Compton Scattering Off Polarized Nucleons Free from Kinematical Singularities, Zeros and Constraints", Nuovo Cim. A **28**, 409 (1975).

[215] D. Drechsel, G. Knochlein, A. Y. Korchin, A. Metz, and S. Scherer, "Structure analysis of the virtual Compton scattering amplitude at low-energies", Phys. Rev. C **57**, 941–952 (1998), arXiv:nucl-th/9704064.

[216] G. Colangelo, M. Hoferichter, M. Procura, and P. Stoffer, "Dispersion relation for hadronic light-by-light scattering: theoretical foundations", JHEP **09**, 074 (2015), arXiv:1506.01386 [hep-ph].

[217] O. Deineka, I. Danilkin, and M. Vanderhaeghen, "Theoretical analysis of the $\gamma\gamma^{(*)} \to \pi^0\eta$ process", EPJ Web Conf. **199**, edited by N. Wrońska, A. Magiera, and W. Przygoda, 02005 (2019), arXiv:1808.04117 [hep-ph].

[218] H. W. Fearing and S. Scherer, "Virtual Compton scattering off spin zero particles at low-energies", Few Body Syst. **23**, 111–126 (1998), arXiv:nucl-th/9607056.

[219] F. E. Low, "Bremsstrahlung of very low-energy quanta in elementary particle collisions", Phys. Rev. **110**, 974–977 (1958).

[220] D. Morgan and M. R. Pennington, "What Can We Learn From $\gamma\gamma \to \pi\pi$, $K\bar{K}$ in the Resonance Region", Z. Phys. C **37**, [Erratum: Z.Phys.C 39, 590 (1988)], 431 (1988).

[221] L.-Y. Dai and M. R. Pennington, "Two photon couplings of the lightest isoscalars from BELLE data", Phys. Lett. B **736**, 11–15 (2014), arXiv:1403.7514 [hep-ph].

[222] E. B. Dally et al., "Measurement of the π^- Form-factor", Phys. Rev. D **24**, 1718–1735 (1981).

[223] S. R. Amendolia et al., "A Measurement of the Pion Charge Radius", Phys. Lett. B **146**, 116–120 (1984).

[224] V. Tadevosyan et al., "Determination of the pion charge form-factor for Q**2 = 0.60-GeV**2 - 1.60-GeV**2", Phys. Rev. C **75**, 055205 (2007), arXiv:nucl-ex/0607007.

[225] E. B. Dally et al., "DIRECT MEASUREMENT OF THE NEGATIVE KAON FORM-FACTOR", Phys. Rev. Lett. **45**, 232–235 (1980).

[226] S. R. Amendolia et al., "A Measurement of the Kaon Charge Radius", Phys. Lett. B **178**, 435–440 (1986).

[227] M. Carmignotto et al., "Separated Kaon Electroproduction Cross Section and the Kaon Form Factor from 6 GeV JLab Data", Phys. Rev. C **97**, 025204 (2018), arXiv:1801.01536 [nucl-ex].

[228] I. V. Danilkin, C. Fernández-Ramírez, P. Guo, V. Mathieu, D. Schott, M. Shi, and A. P. Szczepaniak, "Dispersive analysis of $\omega/\phi \to 3\pi, \pi\gamma^*$", Phys. Rev. D **91**, 094029 (2015), arXiv:1409.7708 [hep-ph].

[229] S. J. J., *Currents and mesons* (University of Chicago Press, Chicago, USA, 1969).

[230] S. P. Schneider, B. Kubis, and F. Niecknig, "The $\omega- > \pi^0\gamma^*$ and $\phi- > \pi^0\gamma^*$ transition form factors in dispersion theory", Phys. Rev. D **86**, 054013 (2012), arXiv:1206.3098 [hep-ph].

[231] R. Karplus, C. M. Sommerfield, and E. H. Wichmann, "Spectral Representations in Perturbation Theory. 1. Vertex Function", Phys. Rev. **111**, 1187–1190 (1958).

[232] M. Hoferichter, G. Colangelo, M. Procura, and P. Stoffer, "Virtual photon-photon scattering", Int. J. Mod. Phys. Conf. Ser. **35**, edited by P. Gauzzi and G. Venanzoni, 1460400 (2014), arXiv:1309.6877 [hep-ph].

[233] J. Bernabeu and J. Prades, "The sigma –> gamma gamma Width from Nucleon Electromagnetic Polarizabilities", Phys. Rev. Lett. **100**, 241804 (2008), arXiv:0802.1830 [hep-ph].

[234] V. Pascalutsa and M. Vanderhaeghen, "Sum rules for light-by-light scattering", Phys. Rev. Lett. **105**, 201603 (2010), arXiv:1008.1088 [hep-ph].

[235] V. Pascalutsa, V. Pauk, and M. Vanderhaeghen, "Light-by-light scattering sum rules constraining meson transition form factors", Phys. Rev. D **85**, 116001 (2012), arXiv:1204.0740 [hep-ph].

[236] L.-Y. Dai and M. R. Pennington, "Pascalutsa-Vanderhaeghen light-by-light sum rule from photon-photon collisions", Phys. Rev. D **95**, 056007 (2017), arXiv:1701.04460 [hep-ph].

[237] M. R. Pennington, "Sigma coupling to photons: Hidden scalar in gamma gamma —> pi0 pi0", Phys. Rev. Lett. **97**, 011601 (2006).

[238] C. Adolph et al., "Measurement of the charged-pion polarizability", Phys. Rev. Lett. **114**, 062002 (2015), arXiv:1405.6377 [hep-ex].

[239] T. Fuchs, B. Pasquini, C. Unkmeir, and S. Scherer, "Virtual Compton scattering off the pseudoscalar meson octet", Czech. J. Phys. **52**, edited by J. Adam, P. Bydzovsky, and J. Mares, B135–B144 (2002), arXiv:hep-ph/0010218.

[240] G. Ecker, "Chiral low-energy constants", Acta Phys. Polon. B **38**, edited by H. Czyz, M. Krawczyk, and G. Pancheri, 2753–2762 (2007), arXiv:hep-ph/0702263.

[241] V. M. Budnev, I. F. Ginzburg, G. V. Meledin, and V. G. Serbo, "The Two photon particle production mechanism. Physical problems. Applications. Equivalent photon approximation", Phys. Rept. **15**, 181–281 (1975).

[242] J. Boyer et al., "Two photon production of pion pairs", Phys. Rev. D **42**, 1350–1367 (1990).

[243] H. J. Behrend et al., "An Experimental study of the process gamma gamma —> pi+ pi-", Z. Phys. C **56**, 381–390 (1992).

[244] H. Marsiske et al., "A Measurement of $\pi^0\pi^0$ Production in Two Photon Collisions", Phys. Rev. D **41**, 3324 (1990).

[245] S. Ropertz, C. Hanhart, and B. Kubis, "A new parametrization for the scalar pion form factors", Eur. Phys. J. C **78**, 1000 (2018), arXiv:1809.06867 [hep-ph].

[246] S. K. Choi et al., "Observation of a narrow charmonium-like state in exclusive $B^{\pm} \to K^{\pm}\pi^+\pi^- J/\psi$ decays", Phys. Rev. Lett. **91**, 262001 (2003), arXiv:hep-ex/0309032.

[247] H.-X. Chen, W. Chen, X. Liu, and S.-L. Zhu, "The hidden-charm pentaquark and tetraquark states", Phys. Rept. **639**, 1–121 (2016), arXiv:1601.02092 [hep-ph].

[248] A. Esposito, A. Pilloni, and A. D. Polosa, "Multiquark Resonances", Phys. Rept. **668**, 1–97 (2017), arXiv:1611.07920 [hep-ph].

[249] S. L. Olsen, T. Skwarnicki, and D. Zieminska, "Nonstandard heavy mesons and baryons: Experimental evidence", Rev. Mod. Phys. **90**, 015003 (2018), arXiv:1708.04012 [hep-ph].

[250] F.-K. Guo, C. Hanhart, U.-G. Meißner, Q. Wang, Q. Zhao, and B.-S. Zou, "Hadronic molecules", Rev. Mod. Phys. **90**, 015004 (2018), arXiv:1705.00141 [hep-ph].

[251] M. Karliner, J. L. Rosner, and T. Skwarnicki, "Multiquark States", Ann. Rev. Nucl. Part. Sci. **68**, 17–44 (2018), arXiv:1711.10626 [hep-ph].

[252] N. Brambilla, S. Eidelman, C. Hanhart, A. Nefediev, C.-P. Shen, C. E. Thomas, A. Vairo, and C.-Z. Yuan, "The XYZ states: experimental and theoretical status and perspectives", Phys. Rept. **873**, 1–154 (2020), arXiv:1907.07583 [hep-ex].

[253] S. Uehara et al., "Observation of a chi-prime(c2) candidate in gamma gamma —> D anti-D production at BELLE", Phys. Rev. Lett. **96**, 082003 (2006), arXiv:hep-ex/0512035.

[254] B. Aubert et al., "Observation of the $\chi_{c2}(2p)$ Meson in the Reaction $\gamma\gamma \to D\bar{D}$ at BaBar", Phys. Rev. D **81**, 092003 (2010), arXiv:1002.0281 [hep-ex].

[255] R. Aaij et al., "Near-threshold $D\bar{D}$ spectroscopy and observation of a new charmonium state", JHEP **07**, 035 (2019), arXiv:1903.12240 [hep-ex].

[256] R. Aaij et al., "Amplitude analysis of the $B^+ \to D^+D^-K^+$ decay", Phys. Rev. D **102**, 112003 (2020), arXiv:2009.00026 [hep-ex].

[257] K. Abe et al., "Observation of a near-threshold omega J/psi mass enhancement in exclusive B —> K omega J/psi decays", Phys. Rev. Lett. **94**, edited by H.-S. Chen, D.-S. Du, W.-G. Li, and C.-D. Lu, 182002 (2005), arXiv:hep-ex/0408126.

[258] B. Aubert et al., "Observation of Y(3940) $\to J/\psi\omega$ in $B \to J/\psi\omega K$ at BABAR", Phys. Rev. Lett. **101**, 082001 (2008), arXiv:0711.2047 [hep-ex].

[259] P. del Amo Sanchez et al., "Evidence for the decay X(3872) —> J/ psi omega", Phys. Rev. D **82**, 011101 (2010), arXiv:1005.5190 [hep-ex].

[260] S. Uehara et al., "Observation of a charmonium-like enhancement in the gamma gamma —> omega J/psi process", Phys. Rev. Lett. **104**, 092001 (2010), arXiv:0912.4451 [hep-ex].

[261] X. Liu, Z.-G. Luo, and Z.-F. Sun, "X(3915) and X(4350) as new members in P-wave charmonium family", Phys. Rev. Lett. **104**, 122001 (2010), arXiv:0911.3694 [hep-ph].

[262] J. P. Lees et al., "Study of $X(3915) \to J/\psi\omega$ in two-photon collisions", Phys. Rev. D **86**, 072002 (2012), arXiv:1207.2651 [hep-ex].

[263] N. Brambilla et al., "Heavy Quarkonium: Progress, Puzzles, and Opportunities", Eur. Phys. J. C **71**, 1534 (2011), arXiv:1010.5827 [hep-ph].

[264] E. J. Eichten, K. Lane, and C. Quigg, "New states above charm threshold", Phys. Rev. D **73**, [Erratum: Phys.Rev.D 73, 079903 (2006)], 014014 (2006), arXiv:hep-ph/0511179.

[265] F.-K. Guo, C. Hanhart, G. Li, U.-G. Meissner, and Q. Zhao, "Effect of charmed meson loops on charmonium transitions", Phys. Rev. D **83**, 034013 (2011), arXiv:1008.3632 [hep-ph].

[266] Z.-Y. Zhou, Z. Xiao, and H.-Q. Zhou, "Could the $X(3915)$ and the $X(3930)$ Be the Same Tensor State?", Phys. Rev. Lett. **115**, 022001 (2015), arXiv:1501.00879 [hep-ph].

[267] F.-K. Guo and U.-G. Meissner, "Where is the $\chi_{c0}(2P)$?", Phys. Rev. D **86**, 091501 (2012), arXiv:1208.1134 [hep-ph].

[268] V. Baru, C. Hanhart, and A. V. Nefediev, "Can X(3915) be the tensor partner of the X(3872)?", JHEP **06**, 010 (2017), arXiv:1703.01230 [hep-ph].

[269] S. L. Olsen, "Is the $X(3915)$ the $\chi_{c0}(2P)$?", Phys. Rev. D **91**, 057501 (2015), arXiv:1410.6534 [hep-ex].

[270] K. Chilikin et al., "Observation of an alternative $\chi_{c0}(2P)$ candidate in $e^+e^- \to J/\psi D\bar{D}$", Phys. Rev. D **95**, 112003 (2017), arXiv:1704.01872 [hep-ex].

[271] P. G. Ortega, J. Segovia, D. R. Entem, and F. Fernández, "Charmonium resonances in the 3.9 GeV/c^2 energy region and the $X(3915)/X(3930)$ puzzle", Phys. Lett. B **778**, 1–5 (2018), arXiv:1706.02639 [hep-ph].

[272] E. Wang, W.-H. Liang, and E. Oset, "Analysis of the $e^+e^- \to J/\psi D\bar{D}$ reaction close to the threshold concerning claims of a $\chi_{c0}(2P)$ state", Eur. Phys. J. A **57**, 38 (2021), arXiv:1902.06461 [hep-ph].

[273] E. Wang, H.-S. Li, W.-H. Liang, and E. Oset, "Analysis of the $\gamma\gamma \to D\bar{D}$ reaction and the $D\bar{D}$ bound state", Phys. Rev. D **103**, 054008 (2021), arXiv:2010.15431 [hep-ph].

[274] D. Gamermann, E. Oset, D. Strottman, and M. J. Vicente Vacas, "Dynamically generated open and hidden charm meson systems", Phys. Rev. D **76**, 074016 (2007), arXiv:hep-ph/0612179.

[275] S. Prelovsek, S. Collins, D. Mohler, M. Padmanath, and S. Piemonte, "Charmonium-like resonances with $J^{PC} = 0^{++}$, 2^{++} in coupled $D\overline{D}$, $D_s\overline{D}_s$ scattering on the lattice", JHEP **06**, 035 (2021), arXiv:2011.02542 [hep-lat].

[276] L. Liu, G. Moir, M. Peardon, S. M. Ryan, C. E. Thomas, P. Vilaseca, J. J. Dudek, R. G. Edwards, B. Joo, and D. G. Richards, "Excited and exotic charmonium spectroscopy from lattice QCD", JHEP **07**, 126 (2012), arXiv:1204.5425 [hep-ph].

[277] R. Aaij et al., "A model-independent study of resonant structure in $B^+ \to D^+D^-K^+$ decays", Phys. Rev. Lett. **125**, 242001 (2020), arXiv:2009.00025 [hep-ex].

[278] D. Drechsel, M. Gorchtein, B. Pasquini, and M. Vanderhaeghen, "Fixed t subtracted dispersion relations for Compton Scattering off the nucleon", Phys. Rev. C **61**, 015204 (1999), arXiv:hep-ph/9904290.

[279] D.-Y. Chen, J. He, X. Liu, T. Matsuki, and T. Matsuki, "Does the enhancement observed in $\gamma\gamma \to D\bar{D}$ contain two P-wave higher charmonia?", Eur. Phys. J. C **72**, 2226 (2012), arXiv:1207.3561 [hep-ph].

[280] F. Niecknig, B. Kubis, and S. P. Schneider, "Dispersive analysis of $\omega - > 3\pi$ and $\phi - > 3\pi$ decays", Eur. Phys. J. C **72**, 2014 (2012), arXiv:1203.2501 [hep-ph].

[281] M. Albaladejo, I. Danilkin, S. Gonzalez-Solis, D. Winney, C. Fernandez-Ramirez, A. N. H. Blin, V. Mathieu, M. Mikhasenko, A. Pilloni, and A. Szczepaniak, "$\omega \to 3\pi$ and $\omega\pi^0$ transition form factor revisited", Eur. Phys. J. C **80**, 1107 (2020), arXiv:2006.01058 [hep-ph].

[282] K. Chilikin et al., personal communication.

[283] C.-Y. Wong, "Molecular states of heavy quark mesons", Phys. Rev. C **69**, 055202 (2004), arXiv:hep-ph/0311088.

[284] Y.-J. Zhang, H.-C. Chiang, P.-N. Shen, and B.-S. Zou, "Possible S-wave bound-states of two pseudoscalar mesons", Phys. Rev. D **74**, 014013 (2006), arXiv:hep-ph/0604271.

[285] J. Nieves and M. P. Valderrama, "The Heavy Quark Spin Symmetry Partners of the X(3872)", Phys. Rev. D **86**, 056004 (2012), arXiv:1204.2790 [hep-ph].

[286] C. Hidalgo-Duque, J. Nieves, and M. P. Valderrama, "Light flavor and heavy quark spin symmetry in heavy meson molecules", Phys. Rev. D **87**, 076006 (2013), arXiv:1210.5431 [hep-ph].

[287] C. Hidalgo-Duque, J. Nieves, A. Ozpineci, and V. Zamiralov, "X(3872) and its Partners in the Heavy Quark Limit of QCD", Phys. Lett. B **727**, 432–437 (2013), arXiv:1305.4487 [hep-ph].

[288] V. Baru, E. Epelbaum, A. A. Filin, C. Hanhart, U.-G. Meißner, and A. V. Nefediev, "Heavy-quark spin symmetry partners of the X (3872) revisited", Phys. Lett. B **763**, 20–28 (2016), arXiv:1605.09649 [hep-ph].

[289] X.-K. Dong, F.-K. Guo, and B.-S. Zou, "A survey of heavy-antiheavy hadronic molecules", Progr. Phys. **41**, 65–93 (2021), arXiv:2101.01021 [hep-ph].

[290] M. Ablikim et al., "Measurement of the branching fraction for $\psi(3770) \to \gamma\chi_{c0}$", Phys. Lett. B **753**, 103–109 (2016), arXiv:1511.01203 [hep-ex].

[291] G. Breit and E. Wigner, "Capture of Slow Neutrons", Phys. Rev. **49**, 519–531 (1936).

[292] D. Spehler and S. F. Novaes, "Helicity wave functions for massless and massive spin-2 particles", Phys. Rev. D **44**, 3990–3993 (1991).

[293] J. M. Blatt and V. F. Weisskopf, *Theoretical nuclear physics* (Springer, New York, 1952).

List of acronyms

BES	Beijing Spectrometer
BNL	Brookhaven National Laboratory
BSE	Bethe-Salpeter Equation
BSM	Beyond the Standard Model
BW	Breit-Wigner
CC	Coupled-Channels
CDD	Castillejo-Dalitz-Dyson
CERN	European Organization for Nuclear Research
χPT	Chiral Perturbation Theory
COMPASS	Common Muon and Proton Apparatus for Structure and Spectroscopy
DR	Dispersion Relation
EFT	Effective Field Theory
EIC	Electron-Ion Collider
EW	ElectroWeak
FAIR	Facility for Antiproton and Ion Research
Fermilab	Fermi National Accelerator Laboratory
HLbL	Hadronic Light-by-Light scattering
HVP	Hadronic Vacuum Polarization
IAM	Inverse Amplitude Method
JLab	Thomas Jefferson National Accelerator Facility
J-PARC	Japan Proton Accelerator Research Complex
LEC	Low-Energy Constant
LHC	Large Hadron Collider
LO	Leading Order
mIAM	modified Inverse Amplitude Method
MO	Muskhelishvili-Omnès
NLO	Next-to-Leading Order
NNLO	Next-to-Next-to-Leading Order
PANDA	antiProton ANnihilation at DArmstadt
PDG	Particle Data Group
QED	Quantum ElectroDynamics
QCD	Quantum ChromoDynamics
SC	Single-Channel
SM	Standard Model
TFF	Transition Form Factor
UχPT	Unitarized Chiral Perturbation Theory
VMD	Vector Meson Dominance

Curriculum vitae

Acknowledgements